The clumped and oxygen isotope compositions of biogenic carbonate archives: kinetic effects and reconstruction of seawater temperatures and seawater $\delta^{18}O$

Dissertation zur Erlangung des Doktorgrades der Naturwissenschaften

vorgelegt beim Fachbereich 11
der Johann Wolfgang Goethe-Universität
in Frankfurt am Main

von
David Bajnai
aus Veszprém, Ungarn

Frankfurt am Main (2019)

(D 30)

Vom Fachbereich 11 der Johann Wolfgang Goethe-Universität Frankfurt am Main
als Dissertation angenommen.

Dekan: Prof. Dr. Georg Rümpker

Gutachter: apl. Prof. Dr. Jens Fiebig
Johann Wolfgang Goethe-Universität Frankfurt am Main, DE

Prof. Dr. Gregory D. Price
University of Plymouth, UK

Prof. Dr. Silke Voigt
Johann Wolfgang Goethe-Universität Frankfurt am Main, DE

Datum der Disputation: 09.07.2019

Table of Contents

List of Figures

List of Tables

List of Supplementary Data (e-attachments)

Supplementary Data 2.1 (*e-attachment*) | Results of the clumped isotope measurements including all replicate analyses for the samples (modern brachiopods), standards and equilibrated gases, as well as the ETFs.

Supplementary Data 2.2 (*e-attachment*) | A summary table for the results of the stable isotope and trace element analyses, for the environmental and growth parameters of the modern brachiopods investigated in this study, and the calculations for the offset Δ_{47} and offset $\delta^{18}O$ values.

Supplementary Data 2.3 (*e-attachment*) | A summary table for the SIMS analyses.

Supplementary Data 3.1 (*e-attachment*) | Results of the clumped isotope measurements including all replicate analyses for the samples (DSDP Site 511), standards and equilibrated gases, as well as the ETFs.

Supplementary Data 3.2 (*e-attachment*) | Results of the clumped isotope measurements including all replicate analyses for the samples (Valanginian belemnites from the northern hemisphere), standards and equilibrated gases, as well as the ETFs.

Supplementary Data 4.1 (*e-attachment*) | Results of the clumped isotope measurements including all replicate analyses for the samples (Jurassic belemnites and ammonites from Russia), standards and equilibrated gases, as well as the ETFs.

Supplementary Data 5.1 (*e-attachment*) | Results of the clumped isotope measurements for the equilibrated (1000 °C and 25 °C) gases, calculations of natural abundances of CO_2 and N_2O isotopologues, and calculation of the shot noise limit for Δ_{47} and Δ_{48} measurements.

Supplementary Data 6.1 (*e-attachment*) | Results of the clumped isotope measurements including all replicate analyses for the standards (ETH1–4) and equilibrated gases, and the ETFs.

Supplementary Data 7.1 (*e-attachment*) | A compilation of belemnite $\delta^{18}O$ values for the Mesozoic.

Supplementary Data 7.2 (*e-attachment*) | Results of the clumped isotope measurements including all replicate analyses for the samples (Cenomanian belemnites), standards and equilibrated gases, as well as the ETFs.

Acknowledgements

First, I would like to express my gratitude to my supervisor, Jens Fiebig, who mentored me throughout my PhD. Thank you for your encouragement, constant support, scientific advice, and for always being available for my questions! I feel honoured that I was able to participate in many international conferences and that you introduced me to the scientific community. I am grateful to Sven Hofmann for kindly helping me with the proper laboratory techniques and his assistance. Thanks to the rest of the Frankfurt clumped team, Ulrike Wacker, Niklas Löffler, Katharina Methner, Emilija Krsnik, Charlotte Prud'homme, Christoph Schreiber, and Manuel Schumann, for helping with the lab work.

Over the years, I greatly benefitted from the tutelage of Gregory. D. Price, Silke Voigt, Jacek Raddatz, Uwe Brand, Adam Tomašových, Claire Rollion-Bard, Michael Joachimski, Bernd R. Schöne, and Hubert Wierzbowski. My co-authors, Madeleine Vickers, Jolien Linckens, Sándor Kele, Sara Milner Garcia, Jacek Raddatz, Cristina Primo-Ramos, Daniela Henkel, Lucia Angiolini, Mikhail A. Rogov, Ekaterina M. Tesakova, and Andreas Mulch all contributed to this thesis.

Thanks for the BASE-LiNE Earth ITN, especially Daniela Henkel and Anton Eisenhauer, for organising workshops and conferences that made a positive impact on me. This study was supported by the European Union's Horizon 2020 research and innovation program under the Marie Skłodowska-Curie grant no. 643084.

I want to thank my friends in Frankfurt, Konstantin, Dagmar, Rosie, Alex, David, Pia, Severin, Linda, Richard, Leo, and Jens, for their support, constructive comments, fruitful discussions, and making my time here pleasant and cheerful. I am grateful to the staff of the Goethe University Frankfurt and the colleagues at the Institute of Geosciences for being welcoming. Special thanks to Cornelia Anhalt for helping with the contracts and travel arrangements.

Hálával tartozom a szüleimnek, nagymamámnak és testvéreimnek a pozitív hozzáállásukért és támogatásukért. Köszönöm Dalmának a bizalmát és a bátorítását. Köszönöm az otthoni barátaimnak és kollégáimnak a segítségüket és támogatásukat.

Abstract

During my PhD, I was applying the clumped isotope technique to modern brachiopods and fossil belemnites, and I conducted methodological work. Carbonate clumped isotope thermometry is a tool to reconstruct carbonate precipitation temperatures. In contrast to oxygen isotope thermometry, *i.e.,* the $\delta^{18}O$-thermometer, the carbonate clumped isotope thermometer does not require an estimate for the oxygen isotope composition of the seawater, as it considers the fractionation of isotopes exclusively amongst carbonate isotopologues. The Δ_{47} value of a carbonate expresses the abundance of the $^{13}C–^{18}O$ bond bearing carbonate isotopologue, within the carbonate, relative to its random distribution. In thermodynamic equilibrium, the Δ_{47} value of a given carbonate is solely a function of the carbonate precipitation temperature. However, kinetic isotope fractionations, *i.e.,* vital effects, driven by diffusion, pH or incomplete oxygen isotope exchange between water and dissolved inorganic carbonate species can cause the carbonate to be precipitated with isotopic compositions that are offset from those predicted for thermodynamic equilibrium.

Brachiopods serve as important geochemical archives of past climate conditions. To investigate the nature and significance of kinetic controls on brachiopod shell $\delta^{18}O$ and Δ_{47} values, in collaboration with the BASE-LiNE Earth ITN, I analysed the bulk and clumped isotope compositions of eighteen modern brachiopod shells, collected from different geographic locations and water depths that cover a substantial range of growth temperatures. Growth temperatures and seawater $\delta^{18}O$ values for each brachiopod were independently determined. Most of the analysed brachiopods exhibit combined offsets from clumped and oxygen isotope equilibrium, and there is a significant negative correlation between the offset values. The observed correlation slope between offset Δ_{47} and offset $\delta^{18}O$ point to the importance of kinetic effects associated with Knudsen diffusion and incomplete hydration and hydroxylation of $CO_{2\,(aq)}$, occurring during biomineralisation. The correlations between the growth rates of the analysed brachiopods and both the offset Δ_{47} and the offset $\delta^{18}O$ values provide further arguments for the presence of kinetic effects. In conclusion, the oxygen and clumped isotope composition of modern brachiopod shells are affected by growth rate-induced kinetic effects that hinder their use for palaeoceanography.

After identifying kinetic effects in modern brachiopods, I turned to fossil belemnites to reconstruct palaeoseawater temperatures. Belemnite rostra are calcite remains of extinct cephalopods that are commonly used for Jurassic and Cretaceous palaeoceanography. In collaboration with Gregory D. Price (University of Plymouth, UK), I analysed exceptionally well-preserved belemnite rostra from the Jurassic and Cretaceous periods (ca. 160–125 million years ago). Samples were collected from five localities corresponding to a wide range of palaeolatitudes. Our clumped isotope measurements yield balmy seawater temperatures and a shallow latitudinal temperature gradient for the Valanginian (Early Cretaceous, ca. 135 million years ago) northern hemisphere. Our Cretaceous seawater $\delta^{18}O$ values, reconstructed from belemnite $\delta^{18}O$ and Δ_{47}, are in the range of modern values and are more positive than expected for ice-free oceans. Since an erroneous assumption on seawater $\delta^{18}O$ leads to inaccurate carbonate $\delta^{18}O$-based estimates, in collaboration with Hubert Wierzbowski (Polish Geological Institute, Warsaw), we re-investigated a nearly 10 million years long belemnite $\delta^{18}O$-based temperature record from the Jurassic of the Russian Platform. The existing record that assumes a constant seawater $\delta^{18}O$ for the entire period, shows a ca. 10 °C warming. In contrast, our new belemnite clumped isotope record suggests constant seawater temperatures for the whole interval. Thus, the trend in belemnite $\delta^{18}O$ that was interpreted before as a temperature increase is related to a decrease in seawater $\delta^{18}O$, which we postulate to be most likely related to the freshening of the basin.

It is not possible to eliminate the presence of kinetics in belemnites since they went extinct and; thus, their growth temperatures and seawater $\delta^{18}O$ cannot be independently resolved. However, high-precision combined Δ_{47} and Δ_{48} analyses of carbonates has excellent potential to determine accurate palaeotemperatures and to identify rate-limiting biomineralisation processes. In this dissertation, I present methodological work that explores the possibility of such analyses. First, I tested the precision of Δ_{47} and Δ_{48} measurements of equilibrated gases, acquired using two sample preparation techniques. Secondly, I show that high-precision and accuracy carbonate Δ_{48} analyses are possible using the analytical setup at the Goethe University, that consists of a custom-built carbonate digestion and purification line and a Thermo Scientific™ 253 Plus™ mass spectrometer. A combined analysis of Δ_{47} and Δ_{48} in belemnites, may shed light on the relevance, nature and extent of kinetic effects in these archives. If applied to brachiopods, such investigations may further constrain the kinetics involved during shell secretion.

Chapter 1: Introduction

1.1. Historical context of clumped isotope thermometry

Stable isotope analyses form a crucial part of stratigraphy, palaeontology and palaeoclimate research. Isotopes are variants of an atom that have different masses; they are built up from the same number of protons but have a different number of neutrons. The history of stable isotope geochemistry stretches back to the first half of the 20th century. Alfred Nier built the first isotope ratio mass spectrometer in 1947. During this early times, Urey (1947) and Bigeleisen and Mayer (1947) published their pioneering works on the physical properties of isotopes, addressing isotope fractionation between two substances and within a single substance between its different isotopologues. The isotopologues are molecules that differ only in their isotopic composition. For example, $^{12}C^{16}O^{16}O$ and $^{\mathbf{13}}\mathbf{C}^{16}O^{16}O$ are isotopologues of each other. Multiply-substituted isotopologues, also referred to as "clumped isotopes" (Eiler, 2007), contain two or more rare isotopes. For example, in $^{\mathbf{13}}\mathbf{C}^{\mathbf{18}}\mathbf{O}^{16}O$, which is a multiply-substituted isotopologue of $^{12}C^{16}O^{16}O$, two heavy isotopes ($^{\mathbf{13}}\mathbf{C}$ and $^{\mathbf{18}}\mathbf{O}$) substitute their light counterparts (^{12}C and ^{16}O). Since the relative abundance of multiply-substituted CO_2 isotopologues is very low (Table 1.1), it was impossible to measure them by mass spectrometry until recently. At

Table 1.1 | Relative abundances of the stable carbon and oxygen isotopes and carbon dioxide isotopologues, assuming stochastic distribution.

[1] Assuming isotope ratios equal to VPDB (Chang & Li, 1990). [2] Assuming isotope ratios equal to VSMOW (Baertschi, 1976; Assonov & Brenninkmeijer, 2003; Barkan & Luz, 2005). [3] Calculated for calcite-derived CO_2 using the relative abundances listed above, a 90 °C acid fractionation from Kim et al. (2007), and a $\delta^{18}O_{VPDB}$ of 30.92‰ VSMOW (Coplen et al., 1983). Calculations are found in Supplementary Data 5.1.

C isotopes	atomic weight	rel. abundance[1]
^{12}C	12	98.8820%
^{13}C	13	1.1180%
O isotopes	**atomic weight**	**rel. abundance[2]**
^{16}O	16	99.7610%
^{17}O	17	0.0385%
^{18}O	18	0.2005%
CO_2 isotopologues	**molecular weight**	**rel. abundance[3]**
^{16}O–^{12}C–^{16}O	44	975343.396 ppm
^{16}O–^{13}C–^{16}O	45	11124.690 ppm
^{17}O–^{12}C–^{16}O	45	774.619 ppm
^{18}O–^{12}C–^{16}O	46	4111.203 ppm
^{17}O–^{13}C–^{16}O	46	8.758 ppm
^{17}O–^{12}C–^{17}O	46	0.152 ppm
^{18}O–^{13}C–^{16}O	47	46.483 ppm
^{18}O–^{12}C–^{17}O	47	1.618 ppm
^{17}O–^{13}C–^{17}O	47	0.002 ppm
^{18}O–^{12}C–^{18}O	48	4.295 ppm
^{17}O–^{13}C–^{18}O	48	0.018 ppm
^{18}O–^{13}C–^{18}O	49	0.049 ppm

the beginning of the 2000s at Caltech, John Eiler and Edwin Schauble started studying the multiply-substituted CO_2 isotopologues in the air with the initial aim to constrain the origin and chemistry of atmospheric carbon dioxide. They published the results of their first successful measurements in 2004, in which they postulate that the clumped isotope composition of Los Angeles air is primarily determined by fractionations occurring during plant respiration, with contributions from anthropogenic and other unknown processes (Eiler & Schauble, 2004). The thermodynamic models of Wang *et al.* (2004) and Schauble *et al.* (2006) provided the theoretical basis for using the isotopic composition of multiply-substituted carbonate molecules as palaeothermometers. The first calibration for the carbonate clumped isotope thermometer was published soon after by Ghosh *et al.* (2006). They analysed biogenic and inorganic carbonates precipitated from waters with independently known temperatures for their clumped isotope composition and showed that it is viable to reconstruct carbonate precipitation temperatures using clumped isotope thermometry.

The traditional oxygen isotope thermometer (Urey, 1947; McCrea, 1950; Epstein *et al.*, 1951; Epstein *et al.*, 1953) requires information on the $\delta^{18}O$ of the fluid to calculate carbonate precipitation temperatures: it is based on the temperature dependence of the oxygen isotope fractionation factor between $CaCO_3$ and H_2O ($\alpha^{18}_{c\text{-}w} \equiv [^{18}O/^{16}O]_c$ / $[^{18}O/^{16}O]_w$). The $\alpha^{18}_{c\text{-}w}$ is a function of the carbonate precipitation temperature and the oxygen isotope composition of the ambient water (Epstein *et al.*, 1951; Kim & O'Neil, 1997). For geological samples, the oxygen isotope composition of the seawater is not known; therefore, to calculate palaeoseawater temperatures from the $\delta^{18}O$ of carbonate fossils, a seawater $\delta^{18}O$ must be assumed. The importance of the clumped isotope thermometer is that it does not require information on the composition of the fluid to calculate carbonate precipitation temperatures, as the fractionation of isotopes amongst isotopologues of a single internal phase is addressed.

For deep-time palaeoceanography, *i.e.,* for the Palaeozoic and Mesozoic (541–66 million years ago), respectively, the calcite remains of fossil brachiopods and belemnites provide the most attractive archive, because of their frequent occurrence, good preservation potential, and large size (Veizer & Prokoph, 2015). Came *et al.* (2007) investigated Early Silurian and Pennsylvanian brachiopods for their clumped isotope composition. Their results yielded warm temperatures (> 30 °C) and seawater $\delta^{18}O$ values that are comparable to modern oceans (ca. -1‰ SMOW). Cummins *et al.* (2014)

provided similar results: their brachiopods from the Late Ordovician/Early Silurian (ca. 445 million years ago) gave warm clumped isotopes-based temperature estimates and revealed a slight, ca. 5 °C, cooling during the Hirnantian glaciation. Modern brachiopods were first investigated by Came *et al.* (2014) who determined an apparent relationship between the growth temperatures and the clumped isotope composition of the shells, acquired from 25 °C acid digestion. Price and Passey (2013) used belemnite rostra to investigate the Valanginian (Early Cretaceous, ca. 135 million years ago) climate. They acquired warm seawater temperatures for high northern latitudes and posited that the latitudinal gradient was reduced compared to modern. In the study of Meyer *et al.* (2018), the clumped isotope composition of Maastrichtian (Late Cretaceous, ca. 71 million years ago) belemnites yielded seawater temperatures that are cooler than coeval TEX_{86}-based estimates but similar to modern temperatures at the same latitudes. Clumped isotope analyses of brachiopods and belemnites have great potential for palaeoceanography.

1.2. Theoretical background of clumped isotope thermometry

Multiply-substituted isotopologues (*e.g.,* $^{\mathbf{13}}\mathbf{C}^{\mathbf{18}}\mathbf{O}^{16}O$, $^{12}C^{\mathbf{18}}\mathbf{O}^{\mathbf{17}}\mathbf{O}$, $^{\mathbf{13}}\mathbf{C}^{16}O^{\mathbf{17}}\mathbf{O}$) have different thermodynamic properties, such as bond vibration frequency and zero-point energy, compared to the isotopologues that contain only one heavy isotope ($^{\mathbf{13}}\mathbf{C}^{16}O^{16}O$, $^{12}C^{\mathbf{18}}\mathbf{O}^{16}O$). The substitution a light isotope with its heavy counterpart influences the molecule's stability and its reaction kinetics. For example, the potential energy of the lowest energy level of a diatomic molecule (*e.g.,* H_2) is reduced when a light isotope (H) is substituted by a heavy (D) isotope: the zero-point energy of a bond between two heavy isotopes (D–D) is lower than the zero-point energy of a bond between a heavy and light isotope (H–D), which in turn is lower than the zero-point energy of a bond between two light isotopes (H–D) (Urey, 1947; Bigeleisen, 1955; Bigeleisen, 1965; Eiler, 2007) (Figure 1.1). The decrease in vibrational energy of a doubly-substituted molecule slightly exceeds twice of the decrease in vibrational energy associated with a single heavy isotope substitution. This small difference is a thermodynamic driving force that promotes the clumping of heavy isotopes in multiply-substituted isotopologues. The preferential bonding of heavy isotopes can be described by a homogeneous isotope exchange reaction that involves isotopologues of a single phase:

(Eq. 1.1) $$^{13}C^{16}O_3^{2-} + {}^{12}C^{18}O^{16}O_2^{2-} \rightleftharpoons {}^{13}C^{18}O^{16}O_2^{2-} + {}^{12}C^{16}O_3^{2-}$$

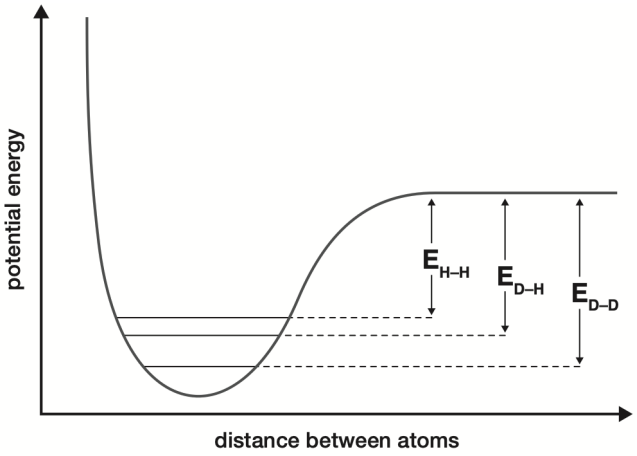

Figure 1.1 | Schematic potential energy (Morse potential) curve of the H_2 molecule. According to the quantum theory, the lowest potential energy level of the molecule is above the minimum of the potential energy curve. The zero-point energy is reduced with a single heavy isotope substitution ($E_{H\text{-}D}$) and reduced further with a second heavy isotope substitution ($E_{D\text{-}D}$). The decrease in zero-point energy after a second heavy isotope substitution is slightly greater than two times the decrease in the zero-point energy after only one heavy isotope substitution; therefore, the $E_{D\text{-}D}$ substitution is the energetically preferable situation. Figure is redrawn after Bigeleisen (1965) and Eiler (2007).

The measure of clumped isotope thermometry is the Δ_{47} value, expressed in ‰. The Δ_{47} value of a carbonate, expresses the abundance of the ^{13}C–^{18}O bond bearing carbonate isotopologue, within the carbonate, relative to its random distribution. In the case of true stochastic distribution Δ_{47} would be 0‰, and it increases with decreasing temperature. The Δ_{47} value of CO_2 is defined by the following equation:

$$\Delta_{47} = -1000 \ln\left(\frac{K}{K^*}\right) = \left[\left(\frac{R^{47}}{R^{47*}} - 1\right) - \left(\frac{R^{46}}{R^{46*}} - 1\right) - \left(\frac{R^{45}}{R^{45*}} - 1\right)\right] \times 1000 \quad \text{(Eq. 1.2)}$$

where K is the equilibrium constant of Equation 1.1, K* is the equilibrium constant of the same equation in case of stochastic distribution, R^i is the abundance ratio of isotopologues mass 47–45 relative to the isotopologue mass 44, and R^i* is the corresponding abundance ratio in case of stochastic distribution. The R^i values can be calculated relative to a reference gas of known isotopic composition:

$$R^i = \left(\frac{\delta_i}{1000} + 1\right) \times R^i_{ref} \quad \text{(Eq. 1.3)}$$

where R^i_{ref} can be calculated from the known isotopic composition of the reference gas and δ_i is:

$$\delta_i = \left(\frac{I^i_{sample}}{I^i_{ref}} - 1\right) \times 1000 \quad \text{(Eq. 1.4)}$$

where the I^i values can be calculated from the intensities measured by the mass spectrometer. The Ri* abundance ratio can be calculated from the $\delta^{18}O$ and $\delta^{13}C$ of the samples, assuming that the $\delta^{13}C$ and $\delta^{18}O$ are independent of the distribution of the isotopologues:

(Eq. 1.5) $$R^{45*} = r^{13} + r^{17}$$

(Eq. 1.6) $$R^{46*} = 2 \times r^{18} + 2 \times r^{13} \times r^{17} + (r^{17})^2$$

(Eq. 1.7) $$R^{47*} = 2 \times r^{13} \times r^{18} + 2 \times r^{17} \times r^{18} + r^{13} \times (r^{17})^2$$

where r^{13}, r^{17}, r^{18} depict the $^{13}C/^{12}C$, $^{17}O/^{16}O$, and $^{18}O/^{16}O$ ratios if the sample, respectively (Huntington *et al.*, 2009).

1.3. Δ_{47}–temperature calibrations

When investigating the temperature dependence of Δ_{47} in carbonates, different laboratories obtained inconsistent calibrations. The slope of the Δ_{47}–$10^6/T^2$ calibration lines that are made with digestion temperatures > 70 °C ranges from 0.33 (Dennis & Schrag, 2010; Wacker *et al.*, 2014; Löffler *et al.*, 2019) to 0.44 (Kele *et al.*, 2015). The observed inconsistencies could relate to partial re-equilibration of CO_2 with water during sample preparation (Wacker *et al.*, 2013), isobaric contamination due to ineffective purification of the analyte gas (Eiler & Schauble, 2004), the pressure baseline effect (Bernasconi *et al.*, 2013; Fiebig *et al.*, 2016), the choice of parameters for ^{17}O-correction (Daëron *et al.*, 2016; Petersen *et al.*, in review), a difference in analytic setup, *i.e.,* the type of capillaries, mass spectrometer, and measurement mode, uncertainties associated with linear regression (Wacker *et al.*, 2014), the set of standards or gases used for correction (Ghosh *et al.*, 2006; Bernasconi *et al.*, 2018), the limited number of analysed samples and replicates, and to a too narrow temperature range that the investigated samples cover (Fernandez *et al.*, 2017).

In Chapter 2, I show that brachiopods yield an apparent Δ_{47}–temperature relationship that has a steep slope (ca. 0.45). Growth rate related kinetic effects in fast-growing brachiopods lead to carbonate Δ_{47} values that are positively offset from expected equilibrium. Kinetic effects are more prominent at colder temperatures because it takes longer for the dissolved inorganic carbon species (DIC) to reach isotopic equilibrium in the calcifying fluid. A positive Δ_{47} offset at colder temperatures may explain why fast-growing carbonates yield steep-sloped Δ_{47}-temperature relationships.

To reconstruct carbonate precipitation temperatures from the Δ_{47} of fossil biogenic carbonates, in this dissertation I use the shallow-slope, in-house Wacker *et al.* (2014) calibration (Figure 1.2). Daëron *et al.* (2016) suggests using the IUPAC, *i.e.,* [*Brand*], set of isotopic parameters to calculate the raw δ_i and Δ_i values: $R^{13}_{PDB} = 0.01118$, $R^{18}_{VSMOW} = 0.0020052$, $R^{17}_{VSMOW} = 0.00038475$, and $\lambda = 0.528$ (Brand *et al.*, 2010). Petersen

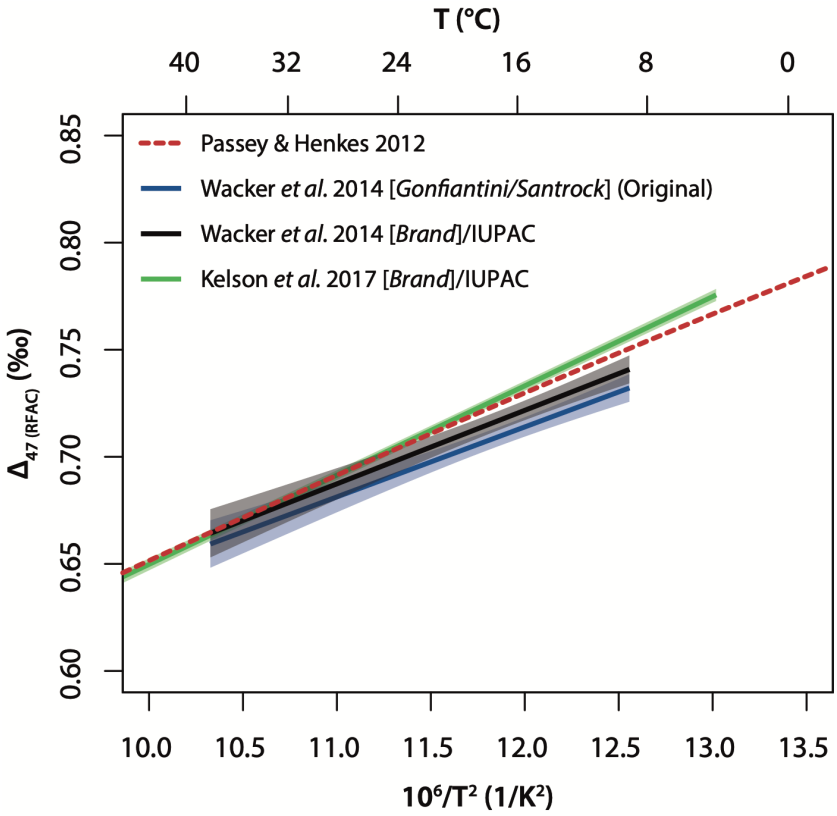

Figure 1.2 | Δ_{47}–temperature calibrations used in this thesis to calculate carbonate precipitation temperatures.
In Chapter 2, we use the theoretical calibration of Passey and Henkes (2012) to calculate expected equilibrium $\Delta_{47\ (CDES\ 25°C)}$ values for modern brachiopods. To calculate seawater temperatures from fossil belemnites in Chapters 3 and 4 we use the in-house Wacker *et al.* (2014) calibration, recalculated using the [*Brand*]/IUPAC isotopic parameters (Equation 1.9). In the 20–40 °C temperature range, the difference between the shallow-sloped Wacker *et al.* (2014) [*Brand*]/*IUPAC*-recalculated and the steep-sloped Kelson *et al.* (2017) [*Brand*]/*IUPAC*-recalculated calibrations is ca. 2 °C, comparable to the external 1σ S.E. of the replicate analyses. On this plot, all equations consider a 25–90 °C acid fractionation factor of 0.088‰ (Petersen *et al.*, in review).

et al. (in review) showed by compiling and re-calculating various calibrations that the use of the [*Brand*]/IUPAC parameters can reduce inter-laboratory discrepancies. The original Wacker *et al.* (2014) calibration was calculated using the [*Gonfiantini/Santrock*] isotopic parameters (R^{13}_{PDB} = 0.0112372, R^{18}_{VSMOW} = 0.0020052, R^{17}_{VSMOW} = 0.0003799 and λ = 0.5164). I reprocessed the original data with Easotope (John & Bowen, 2016) using the [*Brand*]/IUPAC set of isotopic parameters. An error-considering linear regression line fitted on the reprocessed data yields the following relationship:

(Eq. 1.8) $$\Delta_{47\ (RFAC)} = 0.0348(\pm 0.0026) \times 10^6/T^2 + 0.3039(\pm 0.0309)$$

$$N = 7,\ R^2 = 0.97,\ p\text{-value} < 0.001$$

where T is in Kelvin and Δ_{47} is in ‰. For the same set of data but with slightly different data treatment Petersen *et al.* (in review) acquired a relationship indistinguishable to Equation 1.8 (Figure 1.2):

(Eq. 1.9) $$\Delta_{47\ (\mathrm{RFAC})} = 0.0344(\pm 0.0053) \times 10^6/\mathrm{T}^2 + 0.310(\pm 0.065)$$

$$\mathrm{N} = 7,\ \mathrm{R}^2 = 0.96,\ p\text{-value} < 0.001$$

To be consistent with future studies and to produce data that is readily comparable with temperature estimates from other laboratories, in this dissertation I use this latter relationship to calculate carbonate precipitation temperatures.

The calibration lines acquired in different laboratories intersect each other in the 20–40 °C range. Most of the fossil samples investigated in this study are expected to yield temperatures in or close to this range. Thus, the difference in calculated temperatures between the shallow-slope Wacker et al. (2014) and a steeper-sloped calibration, *i.e.*, the Kelson et al. (2017) calibration (Figure 1.2), are smaller the 1σ S.E. of the replicate analyses, generally < 2 °C.

1.4. Equilibrium and vital effects

The overall oxygen isotope equilibrium between carbonate and water is only dependent on the precipitation temperature, and it can only be attained if both the dissolved inorganic carbon (DIC ∋ $CO_{2\ (aq)}$ + CO_3^{2-} + HCO_3^- + H_2CO_3) pool is in equilibrium with H_2O ("solution equilibrium") and if the DIC is in equilibrium with the precipitating carbonate ("crystal equilibrium").

In the "pH-model" of Zeebe (1999), the biogenic carbonate inherits the weighted average isotope composition of the DIC. It assumes that the solution is in equilibrium. With an increase in pH, the relative concentration of HCO_3^- among the DIC species decreases and CO_3^{2-} becomes the major component (Beck *et al.*, 2005) and; thus, the major source of carbon and oxygen for the precipitated calcite (Zeebe, 1999). Since CO_3^{2-} is isotopically lighter than HCO_3^- (Usdowski & Hoefs, 1993), calcite precipitating at high pH will inherit the overall lighter oxygen isotope composition of the DIC.

Biogenic carbonates may not attain thermodynamic equilibrium with seawater due to non-equilibrium biological fractionation processes that occur during calcification, *i.e.*, vital effects. Vital effects can be related to respiration, pH regulation, diffusive isotope transport through membranes, and disassociation of $CO_{2\ (aq)}$ via hydration and

hydroxylation reactions. Vital effects influence the oxygen isotope composition of benthic and planktonic foraminifera (Grossman, 1987; Spero *et al.*, 1997; Zeebe, 1999), coccolithophores (Hermoso *et al.*, 2014), corals (McConnaughey, 1989a, 1989b; Adkins *et al.*, 2003) and brachiopods (Lowenstam, 1961; Carpenter & Lohmann, 1995).

Kinetic isotope effects influence the isotope composition of the carbonate skeleton of non-symbiont corals (McConnaughey, 1989a, 1989b). In the calcification model of McConnaughey (1989b), the carbonate precipitates from the extracellular calcifying fluid (ECF) that is separated from the seawater by bilipid membrane. This organic membrane is only permeable for uncharged $CO_{2\ (aq)}$ but not for other DIC species, such as CO_3^{2-} or HCO_3^- ions. Ca^{2+} ions, necessary for carbonate formation, are transported into the ECF via a CaATPase enzymatic pump, which at the same time removes two H^+ ions to maintain the neutral charge of the ECF. In the ECF, $CO_{2\ (aq)}$ is transformed into HCO_3^- via hydration and hydroxylation reactions. The HCO_3^- subsequently disassociates into H^+ and CO_3^{2-}, which latter, in turn, forms $CaCO_3$ with a Ca^{2+} ion. The hydration and hydroxylation reactions proceed to oxygen isotope equilibrium with ambient water orders of magnitude slower than the rate of oxygen isotope equilibration through the HCO_3^- (dis)association (Johnson, 1982). Both hydration and hydroxylation reactions preferentially select light carbon and oxygen isotopes, but to a different degree. If the carbonate precipitation rate is high, the carbonate may form from DIC that has not reached oxygen and carbon isotopic equilibrium with ambient water. Thus, the carbonate inherits a lighter than expected oxygen and carbon isotope composition from the DIC. The pH of the solution affects the ratio between hydration and hydroxylation reactions as well as the rates of each equilibration reaction, leading to different extents of depletion in heavy isotopes relative to overall equilibrium. A kinetic fractionation, as described by McConnaughey (1989b) can explain the positive correlation between $\delta^{13}C$ and $\delta^{18}O$ values in biogenic carbonates. Carbonic anhydrase, an enzyme that accelerates oxygen isotope exchange between CO_3^{2-}, HCO_3^- and H_2O, can explain the different slopes between $\delta^{13}C$ and $\delta^{18}O$ (Chen *et al.*, 2018).

In an alternative calcification model of Adkins *et al.* (2003), the covariation of $\delta^{13}C$ and $\delta^{18}O$ results from two separate mechanisms for carbon and oxygen, which both lead to a depletion in heavy isotopes. The sources of carbon in the ECF are the $CO_{2\ (aq)}$ that diffused through the cell membrane or a DIC leak. The amount of $CO_{2\ (aq)}$ that diffuses is dependent on the calcification rate, while the carbon originating from the DIC leak is assumed constant. Diffusion preferentially selects light isotopes. When the calcification

rate is high, and the primary source of carbon in the ECF DIC becomes the light diffused carbon, the solid carbonate will inherit a ^{13}C-depleted carbon isotope composition. Diffusion cannot account for the variation in carbonate $\delta^{18}O$ values because the amount of oxygen in the DIC pool is too large to be affected by the light ^{16}O introduced via diffusion. Instead, the Adkins *et al.* (2003) model for oxygen isotopes is identical to the "pH-model" of Zeebe (1999), where the solution oxygen isotope composition is quenched into the carbonate. High precipitation rates, *i.e.,* active enzymatic Ca^{2+} pumping in the ECF and concurrent H^+ pumping out of the ECF, drive the pH of the ECF towards higher values. At high pH, the DIC becomes dominated by CO_3^{2-} that is depleted in heavy oxygen compared to HCO_3^- and water. Since, according to this model the solid carbonate forms proportionally from the available DIC species, at high pH, *i.e.,* at high growth rates, the $CaCO_3$ will have a light oxygen isotope composition.

Kinetics at the crystal/fluid interface may also play an essential role in determining the oxygen isotope composition of the solid carbonate. In the "growth entrapment model" of Watson (2004), the mineral surface captures the isotope composition of the DIC. Due to the diffusion of ions in the outermost layer of the solid; however, the bulk crystal will have a different composition. At high growth rates, ion mobility in the surface region is outpaced by $CaCO_3$ formation; thus, the crystal will be in kinetic disequilibrium, whereas at slow growth rates, diffusion may proceed to equilibrium. The ratio of carbonate dissolution and precipitation is an additional factor that controls the carbonate–fluid fractionation (DePaolo, 2011). The ion-by-ion crystal growth model explains the kinetic apparent oxygen isotope fractionation factor between calcite and water ($1000\ln\alpha^{18}_{c\text{-}w} \equiv \Delta^{18}O_{c\text{-}w}$) as a function of temperature, calcifying fluid pH, *i.e.,* DIC speciation, and crystal growth rate (Wolthers *et al.*, 2012; Watkins *et al.*, 2013; Watkins *et al.*, 2014). Precipitation rate determines if isotope exchange in the DIC and diffusion at the crystal/liquid interface proceed to equilibrium. If the precipitation rate is extremely slow, diffusion on the liquid/crystal interface may proceed to equilibrium, but the carbonate may not attain overall equilibrium unless equilibrium between DIC and H_2O is also attained. In case of fast precipitation rates, despite an equilibrium solution, surface kinetics alone may account for a negative offset in $\delta^{18}O$ values relative to the overall equilibrium of up to 2‰ (Devriendt *et al.*, 2017). The carbonate may only attain overall equilibrium at low carbonate growth rates, low carbonate saturation levels, and low ionic strength of the solution (Coplen, 2007; Devriendt *et al.*, 2017).

Laboratory carbonates are often precipitated faster than the time require to attain isotopic equilibrium in the DIC (Zeebe & Wolf-Gladrow, 2001; Beck *et al.*, 2005). By investigating slowly precipitating natural systems (ca. 30 µg/year for Devils Hole) Coplen (2007) determined the equilibrium temperature dependence of the calcite-water oxygen isotope fractionation factor:

(Eq. 1.10) $$1000\ln\alpha_{c-w} = 17.4 \times 1000/T - 28.6$$

where α_{c-w} is the oxygen isotope fractionation factor between calcite and water, and T is the temperature in K. Experimental and theoretical studies substantiate this finding that the temperature dependence of the calcite-water oxygen isotope fractionation factor as described by earlier laboratory research (Epstein *et al.*, 1953; Kim & O'Neil, 1997) does not represent the thermodynamic equilibrium relationship (Dietzel *et al.*, 2009; Watkins *et al.*, 2014; Devriendt *et al.*, 2017; Levitt *et al.*, 2018; Daëron *et al.*, 2019).

Kinetic effects also influence the clumped isotope composition of biogenic carbonates (Tripati *et al.*, 2015; Watkins & Hunt, 2015). Previous investigations recognised vital effects in the clumped isotope composition of warm and cold-water corals and in certain foraminifera species (Thiagarajan *et al.*, 2011; Saenger *et al.*, 2012; Grauel *et al.*, 2013; Kimball *et al.*, 2016; Spooner *et al.*, 2016). This prompts a closer look at other calcifying marine organisms used to reconstruct palaeoseawater temperatures, such as brachiopods.

1.5. Objectives and outline

The primary objectives of this thesis are:

- To assess if the clumped isotope composition of brachiopod shells accurately records ambient seawater temperatures.
- To apply the clumped isotope method to belemnites to reconstruct Late Jurassic–Early Cretaceous southern high-latitude palaeoseawater temperatures and an Early Cretaceous latitudinal palaeoseawater temperature gradient.
- To apply the clumped isotope method to Middle–Late Jurassic belemnites to re-investigate an apparent temperature increase based on oxygen isotope thermometry.
- To compare the precision of clumped isotope measurements after manual and automated sample preparation.
- To show that high-precision Δ_{48} measurements of carbonates are possible using the analytical setup at the Goethe University Frankfurt.

The chapters of this thesis are based on my peer-reviewed (Chapters 1, 2, and 4), submitted (Chapters 3 and 6) and to be submitted (Chapter 5) publications. To better fit the format of the current dissertation, I amended the original manuscripts. The changes are detailed below.

Chapter 1

This introductory chapter is mainly based on my Hungarian review article on clumped isotope thermometry: Kele and Bajnai (2017). The original text was translated to English and supplemented in parts with new information.

Chapter 2

The aim of this study was to assess if the clumped isotope composition of brachiopod shells accurately records ambient seawater temperatures. For this reason, we investigated the clumped and oxygen isotope composition of modern brachiopod shells with independently known growth temperatures and seawater oxygen isotope compositions. We determined that brachiopod Δ_{47} and $\delta^{18}O$ are affected by growth rate related kinetic effects.

This chapter is based on my published first-author paper: Bajnai *et al.* (2018). For this dissertation, I merged the supplementary information and the main manuscript text that were initially written separately to suit journal guidelines. A reprint of the published manuscript is attached to this dissertation.

Chapter 3

This chapter deals with Late Jurassic–Early Cretaceous belemnites, collected from five locations across different palaeolatitudes. At DSDP Site 511 we addressed the > 10 °C discrepancy between latest Jurassic–Early Cretaceous belemnite $\delta^{18}O$ (-1‰ SMOW + Kim and O'Neil (1997)) and TEX_{86}^{H}-based temperature estimates. Additionally, we analysed 20 Valanginian belemnites from four other locations, to be able to reconstruct an Early Cretaceous seawater temperature and $\delta^{18}O_{sw}$ gradient.

This chapter is based on two of my second-author studies: Price *et al.* (in review); Vickers *et al.* (in review). For this dissertation, I merged the two papers because they complement each other and have similar implications.

Chapter 4

In this study, we investigate Middle–Late Jurassic (ca. 165–145 Ma) belemnites from the subboreal Middle Russian Sea. Previous studies made on belemnites from these locations, assuming a constant $\delta^{18}O_{sw}$ of -1‰ SMOW, inferred a ca. 10 °C warming, during a 10-Myr-long interval. Our new belemnite clumped isotope record; however, suggests constant seawater temperatures for the entire studied interval. Thus, the trend in belemnite $\delta^{18}O$ that was previously interpreted as a temperature increase is related to a decrease in seawater $\delta^{18}O$. We interpret this decrease in seawater $\delta^{18}O$ as a freshening trend that is related to an increased freshwater influx.

This chapter is based on my published second-author paper: Wierzbowski *et al.* (2018). For this dissertation, I recalculated the clumped isotope data using the [*Brand*]/IUPAC set of isotopic parameters as suggested by Daëron *et al.* (2016). To calculate water $\delta^{18}O$ values from belemnite $\delta^{18}O$ and the independently constrained clumped isotope temperatures, I used the 1000lnα–temperature relationship of Coplen (2007), instead of Friedman and O'Neil (1977), which was used in the original publication. Theoretical calculations and laboratory experiments argue that the Coplen (2007) relationship reflects true equilibrium, whereas the Friedman and O'Neil (1977) equation is affected by kinetics (Dietzel *et al.*, 2009; Watkins *et al.*, 2013). Contrary to the original article, in this dissertation, the water temperature and the water $\delta^{18}O$ trends are solely based on cylindroteuthid belemnites to minimise the possible impact of species-specific vital effects on the calculated values. I excluded the chapter of the published paper from this dissertation, in which the water salinity values were calculated. To calculate water salinity values, one has to assume a mean salinity for the Jurassic seawater and a mean seawater oxygen isotope composition (Railsback *et al.*, 1989; Hay *et al.*, 2006). Since both unknowns cannot be constrained independently, the result of the salinity equations will have substantial uncertainty. A reprint of the published manuscript is attached to this dissertation.

Chapter 5

In this study, I compare two CO_2 purification methods. Equilibrated gases were prepared for mass spectrometric analyses by a manual technique or by an automated purification line. We observe that using the automated technique the external standard deviation of

the measured Δ_{47} and Δ_{48} values get smaller. An increase in the precision is likely related to a decreased contamination of the analyte gas.

This chapter is being prepared for submission as a first-author paper.

Chapter 6

The aim of this study is to show that highly precise and accurate Δ_{47} and Δ_{48} analyses of carbonates are possible using the mass spectrometric setup at the Goethe University. With ten replicate analyses of carbonate standards, we attain an external standard error close to the shot noise limit. Combined analysis of Δ_{48} and Δ_{47} in carbonates may open new avenues in the determination of carbonate formation temperatures irrespective of the kinetics involved in carbonate precipitation, and biomineralisation kinetics.

This study is based on my submitted second-author paper: Fiebig *et al.* (in review).

Chapter 7

In this concluding chapter I summarise the findings of this thesis and give an outlook to future investigations.

Chapter 2: Assessing kinetic fractionation in brachiopod calcite using clumped isotopes

Abstract

Brachiopod shells are the most widely used geological archive for the reconstruction of the temperature and the oxygen isotope composition of Phanerozoic seawater. However, it is not conclusive whether brachiopods precipitate their shells in thermodynamic equilibrium. In this study, we investigated the potential impact of kinetic controls on the isotope composition of modern brachiopods by measuring the oxygen and clumped isotope compositions of their shells. Our results show that clumped and oxygen isotope compositions depart from thermodynamic equilibrium due to growth rate-induced kinetic effects. These departures are in line with incomplete hydration and hydroxylation of dissolved CO_2. These findings imply that the determination of taxon-specific growth rates alongside clumped and bulk oxygen isotope analyses is essential to ensure accurate estimates of past ocean temperatures and seawater oxygen isotope compositions from brachiopods.

Collaborators

Jens Fiebig[1], Adam Tomašových[2], Sara Milner Garcia[3], Claire Rollion-Bard[3], Jacek Raddatz[1], Niklas Löffler[1,4], Cristina Primo-Ramos[1], Daniela Henkel[5], Lucia Angiolini[6], Uwe Brand[7] — ([1] Goethe University Frankfurt, [2] Slovak Academy of Sciences, [3] Institut de Physique du Globe de Paris, [4] Senckenberg Biodiversity and Climate Research Centre, [5] GEOMAR, [6] University of Milan, [7] Brock University).

2.1. Introduction

Biomineralising marine organisms serve as important geochemical archives of past climate conditions. Brachiopods constitute one group of calcifying invertebrates that have great potential for palaeoenvironmental reconstructions due to their common occurrences in Phanerozoic sediments since the Cambrian (Curry & Brunton, 2007). Their high abundance in Palaeozoic sediments makes them particularly valuable for deep-time seawater temperature reconstructions based on shell oxygen isotope compositions (Veizer & Prokoph, 2015). Unlike many other biogenic archives fossil and modern brachiopods can be found from tropical to polar environments and from a great range of water depths (Brand *et al.*, 2007; Curry & Brunton, 2007).

A limitation of the conventional oxygen isotope palaeothermometer method is that it requires an assumption for the oxygen isotope composition of the palaeo-seawater (Urey, 1947). The common assumption that $\delta^{18}O_{sw}$ values remained constantly between -1‰ and 0‰ SMOW during the Phanerozoic leads to relatively low apparent oxygen isotope fractionation between ancient seawater and brachiopod calcite, and hence to unrealistically high seawater temperature estimates (Veizer & Prokoph, 2015). Alternatively, it has been claimed that the progressive ^{18}O depletion of brachiopod shells with age during the Phanerozoic reflects increasing post-depositional alteration or a secular decline in seawater $\delta^{18}O$ values of about -6‰ compared to the modern ocean (Veizer & Prokoph, 2015). To investigate the underlying cause of presumably erroneous extremely warm Phanerozoic temperature estimates, independent constraints on past seawater temperatures and $\delta^{18}O$ values are needed.

In contrast to oxygen isotope thermometry, the carbonate clumped isotope thermometer does not require an estimate for the oxygen isotope composition of the seawater, as it considers the fractionation of isotopes exclusively amongst carbonate isotopologues (Ghosh *et al.*, 2006). In thermodynamic equilibrium, the clumped isotope composition (Δ_{47}) of a given carbonate is solely a function of the carbonate precipitation temperature. Fossil brachiopod shells have been analysed both for both their oxygen and clumped isotope composition to independently constrain ocean temperatures and seawater $\delta^{18}O$ (Came *et al.*, 2007; Brand *et al.*, 2014; Cummins *et al.*, 2014). However, previous investigations into the temperature dependence of the clumped isotope composition of modern brachiopod shells have reported inconsistent results. Came *et al.* (2014) reported a significantly steeper Δ_{47}–temperature slope compared to the

theoretical calibration (Passey & Henkes, 2012) and to the empirical calibration based on brachiopods and molluscs (Henkes *et al.*, 2013). Came *et al.* (2014) exclusively investigated brachiopods, whereas the calibration of Henkes *et al.* (2013) was primarily based on molluscs. Differences in phosphoric acid digestion temperatures (90 °C *vs.* 25 °C) were suggested as a possible explanation for the discrepant Δ_{47}–temperature slopes (Came *et al.*, 2014). However, it remains an open question whether kinetic fractionation processes may account for the observed discrepancies in the Δ_{47}–temperature slopes.

Kinetic isotope fractionations driven by diffusion, pH or incomplete oxygen isotope exchange between water and dissolved inorganic carbonate species can cause calcite to be precipitated with isotope values that are offset from those predicted for thermodynamic equilibrium (Adkins *et al.*, 2003; Saenger *et al.*, 2012; Spooner *et al.*, 2016). Kinetic fractionation effects have been recognised in other important calcifying groups, including in warm and cold-water corals and in certain foraminifera species (Saenger *et al.*, 2012; Grauel *et al.*, 2013; Kimball *et al.*, 2016; Spooner *et al.*, 2016). It has been postulated that brachiopods incorporate oxygen isotopes into shell calcite (secondary and tertiary layers) in equilibrium with ambient seawater, although certain parts of the shell (*i.e.*, primary layer, uppermost part of the secondary layer, umbo and muscle scar areas) yield depleted $\delta^{18}O$ values (Lowenstam, 1961; Carpenter & Lohmann, 1995; Parkinson *et al.*, 2005; Cusack *et al.*, 2012; Brand *et al.*, 2013). In these shell areas, the observed ^{18}O-depletion has been linked to growth-rate-driven kinetic isotope fractionation (Carpenter & Lohmann, 1995; Auclair *et al.*, 2003; Yamamoto *et al.*, 2010a, 2010b; Jean *et al.*, 2015; Rollion-Bard *et al.*, 2016).

Here, we investigate the significance of kinetic controls (also called vital effects) on brachiopod shell Δ_{47} and $\delta^{18}O$ values. We analysed the bulk and clumped isotope compositions of eighteen modern brachiopod shells at a phosphoric acid digestion temperature of 90 °C. Growth temperatures and seawater $\delta^{18}O$ values for each brachiopod were independently-determined and we complemented our measurements with trace element and ion probe-based *in situ* oxygen isotope analyses.

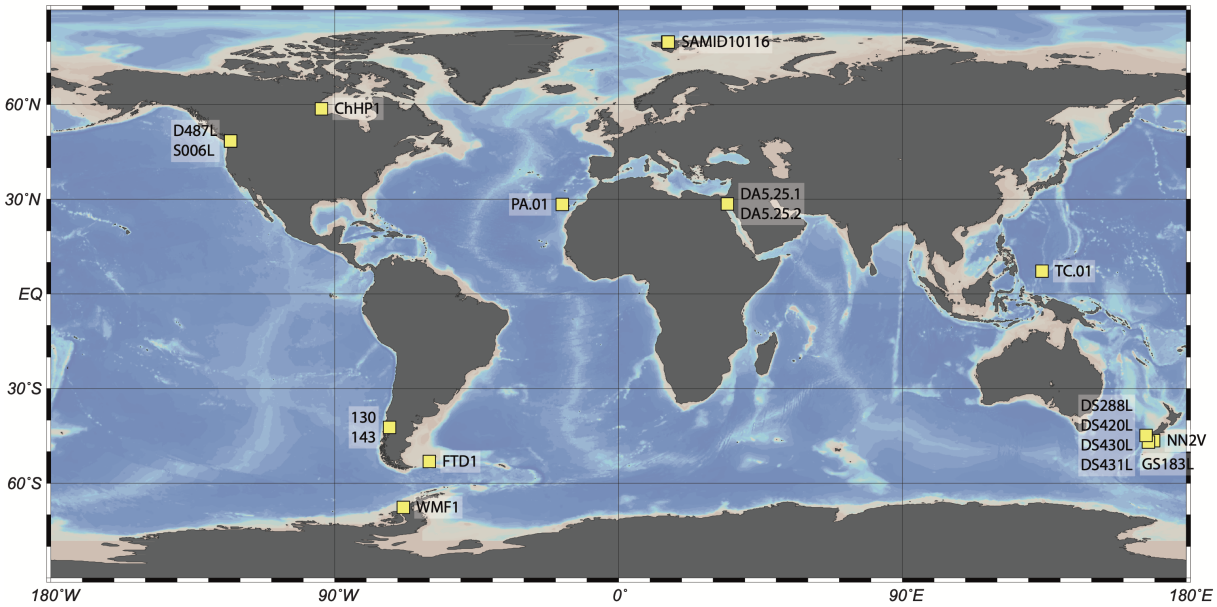

Figure 2.1 | Map of the locations where the modern brachiopods were collected.
The environmental parameters corresponding to the locations are listed in Table A2.1.

2.2. Materials and methods

2.2.1. Sampling of shells

The studied specimens represent fourteen species collected from different geographic locations and water depths that cover a substantial range of growth temperatures (Figure 2.1, Table A2.1). Organic tissue and encrusting organisms were removed from the brachiopod shells using a metal pin and a brush. Specimen S006L, DS420L, and DS430L were submerged in diluted NaOCl for 5–10 minutes to soften the organic material. The shells were cleaned in an ultrasonic bath using deionized water. Afterwards, the shells were dried using pressured air and stored at room temperature. For the larger species, the primary layer of the shells was mechanically removed using a hand-held electric drill (Proxxon Micromot IBS/E) on the lowest speed setting and only the secondary and/or tertiary layers were sampled. An approximately 0.5 cm^2 area from the anterior part of the ventral valve was crushed and homogenised using an agate mortar and pestle. We avoided sampling the umbo area, the hinge area, the muscle scar area and the youngest parts of the shell. Exceptions to this were the micromorphic shells of *P. atlantica, T. congregata, Argyrotheca* sp., and *Megerlia* sp., where 4 to 20 whole shells had to be crushed to acquire enough material for multiple replicate analyses.

2.2.2. Growth rate

The growth of brachiopods can be described by the von Bertalanffy asymptotic function (Baumgarten *et al.*, 2014). Juvenile individuals grow the fastest and the growth rate decreases with age, before reaching the species-specific maximum size. To acquire comparable, species-specific growth rates, we estimated a minimum and a maximum growth rate for each analysed species (Table A2.1). The maximum growth rate, in our case, depicted the average growth rate of the brachiopod until it reached 50% of its maximum size. Similarly, the minimum estimate was the average growth rate after the brachiopod had already reached 50% of its maximum size. For *M. venosa* (Baumgarten *et al.*, 2014), *M. fragilis* (Brey *et al.*, 1995), *M. sanguinea* (Ostrow, 2004), *C. inconspicua* (Doherty, 1979), *T. transversa* (Paine, 1969) and *L. neozelanica* (Baird *et al.*, 2013), detailed studies were available, thus both a maximum and a minimum growth rate estimate could be calculated. Such a study has not, to date, been made for *N. nigricans;* therefore, we used the available average juvenile growth rate (Lee *et al.*, 2010) as a maximum estimate. For the micromorphic brachiopods *P. atlantica*, *Argyrotheca* sp., *Megerlia* sp., and *T. congregata*, we assumed a 0.5 mm/yr and a 1.2 mm/yr as a minimum and as a maximum growth rate estimate, respectively. These growth rates are characteristic for micromorphic brachiopods (Pakhnevich, 2010).

2.2.3. Trace element analyses

The magnesium content of the studied brachiopod shells was analysed using a Thermo Scientific™ iCap™ 6000 dual view ICP-OES (Inductively Coupled Plasma - Optical Emission Spectrometry) at the Goethe University, Frankfurt, Germany. For the analyses, we took 120–150 µg of carbonate powder from the homogenised batches that were also used for the isotope measurements and dissolved them in 0.500 cm^3 2% HNO_3. An aliquot of 0.300 cm^3 of the sample solution was diluted with 1.500 cm^3 yttrium water (until 1.000 mg/dm^3) prior to measurement to correct for matrix biases during analyses. The Mg/Ca measurements were drift-corrected and standardized to an internal consistency standard (ECRM 752-1) measured alongside with the samples. The external reproducibility (2σ S.E.) for this standard was ±0.1 mmol/mol Mg/Ca. Finally, the $MgCO_3$ concentration values (mol%) were adjusted to a 100% carbonate basis and were normalised to a combined Ca and Mg value of 395,000 ppm (Brand *et al.*, 2013).

2.2.4. Stable isotope analyses

Clumped isotope analyses were made between July 2016 and April 2017, using a fully automated gas extraction and purification line connected to a ThermoFisher™ MAT 253™ gas-source isotope-ratio mass spectrometer at the Goethe University Frankfurt, Frankfurt am Main, Germany. Each sample was analysed in 4–10 replicates. At the extraction line, 4–8 mg of homogenised carbonate powder was reacted for 30 minutes at 90 °C with > 105% phosphoric acid. The resultant CO_2 was led through a U-trap submerged into ethanol, cooled to -80 °C and frozen out immediately using a second U-trap that was submerged into liquid nitrogen. On completion of the reaction, the U-trap containing the solid CO_2 was submerged into -80 °C ethanol and a third U-trap was submerged into liquid nitrogen. The CO_2 sublimes from the ethanol-cooled U-trap and freezes out in the subsequent liquid-nitrogen-cooled U-trap, while water stays frozen in the U-trap kept at -80 °C. The process of CO_2 sublimation at -80 °C was repeated altogether three times. For further purification, the CO_2 gas was entrained into a helium carrier gas and led through a Porapak Q trap, cooled down to -15 °C, to filter out hydrocarbons and other contaminants. Finally, the helium carrier gas was pumped away, and the CO_2 gas enters the dual inlet system of the mass spectrometer, where it was analysed alternately with a reference gas of known isotope composition (ISO-TOP, Air Liquide, Paris, France; $\delta^{18}O_{VSMOW}$ = 25.56‰, $\delta^{13}C_{VPDB}$ = -4.30‰). Each analysis output of the mass spectrometer consisted of 10 acquisitions, made up of 10 cycles with 20 s integration time each and an additional pre-measurement of the reference gas. In each cycle, the peak intensities were measured for m/z 44 through m/z 49 for both the sample and the reference gas. Bellow pressure was adjusted to 16,000(±150) mV for m/z 44 before each acquisition. Background correction was performed for the sample and the reference gas separately, as described in Fiebig *et al.* (2016). Isobaric contaminant masses, monitored by comparing the correlation of off-peak m/z 47 and on-peak m/z 49 intensities for both the sample and the reference gas, were not observed (Figure A2.1). For all samples, at least 4 replicates have been measured. The corresponding shot noise limit for 4 replicates is 0.004‰ and further decreases with increasing number of replicates (Merrit & Hayes, 1994). For each sample analysed the 1σ standard error is always larger than the corresponding shot noise limit.

The raw Δ_{47}, $\delta^{18}O$ and $\delta^{13}C$ values were calculated using two sets of isotope parameters (Daëron *et al.*, 2016). In the [*Gonfiantini/Santrock*] set, the parameters are as

follows: R^{13}_{PDB}= 0.0112372, R^{18}_{VSMOW} = 0.0020052, R^{17}_{VSMOW}=0.0003799 and λ=0.5164. In the [*Brand*]/IUPAC set, the parameters are: R^{13}_{PDB}= 0.01118, R^{18}_{VSMOW} = 0.0020052, R^{17}_{VSMOW}=0.00038475 and λ=0.528. The raw Δ_{47} values were projected to the CDES (Carbon Dioxide Equilibrium Scale (Dennis *et al.*, 2011)) using equilibrated gases. Empirical transfer functions (ETFs) were determined using gases of various bulk isotope compositions equilibrated at 25 °C and at 1000 °C, respectively. The intercept values of the equilibrated gases in the Δ_{47}–δ_{47} space were constant between 06.06.2016–12.22.2016 and 01.06.2017–04.05.2017 (Supplementary Data 2.1). For referencing the Δ_{47} values to 25 °C, we used an acid fractionation factor of 0.081‰ (Passey & Henkes, 2012). Two internal carbonate reference materials were analysed along with the samples to verify the precision and the stability of clumped isotope measurements: Carrara marble calcite (Carrara) and *Arctica islandica* (mollusc) shell aragonite (MuStd). The mean $\Delta_{47\ (CDES\ 25°C)}$ values (±1σ S.E.) for the Carrara (N = 123) and the MuStd (N = 83) reference materials, calculated using the [*Gonfiantini/Santrock*] set of isotopic parameters were 0.396(±0.001)‰ and 0.743(±0.002)‰, and using the [*Brand*]/IUPAC set of isotopic parameters were 0.395(±0.001)‰ and 0.738(±0.002)‰, respectively. The 1σ S.D. of the Δ_{47} values for the reference materials is 0.014‰. The [*Gonfiantini/Santrock*] values agree within ≤ 0.005‰ with corresponding $\Delta_{47\ (CDES\ 25°C)}$ values reported elsewhere for Carrara (Dennis *et al.*, 2011; Henkes *et al.*, 2013; Bonifacie *et al.*, 2017) and MuStd (Kele *et al.*, 2015) after applying a consistent acid fractionation factor to these datasets.

Our $\delta^{18}O$ values for calcite were obtained applying a 90 °C acid fractionation factor of 1.00813, extrapolated from Kim *et al.* (2007). For 25 °C a fractionation factor of 1.01031 is obtained according to the same study. In their original calibration Kim and O'Neil (1997) applied a 25 °C fractionation factor of 1.01050. To calculate the oxygen isotope fractionation between seawater and calcite we used the following modified equation of Kim and O'Neil (1997):

(Eq. 2.1) $$1000\ln\alpha_{cc-water} = 18.03 \times (1000/T) - 32.23$$

where α is the fractionation factor and T is the temperature in K. The original intercept of -32.42 has been corrected by +0.19, which takes into account the difference in the 25 °C acid fractionation factors of Kim *et al.* (2007) relative to Kim and O'Neil (1997).

2.2.5. Secondary Ion Mass Spectrometry

The ion probe analyses were carried out using the Caméca IMS 1280-HR2 at CRPG-CNRS (Nancy, France) and the method described in detail in Rollion-Bard *et al.* (2007). Oxygen isotope compositions were analysed using a 5 nA Cs^+ primary beam with a charge compensation by a normal-incidence electron gun and mass resolving power of M/ΔM ~5000. Oxygen isotopes were measured simultaneously in multi-collection mode by using two off-axis Faraday cups, L'2 and H1. Gains of Faraday cups were calibrated at the beginning of the analytical session. Each analysis was performed with a pre-sputtering time of 30 seconds followed by 30 cycles of data collection, 4 seconds each. Typical ion intensities of 6 x 10^6 cps and 3 x 10^9 cps were obtained on $^{18}O^-$ and $^{16}O^-$, respectively. After few minutes of counting, the internal $2\sigma_n$ error was less than ±0.1‰. An in-house carbonate standard (CCciAg; $\delta^{18}O_{VSMOW}$ = 18.94‰; $\delta^{13}C_{VPDB}$ = -11.61‰) was measured before and after each analytical session to correct for instrumental mass fractionation (IMF). The external reproducibility (1σ S.D.), based on the replicates of the carbonate standard was between ±0.27–0.40‰, depending on the analytical session. The IMF of sample was also corrected from Mg-content by applying the correction -0.3 x $MgO\%_{wt}$ (Rollion-Bard & Marin-Carbonne, 2011). In addition to the ion probe analyses, the $\delta^{18}O$ values of the secondary layer of the studied shells were also determined by conventional mass spectrometry and an adjustment was applied to the ion probe $\delta^{18}O$ values as shown in Cusack *et al.* (2012).

The exact location of the ion probe transects, and the analysed points are shown in Figure A2.2. The two analysed shells were also investigated for clumped isotopes. The ventral valve of each brachiopod was cut in half from anterior to posterior part to produce a longitudinal section. One half was mounted in epoxy and polished with diamond paste down to 1 µm. Transects from the outermost (primary layer) to the innermost part (closest to the mantle cavity) of the shell were performed with 20 µm spots and with a constant step of 50 µm. The number of analysis was determined by the shell thickness. The location of the transect was approximately 3 mm above the anterior margin, at the exact location where the shell was sampled for the clumped and trace element analyses.

2.3. Results

2.3.1. Trace element analyses

The magnesium concentration of the studied modern brachiopod shells was between 0.27 mol% (*Terebratalia transversa*) and 6.8 mol% (*Pajaudina atlantica*) $MgCO_3$. Our results are consistent with the expected range of modern brachiopod calcite and fall along the Global Brachiopod Mg Line (Brand *et al.*, 2013) (Figure A2.3a).

2.3.2. Bulk and clumped isotope analyses

The $\delta^{18}O_{VPDB}$ values of the modern brachiopod shells analysed in this study range between -2.20(±0.02)‰ and 3.92(±0.02)‰, while the $\delta^{13}C_{VPDB}$ values range between -0.88(±0.02)‰ and 2.44(±0.01)‰. These values are consistent with the range in isotope compositions of modern brachiopod shells (secondary and tertiary layers) reported elsewhere (Parkinson *et al.*, 2005; Brand *et al.*, 2013; Rollion-Bard *et al.*, 2016; Ullmann *et al.*, 2017). The difference between the oxygen and carbon isotope composition of the shells determined using the [*Gonfiantini/Santrock*] and the [*Brand*]/IUPAC sets of isotopic parameters (Daëron *et al.*, 2016) is ca. 0.01‰. This is similar or less than the 1σ S.E. of replicate measurements and can; therefore, be ignored (see Chapter 2.2.4).

The $\Delta_{47\ (CDES\ 25°C)}$ values measured for the modern brachiopods shells calculated with the [*Gonfiantini/Santrock*] parameters range between 0.671(±0.007)‰ and 0.775(±0.004)‰, while the 1σ S.E., calculated from 4–10 replicate analyses, ranges between 0.004–0.014‰. The $\Delta_{47\ (CDES\ 25°C)}$ values for the brachiopods calculated with the [*Brand*]/IUPAC parameters are between 0.664(±0.007)‰ and 0.767(±0.004)‰, while the 1σ S.E., calculated from 4–10 replicate analyses, ranges between 0.004–0.013‰. The difference between $\Delta_{47\ (CDES\ 25°C)}$ values calculated with the [*Gonfiantini/Santrock*] and the [*Brand*]/IUPAC sets of isotopic parameters is between 0.005‰ and 0.008‰.

2.3.3. Apparent Δ_{47}–temperature relationship

To obtain a Δ_{47}–temperature relationship for modern brachiopod calcite, a least-squares fit linear regression (York *et al.*, 2004; Wacker *et al.*, 2014) was performed on the measured $\Delta_{47\ (CDES\ 25°C)}$ values and the independently-sourced brachiopod growth temperatures (Locarnini *et al.*, 2013) (Tables A2.1 and A2.2). This approach considered uncertainties arising from both the clumped isotope measurements and the growth temperatures. The statistical analyses yielded the following Δ_{47}–temperature relationship (Figures 2.2a and A2.4a):

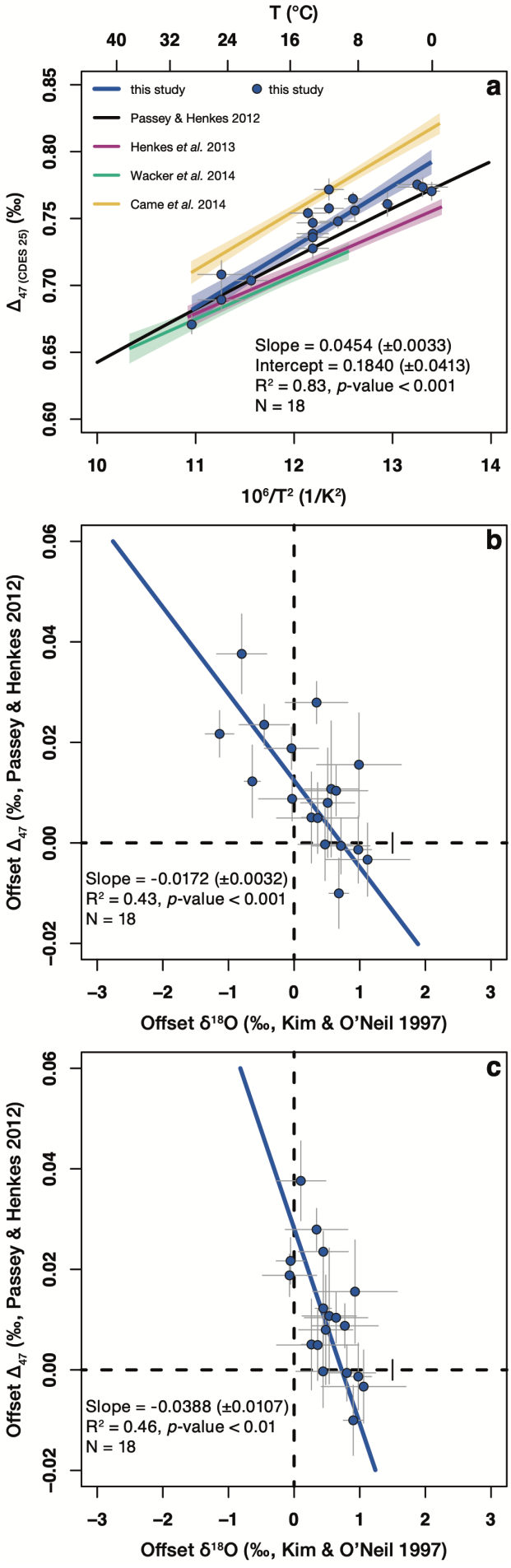

Figure 2.2 | Brachiopods show an offset from equilibrium Δ_{47} and $\delta^{18}O$ values.
(A) Δ_{47}–temperature dependence derived from the eighteen modern brachiopods analysed in this study, calculated using the [*Gonfiantini/Santrock*] set of isotopic parameters. **(B)** The offset $\delta^{18}O$ and offset Δ_{47} values show a significant negative correlation. The brachiopods, which show apparent clumped isotope equilibrium are enriched by up to +1‰, relative to Kim and O'Neil (1997). Seawater $\delta^{18}O$ values were acquired from the Global Seawater Oxygen-18 Database (LeGrande & Schmidt, 2006). **(C)** The correlation between offset $\delta^{18}O$ and offset Δ_{47} values is still present if, where available, the directly measured seawater $\delta^{18}O$ values (Table A2.1) were used for the calculations. For all plots: linear regression lines fitted to our data consider the errors. Corresponding two-tailed *p*-values are computed using a t-test. Error bars for the offset $\delta^{18}O$ values indicate the mean deviation from oxygen isotope equilibrium calculated using the minimum and the maximum temperature estimates. Error bars for the offset Δ_{47} values indicate the 1σ S.E. of the replicate measurements.

(Eq. 2.2) $$\Delta_{47\ (\text{CDES }25°\text{C})} = 0.0454(\pm 0.0033) \times 10^6/\text{T}^2 + 0.1840(\pm 0.0413)$$

$$\text{N} = 18,\ \text{R}^2 = 0.83,\ p\text{-value} < 0.001,\ [\textit{Gonfiantini}]$$

(Eq. 2.3) $$\Delta_{47\ (\text{CDES }25°\text{C})} = 0.0453(\pm 0.0033) \times 10^6/\text{T}^2 + 0.1789(\pm 0.0415)$$

$$\text{N} = 18,\ \text{R}^2 = 0.83,\ p\text{-value} < 0.001,\ [\textit{Brand}]/\text{IUPAC}$$

where Δ_{47} is in ‰, T (temperature) is in K and the two-tailed *p*-values are calculated using a t-test.

The slope of our Δ_{47}–temperature calibration line (Equations 2.2 and 2.3) is steeper compared to the theoretical calibration (Passey & Henkes, 2012) and to previous calibrations made at ≥ 70 °C (Henkes *et al.*, 2013; Wacker *et al.*, 2014; Bonifacie *et al.*, 2017), and shallower than most 25 °C calibrations (Zaarur *et al.*, 2013). However, the slope of our Δ_{47}–temperature calibration line is indistinguishable from the brachiopod-only calibration of Came *et al.* (2014), made at 25 °C.

2.3.4. Δ_{47} and $\delta^{18}O$ offsets from apparent equilibrium

The difference between the measured and apparent equilibrium values are here referred to as offset values (Supplementary Data 2.2). Annual mean habitat temperatures (*i.e.*, brachiopod growth temperatures) were acquired from the World Ocean Atlas 2013 (Locarnini *et al.*, 2013). Annual mean seawater $\delta^{18}O$ values representative of the sampling location and depth were taken from the Global Seawater Oxygen-18 Database (LeGrande & Schmidt, 2006). For thirteen out of eighteen specimens, directly measured seawater $\delta^{18}O$ values were also available, giving actual seawater oxygen isotope compositions at the water depth where the brachiopods were collected (Brand *et al.*, 2013) (Table A2.1). To remain consistent, we distinguish between the two datasets: one using only the seawater $\delta^{18}O$ values acquired from the Global Seawater Oxygen-18 Database (LeGrande & Schmidt, 2006) and the other in which gridded $\delta^{18}O$ values were replaced by the directly measured $\delta^{18}O$ values where available.

Apparent $\delta^{18}O_{calcite}$ equilibrium values were calculated using the $1000\ln\alpha_{calcite\text{-}water}$–temperature relationship of Kim and O'Neil (1997) and that of Brand *et al.* (2013), respectively. The latter includes a correction for the Mg-effect, which accounts for a 0.17‰ change per mol% $MgCO_3$ in the $\delta^{18}O$ values of the calcite, in agreement with laboratory precipitation experiments (Brand *et al.*, 2013) (Figure A2.3). Apparent Δ_{47} equilibrium values were calculated using the theoretical calibration of Passey and Henkes (2012), *i.e.,* their Equation 5, with the empirically determined

intercept of 0.280 (Figures 2.2b,c and A2.4b,c). This equation considers a 25–90 °C acid fractionation factor of 0.081‰ that has been verified in the 0–40 °C temperature range by empirical and experimental approaches (Henkes *et al.*, 2013; Tang *et al.*, 2014; Wacker *et al.*, 2014; Defliese *et al.*, 2015). In addition, offset Δ_{47} values were also calculated assuming that the most recent calibrations of Bonifacie *et al.* (2017) or Kelson *et al.* (2017) represent the clumped isotope equilibrium (Figure A2.5). Offset Δ_{47} values were computed using both the [*Gonfiantini/Santrock*] and the [*Brand*]/IUPAC processed data.

Most of the analysed brachiopods in this study exhibit combined offsets from clumped and oxygen isotope equilibrium, irrespective how the offset values were calculated (Figures 2.2b,c, A2.3b,c, and A2.5). The largest deviations from the equilibrium Δ_{47} values were observed in the temperate- to cold-water brachiopod species, particularly those of the species *Magellania venosa* and *Magasella sanguinea*. In contrast, most of the warm-water (> 20 °C) taxa, such as *Thecidellina congregata, Argyrotheca* sp., *Megerlia* sp., and *P. atlantica,* exhibit apparent clumped isotope equilibrium.

2.3.5. Oxygen isotope analyses with ion probe

High resolution (20 µm) *in situ* oxygen isotope analysis was performed on two *M. venosa* shells using SIMS (Secondary Ion Mass Spectrometry). In the secondary layer of the two investigated *M. venosa* shells, the $\delta^{18}O$ values range from -2.91‰ to 1.35‰ (sample 130) and from -2.02‰ to 0.60‰ (sample 143; Figure 2.3). This species does not have a tertiary layer and the primary layer was too thin to be analysed. The variation in $\delta^{18}O$

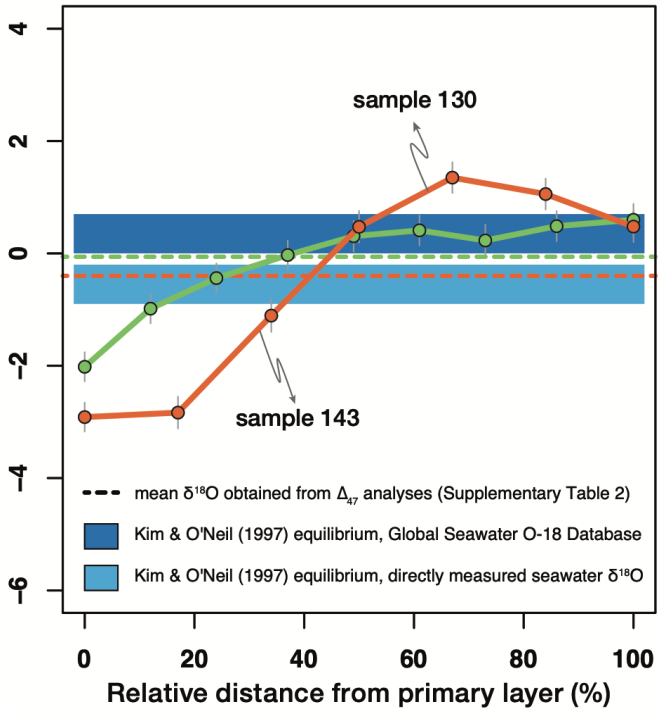

Figure 2.3 | Variations in $\delta^{18}O$ between the outer and the inner part of the secondary layer of a brachiopod shell.
Results of the SIMS transects made on two *M. venosa* shells (samples 130 and 143) also analysed for clumped isotopes. Apparent equilibrium ranges for $\delta^{18}O$ were calculated according to Kim and O'Neil (1997) using the minimum and maximum habitat temperature estimates and the two sets of seawater $\delta^{18}O$ values (Table A2.1). Error bars for the $\delta^{18}O$ indicate the external reproducibility (1σ S.D.) based on replicate measurements of carbonate standards.

between the outer and inner part of the shell was 4.3‰ for sample 130 and 2.6‰ for sample 143 (Supplementary Data 2.3).

2.4. Discussion

Multiple processes can lead to the deviation of measured $\delta^{18}O$ and Δ_{47} values from thermodynamic equilibrium. If the offset seen in the modern brachiopod $\delta^{18}O$ values would arise solely from the varying Mg-content of the analysed shells, one would expect that this offset would disappear if the equilibrium values were calculated using the equation of Brand *et al.* (2013) instead of Kim and O'Neil (1997), since the former includes a correction for the Mg-effect. However, the scatter of the brachiopod $\delta^{18}O$ values around the assumed oxygen isotope equilibrium is even greater if the Brand *et al.* (2013) equation is used, thus the offset $\delta^{18}O$ values cannot be explained by the Mg-content of the shells (compare Figures 2.2b,c to Figures A2.3b,c). We also exclude a direct effect of the Mg-content of the shells on the Δ_{47} values, considering the recent findings of Bonifacie *et al.* (2017) who, for a given precipitation temperature, did not find any difference in the clumped isotope composition between dolomite and calcite reacted at 90 °C.

A mixture of carbonates of different compositions will mix linearly with respect to $\delta^{13}C$ and $\delta^{18}O$ but non-linearly with respect to Δ_{47}. The resulting mixture can; therefore, have a greater or lower Δ_{47} value than the weighted sum of the end-member Δ_{47} values, introducing an artificial bias in Δ_{47} (Eiler & Schauble, 2004; Defliese & Lohmann, 2015). The range of variation in $\delta^{18}O$ and $\delta^{13}C$ in modern brachiopod shells is usually not larger than 6‰, considering both the variation within secondary layer calcite (Auclair *et al.*, 2003; Parkinson *et al.*, 2005; Yamamoto *et al.*, 2010b, 2010a; Cusack *et al.*, 2012; Penman *et al.*, 2013) and between the juvenile and the adult parts of the shell (Auclair *et al.*, 2003; Parkinson *et al.*, 2005; von Allmen *et al.*, 2010; Yamamoto *et al.*, 2010a; Penman *et al.*, 2013; Yamamoto *et al.*, 2013; Jean *et al.*, 2015; Rollion-Bard *et al.*, 2016; Ullmann *et al.*, 2017). Assuming the most-extreme scenario of 50-50% mixing of carbonates precipitated at the same temperature with a 6‰ difference in both their $\delta^{13}C$ and $\delta^{18}O$ values, the maximum effect of carbonate mixing on Δ_{47} in modern brachiopods would be +0.009‰ (Defliese & Lohmann, 2015). To further investigate the role of sample heterogeneity on our data, we assessed the range of variation in $\delta^{18}O$ values in two *M. venosa* shells that exhibited a high (0.024‰ and 0.038‰, respectively) Δ_{47} offset with respect to Passey and Henkes (2012). Our data show that the difference in $\delta^{18}O$ values in brachiopod secondary layer calcite can be as high as 4.3‰ between the outer and the

inner part of the shell (Figure 2.3). A covariance of $\delta^{18}O$ and $\delta^{13}C$ along the depth transects of modern brachiopods shells suggests that the range of variation in $\delta^{13}C$ will be comparable to that of $\delta^{18}O$ (Auclair *et al.*, 2003; Yamamoto *et al.*, 2010a, 2010b; Penman *et al.*, 2013; Yamamoto *et al.*, 2013). A 50-50% mixing of carbonates precipitated at the same temperature with a 4.3‰ difference in both their $\delta^{13}C$ and $\delta^{18}O$ values results in a Δ_{47} mixing effect of +0.005‰ (Defliese & Lohmann, 2015). This bias is much smaller than the observed maximum offset Δ_{47} value of 0.038‰ and unresolvable from the external analytical precision (1σ S.E.) received for most replicates. Thus, it is highly unlikely that a mixing of carbonates of different compositions through the shell significantly contributes to the positive Δ_{47} offsets observed in this study.

Differences in laboratory procedures, such as reaction temperatures, have previously been suggested as a possible explanation for the discrepancy in the slopes between the Came *et al.* (2014) calibration, made at 25 °C, and the Henkes *et al.* (2013) calibration, made at 90 °C. Although, Henkes *et al.* (2013) also analysed brachiopods (N = 4), their calibration is predominantly based on molluscs (N = 40). Since our study and that of Came *et al.* (2014) yielded the same calibration slope despite using two different acid digestion temperatures, we consider this slope gradient to be characteristic of brachiopods and exclude acid digestion temperature as a valid explanation for the difference between the lower (25 °C) and the higher (≥ 70 °C) temperature calibration slopes.

Growth rates of the modern brachiopods analysed in this study correlate well with both the offset Δ_{47} ($R^2 \approx 0.55$, *p*-value < 0.01; Figure 2.4a) and the offset $\delta^{18}O$ values ($R^2 > 0.52$, *p*-value < 0.01; Figures 2.4b,c). The slowest growing brachiopods (*T. congregata, Argyrotheca* sp., *Megerlia* sp., *P. atlantica*) are in apparent clumped isotope equilibrium (Passey & Henkes, 2012), whereas the fastest growing brachiopods (*M. venosa*, *T. transversa*) show a positive Δ_{47} offset. The offset $\delta^{18}O$ values show a negative correlation with growth rate. A similar depletion of ^{18}O with increasing growth rate was observed in other modern brachiopod species by Takayanagi *et al.* (2015). The slowest growing brachiopods that are closest to clumped isotope equilibrium relative to Passey and Henkes (2012) are enriched in ^{18}O relative to the apparent oxygen isotope

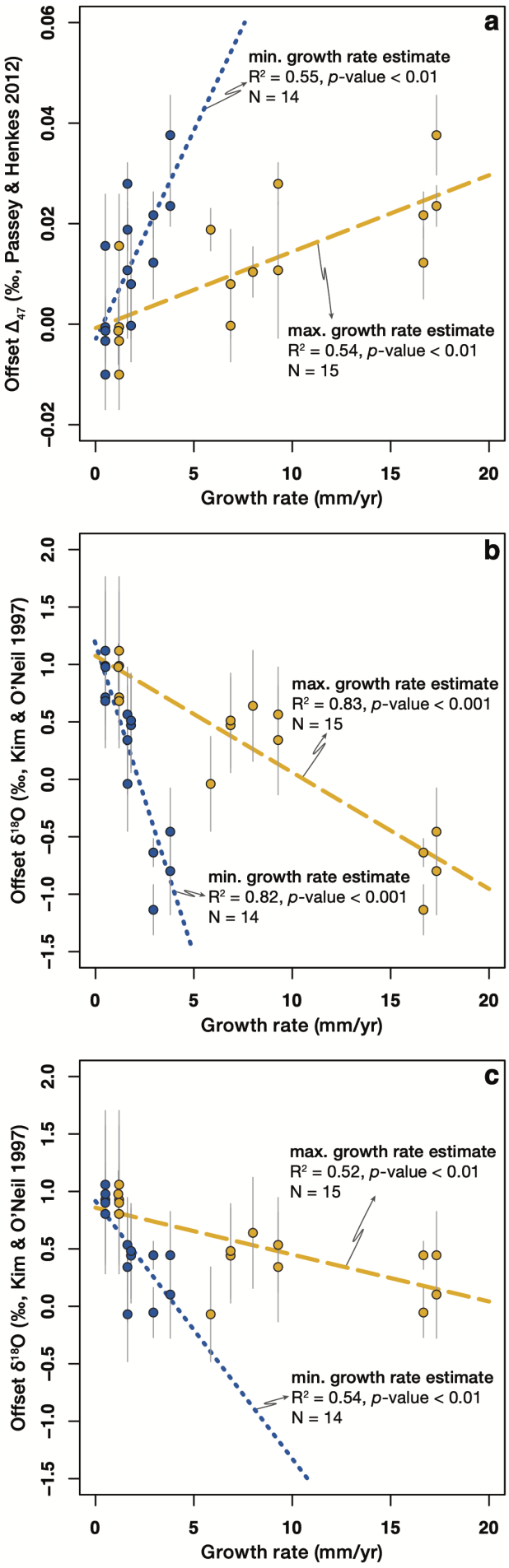

Figure 2.4 | Offset Δ_{47} and offset $\delta^{18}O$ values correlate with brachiopod growth rates.
The dashed and dotted lines are simple linear regressions calculated using the maximum and the minimum growth rate estimates, respectively. **(A)** Offset Δ_{47} values positively correlate with brachiopod growth rates. **(B)** Offset $\delta^{18}O$ values negatively correlate with brachiopod growth rates. Seawater $\delta^{18}O$ values were acquired from the Global Seawater Oxygen-18 Database (LeGrande & Schmidt, 2006). **(C)** The correlation between offset $\delta^{18}O$ and brachiopod growth rates is still present if, where available, the directly measured seawater $\delta^{18}O$ values were used for the calculations. For all plots: two-tailed *p*-values are calculated using a t-test. Error bars for the offset $\delta^{18}O$ values indicate the mean deviation from oxygen isotope equilibrium calculated using the minimum and the maximum temperature estimates. Error bars for the offset Δ_{47} values indicate the 1σ S.E. of the replicate measurements.

equilibrium as predicted by Kim and O'Neil (1997). This strongly implies that growth rate exerts control on the kinetic mechanisms responsible for the observed departures from apparent clumped and oxygen isotope equilibria.

The calcite shells of articulated brachiopods are secreted in the outer epithelium of the mantle. The primary layer is formed by indirect secretion in the extrapallial fluid, while the secondary layer is formed by extracellular mineralisation (Williams, 1977; Simkiss & Wilbur, 1989). To aid our discussion, we consider a simplified model of calcification, introduced for molluscs and corals, but that has also been applied to brachiopods (Hughes *et al.*, 1988; Takayanagi *et al.*, 2013) (Figure 2.5a). In this model, carbonate formation occurs in a semi-isolated volume, separated from the ambient environment by an organic membrane (McConnaughey, 1989b; Simkiss & Wilbur, 1989; Adkins *et al.*, 2003). The organism requires calcium (Ca^{2+}) and carbonate (CO_3^{2-}) ions to enable the precipitation of $CaCO_3$. In marine calcifiers, such as corals and molluscs, the organic membrane pumps Ca^{2+} into the calcifying fluid using an enzyme (Ca-ATPase), while increasing the pH of the fluid by removing an equivalent number of protons ($2H^+$) (Adkins *et al.*, 2003). We note that the presence of this enzyme, to the best of our

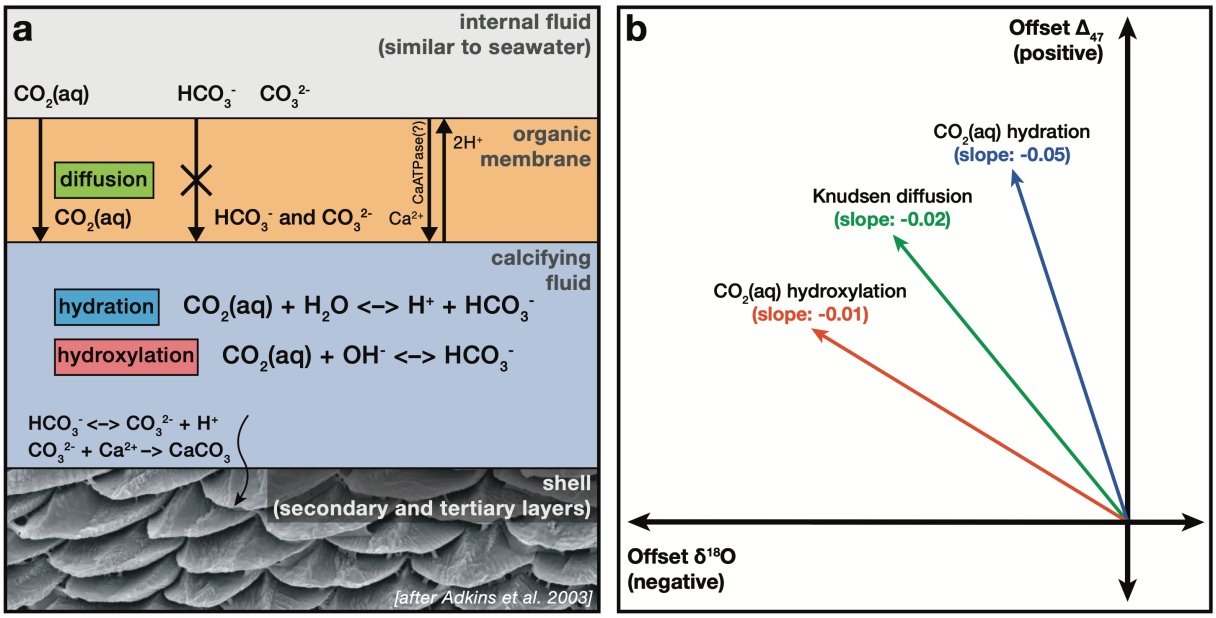

Figure 2.5 | A model explaining the possible causes of kinetic effects occurring during biogenic calcite precipitation in modern brachiopods.
(A) A simplified model of biogenic calcite precipitation in brachiopods (Simkiss & Wilbur, 1989; Adkins *et al.*, 2003). Isotope fractionation occurs during the diffusion of $CO_{2\,(aq)}$ through an organic membrane and during the transformation of $CO_{2\,(aq)}$ to bicarbonate (HCO_3^-) via hydration and hydroxylation reactions. For a detailed discussion, see the main text. **(B)** Each specific kinetic effect causes a different gradient on the plot between offset $\delta^{18}O$ and offset Δ_{47} (Guo *et al.*, 2009; Thiagarajan *et al.*, 2011; Loyd *et al.*, 2016; Spooner *et al.*, 2016).

knowledge, has not been reported from brachiopods to date. As the membrane is only permeable for aqueous carbon dioxide ($CO_{2\,(aq)}$), the $CO_{2\,(aq)}$ in the mineralising fluid is transformed into bicarbonate (HCO_3^-) and CO_3^{2-} ions via hydration (Equation 2.4) and hydroxylation (Equation 2.5) reactions:

(Eq. 2.4) $$CO_{2\,(aq)} + H_2O \rightleftharpoons H^+ + HCO_3^-$$

(Eq. 2.5) $$CO_{2\,(aq)} + OH^- \rightleftharpoons HCO_3^-$$

It has recently been demonstrated that kinetic effects related to the $CO_{2\,(aq)}$ hydration and hydroxylation reactions, as well as diffusion, can produce a positive Δ_{47} and a negative $\delta^{18}O$ offset from thermodynamic equilibrium (Thiagarajan *et al.*, 2011; Tripati *et al.*, 2015; Spooner *et al.*, 2016) (Figure 2.5b).

Knudsen-diffusion predicts that a gas diffusing through a membrane will be depleted in ^{18}O but enriched in Δ_{47}, relative to the residual gas (Thiagarajan *et al.*, 2011). When correlating the Δ_{47} and $\delta^{18}O$ offsets from equilibrium, the diffused and residual gas fractions would plot along a slope of -0.023. An identical kinetic slope would be obtained by diffusion of $CO_{2\,(aq)}$ through water (Thiagarajan *et al.*, 2011).

The reaction rate of hydration and hydroxylation of the dissolved CO_2 is orders of magnitude slower than the reaction rate of bicarbonate dissociation (Johnson, 1982). Both $CO_{2\,(aq)}$ hydration and hydroxylation preferentially select light isotopes (^{16}O, ^{12}C) and discriminate against heavy isotopes (^{18}O, ^{13}C). If the carbonate precipitation rate is high, HCO_3^- can dissociate into CO_3^{2-} and H^+ before reaching equilibrium with $CO_{2\,(aq)}$ in the calcifying fluid; therefore, the solid carbonate will inherit lighter $\delta^{18}O$ values (McConnaughey, 1989a, 1989b). Simultaneously, incomplete $CO_{2\,(aq)}$ hydration or hydroxylation results in an increased Δ_{47} value of the aqueous HCO_3^-, which can be inherited by the solid carbonate if the precipitation rate is high (Saenger *et al.*, 2012). Theoretical calculations predict a regression slope between the offset Δ_{47} offset and offset $\delta^{18}O$ values in the order of -0.05 and -0.01 for kinetic controls associated with hydration and hydroxylation reactions, respectively (Guo *et al.*, 2009; Spooner *et al.*, 2016) (Figure 2.5b). Carbonic anhydrase, an enzyme often present in calcifying organisms, such as corals, promotes rapid oxygen isotope exchange between dissolved inorganic carbon species (Uchikawa & Zeebe, 2012; Watkins *et al.*, 2014). If this enzyme was present in brachiopods, it could reduce or eliminate the kinetic isotope effects caused by the slow

hydration and hydroxylation reactions. However, carbonic anhydrase has not been identified in the calcifying fluid of modern brachiopods (Jackson *et al.*, 2015).

Our data exhibits an offset Δ_{47}–$\delta^{18}O$ slope of -0.017(±0.03) if the offset $\delta^{18}O$ values are calculated using the seawater oxygen isotope compositions acquired from the Global Seawater Oxygen-18 Database (LeGrande & Schmidt, 2006) (Figure 2.2b). If the offset $\delta^{18}O$ values are calculated using directly measured water $\delta^{18}O$ values where possible, the offset Δ_{47}–$\delta^{18}O$ slope becomes as steep as -0.039(±0.01) (Figure 2.2c). Both slopes are significant and stay consistent, irrespective of data processing, *i.e.*, [*Gonfiantini/Santrock*] *vs.* [*Brand*]/IUPAC parameters, and the clumped isotope calibration we used to calculate the offset values (Figures A2.4b,c and A2.5).

The observed correlation slopes (-0.017 to -0.039, depending on the seawater $\delta^{18}O$ dataset) between offset Δ_{47} and offset $\delta^{18}O$ point to the importance of kinetic effects associated with diffusion and incomplete hydration and hydroxylation of $CO_{2\,(aq)}$. The hydration and hydroxylation reactions occur superimposed onto the diffusion of $CO_{2\,(aq)}$. Consequently, diffusion alone cannot be the sole kinetic mechanism responsible for the observed trend in our data. If heterogeneous oxygen isotope exchange between water and $CO2_{(aq)}$ proceeds to equilibrium, it would erase the offsets from equilibrium Δ_{47} and $\delta^{18}O$ generated during diffusion. Tang *et al.* (2014) precipitated calcites at a pH < 9 and > 10 and observed that Δ_{47} values increased by approximately 0.016‰ for every 1‰ decrease in $\delta^{18}O$ at high (> 10) pH. They suggested that a combined effect of diffusion and hydroxylation could be responsible for the observed slope. Interestingly, their slope is indistinguishable from the one we observe when we exclusively use the Global Seawater Oxygen-18 Database (LeGrande & Schmidt, 2006) to infer seawater $\delta^{18}O$. However, pH > 10 would be inconsistent with the internal pH range of modern brachiopods, which is likely to be between 7.7 and 8.2, calculated from $\delta^{11}B$ values (Penman *et al.*, 2013). Hydration is more prominent at low (< 8.4) pH while hydroxylation is more prominent at high (> 8.4) pH, assuming temperature and salinity values characteristic of modern seawater (Johnson, 1982; McConnaughey, 1989b) (Figure 2.6). In the pH range characteristic for modern brachiopods, only 10–40% of the oxygen isotope exchange between water and $CO_{2\,(aq)}$ should occur via the hydroxylation reaction, whereas 60–90%

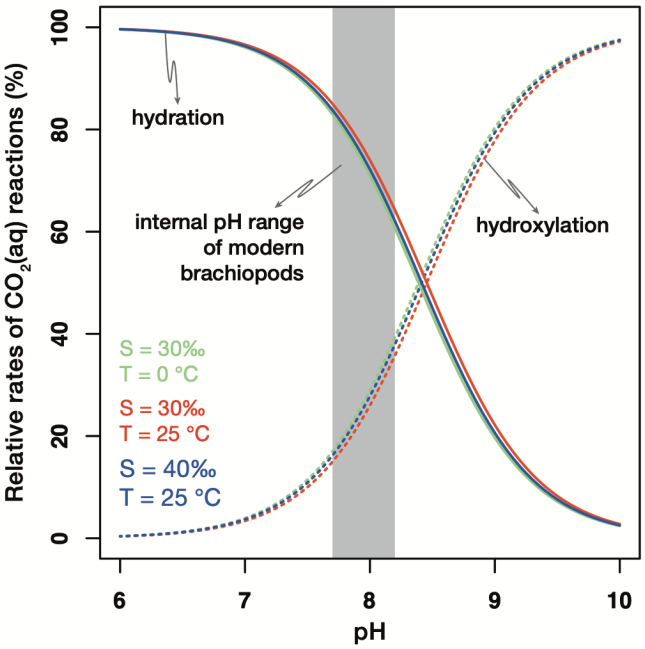

Figure 2.6 | At conditions characteristic to modern seawater, hydration is the dominant reaction at which $CO_{2\,(aq)}$ transforms into HCO_3^- in the brachiopod calcifying fluid. The balance between the rates of hydration (Equation 2.4) and hydroxylation (Equation 2.5) reactions is defined as $R = (k_{CO2} / (k_{CO2} + k_{OH}/aH) * 100$, where k_{CO2} and k_{OH} are the rate constants for $CO_{2\,(aq)}$ hydration and hydroxylation, respectively and aH is the H^+ activity (Johnson, 1982). R is calculated for three salinity (S) – temperature (T) scenarios, characteristic to modern seawater. The shaded area represents the internal pH range of modern brachiopods (Penman *et al.*, 2013).

should proceed via the hydration reaction (Johnson, 1982) (Figure 2.6). Such a dominance of hydration over hydroxylation would result in an offset Δ_{47}–$\delta^{18}O$ slope of -0.034 to -0.046, assuming estimated slopes of -0.05 and -0.01 to be characteristic of the hydration and hydroxylation reactions, respectively (Guo *et al.*, 2009; Spooner *et al.*, 2016). This range of slopes agrees with our result based on the dataset that combines gridded seawater $\delta^{18}O$ data with directly measured values (Figures 2.2c and A2.4c).

The $\delta^{18}O$ values of the temperate modern brachiopod shells analysed in this study correlate well with corresponding $\delta^{13}C$ values ($R^2 = 0.89$, p-value < 0.001; Figure 2.7a). Brand *et al.* (2015) showed that parallel correlations are present between shell $\delta^{18}O$ and $\delta^{13}C$ among tropical (latitudes < 30°), temperate (latitudes 30°–60°) and polar (latitudes > 60°) brachiopods, respectively. These parallel trends are related to the distinct habitat seawater temperatures and oxygen isotopic compositions of these groups (Brand *et al.*, 2015). With the exchange of the shell $\delta^{18}O$ values for the offset $\delta^{18}O$ values, the seawater and temperature effect on the shell $\delta^{18}O$ can be eliminated. The offset $\delta^{18}O$ values of the all modern brachiopod shells analysed in this study correlate with corresponding $\delta^{13}C$ values ($R^2 > 0.29$, p-value < 0.05; Figures 2.7b,c). A covariation of $\delta^{18}O$ and $\delta^{13}C$ have been also observed in single brachiopod shells by other authors (Auclair *et al.*, 2003; Yamamoto *et al.*, 2010a, 2010b; Penman *et al.*, 2013; Yamamoto *et al.*, 2013). A synchronous depletion of the heavy isotopes (^{18}O and ^{13}C) in biogenic carbonates, as observed for the modern brachiopods analysed in this study (Figure 2.7), agrees with the preferential

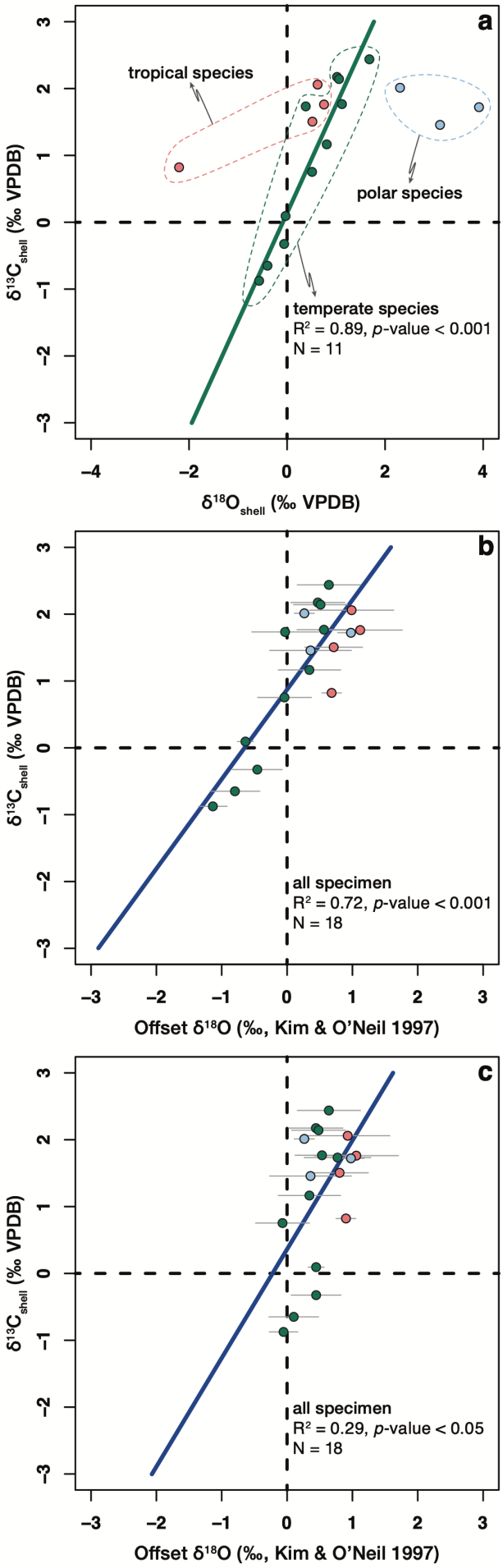

Figure 2.7 | Correlation between brachiopod shell oxygen and carbon isotope compositions. **(A)** The shell $\delta^{18}O$ values of the temperate modern brachiopods analysed in this study positively correlate with corresponding $\delta^{13}C$ values. **(B)** Shell $\delta^{13}C$ values positively correlate with offset $\delta^{18}O$ values for all modern brachiopods analysed in this study. Seawater $\delta^{18}O$ values were acquired from the Global Seawater Oxygen-18 Database (LeGrande & Schmidt, 2006). **(C)** The correlation between shell $\delta^{13}C$ and offset $\delta^{18}O$ is still present if, where available, the directly measured seawater $\delta^{18}O$ values were used for the calculations. For all plots: two-tailed *p*-values are calculated using a t-test for the simple linear regressions. Error bars for the offset $\delta^{18}O$ values indicate the mean deviation from oxygen isotope equilibrium calculated using the minimum and the maximum temperature estimates.

selection of light isotopes during $CO_{2\,(aq)}$ hydration and hydroxylation reactions (Keith & Weber, 1965; McConnaughey, 1989a, 1989b).

There is still an ongoing debate if the experiments of Kim and O'Neil (1997) are characteristic for the attainment of overall equilibrium between calcite and water. A natural example for equilibrium precipitation might be the Devil's Hole carbonate that grew extremely slowly in a constant geochemical environment. Its isotope composition has; therefore, been postulated not to be affected by kinetics (Coplen, 2007). The $\delta^{18}O$ value of the Devil's Hole carbonate is approximately +1.5‰ higher than could be calculated using the equation of Kim and O'Neil (1997). Laboratory experiments, comparing oxygen isotope fractionation factors of slowly and rapidly precipitated synthetic calcites (Dietzel *et al.*, 2009), and theoretical computations (Watkins *et al.*, 2013) provide further evidence that the Kim and O'Neil (1997) equation is not representative of thermodynamic equilibrium between calcite and water. The $\delta^{18}O$ values of the modern brachiopods analysed in this study, which show apparent clumped isotope equilibrium, are enriched by up to 1‰, relative to the Kim and O'Neil (1997) equilibrium (Figures 2.2b,c and A2.4b,c, and A2.5). This finding is in line with the hypothesis (Coplen, 2007; Dietzel *et al.*, 2009; Watkins *et al.*, 2013) that oxygen isotope equilibrium between calcite and water is expressed by fractionations exceeding those of Kim and O'Neil (1997).

In summary, the oxygen and clumped isotope composition of modern brachiopod shells are affected by growth rate-induced kinetic effects (*i.e.*, incomplete hydration and/or hydroxylation of $CO_{2\,(aq)}$ at higher growth rates) as indicated by (1) the negative correlation between offset Δ_{47} and offset $\delta^{18}O$ values, (2) the correlation between growth rates and both Δ_{47} and $\delta^{18}O$ offsets and (3) the positive correlation between shell $\delta^{13}C$ and $\delta^{18}O$ values. Kinetic effects may significantly contribute to the bottom seawater temperatures calculated from brachiopod shell $\delta^{18}O$ and Δ_{47}. Combining isotope data derived from multiple species is likely to result in higher variability in observed $\delta^{18}O$ and Δ_{47} that does not reflect real temperature changes. Based on our findings, information about taxon-specific growth rate and kinetics involved in calcite precipitation is essential whenever constraining seawater temperatures from Δ_{47} and $\delta^{18}O$ values in brachiopods. A future study considering seasonal variations in seawater $\delta^{18}O$ values and in growth rates could further improve our understanding of the nature and extent of the kinetic isotope effect in brachiopods.

Chapter 3: Balmy seas during the Early Cretaceous

Abstract

Much of what we know about the deep-time history of ocean temperature is derived from the oxygen isotope analysis of marine calcite fossils. This record is biased due to unreliable assumptions on the oxygen isotope composition of the seawater. In this study, we investigated Late Jurassic to Early Cretaceous sub-arctic, boreal, and sub-tropical fossil belemnites (Mollusca: Cephalopoda). Combined carbonate clumped isotope and oxygen isotope data provide new palaeotemperature estimates as well as a constraint on the oxygen isotope composition of seawater.

Our belemnite data reveal an average temperature of 25(±4) °C for the Late Jurassic–Early Cretaceous Southern Atlantic Ocean. For the northern hemisphere, we infer balmy high-latitude marine temperatures (> 21±5 °C) and warm sub-tropical temperatures (31±6 °C) for the Valanginian (ca. 135 million years ago). Supplementing our clumped isotope-based temperature estimates with TEX_{86} data, we reconstruct a latitudinal temperature gradient that is reduced compared to modern conditions. We find that modelling efforts are close to reproducing tropical temperatures when not only high pCO_2 levels but polar amplification and latitudinal heat transfer are also considered.

Early Cretaceous seawater oxygen isotope values show a modern profile and are much more positive (up to 1.5‰ SMOW) than typically assumed. We imply that Cretaceous seawater $\delta^{18}O$ is unlikely to have been homogeneous across different palaeolatitudes and basins. Incorrectly assuming seawater $\delta^{18}O$ results in an underestimation of carbonate $\delta^{18}O$-based temperatures, most acute at middle and tropical latitudes.

Collaborators

Gregory D. Price[1], Madeleine Vickers[2], Jolien Linckens[3], Jens Fiebig[3] — ([1] University of Plymouth, [2] University of Copenhagen, [3] Goethe University Frankfurt).

3.1. Introduction

Existing proxy data suggests a greatly reduced Cretaceous latitudinal sea-surface temperature (SST) gradient (Barron, 1983; Huber *et al.*, 1995; Pucéat *et al.*, 2003; Voigt *et al.*, 2003; Littler *et al.*, 2011; Naafs & Pancost, 2016). During much of the Cretaceous, although ocean temperatures were variable, equatorial surface waters were warmer (ca. 30–38 °C) than the maximum SST recorded in the modern ocean, and mid to higher latitude surface waters were also 10–20 °C warmer than today (Huber *et al.*, 1995; Erbacher *et al.*, 2011; Littler *et al.*, 2011; Jenkyns *et al.*, 2012; Naafs & Pancost, 2016; O'Brien *et al.*, 2017; Gómez Dacal *et al.*, 2019). The presence of Early Cretaceous polar ice implied by drop-stone and glendonite occurrences (Frakes & Francis, 1988; Galeotti *et al.*, 2009; Grasby *et al.*, 2017) is at odds with contemporaneous warm polar ocean temperatures, high atmospheric pCO_2, and the occurrence of tropical flora at mid- to high latitudes (Miller, 2009; Föllmi, 2012). Cretaceous atmospheric pCO_2 reached up to 8x pre-industrial levels (Berner & Kothavala, 2001; Wang *et al.*, 2014; Foster *et al.*, 2017). This implied climatic warmth is consistent with the presence of thermophilic faunas (Tarduno *et al.*, 1998) and floras from high latitude regions (Barron & Washington, 1982; Hurum *et al.*, 2006; Spicer & Herman, 2010). However, contrary to what the most of the geological record suggests, Cretaceous general climate model (GCM) simulations indicate that the latitudinal temperature gradient was much steeper (Otto-Bliesner & Upchurch, 1997; Poulsen *et al.*, 2007; Zhou *et al.*, 2008; Donnadieu *et al.*, 2016). Reconstructions of marine ocean temperatures are contradictory, particularly for the high latitudes (Huber *et al.*, 1995; Bice *et al.*, 2003; Jenkyns *et al.*, 2012; Price & Passey, 2013; O'Brien *et al.*, 2017). There is disagreement between different proxy temperature reconstructions, *e.g.,* TEX_{86} *vs.* $\delta^{18}O$ (Price & Gröcke, 2002; Jenkyns *et al.*, 2012) as well as proxy *vs.* climate model reconstructions (Barron & Washington, 1982; Poulsen, 2004; Spicer *et al.*, 2008; O'Brien *et al.*, 2017).

The stable oxygen isotope composition of marine calcite is the most extensively used temperature proxy (Veizer & Prokoph, 2015; O'Brien *et al.*, 2017). High latitude sea-surface temperatures derived from organic palaeothermometers, *e.g.,* TEX_{86}, disagree with $\delta^{18}O$-based temperature reconstructions that yield cooler estimates. Furthermore, both proxies show a mismatch with model predictions. These differences have led some authors to suggest that these high TEX_{86} temperature estimates are too warm (Hollis *et al.*, 2009). Conversely, $\delta^{18}O$-based palaeotemperature reconstructions rely on several

assumptions, amongst which is the oxygen isotopic composition of the seawater ($\delta^{18}O_{sw}$) (Huber *et al.*, 1995; Price & Sellwood, 1997; Price & Gröcke, 2002; Bice *et al.*, 2003). Obtaining a value for $\delta^{18}O_{sw}$ is complicated because of variables that cannot be easily independently quantified, such as freshwater input, evaporation, and the waxing and waning of polar ice (Frakes & Francis, 1988; Price, 1999; Wierzbowski *et al.*, 2018). Additionally, a proposed change in the mode of mid-ocean ridge hydrothermal alteration over million year timescales suggests that $\delta^{18}O_{sw}$ has increased gradually through Earth's history, from ca. -6‰ SMOW in the Cambrian to its present value of ca. 0‰ SMOW (Jaffrés *et al.*, 2007; Veizer & Prokoph, 2015). The clumped isotope palaeothermometry technique measures the abundance of heavy (^{13}C–^{18}O bond bearing; mass 47) carbonate isotopologues within a single carbonate phase relative to its stochastic distribution. This proxy provides seawater temperature estimates independent of $\delta^{18}O_{sw}$ (Ghosh *et al.*, 2006; Price & Passey, 2013; Wierzbowski *et al.*, 2018).

Belemnite rostra are fossil remains of extinct cephalopods that are commonly used for the reconstruction of the temperature and the oxygen isotopic composition of the Jurassic and Cretaceous seawater (Bodin et al., 2009; Dera et al., 2011; Price et al., 2013; Korte et al., 2015; Veizer & Prokoph, 2015). They precipitated a low-Mg calcite inner guard that fossilizes well and are abundant in Mesozoic sequences.

In this study, we provide new data for the Late Jurassic–Early Cretaceous equator-to-pole seawater temperature and $\delta^{18}O_{sw}$ profile. The aim of this effort is to help resolving discrepancies between models and different proxy data. For this, we have analysed 31 exceptionally well-preserved belemnites from biostratigraphically well-constrained sections that cover a wide range of palaeolatitudes for carbonate $\delta^{18}O$, $\delta^{13}C$, and Δ_{47}. We use our independent temperature estimates in conjunction with the $\delta^{18}O$ of the belemnite rostra to reconstruct $\delta^{18}O_{sw}$.

3.2. Materials and methods

3.2.1. Stratigraphic framework

For this study we investigated belemnites from five locations: DSDP Site 511, Falkland Plateau (51.004667° S, 46.971667° W); Khatanga Basin (Boyarka River), Russia (70.592611° N, 97.369083° E); Pechora Basin (Izhma River), Russia (64.835150° N,

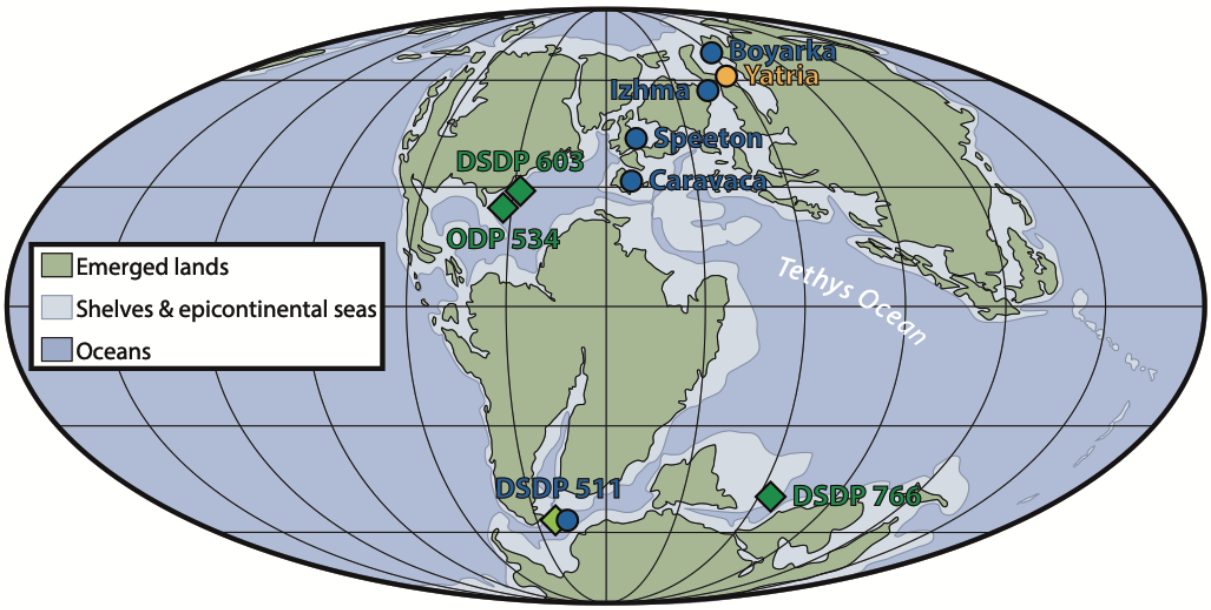

Figure 3.1 | Early Cretaceous palaeogeographic reconstruction with locations of the sites discussed in this study.
Map modified after Dercourt *et al.* (2000). The palaeolatitude estimates are consistent with Young *et al.* (2018) that is used for the subsequent figures

53.782200° E), Cleveland Basin, Speeton, UK (54.160555° N, 0.236111° W); and Caravaca, Spain (38.086944° N, 1.853889° W) (Figure 3.1).

The samples from Deep Sea Drilling Project Site 511 (Leg 71), cores number 59–70, cover the Middle Jurassic to Early Cretaceous. These sediments contain a diverse and abundant bivalve, belemnite and ammonite macrofauna. The lithology of the sampled section of DSDP Site 511 consists of grey-black, thinly laminated mudstones and soft, grey claystones, which were deposited in a periodically anoxic, low-energy, shallow water basin (Jeletzky, 1983). The water depth at DSDP Site 511 during the Jurassic–Cretaceous interval did not exceed 400 meters (Basov & Krasheninnikov, 1983). Since the Cretaceous, these sediments have experienced only mild burial diagenetic conditions. A geothermal gradient of 7.4 °C/100 m at DSDP Site 511 yield a maximum burial temperature of ca. 50 °C for the samples analysed in this study (Langseth & Ludwig, 1983).

The Cretaceous part of the of the Boyarka River section is ca. 300 m thick and consists of shallow marine sandstones, siltstones, and clays (Nunn *et al.*, 2010). Macrofauna includes belemnite rostra and ammonites, allowing a detailed biostratigraphic zonation from the Ryazanian *Heteroceras kochi* Zone to the Late Valanginian *Homolsomites bojarkensis* Zone (Shulgina *et al.*, 1994; Nunn *et al.*, 2010). Based on sediment thickness, the burial depth of the Boyarka River succession of the

Khatanga Basin, is likely to be ca. 500 m, and thermal gradients moderate ca. 40 °C/km (Klett *et al.*, 2011; Dobretsov *et al.*, 2013).

The ca. 62 m thick Izhma River section comprises shallow marine clastics from the Ryazanian ("*Pseudocraspedites* & *Surites*" Zone) to Valanginian (*Dichotomites bidichotomus* Zone) (Baraboshkin, 2007; Nunn *et al.*, 2010). Based on sediment thickness, the burial depth is likely to be no more than 1000 m, and the present thermal gradients in the Pechora Basin are moderate, ca. 19–35 °C/km (Lindquist, 1999).

The Cretaceous successions located near Caravaca consist of nodular limestones with abundant crinoid fragments, overlain by hemipelagic marl-limestone alternations (Aguado *et al.*, 2000). The sediments deposited in a low-energy, few hundred metres deep marine basin (Janssen, 2003). Macrofauna consists mainly of belemnite rostra and well-preserved ammonites, allowing detailed biostratigraphic zonation and correlation of the sections (Aguado *et al.*, 2000; Janssen, 2003; Company & Tavera, 2015; Price *et al.*, 2018). The maturity of the organic matter and other diagenetic observations imply a burial depth of no more than 1000 m (Reicherter *et al.*, 1996).

The Speeton Clay Formation of the Cleveland Basin comprises about 100 m of interbedded shallow marine claystones. The stratigraphical succession contains abundant belemnite rostra and well-preserved ammonites, allowing detailed biostratigraphic zonation (McArthur *et al.*, 2004). Measured $^{87}Sr/^{86}Sr$ values (McArthur *et al.*, 2004) show a good agreement between the biostratigraphic data. A number of lines of evidence, *e.g.,* vitrinite reflectance, indicates that the maximum burial depth of the Cretaceous sediments in the Cleveland Basin was ca. 2000 m (Holliday, 1999).

3.2.2. Sample Selection

A subset of 31 belemnite rostra were selected for clumped isotope analysis. *Acroteuthis* sp. from Speeton from the "*polyptychites"* Zone; *Berriasibelus* sp. and *Duvalia* sp. from Caravaca, Spain from the "*T." pertransien*s to *S. verrucosum* Zones; *Acroteuthis* sp. and *Pachyteuthis* sp. from Pechora Basin from the *Neotolia klimovskiensis* to *Polyptychites michalskii* Zones; *Acroteuthis* sp., *Lagonibelus* sp., and *Pachyteuthis* sp. from Khatanga Basin from the *Neotolia klimovskiensis* to *Polyptychites michalskii* Zones; and Late Jurassic to Early Cretaceous *Belemnopsis* sp. from DSDP Site 511.

Belemnite samples were filtered to include the best-preserved samples, as indicated by trace element concentrations and petrographic analyses including

cathodoluminescence (McArthur *et al.*, 2004; Nunn *et al.*, 2010; Price *et al.*, 2018). We paid attention to investigate only a narrow range of related taxa to minimize the possibility of species-specific vital effects. Subsamples were derived avoiding the margins, surface and juvenile portions of the belemnites and parts around the apical zone. Visual inspection shows belemnite rostra preservation is excellent, with all displaying honey-coloured translucent calcite. Rostra are non-luminescent, except calcite associated with the outermost concentric growth bands and the apical line, areas which we avoided during sampling. From each belemnite rostra we subsampled ca. 50 mg carbonate powder across multiple growth bands.

At elevated temperatures, diffusion of carbon and oxygen isotopes in the carbonate mineral lattice may reset the initial bond-ordering (Passey & Henkes, 2012). However, theoretical calculations based on laboratory experiments evidence that solid-state diffusion, even in wet and high-pressure conditions, is insignificant below 100 °C burial temperatures on a time-scale of 100–160 Ma (Henkes *et al.*, 2014; Brenner *et al.*, 2018). Thus, it is implausible that the belemnite rostra analysed in this study were affected by solid state reordering.

3.2.3. Electron Microscopy

In addition to the already available trace element data and cathodoluminescence analyses (Price & Sellwood, 1997), we made EBSD (electron backscatter diffraction) analyses and SEM-BSE (secondary electron microscopy – backscattered electrons) images of selected rostra for the belemnites collected from DSDP Site 511, at the Goethe University Frankfurt, Frankfurt am Main, Germany on a JEOL JSM-6490 scanning electron microscope equipped with an Oxford Instruments Nordlys EBSD detector, using a 15 kV acceleration voltage and a beam current of ca. 8 nA. The mapping stepsize was set either 2 µm, 6 µm or 7 µm. During EBSD data processing misindexed points were removed (wild spikes) followed by the removal of some zero solutions based on four indexed neighbours.

3.2.4. Clumped isotope analyses

We performed the clumped isotope analyses using a ThermoFisher™ MAT 253™ gas-source isotope-ratio mass spectrometer connected to an automated gas extraction and purification line. Carbonate digestion at 90 °C, GC-based CO_2 purification and subsequent measurement procedures are detailed in Chapter 6. Raw isotope values were calculated using the IUPAC isotopic parameters and were projected to the carbon dioxide equilibrium scale using equilibrated gases (25 °C and 1000 °C, respectively) of various

bulk isotope composition (Petersen *et al.*, in review). A 90–25 °C acid fractionation factor of +0.088‰ was applied to all $\Delta_{47\ (RFAC)}$ values (Petersen *et al.*, in review). To verify the consistency and precision of the clumped isotope measurements five carbonate standards were analysed along the samples. The $\Delta_{47\ (RFAC)}$ (1σ S.D., N = number of replicates) values of the reference material are: Carrara 0.407‰ (0.019‰, N = 339), MuStd 0.749‰ (0.018‰, N = 184), ETH1 0.301‰ (0.016‰, N = 91), ETH2 0.303‰ (0.019‰, N = 45), ETH3 0.711‰ (0.018‰, N = 92), ETH4 0.556‰ (0.020‰, N = 10) (Supplementary Data 3.1 and 3.2). To convert Δ_{47} values to temperatures, we used the reprocessed version of our in-house Wacker *et al.* (2014) calibration (Equation 1.9).

Temperature uncertainties are based on external 1σ S.E. (including the *t*-value) that is always larger than or identical to the best attainable internal precision as represented by the shot noise limit (0.004–0.005‰). The uncertainties for the mean seawater temperatures for each studied location, combine the external 1σ S.E. of the of the $\Delta_{47\ (RFAC)}$ values of the individual belemnites and the 1σ S.E. of the mean Δ_{47} values calculated from 4–6 belemnites per location.

Reconstructed $\delta^{18}O_{sw}$ values were calculated for each clumped isotope sample from the Δ_{47}-derived temperature and the calcite $\delta^{18}O$ of each belemnite, using two $1000\ln\alpha_{calcite-water}$–temperature relationships (Kim & O'Neil, 1997; Coplen, 2007) (Equations 2.1 and 1.10, respectively). The error in the calculated $\delta^{18}O_{sw}$ correspond to the 1σ S.E. of the $\Delta_{47\ (RFAC)}$, whereas the uncertainties for the mean $\delta^{18}O_{sw}$ values integrate the combined temperature error and the 1σ S.E. of the belemnite $\delta^{18}O$ values calculated from the 4–6 rostra per location.

3.3. Results

3.3.1. Electron Microscopy

All investigated rostra, excluding the areas adjacent to the apical line, are made up of optical calcite and the c-axis of the calcite grains point radially outwards (Figures A3.1–A3.4). The distribution of the crystallographic a-axes also follows a pattern. This is analogous to pristinely preserved rostra (Stevens *et al.*, 2017). Our EBSD and SEM-BSE analyses suggest that recrystallization, that would change the original orientation of the biogenic calcite grains, did not occur in the sampled areas.

3.3.2. Clumped Isotope Analyses

The $\Delta_{47\ (RFAC)}$ values are reported in Table A3.1. The 1σ S.E. for the clumped isotope measurements, calculated from 2–7 replicate analyses are between 0.003‰ and 0.020‰ (mean 0.008‰). For DSDP Site 511 (Late Jurassic–Early Cretaceous), the $\Delta_{47\ (RFAC)}$ values yield seawater temperatures ranging between 21(±6) °C and 28(±4) °C (mean 25±4 °C) and show no significant stratigraphic trend (Figure 3.2). The average Δ_{47}-derived temperatures for the Valanginian from the Tethyan and Boreal sites (palaeolatitudes from 24° N to 74 °N, Figure 3.1) range from 21(±5) °C to 31(±6) °C (Figures 3.2 and 3.3). The

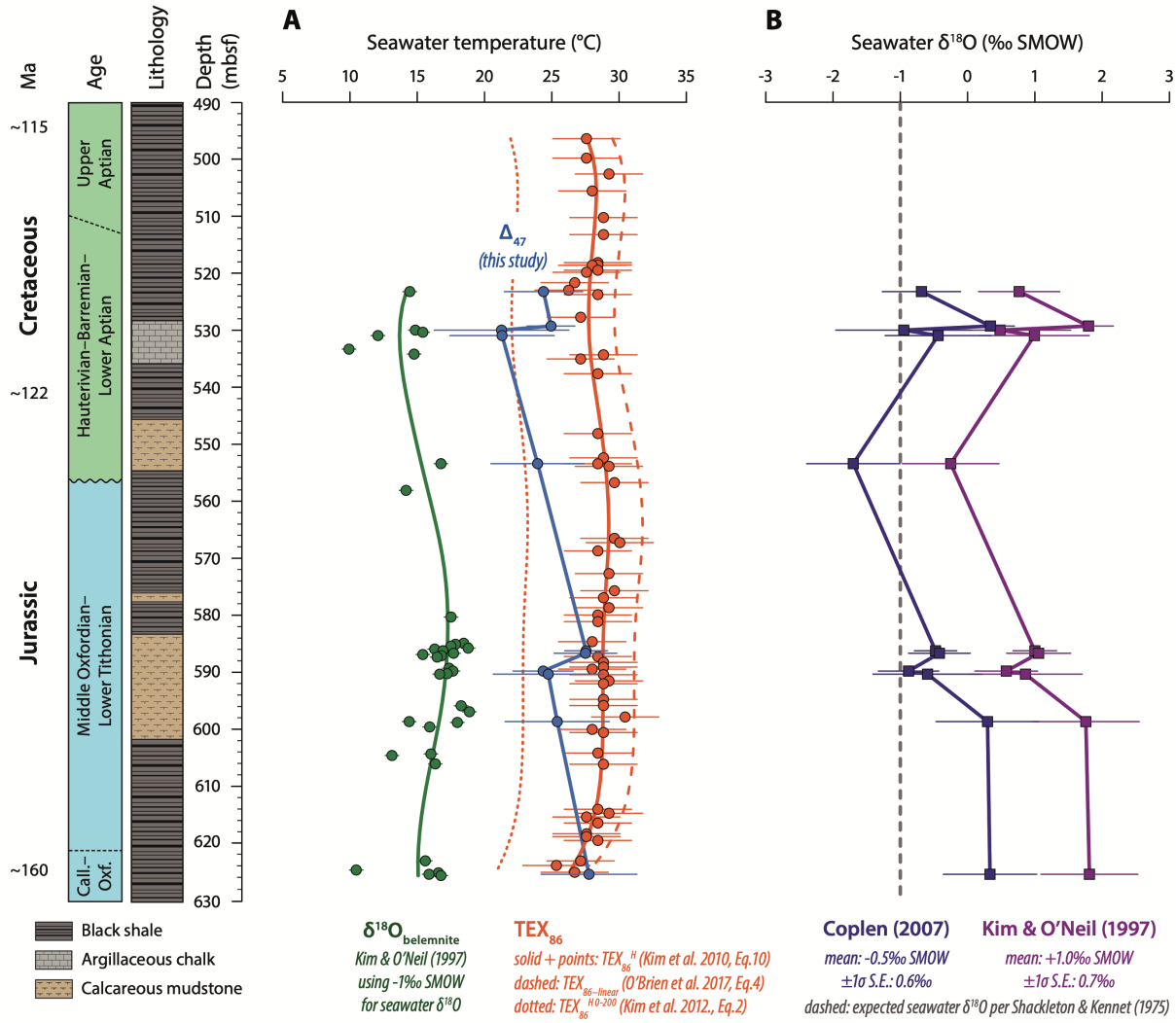

Figure 3.2 | Jurassic and Early Cretaceous temperatures and seawater $\delta^{18}O$ from DSDP Site 511. **(A)** A comparison of the clumped isotope temperature reconstructions for DSDP Site 511 compared to those based on stable oxygen isotopes (Price & Sellwood, 1997; Price & Gröcke, 2002) and TEX_{86} sea-surface temperature reconstructions (Jenkyns *et al.*, 2012). **(B)** Reconstructed $\delta^{18}O_{sw}$ values (this study) are shown, comparing different temperature equations (Coplen (2007) *vs.* Kim and O'Neil (1997)). Belemnite $\delta^{18}O$ yield anomalously low temperatures mostly due to the erroneous assumption about the equilibrium oxygen isotope fractionation between calcite and water. Smoothed curves are estimated using locally-weighted regressions. Error bars represent for $\delta^{18}O_{belemnite}$ and Δ_{47} the 1σ S.E. of multiple replicate analyses; for TEX_{86}^{H} the calibration error; and for $\delta^{18}O_{sw}$ the 1σ S.E. corresponding to the Δ_{47} measurements. Age model construction is described in the supplements. Data for this figure can be found in Supplementary Data 3.1.

mean error for the reconstructed temperatures for individual belemnites is ±3 °C (1σ S.E.) and ±5 °C for the different locations. Steeper-sloped calibration compared to the applied Wacker *et al.* (2014) calibration, *i.e.,* Kelson *et al.* (2017) yield indistinguishable temperatures within ±1σ S.E. (Supplementary Data 3.1 and 3.2).

3.4. Discussion

3.4.1. Belemnite Δ_{47} temperatures

Since belemnites went extinct at the K/Pg boundary, it is difficult to determine if they precipitated their rostra in thermodynamic equilibrium with seawater and; thus, if their isotopic composition record true seawater temperatures. Recent studies identified correlations between belemnite $\delta^{18}O$ and $\delta^{13}C$ along ontogenetic profiles in specific specimens, which agree with the preferential selection of light isotopes due to kinetic effects (Stevens *et al.*, 2015; Ullmann *et al.*, 2015; Stevens *et al.*, 2017). The co-variation of trace element ratios (Mg/Ca, Sr/Ca) and rostrum secretion rates further argue that belemnite proxy signals may be influenced by growth rate related kinetics (Stevens *et al.*, 2017; Ullmann *et al.*, 2017; Ullmann & Pogge von Strandmann, 2017).

Among the belemnites investigated in this study, there is no significant correlation between calcite $\delta^{18}O$ and $\delta^{13}C$. Also, multiple studies have reported colder $\delta^{18}O$-derived belemnite palaeotemperatures compared to coeval brachiopod-based temperature estimates, when using the same $\delta^{18}O$–temperature relationship for both groups of animals and assuming a constant oxygen isotope composition for the seawater (Voigt *et al.*, 2003; Alberti *et al.*, 2012a; Veizer & Prokoph, 2015). It is hard to explain this discrepancy by ecological behaviour. Brachiopods are benthic organisms. Some studies postulated that belemnites calcified their rostra in the upper part of the water column (Monks *et al.*, 1996; Lukeneder, 2005; Stevens *et al.*, 2014; Price *et al.*, 2015; Klug *et al.*, 2016), whereas others considered belemnites as nektobenthic organisms (Wierzbowski *et al.*, 2013). Nevertheless, for shallow marine settings like the locations investigated in this study (Chapter 3.2.1.), one could assume a low temperature gradient in the water column. Although the spread of belemnites on a higher taxonomic level is documented, *e.g.,* Middle Cenomanian Event (Voigt *et al.*, 2006), belemnite faunal realms are geographically well defined, which together with the frequent co-occurrence of juvenile and adult specimen makes the seasonal migration of belemnites unlikely (Stevens, 1963). Kinetic effects in brachiopods; however, bias their carbonate

$\delta^{18}O$-based temperatures to warmer values (Bajnai *et al.*, 2018). It is likely; therefore, that belemnites precipitated their rostra closer to thermodynamic equilibrium with ambient seawater compared to brachiopods. Laboratory experiments and theoretical calculations (Dietzel *et al.*, 2009; Watkins *et al.*, 2013; Devriendt *et al.*, 2017; Levitt *et al.*, 2018) provide evidence that oxygen isotope equilibrium between calcite and water is expressed by fractionations exceeding those of Kim and O'Neil (1997) by ca. 1.5‰. Near equilibrium precipitation justifies the use of the Coplen (2007) equation to calculate seawater temperatures from belemnite $\delta^{18}O$ and Δ_{47}. However, since kinetic effects in belemnites cannot be excluded entirely, we consider belemnite Δ_{47} temperatures as maximum estimates, and belemnite data-derived $\delta^{18}O_{sw}$ as minimum estimates.

3.4.2. Palaeoseawater temperatures at DSDP Site 511

Deep Sea Drilling Project Site 511, located on the Falkland Plateau, is particularly well suited for studying Jurassic–Cretaceous climate due to its abundant and exceptionally preserved macrofossils, including belemnites (Jeletzky, 1983; Price & Sellwood, 1997; Price & Gröcke, 2002). The Falkland Plateau was located at approximately 53° S during the Late Jurassic–Early Cretaceous (Young *et al.*, 2018) (Figure 3.1). Mean annual temperatures derived from General Circulation Models (GCM) for the Late Jurassic and Early Cretaceous indicate that the temperatures of the Falkland Plateau region are representative of other similar southern hemisphere palaeolatitudes (Lunt *et al.*, 2016).

Earlier research at DSDP Site 511 that used the TEX_{86} palaeotemperature proxy suggests that warm sea-surface conditions (26–35 °C) existed during the Late Jurassic–Early Cretaceous interval (Jenkyns *et al.*, 2012). In their study, Jenkyns *et al.* (2012) used the global core-top TEX_{86}^{H} calibration of Kim *et al.* (2010) to calculate seawater temperatures. For the studied interval, the linear calibrations of Kim *et al.* (2010) and O'Brien *et al.* (2017), as well as the BAYSPAR calibration of Tierney and Tingley (2015) yield ca. 2–3 °C warmer temperatures than TEX_{86}^{H}. In contrast, other calibrations such as the foraminifera-linked calibration of Hollis *et al.* (2012), and the calibrations that assume a non-surface export depth of GDGTs (Kim *et al.*, 2012; Schouten *et al.*, 2013) yield ca. 5–6 °C colder estimates. Compared to independent coeval temperature estimates in deep-time palaeoceanographic studies, the TEX_{86}^{H} calibration yields the least discrepant values among the calibrations that we can apply to published data (Meyer *et al.*, 2018; de Bar *et al.*, 2019). In this study, we consistently calculate all TEX_{86} temperatures using the TEX_{86}^{H} calibration, but acknowledge that such temperatures, given the shallow water and at high

latitude settings of DSDP Site 511 may be biased toward warmer values (Schouten *et al.*, 2013; Taylor *et al.*, 2013). Regardless of the calibration used, TEX_{86}-derived palaeotemperatures are consistently warmer (by ca. 7–12 °C) than palaeotemperature estimates based on belemnite $\delta^{18}O$ (-1‰ SMOW $\delta^{18}O_{sw}$ + Kim and O'Neil (1997)) (Jenkyns *et al.*, 2012). Another study, undertaken on Barremian to Lower Aptian (ca. 130 million years ago, Early Cretaceous) sediments from two outcrops in northern Germany, yields a similar discrepancy between belemnite $\delta^{18}O$-derived palaeotemperatures and TEX_{86}-based estimates (Mutterlose *et al.*, 2010).

Our Δ_{47}-derived temperature range (21±6 °C to 28±4 °C, mean 25±4 °C) for the entire section is considerably higher than those temperatures reconstructed via stable oxygen isotope palaeothermometry (ranging from 10 °C to 19 °C, mean 16 °C, -1‰ SMOW $\delta^{18}O_{sw}$ + Kim and O'Neil (1997)) (Price & Sellwood, 1997; Price & Gröcke, 2002), and cooler, though within error, of sea-surface temperature estimates derived from TEX_{86} analyses (28±3 °C to 31±3 °C; TEX_{86}^{H}; Figure 3.2a) (Jenkyns *et al.*, 2012). Besides the discussed TEX_{86}^{H} bias towards warmer temperatures, a seasonal bias in either proxy may provide a further explanation: belemnites may reflect mean annual temperatures (Price

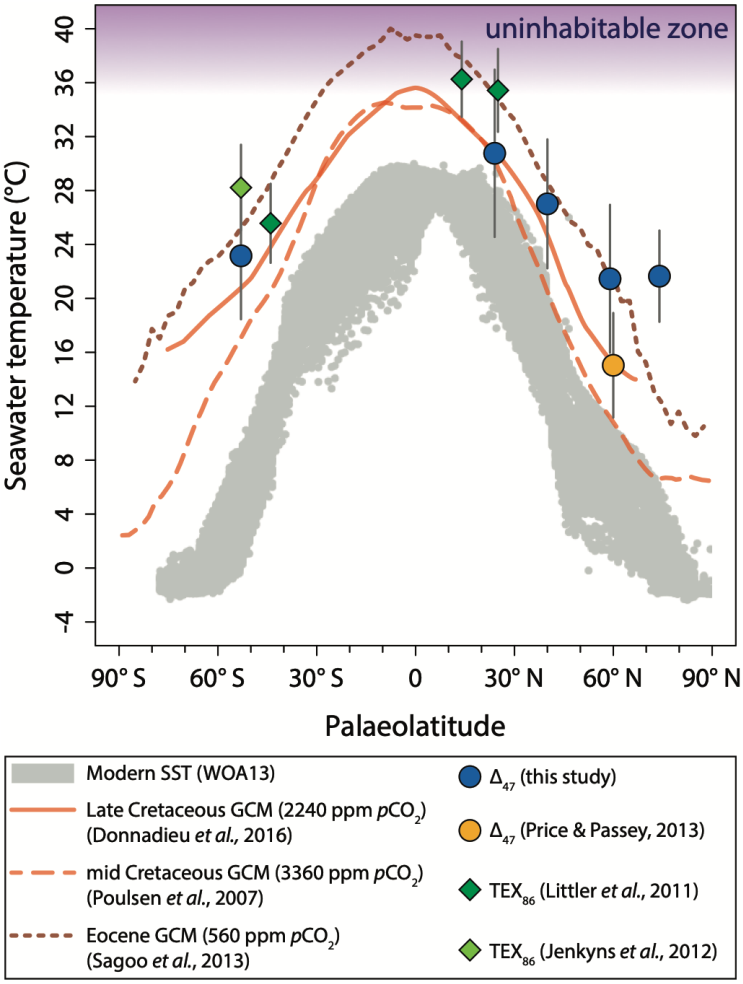

Figure 3.3 | Valanginian (Early Cretaceous, ca. 135 Ma) latitudinal temperature reconstruction. Mean annual temperature observations from the World Ocean Atlas (Locarnini *et al.*, 2013). Valanginian TEX_{86} temperatures (Littler *et al.*, 2011; Jenkyns *et al.*, 2012) were recalculated using the TEX_{86}^{H} calibration (Kim *et al.*, 2010). Additional Valanginian Δ_{47} data is from Price and Passey (2013). Early Cretaceous data are compared with a Late Cretaceous GCM made with 8x pre-industrial pCO_2 (Donnadieu *et al.*, 2016), a mid-Cretaceous GCM made with 12x pre-industrial pCO_2 (Poulsen *et al.*, 2007), and an Eocene GCM made with 2x pre-industrial pCO_2 (Sagoo *et al.*, 2013). Uninhabitable zone *sensu* Brock (1967). The ± uncertainties are combined errors (see Table 3.1). Data for this figure can be found in Tables 3.1 and A3.1, Supplementary Data 3.1 and 3.2.

& Sellwood, 1997) contrary to TEX_{86} that may rather indicate summer temperatures (Leider *et al.*, 2010; Hollis *et al.*, 2012).

All three records from Site 511 show less than 7 °C variability across the entire Upper Jurassic and Lower Cretaceous interval, although the low sampling resolution means it is not possible to derive more detailed information on Jurassic and Cretaceous climate evolution. Nevertheless , these data confirm warm Late Jurassic–Early Cretaceous high latitude ocean temperatures, precluding the possibility of substantial land ice, and are consistent with estimated mean annual temperatures from fossil plant assemblages from the Antarctic Peninsula (Cantrill, 1998; Francis & Poole, 2002) and Mesozoic polar Australia (Douglas & Williams, 1982).

3.4.3. Valanginian seawater temperatures from the northern hemisphere

Our Δ_{47}-derived temperature estimate for the Valanginian northern hemisphere low latitudes (31±6 °C) are consistent with high average temperature values of ca. 35 °C obtained from Early Cretaceous TEX_{86} (Littler *et al.*, 2011; Naafs & Pancost, 2016; O'Brien *et al.*, 2017) (Figure 3.3, Table 3.1). Furthermore, our Valanginian temperature estimates for the northern hemisphere middle latitudes (21±5 °C to 27±5 °C) are warmer than other Early Cretaceous temperature estimates derived from $\delta^{18}O$ thermometry (Pucéat *et al.*,

Location	Palaeolatitude	N	Temperature (°C)	$\delta^{18}O_{sw}$ (‰, SMOW)
DSDP 511 *,1	53° S	5	23±5	-0.7±1.1
Caravaca *,1	24° N	5	31±6	1.5±1.4
Speeton *,1	40° N	6	27±5	0.7±1.4
Izhma *,1	59° N	4	21±5	0.5±1.9
Boyarka *,1	74° N	5	22±3	-0.8±1.6
Yatria *,2	60° N	8	15±4	-1.2±1.0
ODP 534 #,3	14° N	34	36±3	
DSDP 603 #,3	25° N	15	35±3	
DSDP 766 #,3	44° S	17	26±3	
DSDP 511 #,4	53° S	8	28±3	

Table 3.1 | Mean seawater temperatures and $\delta^{18}O_{sw}$ for the Valanginian (Early Cretaceous).
* Δ_{47}-derived palaeotemperatures. Temperatures are calculated using Wacker *et al.* (2014) (Equation 1.9). For the whole set of samples from DSDP Site 511 (11 rostra) see Figure 3.2. The ± uncertainties for the mean temperatures combine the external 1σ S.E. (including *t*-value) of the of the $\Delta_{47\,(RFAC)}$ values of the individual belemnites (Table A3.1) and the 1σ S.E. of the mean Δ_{47} values calculated from 4–6 belemnites per location (N). The ± uncertainties for the mean $\delta^{18}O_{sw}$ values integrate the combined temperature error and the 1σ S.E. of the belemnite $\delta^{18}O$ values calculated from the 4–6 rostra per location. # TEX_{86}-derived palaeotemperatures. The ± uncertainties for the mean temperatures combine the error of the TEX_{86}^{H}calibration (Kim *et al.*, 2010; O'Brien *et al.*, 2017) and the external 1σ S.D. of the analyses. All palaeolatitude estimates are from Young *et al.* (2018). Data is compiled from: [1] this study, [2] Price and Passey (2013), [3] Littler *et al.* (2011), [4] Jenkyns *et al.* (2012).

2003; McArthur *et al.*, 2004; Mutterlose *et al.*, 2010), but they are comparable to data from other Cretaceous (Naafs & Pancost, 2016; O'Brien *et al.*, 2017) and Paleogene (Evans *et al.*, 2018) greenhouse intervals. The new temperature estimates from higher palaeolatitudes (22±3 °C) are warmer than previous carbonate $\delta^{18}O$-based estimates (Ditchfield, 1997; Price & Nunn, 2010; Bernard *et al.*, 2017) but are consistent with warm Late Cretaceous TEX_{86} seawater (Super *et al.*, 2018) and Δ_{47} terrestrial (Burgener *et al.*, 2019) temperatures. Our Valanginian seawater temperatures across all latitudes are 4–14 °C warmer than modern observations, although at middle latitudes they approach the warmest modern observations (Locarnini *et al.*, 2013). The congruence of our Δ_{47}-derived temperature estimates with data from the organic TEX_{86} palaeothermometer is consistent with no substantial bias towards higher temperatures in the clumped isotope record.

Our interpretation of relatively warm past ocean temperatures at northern hemisphere middle–high latitudes is consistent with fossil records, *e.g.,* Early Cretaceous dinosaur assemblages reported from Svalbard and the Arctic (Tarduno *et al.*, 1998; Hurum *et al.*, 2006), and palaeobotanical temperature constraints derived from fossil floras (Spicer & Herman, 2010). In contrast, data from the Early Cretaceous of Canada (Grasby *et al.*, 2017), Svalbard (Vickers *et al.*, 2016), and Siberia (Rogov *et al.*, 2017a) suggests that numerous boreal cool events perturbed otherwise warm conditions. These authors describe abundant glendonites in Valanginian to Aptian strata that are thought to be critical markers of cold conditions. The occurrence of glacial deposits also implies the presence of polar ice cover, at least for short periods. The cold-snaps are not incompatible with our data from the Valanginian presented here. Grasby *et al.* (2017) concludes that cold periods were brief, punctuating an overall warm Early Cretaceous climate. The low temporal resolution of the studied sections, concerning belemnite occurrences, do not allow us to exclude interim freezing periods at high latitudes.

3.4.4. Valanginian latitudinal temperature gradient

Using the average palaeotemperatures and palaeolatitude (Young *et al.*, 2018) at each of our sites together with Valanginian Δ_{47} data from Price and Passey (2013) and TEX_{86}^{H} data from Littler *et al.* (2011) and Jenkyns *et al.* (2012), we can reconstruct an Early Cretaceous latitudinal temperature profile for the northern hemisphere with an estimated gradient of 0.31 °C/° lat. ($N = 7$, $R^2 = 0.80$, p-value < 0.01), between 24° N and 74° N (Figure 3.3). The gradient becomes even shallower, 0.20–0.24 °C/° lat. ($R^2 > 0.67$, p-

value < 0.01) if the "colder" TEX_{86}^{H0-200} calibration is considered (Kim *et al.*, 2012), or only the Δ_{47}-derived temperatures are taken into account. Early to Late Cretaceous TEX_{86} (Littler *et al.*, 2011; Naafs & Pancost, 2016; O'Connor *et al.*, 2019) and $\delta^{18}O$-derived (Pucéat *et al.*, 2003; Voigt *et al.*, 2003) palaeotemperatures also reveal a shallow latitudinal temperature gradient.

The implied Cretaceous shallow latitudinal temperature gradient contrasts with a modern average northern hemisphere gradient of ca. 0.4 °C/° lat. (Locarnini *et al.*, 2013). The presence of such a reduced temperature gradient requires a climate mechanism in a high pCO_2-world that yields temperate polar regions while not overheating the tropics. Proposed mechanisms to increase the transfer of heat toward the poles include increased oceanic heat flux (Frakes, 1979; Schmidt & Mysak, 1996) together with amplification of polar warmth by cloud feedbacks (Kump & Pollard, 2008; Sagoo *et al.*, 2013).

3.4.5. Cretaceous model-data comparisons

Climate modelling of past warm periods has received much attention as it has long been suggested that simulations may not capture the extent to which the latitudinal temperature gradient is reduced (Spicer *et al.*, 2008). The shallow meridional temperature gradients of the past greenhouse climates pose a significant challenge to numerical climate models (Barron & Washington, 1982; Huber & Caballero, 2011), in that increased greenhouse gases may yield warm polar regions, but also overheat the tropics. Our Δ_{47} reconstructions and temperature compilation (Figure 3.3, Table 3.1) demonstrate that Cretaceous tropical warming was of a magnitude consistent with most models (Otto-Bliesner & Upchurch, 1997; Poulsen *et al.*, 2007; Zhou *et al.*, 2008; Donnadieu *et al.*, 2016). However, model results from Poulsen *et al.* (2007) and Donnadieu *et al.* (2016); for example, approach our proxy data at 12-times pre-industrial pCO_2 (3360 ppm), which exceed estimates of Cretaceous pCO_2 derived from fossil leaf stomatal index measurements and isotope-based or geochemical model estimates (Wang *et al.*, 2014; Foster *et al.*, 2017).

For higher latitudes, our temperature proxy data are warmer than simulations made even with unlikely high pCO_2 levels (Poulsen *et al.*, 2007; Donnadieu *et al.*, 2016). In contrast, the Eocene climate model of Sagoo *et al.* (2013) shows a considerably closer fit at higher latitudes. A feature of Sagoo *et al.* (2013) is that this model has substantially modified parameters related to cloud formation. Although many aspects contributed to the warmth seen at higher latitudes in the model, a strong sensitivity to albedo changes

associated with cloud cover was apparent (Kiehl & Shields, 2013; Sagoo *et al.*, 2013). However, for the highest latitude proxy data, the magnitude of warming simulated by all climate models is still less than indicated by our Δ_{47} data and published TEX_{86} temperatures estimates (Jenkyns *et al.*, 2012). This could suggest that climate models are still missing key processes. Additional proposed mechanisms to increase the transfer of heat toward the poles, include sensible and latent heat transfer via the atmosphere and heat transfer via the oceans (Frakes, 1979; Schmidt & Mysak, 1996; Hotinski & Toggweiler, 2003). It is important to note that Cretaceous TEX_{86} data and Δ_{47}-derived temperatures are limited by the distribution of suitably preserved sediments, at high latitudes. Indeed, Cretaceous TEX_{86} data is available from just a few Arctic sites (Jenkyns *et al.*, 2004; Super *et al.*, 2018). As such, the high temperatures so far identified may reflect local conditions and not be fully representative of zonal averages.

3.4.6. Latitudinal oxygen isotope gradient

Estimations of $\delta^{18}O_{sw}$ are complicated because of variables such as the input of freshwater and balance of precipitation and evaporation. The presence or absence of polar ice provides further complications, as this also influences both local and global $\delta^{18}O_{sw}$. Since the clumped isotope proxy gives an independent temperature estimate, we can determine $\delta^{18}O_{sw}$ from belemnite $\delta^{18}O$ and the Δ_{47} data.

For DSDP Site 511, the two different $\delta^{18}O$–temperature equations, that of Kim and O'Neil (1997) and that of Coplen (2007), indicate that $\delta^{18}O_{sw}$ averaged either 1.0(±1.1)‰ or -0.5(±1.1)‰ SMOW, respectively, calculated for the entire studied period (Figure 3.2b, Supplementary Data 3.1). Valanginian samples from this location average -0.7(±1.1)‰ and 0.8(±1.1)‰, for the Coplen (2007) and the Kim and O'Neil (1997) equations, respectively (Table 3.1, Supplementary Data 3.1). For the northern hemisphere locations investigated in this study, the Coplen (2007) equation yields an average $\delta^{18}O_{sw}$ of 0.5(±1.6)‰ SMOW (Figure 3.4), and the Kim and O'Neil (1997) equation yields an average of 2.0(±1.6)‰ SMOW (Supplementary Data 3.1 and 3.2). Both of the northern hemisphere Valanginian estimates are more positive than the estimated global average $\delta^{18}O_{sw}$ for an ice-free world of -1.0‰ SMOW (Shackleton & Kennett, 1975). Even, Cretaceous northern hemisphere $\delta^{18}O_{sw}$ plots in the upper portion of the field of modern seawater (LeGrande & Schmidt, 2006) (Figure 3.4). If belemnites precipitated in close equilibrium with ambient seawater, it is the $\delta^{18}O_{sw}$ values calculated using the equation of Coplen (2007) that should reflect the true oxygen isotopic composition of the seawater.

Our Valanginian seawater oxygen isotope reconstructions produce a gradual decrease towards the poles: the values are the highest around the tropics (24° N, 1.5±1.4‰ SMOW) and lowest at high latitudes (74° N, -0.8±1.6‰ SMOW; 53° S, -0.7±1.1‰ SMOW) (Figure 3.4, Table 3.1). The Δ_{47}-based $\delta^{18}O_{sw}$ gradient, assuming that the calculated values are representative of the corresponding latitude, is close to the modern gradient (Zachos *et al.*, 1994; LeGrande & Schmidt, 2006) and to the model of Zhou *et al.* (2008) made for the Cretaceous, although the model values are more negative as the model was initialised to -1.0‰ SMOW, in order to reflect the absence of ice sheets.

As our data plot along a modern gradient and is more positive than -1‰ SMOW used in many studies, we suggest that latitudinally corrected $\delta^{18}O_{sw}$ value estimates, normalised to modern-like $\delta^{18}O_{sw}$, *i.e.,* to ca. 0‰ SMOW, should be used to constrain Cretaceous belemnite $\delta^{18}O$-based temperatures. Figure 3.5 presents a compilation (Supplementary Data 7.1) of Berriasian–Valanginian–Hauterivian belemnite $\delta^{18}O$-based temperatures that were calculated using the Coplen (2007) equation assuming a latitude-corrected $\delta^{18}O_{sw}$ normalised to 0.5‰ SMOW, *i.e.,* our Valanginian average for the northern hemisphere. Such $\delta^{18}O$-based temperatures agree well with Δ_{47} and TEX_{86}-based

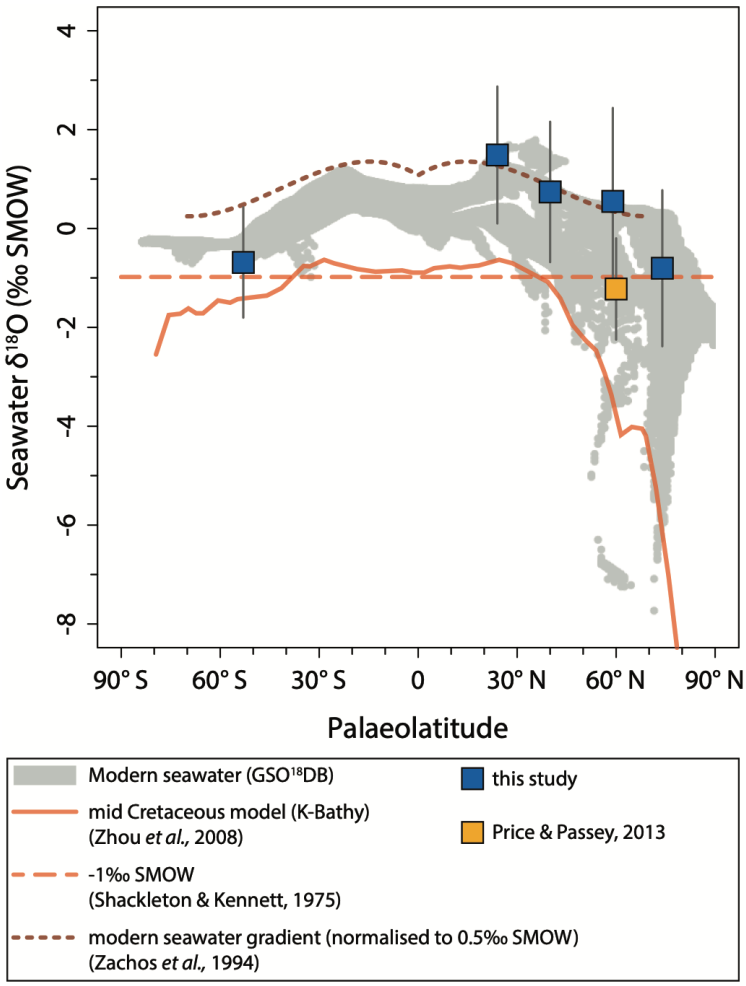

Figure 3.4 | Valanginian latitudinal seawater oxygen isotope gradient. Modern gridded mean annual $\delta^{18}O$ values from LeGrande and Schmidt (2006). Additional Valanginian belemnite Δ_{47}-based data is from Price and Passey (2013). Modelled mid-Cretaceous mean annual zonal average of $\delta^{18}O_{sw}$ after Zhou *et al.* (2008). Modelled modern mean annual zonal $\delta^{18}O_{sw}$ average is after Zachos *et al.* (1994), normalised to a $\delta^{18}O_{sw}$ of 0.5‰ SMOW that is the Valanginian northern hemisphere average from this study. The ± uncertainties are combined errors (see Table 3.1). Data for this figure can be found in Tables 3.1 and A3.1, Supplementary Data 3.1 and 3.2.

estimates, even across different basins. Using a value of -1.0‰ SMOW for the $\delta^{18}O_{sw}$ of the Cretaceous seawater, as opposed to a value of 0.5‰ SMOW, yields temperature estimates that would be underestimated by up to 12 °C. The underestimation of carbonate $\delta^{18}O$-based seawater temperatures would be most acute at middle and tropical latitudes where the difference between -1.0‰ and the Δ_{47}-derived $\delta^{18}O_{sw}$ profile is greatest (compare Figures 3.5 and A3.5).

A proposed secular change in $\delta^{18}O_{sw}$ over longer timescales (Jaffrés *et al.*, 2007; Veizer & Prokoph, 2015) suggests that $\delta^{18}O_{sw}$ has decreased gradually through Earth's history, from its present value of 0‰ to -6‰ SMOW in the Cambrian. Our $\delta^{18}O_{sw}$ results; however, favour studies that indicate more or less constant $\delta^{18}O_{sw}$ values through geologic time (Henkes *et al.*, 2018; Ryb & Eiler, 2018; Coogan *et al.*, 2019). If the nature of the $\delta^{18}O$ of Cretaceous seawater is modern in character, this potentially poses a challenge as the value of modern $\delta^{18}O_{sw}$ is a consequence of ice accumulation largely on Greenland and Antarctica. Elevated evaporation, due to the warm Cretaceous temperatures, that preferentially removes light ^{16}O from the seawater may explain the calculated generally high $\delta^{18}O_{sw}$ estimates. The effect of evaporation may have been the strongest around the

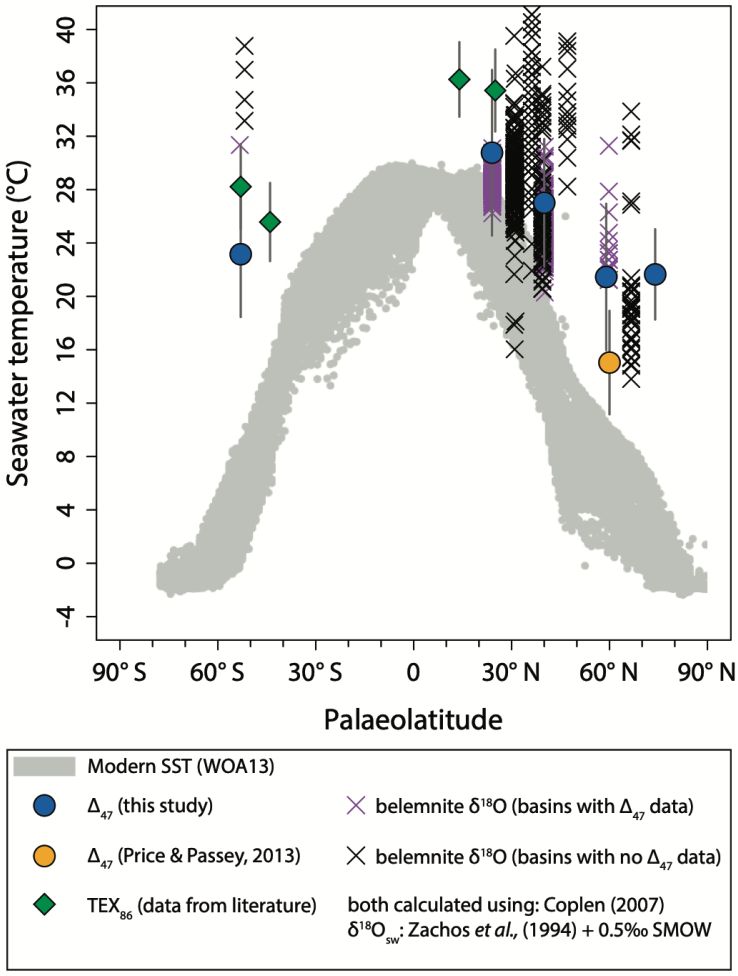

Figure 3.5 | Compilation of Early Cretaceous belemnite $\delta^{18}O$-based seawater temperatures. To calculate temperatures from calcite $\delta^{18}O$ the Coplen (2007) equation was utilised, along with a latitude-corrected $\delta^{18}O_{sw}$ (Zachos *et al.*, 1994) normalised to 0.5‰ SMOW (Valanginian mean value from this study) (Figure 3.4). Plotted belemnites are Berriasian to Hauterivian in age and show no stratigraphically significant temporal temperature evolution. Belemnites deriving from basins that have no Δ_{47} data are highlighted to indicate that the suggested $\delta^{18}O_{sw}$ estimate works well across multiple basins. Data for this figure can be found in Tables 3.1 and A3.1, Supplementary Data 3.1, 3.2, and 7.1. For comparison, Figure A3.5 shows belemnite $\delta^{18}O$-based temperatures that were calculated using the Kim and O'Neil (1997) equation and a constant $\delta^{18}O_{sw}$ of -1‰ SMOW, as often done in palaeoceanography.

tropics yielding $\delta^{18}O_{sw}$ estimates larger than 0‰ SMOW; whereas, at higher latitudes, increased contribution from isotopically light freshwater input (Rohling, 2013) may have played a role dragging the $\delta^{18}O_{sw}$ into the negative range. Alternatively, a modest-sized Cretaceous ice sheet may have been located on Antarctica given its vast areas of elevated terrain (DeConto & Pollard, 2003).

As our study suggests that the latitudinal temperature gradient during the Early Cretaceous was less steep than today, it is conceivable that the $\delta^{18}O_{ice}$ was less extreme. Changes in the hydrological cycle, as a consequence of a reduced temperature gradient, are expected to be reflected in the isotopic composition of precipitation. The ice-free global average of -1‰ SMOW assumes that the $\delta^{18}O$ of polar ice ($\delta^{18}O_{ice}$) was as light as it is today (ca. -50‰ SMOW) (Shackleton & Kennett, 1975). The effect of a reduced equator-to-pole temperature gradient implies less isotopic distillation (Rayleigh condensation) during poleward transport. Studies estimated a $\delta^{18}O_{ice}$ of -35‰ SMOW for the Antarctic ice sheet when the latitudinal temperature gradient was also less extreme (Pekar & DeConto, 2006). Although a substantial increase in hydrological cycling and isotopic fractionation of water vapour has been considered to account for depleted palaeosol sphaerosiderite $\delta^{18}O$ of North America (White *et al.*, 2001), our results do not support this conceptual model. Climate models (Poulsen *et al.*, 2007) also do not predict increases in large-scale isotopic fractionation with elevated pCO_2.

3.5. Conclusions

Our Early Cretaceous Δ_{47}-derived palaeotemperature estimates are inconsistent with an extended ice sheet in the northern and southern hemispheres and shows a congruence with TEX_{86} temperatures. The temperatures recorded at DSDP Site 511 from belemnites using clumped isotope thermometry are 2–3 °C cooler than sea-surface temperature estimates derived from TEX_{86}^{H} analyses. Although slightly cooler, our Δ_{47}-derived temperatures are not inconsistent with the TEX_{86} SST reconstructions when bias in the proxies are considered. The previously observed large inconsistencies between $\delta^{18}O$- and TEX_{86}-based temperatures are largely reduced if one considers that oxygen isotope equilibrium might have been attained during belemnite calcite precipitation.

Our clumped isotope-based temperature reconstruction suggests the existence of a strongly reduced equator-to-pole temperature gradient in the northern hemisphere. We find that modeling efforts are close to reproducing our tropical temperatures, when high pCO_2 levels are invoked; however, our data suggests warmer temperatures at higher

latitudes. Climate simulations for the Eocene that include modified parameters related to cloud formation better fit our data.

Our results indicate that it is unlikely that the oxygen isotope composition of the seawater was homogenous. Early Cretaceous $\delta^{18}O_{sw}$ shows a modern profile with a moderate decrease in values towards the northern pole. A modest-sized ice sheet could have been located on Antarctica. The constraints we provide on the oxygen isotope composition of Cretaceous seawater, in turn, underpins our understanding of the evolution of the Earth's temperature. Without taking into account these new estimates of the Cretaceous $\delta^{18}O_{sw}$ results in an underestimation of $\delta^{18}O$-derived temperatures, most acute at middle and tropical latitudes.

Chapter 4: Freshening in the Subboreal Province at the Middle–Late Jurassic transition

Abstract

In this study, we present clumped isotope, oxygen isotope and trace element analyses of exceptionally well-preserved belemnite rostra and ammonite shells from the uppermost Callovian–Upper Kimmeridgian of the Russian Platform. Despite a significant decrease in belemnite $\delta^{18}O$ values across the Upper Oxfordian–Lower Kimmeridgian, the clumped isotope data shows a constant seawater temperature (21±2 °C) in the studied interval. The decrease in belemnite $\delta^{18}O$ values and lower $\delta^{18}O$ values measured from ammonite shells are interpreted as a result of the salinity decline of the Middle Russian Sea, and salinity stratification of the water column, respectively. We posit that the secular palaeoenvironmental changes are linked to the inflow of subtropical, saline waters from the Tethys Ocean during a sea level highstand at the Middle–Late Jurassic transition, and subsequent progressive isolation and freshening of the Middle Russian Sea during the Late Oxfordian–Kimmeridgian.

The obtained clumped isotope data demonstrate the relative stability of the Late Jurassic climate and a paramount effect of local palaeoceanographic conditions on carbonate $\delta^{18}O$ record of shallow epeiric seas belonging to the Subboreal Province. Variations in Mg/Ca and Sr/Ca ratios of cylindroteuthid belemnite rostra, which are postulated by some authors to be temperature proxies, are, in turn, interpreted as primarily dependent on global changes in seawater chemistry. The palaeoenvironmental variations deduced from clumped and oxygen isotope records of the Russian Platform correspond well with changes in local cephalopod and microfossil faunas, which show increasing provincialism during the Late Oxfordian and the Early Kimmeridgian. Based on the review of literature data we suggest that the observed salinity decrease and restriction of Subboreal basins during the Late Jurassic played a significant role in the formation of periodic bottom water anoxia and sedimentation of organic-rich facies.

Collaborators

Hubert Wierzbowski[1], Ulrike Wacker[2], Mikhail A. Rogov[3], Jens Fiebig[2], Ekaterina M. Tesakova[4] — ([1] Polish Geological Institute, [2] Goethe University Frankfurt, [3] Russian Academy of Sciences, [4] Moscow State University).

4.1. Introduction

A short-term global climate cooling at the Middle–Late Jurassic transition (Late Callovian–Middle Oxfordian) or the incursion of cold Boreal waters are inferred from oxygen isotope records of marine calcareous shells and tooth phosphates of Western and Central Europe, and the Russian Platform (Dromart *et al.*, 2003; Lécuyer *et al.*, 2003; Nunn *et al.*, 2009; Price & Rogov, 2009; Wierzbowski *et al.*, 2009; Wierzbowski & Rogov, 2011; Wierzbowski *et al.*, 2013; Wierzbowski, 2015). A subsequent Late Oxfordian–Early Kimmeridgian warming is suggested for various palaeogeographical areas (Abbink *et al.*, 2001; Brigaud *et al.*, 2008; Nunn *et al.*, 2009; Žák *et al.*, 2011; Alberti *et al.*, 2012a; Alberti *et al.*, 2012b; Jenkyns *et al.*, 2012; Wierzbowski *et al.*, 2013; Wierzbowski, 2015). The oxygen isotope record of restricted European marine basins being a primary proxy for palaeoclimate reconstructions may; however, be affected by local salinity variations linked to changes in the water circulation and the palaeobathymetry. Although the Late Oxfordian–Early Kimmeridgian warming is regarded as a supra-regional, common phenomenon (Dromart *et al.*, 2003; Lécuyer *et al.*, 2003; Brigaud *et al.*, 2008; Nunn *et al.*, 2009; Žák *et al.*, 2011; Alberti *et al.*, 2012a; Alberti *et al.*, 2012b; Wierzbowski *et al.*, 2013; Arabas, 2016) its magnitude in marginal marine basins seems to be overestimated due the effect of increasing freshwater runoff under a global sea level fall (Wierzbowski *et al.*, 2013; Wierzbowski, 2015). A particular case is the oxygen isotope record of belemnite rostra from the Russian Platform showing a dramatic decrease in $\delta^{18}O$ values of ca. 3‰ throughout the Oxfordian–Kimmeridgian (Riboulleau *et al.*, 1998; Dromart *et al.*, 2003; Price & Rogov, 2009), which may be only partially attributed to a temperature rise (Wierzbowski *et al.*, 2013).

The clumped isotope composition of well-preserved calcium carbonate minerals is an independent proxy for precipitation temperatures. Determination of both the clumped and the oxygen isotopic compositions of carbonates allows reconstruction of ancient water $\delta^{18}O_{water}$ values (Ghosh *et al.*, 2006). Clumped isotope analyses have been successfully used for the reconstruction of water temperatures during the growth of carbonate fossils (Price & Passey, 2013; Petersen *et al.*, 2016).

This study aims to determine real variations of water temperature of the Middle Russian Sea belonging to the Subboreal bioprovince during and after the Middle–Late Jurassic transition. For this, we analysed exceptionally well-preserved latest Callovian–earliest Late Kimmeridgian belemnite rostra and ammonite shells from the Volga Basin in

Figure 4.1 | Location of studied outcrops on the Russian Platform.
Abbreviations: Mak. – Makar'ev, Mal. – Mal'gino, Mikh. – Mikhalenino, Tarkh. Pr. – Tarkhanovskaya Pristan', Yak. – Yakimikha.

the European part of Russia. With the combination of cylindroteuthid belemnite Δ_{47} and $\delta^{18}O$ values, we determined changes in palaeowater $\delta^{18}O$. We associated these changes with salinity, *i.e.,* freshwater influx, fluctuations of the restricted Middle Russian Sea. Finally, we compared isotope data and its interpretation with the distribution of macro- and microfossils in the Russian Platform to verify palaeoenvironmental reconstructions. The present study sheds new light on the latest Middle Jurassic–Late Jurassic climate and effects of local palaeobathymetry and palaeocirculation on climate reconstructions based on $\delta^{18}O$ values of marine fossils derived from epicontinental or marginal sea basins.

4.2. Material and methods

4.2.1. Samples

We analysed 19 archival and 5 newly collected well-preserved and stratigraphically well-dated belemnite rostra and ammonite shells for their clumped isotope composition to obtain a continuous record of temperature variations of the epicontinental Middle Russian Sea during and after the Middle–Late Jurassic transition (the latest Callovian–mid-Kimmeridgian; Table A4.1). The archival uppermost Callovian–Lower Kimmeridgian materials (cylindroteuthid and mesohibolitid belemnite rostra and ammonite shells), derived from the Dubki section near Saratov, and the Makar'ev and Mikhalenino sections in the Kostroma Region of Russia (Figure 4.1), comprise samples studied by Wierzbowski and Rogov (2011) and Wierzbowski *et al.* (2013). The newly collected cylindroteuthid rostra, studied for clumped isotopes, are derived from Tarkhanovskaya Pristan' section near Ul'yanovsk in the Tatarstan Republic of the Russian Federation (Figure 4.1). They are dated to the latest Early Kimmeridgian–earliest Late Kimmeridgian, *i.e.,* the late Cymodoce Zone (=Divisum Zone) and the Mutabilis Zone (Rogov *et al.*, 2017b). Some of

these samples have been studied recently for their strontium isotope composition (Wierzbowski *et al.*, 2017). In addition to the clumped isotope measurements, we present the results of new oxygen and carbon isotope analyses of 19 Kimmeridgian cylindroteuthid belemnite rostra along with the published oxygen and carbon isotope values of 175 carbonate fossils (cylindroteuthid and mesohibolitid belemnite rostra, ammonite and gastropod shell (Wierzbowski & Rogov, 2011; Wierzbowski *et al.*, 2013).

The collected carbonate fossils are precisely biostratigraphically dated (Wierzbowski & Rogov, 2011; Wierzbowski *et al.*, 2013). The standard Boreal and the Subboreal ammonite zonal schemes are employed for the dating of uppermost Callovian–Oxfordian and Kimmeridgian sediments, respectively, according to the regional biostratigraphical framework (Table A4.2). It is worth noting that occurrences of Submediterranean ammonites allow the use of Submediterranean biostratigraphical units in some parts of the studied sections (Głowniak *et al.*, 2010; Rogov *et al.*, 2017b). The precise correlation between the (Sub)Boreal ammonite zonal scheme of the Oxfordian–lowermost Upper Kimmeridgian of the Russian Platform and the Submediterranean province of central Europe zonation is presented in Table A4.2. The employed biostratigraphical scale is matched to the assumed equal duration of Submediterranean ammonites subchrons, which are counted successively starting from the base of the studied interval (Wierzbowski *et al.*, 2013). This approach is used to enable a direct comparison between the recorded isotope variations and the previously published isotope data from Western and Central Europe.

4.2.2. Preparation

We studied thin sections that were prepared from newly collected belemnite rostra through an optical microscope coupled with a CCL Mk5-2 Cambridge Image Technology Ltd. cold cathode device. The rostra were cleaned, using a hand-held drill, from adherent sediment, apical-line areas, alveolar fissure infillings and, if necessary, narrow luminescent rims or veins. Fragments of the studied belemnite rostra comprising most growth rings, and derived from *rostrum solidum* (Sælen, 1989) were powdered and homogenised using an agate mortar and pestle. Each specimen yielded 100–300 mg of carbonate powder. Aliquots of the same carbonate powder were used for trace element, oxygen, carbon, and clumped isotope analyses. For the clumped isotope analyses, we also analysed aliquots of carbonate samples studied previously by Wierzbowski and Rogov

(2011) and Wierzbowski *et al.* (2013). These archival samples were prepared and screened for the state of preservation in the same way as the newly collected material (Wierzbowski & Rogov, 2011; Wierzbowski *et al.*, 2013).

4.2.3. Trace element analyses

Ca, Mg, Mn, Fe, Sr and Na concentrations were determined by the ICP-OES (Inductively Coupled Plasma-Optical Emission Spectrometry) method using Thermo Scientific™ iCap™ 6000 Duo system at the Polish Geological Institute–National Research Institute in Warsaw (Poland). 50–100 mg aliquots of the carbonate powders were dissolved in 5wt.% hydrochloric acid. Reproducibility of chemical analyses (2σ S.D.) was controlled by multiple analyses of measured samples and averages as follows: 1.0% for Ca, 2.4% for Mg, 2.2% for Sr, 0.8% for Mn, 2.7% for Fe, and 1.4% for Na. Repeated analyses of JLs-1 calcite and JDo-1 dolomite references (Imai *et al.*, 1996) yielded accuracies of measurements (2σ S.D.) better than 3.5% for Ca, 3.8% for Mg, 1.0% for Sr, and 4.0% for Mn. The accuracy of Fe analyses cannot be given precisely due to the employed dissolution method in weak hydrochloric acid, which is not relevant for the determination of non-carbonate iron compounds present in both standards. Also, Na contents of both references are much lower than those of studied belemnite samples; therefore, the accuracy of measurements of Na concentrations cannot be precisely verified.

4.2.4. Clumped isotope analyses

The clumped isotope analyses were conducted between April 2015 and July 2017 at the Institute of Earth Sciences, Goethe University Frankfurt, Frankfurt am Main, Germany. Clumped isotope composition of all samples was measured in at least five replicates. Carbonate digestion and CO_2 purification were made on a fully automated preparation line (see Chapter 6). For each replicate analysis, ca. 6 mg of homogenised carbonate powder was reacted at 90 °C, for 30 minutes, with >105% phosphoric acid. The resultant CO_2 was purified cryogenically five times using a Porapak Q trap cooled down to -15 °C. The sample gas was measured alternately with a reference gas of known isotopic composition using the dual-inlet system of a ThermoFisher™ MAT 253™ gas-source isotope-ratio mass spectrometer. For measurements carried out before May 2016 an Oztech reference gas ($\delta^{18}O$ = 25.01‰ VSMOW; $\delta^{13}C$ = -3.63‰ VPDB) was used and from May 2016 onwards an ISO–TOP, Air Liquide, reference gas ($\delta^{18}O$ = 25.56‰ VSMOW; $\delta^{13}C$ = -4.30‰ VPDB) was utilized. Background correction was performed for the sample and the reference gas separately, according to the procedure described by Fiebig *et al.* (2016).

Raw Δ_{47} values were calculated using the [*Brand*]/IUPAC, isotopic parameters (R^{13}_{PDB} = 0.01118, R^{18}_{VSMOW} = 0.0020052, R^{17}_{VSMOW} = 0.00038475, λ = 0.528). The values were projected to the CO_2 reference frame using equilibrated gases (Dennis *et al.*, 2011; Petersen *et al.*, in review). Empirical transfer functions (ETFs) were determined using gases of various bulk isotopic compositions equilibrated at 25 °C and 1000 °C (Supplementary Data 4.1). A 25–90 °C acid fractionation factor of 0.088‰ was applied to all $\Delta_{47\ (RFAC)}$ values (Petersen *et al.*, in review).

Seven carbonate standards were analysed along with the samples to confirm the precision and reproducibility of the measurements. The mean $\Delta_{47\ (RFAC)}$ values (±1σ S.D.) of the reference materials, for the whole period of measurements, are: Carrara (marble, calcite, N = 278) 0.409(±0.019)‰, MuStd (*Arctica islandica*, aragonite, N = 166) 0.749(±0.018)‰, Strauss (ostrich egg, calcite, N = 29) 0.674(±0.032)‰, ETH1 (calcite, N = 32) 0.306(±0.016)‰, ETH2 (calcite, N = 9) 0.287(±0.022)‰, ETH3 (calcite, N = 42) 0.715(±0.021)‰, ETH4 (calcite, N = 7) 0.556(±0.035)‰ (Supplementary Data 4.1). The $\Delta_{47\ (RFAC)}$ values obtained for the carbonate standards within this study are indistinguishable within ≤ 0.010% from corresponding values obtained elsewhere (Wacker *et al.*, 2014; Fiebig *et al.*, 2016; Wacker *et al.*, 2016; Bajnai *et al.*, 2018).

We used the Δ_{47}–temperature calibration of Wacker *et al.* (2014), recalculated using the [*Brand*]/IUPAC isotopic parameters, to convert the measured clumped isotope values to precipitation temperatures of calcium carbonate (Equation 1.9). This calibration is based on calcium carbonates of various origin and was made at the Goethe University Frankfurt using a similar analytical setup as in the present study. The Wacker *et al.* (2014) calibration is identical to the empirical calibration of Henkes *et al.* (2013) that is mostly based on molluscs. The steeper sloped calibration of Kelson *et al.* (2017) gives temperatures indistinguishable within ±1σ S.E. from those calculated using the Wacker *et al.* (2014) equation (Supplementary Data 4.1). Previous studies have shown that the Δ_{47}–temperature relationships for calcite and aragonite are indistinguishable from each other (Tripati *et al.*, 2010; Henkes *et al.*, 2013; Defliese *et al.*, 2015), allowing the use of the same calibration for both belemnites (calcite) and ammonites (aragonite).

4.2.5. Oxygen and carbon isotope analyses

Oxygen and carbon isotope analyses of newly collected mid-Kimmeridgian belemnite rostra have been performed at the GeoZentrum Nordbayern, University of Erlangen-Nuremberg, Erlangen, Germany. Samples were reacted with 100% phosphoric acid at

70 °C using a Thermo Scientific™ Gasbench II connected to a Thermo Scientific™ Delta V™ Plus mass spectrometer. All values are reported in per mil relative to VPDB scale by assigning a $\delta^{13}C$ and $\delta^{18}O$ value of +1.95‰ and -2.20‰ to NBS19 and -46.6‰ and -26.7‰ to LSVEC, respectively. The reproducibility and accuracy of the measurements were monitored, throughout the analyses, by replicate analysis of laboratory standards Sol 2 (n = 10) and Erl 5 (n = 8). Reproducibility for $\delta^{13}C$ and $\delta^{18}O$ values was 0.04‰ and 0.03‰ (±1σ S.D.) for Sol 2, and 0.06‰ and 0.05‰ (±1σ S.D.) for Erl 5, respectively. To calculate water $\delta^{18}O$ values from calcite $\delta^{18}O$ values and the clumped isotope temperatures, we used the equation of Coplen (2007) (Equation 1.10).

4.3. Results

4.3.1. Diagenetic alteration

The stable isotope composition of carbonates is susceptible to alteration in burial and meteoric environments. Diagenetic alteration of marine calcites often leads to significant manganese and iron enrichment or strontium depletion (Veizer, 1974; Brand & Veizer, 1980; Veizer, 1983; Marshall, 1992; Ullmann & Korte, 2015). The chemical composition of carbonate fossils can; thus, serve as a tool for evaluating their preservation state. Particularly, the concentrations of Mn < 100 ppm, Fe < 200 ppm, and Sr > 800 ppm are usually regarded as characteristic of well-preserved Jurassic belemnite rostra (Nunn *et al.*, 2009; Price & Rogov, 2009; Nunn & Price, 2010; Price & Teece, 2010; Wierzbowski & Rogov, 2011; Alberti *et al.*, 2012b; Wierzbowski *et al.*, 2013; Price *et al.*, 2015; Wierzbowski, 2015; Arabas, 2016). Diagenetic Mn^{2+} ions are also an activator of orange-red cathodoluminescence in calcites, which is indicative of the alteration under reducing conditions (Marshall, 1992; Savard *et al.*, 1995).

The newly collected mid-Kimmeridgian belemnite samples from Tatarstan are characterised by the lack of luminescence and very low Mn (≤20 ppm) and Fe (≤ 33 ppm) as well as high Sr (≥ 1040 ppm; Supplementary Data 4.1) concentrations. Their minor and trace element contents are similar to those of older belemnite material from the Russian Platform (Wierzbowski & Rogov, 2011; Wierzbowski *et al.*, 2013). Archival and new belemnite materials selected for the clumped isotope analyses show exceptionally low concentrations of Mn (≤9 ppm) and Fe (≤20 ppm) as well as high contents of Sr (≥824 ppm). Low contents of Mn and Fe in studied samples, which are buried in dark, often organic-rich sediments, contradict suggestions that belemnite rostra might have

been initially porous and cemented during early marine diagenesis (Benito *et al.*, 2016; Hoffmann *et al.*, 2016) (Supplementary Data 4.1). Besides, pervasive calcite cementation of fossils could not have occurred in fine-grained siliciclastic sediments of low permeability and carbonate content that predominate the Jurassic of the Russian Platform.

Aragonite is metastable and uncommon in Mesozoic deposits. Diagenetic alteration of aragonite mollusc shells results in the alteration of their microstructure and gradual transformation into calcite (Brand, 1989; Dauphin & Denis, 1990; Anderson *et al.*, 1994; Wierzbowski & Joachimski, 2007; Cochran *et al.*, 2010; Wierzbowski & Rogov, 2011). Wierzbowski and Rogov (2011) and Wierzbowski *et al.* (2013) have documented that ammonite shells studied for oxygen and carbon isotope ratios, and presently for clumped isotope composition (Supplementary Data 4.1, Table A4.1), are composed of pure aragonite (≥99%) and show well-preserved shell microstructure.

Although the physical and chemical screening methods of the preservation state of calcium carbonate are well-established in a case of oxygen and carbon isotope studies the solid-state reordering of C–O bonds in the carbonate lattice can affect its Δ_{47} values without discernible microstructure and chemical changes. Recent studies of Passey and Henkes (2012), Henkes *et al.* (2014), and Brenner *et al.* (2018) imply that Δ_{47} values of calcium carbonate preserve at burial temperatures below 100–120 °C. The geothermal gradient of the Russian Platform is low (0.7–2.5 °C/100 m), and is estimated to have been ca. 3 °C/100 m during the Jurassic and the Cretaceous (Bazhenova, 2008). Jurassic sediments of the Russian Platform occur close to the Earth surface, and there is no evidence that they were deeply buried. The organic matter present in the Upper Jurassic oil shale layers in the study area is immature as it is indicated by low T_{max} in Rock-Eval analyses (Hantzpergue *et al.*, 1998; Shchepetova & Rogov, 2013). High concentrations of original biomolecules provide additional proof for the very low thermal maturity of organic matter from Oxfordian strata near Makar'ev (Bushnev *et al.*, 2006). The presence of metastable aragonite in the studied sediments and similar Δ_{47} values of calcite and metastable aragonite may also point to low thermal alteration. Although organic aragonites transform into calcite on heating above 250 °C (Yoshioka & Kitano, 1985), the aragonite-calcite transformation in aqueous solutions, which are common in diagenetic environments, were observed in the temperature range of 50–175 °C (Bischoff, 1969;

Ritter *et al.*, 2017). Therefore, we can exclude the reordering of the C–O bonds in the analysed carbonate samples.

4.3.2. Clumped isotopes

Measured $\Delta_{47\,(RFAC)}$ (±1σ S.E.) values of belemnite rostra and ammonite shells range between 0.687(±0.005) and 0.731(±0.014)‰ (mean 0.709‰; Table A4.1, Supplementary Data 4.1). The 1σ S.E. of the $\Delta_{47\,(RFAC)}$ measurements, calculated from 4 to 13 replicate analyses, is between ±0.003 and ±0.014‰ (mean ±0.007‰). No significant trends in $\Delta_{47\,(RFAC)}$ values of the investigated fossil groups (cylindroteuthid and mesohibolitid belemnites, and ammonites) are observed in the studied interval (Figure 4.2).

4.3.3. Oxygen isotopes

Various fossil groups, which co-occur in the uppermost Callovian and the Oxfordian of the Russian Platform, are characterised by different $\delta^{18}O$ values (Figure 4.2). Mesohibolitid belemnite rostra are reported to have lower $\delta^{18}O$ values than those of coeval cylindroteuthids (Wierzbowski & Rogov, 2011; Wierzbowski *et al.*, 2013). Ammonites are divided into two groups: one from the Callovian–Oxfordian boundary and from the lower part of the Tenuiserratum Zone of the Middle Oxfordian with $\delta^{18}O$ values between 0.0–1.5‰ (mean: 0.8‰ VPDB) and another one from the Densiplicatum Zone of the Middle Oxfordian and the Middle–Late Oxfordian boundary with much lower $\delta^{18}O$ values between -0.5‰ to -2.5‰ VPDB (mean: -1.3‰ VPDB; Figure 4.2). $\delta^{18}O$ values of aragonitic gastropod shells vary between 1.0 and 1.4‰ VPDB (Figure 4.2).

The $\delta^{18}O$ values of cylindroteuthid belemnite rostra, whose record spans the whole studied interval, show a decreasing trend (Figure 4.2) (Wierzbowski & Rogov, 2011; Wierzbowski *et al.*, 2013). Their $\delta^{18}O$ values range from -0.6‰ to 2.8‰ (mean: 1.6‰ VPDB) in the uppermost Callovian and the Lower–Middle Oxfordian (Figure 4.2).

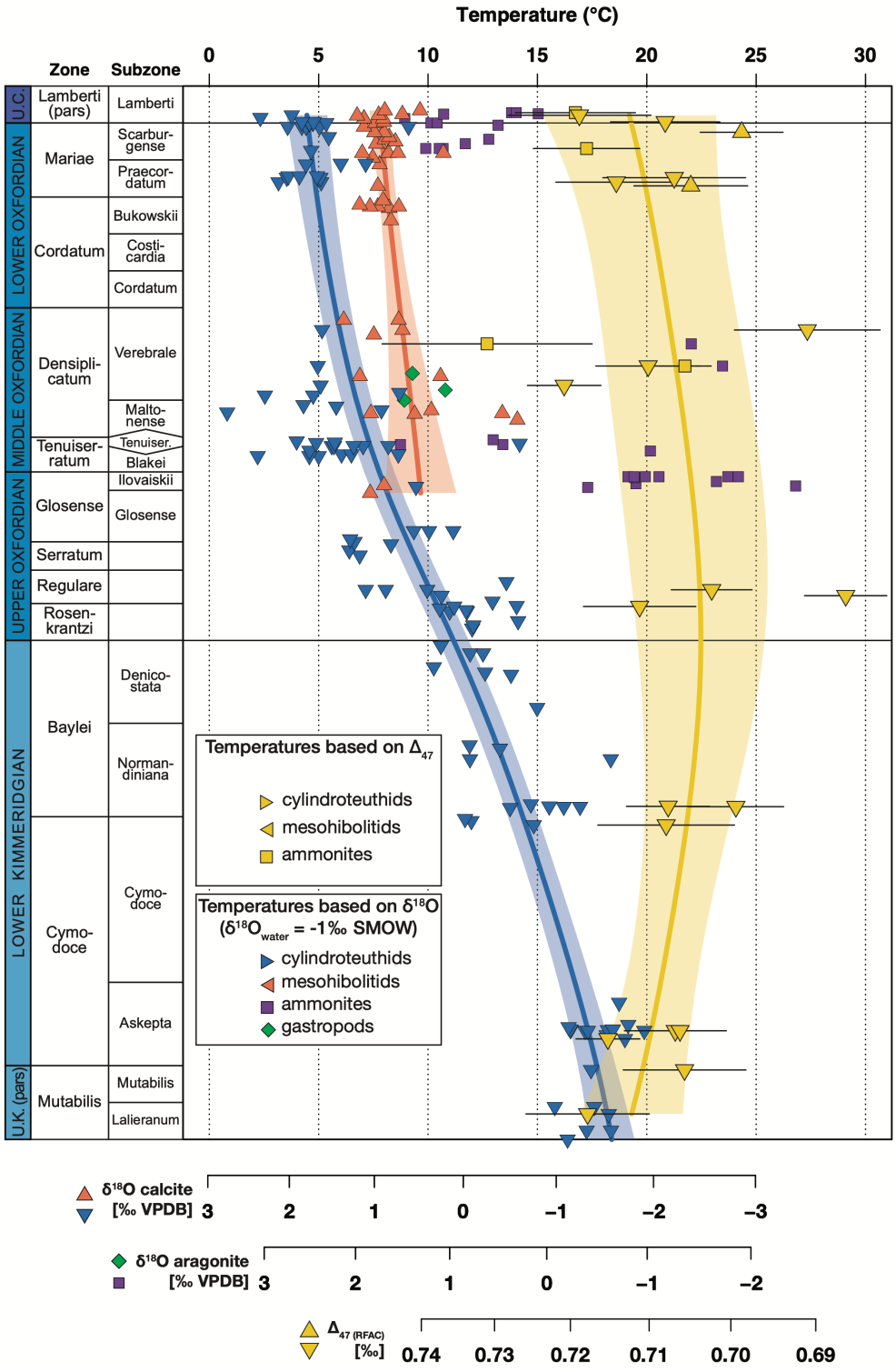

Figure 4.2 | Isotopic data and palaeotemperatures calculated from the $\delta^{18}O$ and Δ_{47} values of well-preserved calcareous fossils from the Middle–Upper Jurassic (the uppermost Callovian–lowermost Upper Kimmeridgian) of the Russian Platform.

Smoothed curves and corresponding 95% confidence intervals (blue, red, and yellow areas) are generated using a locally weighted linear regression with a bandwidth of 5 stratigraphical units, *i.e.,* ca. 0.3 Myr (Chaudhuri & Marron, 1999). The $\delta^{18}O$ values are compiled from Wierzbowski and Rogov (2011); Wierzbowski *et al.* (2013), and from this study. Calcite $\delta^{18}O$-based temperatures were calculated using the Kim and O'Neil (1997) equation, and aragonite $\delta^{18}O$-based temperatures were calculated using the equation of Grossman and Ku (1986). Note the reversed age axis: oldest samples are on top.

The cylindroteuthid $\delta^{18}O$ values decrease gradually in the Upper Oxfordian–Lower Kimmeridgian. The lowest cylindroteuthid $\delta^{18}O$ values of -1.9‰ to -1.0‰ (mean: -1.4‰ VPDB) are documented from the Lower–Upper Kimmeridgian boundary.

4.3.4. Correlation between the isotope and chemical ratios of cylindroteuthids

Temporal trends and relationships between the various isotope and chemical data can be studied within the cylindroteuthid dataset that covers the whole interval from the uppermost Callovian to the lowermost Upper Kimmeridgian (Figures 4.2 and 4.3). There is a weak ($R^2 = 0.17$, *p*-value < 0.001) linear correlation between $\delta^{18}O$ and $\delta^{13}C$ values of

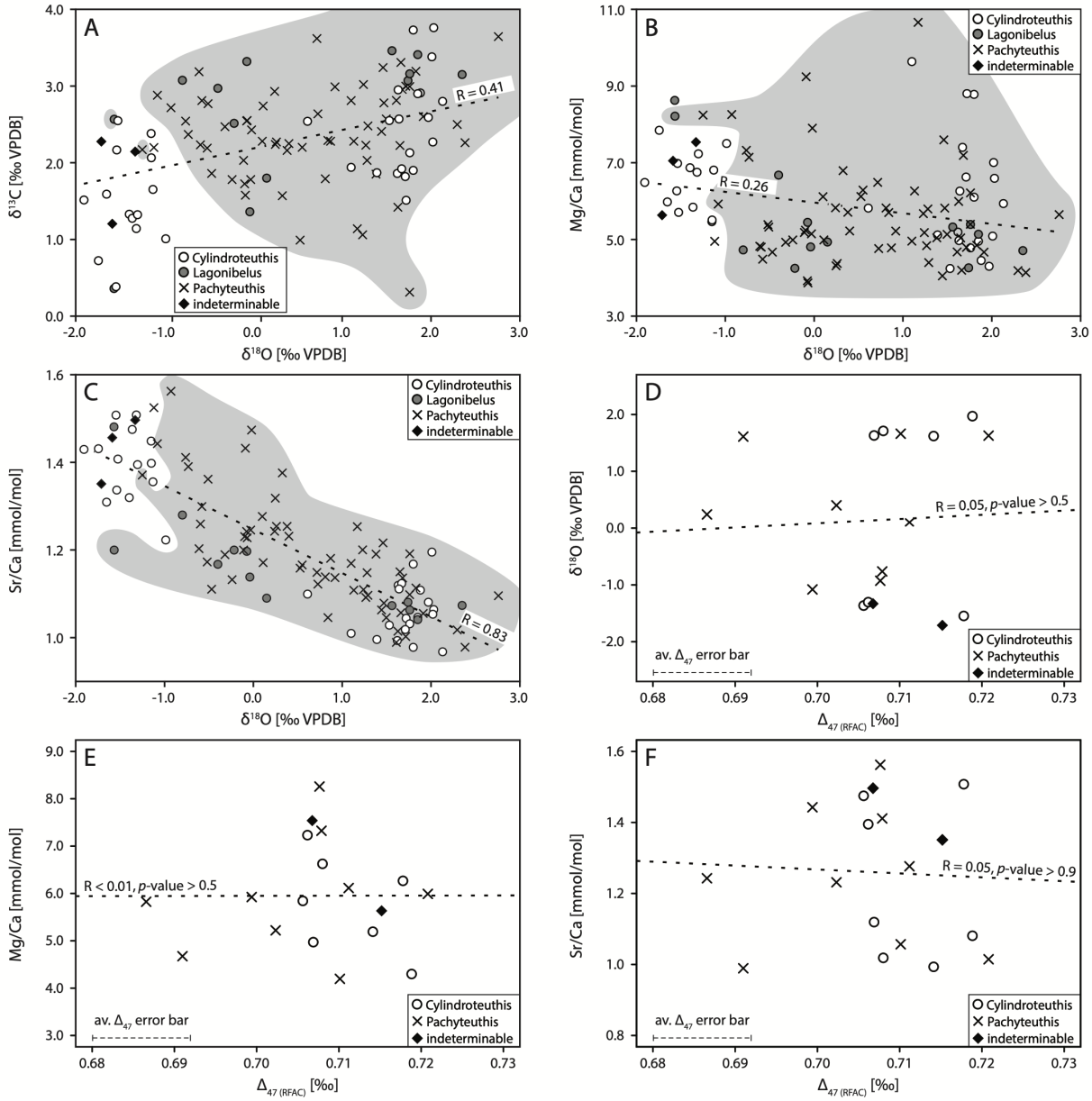

Figure 4.3 | Correlation between isotope values and elemental ratios of cylindroteuthid belemnite rostra from the Middle–Upper Jurassic (the uppermost Callovian–lowermost Upper Kimmeridgian) of the Russian Platform.

Shaded areas represent datasets from Wierzbowski and Rogov (2011); Wierzbowski *et al.* (2013). Note that *Cylindroteuthis, Lagonibelus*, and *Pachyteuthis* are different genera of cylindroteuthid belemnites.

cylindroteuthid rostra (Figure 4.3a) and a strong correlation (R^2 = 0.69, *p*-value < 0.001) between their $\delta^{18}O$ values and Sr/Ca ratios (Figure 4.3c). No correlation is, in turn, noticed between cylindroteuthid $\delta^{18}O$ values and Mg/Ca ratios (R^2 = 0.07, *p*-value > 0.005; Figure 4.3b), cylindroteuthid $\Delta_{47\ (RFAC)}$ and $\delta^{18}O$ values (R^2 = 0.01, *p*-value > 0.5; Figure 4.3d), and cylindroteuthid $\Delta_{47\ (RFAC)}$ and elemental ratios ($R^2 \leq 0.01$, *p*-value > 0.5; Figure 4.3e,f). There is also no discernible differentiation in the isotopic and chemical composition of various genera of studied cylindroteuthid belemnites (Supplementary Data 4.1).

4.4. Discussion

4.4.1. Chemistry of the belemnite rostra

The Mg/Ca and Sr/Ca ratios of brackish waters remain relatively constant at salinities above 10‰ and a salinity effect on the elemental ratios of molluscs is not significant (Dodd & Crisp, 1982; Surge & Lohmann, 2008; Wanamaker *et al.*, 2008). Interestingly, Mg/Ca and Sr/Ca ratios of some belemnite groups are regarded as a temperature proxy (McArthur *et al.*, 2000; Bailey *et al.*, 2003; Rosales *et al.*, 2004; McArthur *et al.*, 2007b; Malkoč & Mutterlose, 2010; Nunn & Price, 2010; Armendáriz *et al.*, 2013), whereas other authors suggest their relationship with biofractionation processes (McArthur *et al.*, 2007a; Wierzbowski & Joachimski, 2009; Stevens *et al.*, 2017; Ullmann & Pogge von Strandmann, 2017). A slight, hardly discernible, increase of Mg/Ca ratios from ca. 5.2–6.5 mmol/mol is concomitant with a huge decrease of belemnite $\delta^{18}O$ values, of ca. 3‰, within the entire dataset. According to the belemnite Mg/Ca–temperature relationship of Nunn and Price (2010), the observed rise in Mg/Ca ratio of cylindroteuthid belemnite rostra may be a response to an increase of ambient water temperature of ca. 2 °C that contradicts the temperature dependence of belemnite $\delta^{18}O$ values across the studied interval. The lack of correlation between cylindroteuthid Mg/Ca ratios and $\delta^{18}O$ values, along with a little change in the Mg/Ca ratios, suggests that other factors controlled the magnesium uptake of belemnite rostra. They may be related to temporal variations in water chemistry. Such an explanation is plausible as the Mg/Ca ratio of seawater is considered to increase slightly in the Late Jurassic (Hardie, 1996; Dickson, 2004). The studied strata were deposited during a geological time of ca. 10 Ma (Ogg *et al.*, 2016; Wierzbowski *et al.*, 2017), which is long enough to record a temporal change of global seawater Mg/Ca ratio. Investigations of modern planktonic foraminifers, brachiopods and bivalves (Lea *et al.*, 1999; Lorrain *et al.*, 2005; Kısakürek *et al.*, 2008; Freitas *et al.*, 2012; Butler *et al.*, 2015; Ullmann *et al.*, 2017) indicate that the

temperature sensitivity of Sr/Ca ratio of biogenic calcites is much weaker than the temperature sensitivity of the Mg/Ca ratio. Also, noticeable changes in the seawater Sr/Ca ratio, concomitant with $^{87}Sr/^{86}Sr$ variations, occurred during the Early and the Middle Jurassic (Ullmann *et al.*, 2013). As the lowest seawater Sr/Ca ratio, which coincides with the Phanerozoic minimum of the $^{87}Sr/^{86}Sr$ ratio, is postulated for the Middle–Late Jurassic transition (Ullmann *et al.*, 2013)) it is probable that the ratio increased after this turning point. The temporal change of the cylindroteuthid Sr/Ca ratio and its correlation with the local record of belemnite $\delta^{18}O$ values (Wierzbowski *et al.*, 2013) (Figure 4.3c) may; thus, be interpreted as arising from global variations in strontium and calcium concentrations in seawater. This explanation for cylindroteuthid Sr/Ca variations differs from that of Wierzbowski *et al.* (2013) but agrees with the lack of significant fluctuations of water temperatures of the Middle Russian Sea during the latest Callovian–Kimmeridgian deduced from clumped isotopes. The small variability in measured $\Delta_{47\ (RFAC)}$ values along with the considerable standard errors of the measurements (Figure 4.3e,f) precludes assessment if Mg/Ca and Sr/Ca ratios of cylindroteuthid calcite were controlled, to some degree, by the ambient water temperature during biomineralisation processes.

The weak positive correlation observed between $\delta^{18}O$ and $\delta^{13}C$ values of the studied fossils could either result from significant salinity fluctuations in marginal marine environments (Surge *et al.*, 2001; Swart *et al.*, 2001; Surge *et al.*, 2003; Surge & Lohmann, 2008) or be related to kinetic effects (McConnaughey, 1989a, 1989b). It is; however, possible that a moderate positive correlation between $\delta^{18}O$ and $\delta^{13}C$ values of Russian cylindroteuthid belemnites (Figure 4.3a) is a result of a more or less casual coincidence between a Kimmeridgian period of decreased belemnite $\delta^{18}O$ values in the Russian Platform and a global fall in $\delta^{13}C$ values of marine carbonates after the Middle Oxfordian positive carbon isotope excursion (Wierzbowski *et al.*, 2013; Wierzbowski, 2015).

4.4.2. Water temperatures

A remarkable decrease (ca. 3‰) in $\delta^{18}O$ values of cylindroteuthid belemnite rostra (Dromart *et al.*, 2003; Wierzbowski & Rogov, 2011; Wierzbowski *et al.*, 2013), if treated solely as a result of a temperature increase, may point to a warming of bottom waters of the Middle Russian Sea of ca. 12 °C during the Oxfordian and the Kimmeridgian (Figure 4.2). Differentiation of oxygen isotope compositions of various fossils (nektobenthic cylindroteuthid and mesohibolitid belemnites, and nektonic ammonites) from the Russian Platform is, in turn, regarded as a result of the presence of a significant

thermal gradient in the water column of the Middle Russian Sea (Wierzbowski & Rogov, 2011; Wierzbowski *et al.*, 2013).

The Middle Russian Sea was a vast and shallow epicontinental basin, whose salinities may have varied during the Jurassic, along with changes in the local palaeobathymetry, circulation patterns and connections with the open Tethys Ocean and the land-locked Boreal Sea (Figure 4.4). Therefore, palaeotemperature reconstructions for this area based on the assumed constant water salinity and seawater $\delta^{18}O$ value should be treated with caution (Wierzbowski *et al.*, 2013). Nevertheless, a Late Oxfordian–Early Kimmeridgian bottom water warming of 7–9 °C was suggested for the Middle Russian Sea as based on the changes in $\delta^{18}O$ values and Sr/Ca ratios of cylindroteuthid belemnite rostra (Wierzbowski *et al.*, 2013).

Obtained clumped isotope data are derived from exceptionally well-preserved fossils of the Russian Platform and are entirely reliable. Similar clumped isotope temperatures of ca. 21 °C are recorded for the whole studied interval encompassing the uppermost Callovian–mid Kimmeridgian (Figure 4.2). Observed temperature variations are broadly within the ranges of measurement errors (ca. ±2 °C) and likely arise from a general scatter of data points. Since studied fossils (belemnites and ammonites) are

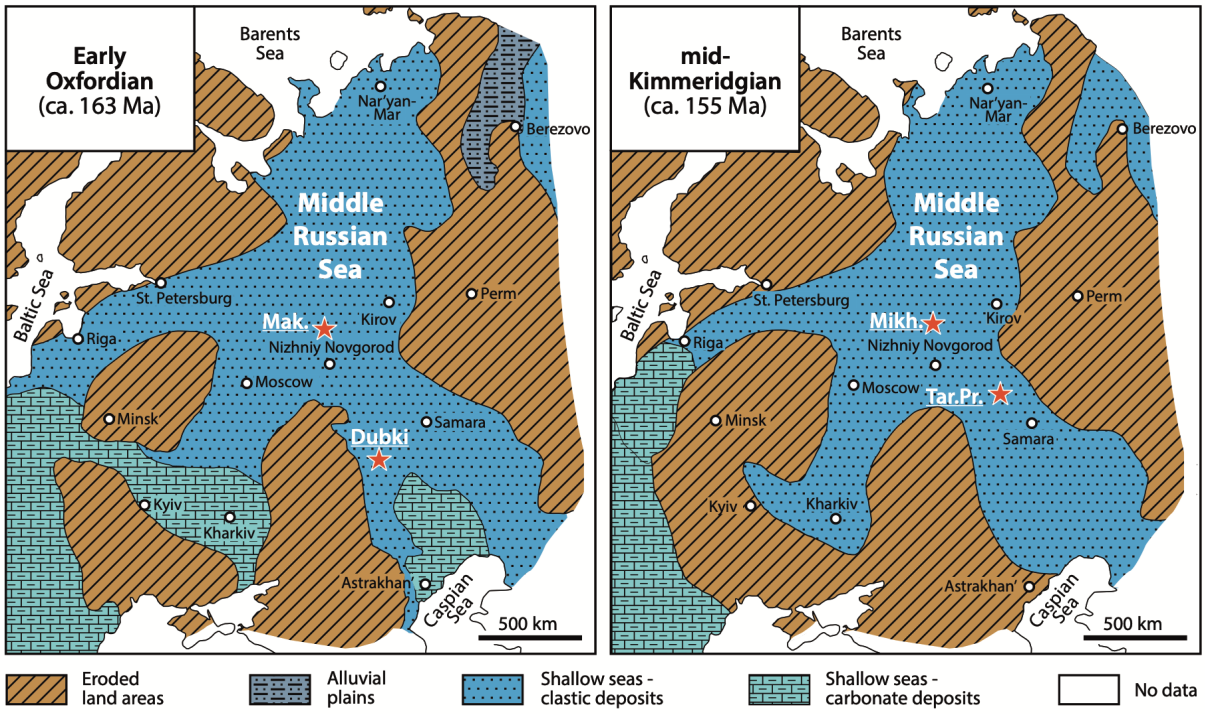

Figure 4.4 | Palaeogeography of the Russian Platform and adjacent areas during the Early Oxfordian and mid-Kimmeridgian.
Modified after Sazonova and Sazonov (1967); Matyja and Wierzbowski (1995); Lyyurov (1996); Wierzbowski *et al.* (2015).

considered to have been nektobenthic and nektonic, respectively (Anderson *et al.*, 1994; Wierzbowski & Joachimski, 2007; Wierzbowski & Rogov, 2011; Wierzbowski *et al.*, 2013), the calculated clumped temperatures are expected to be relevant to bottom and intermediate waters of the Middle Russian Sea.

The studied basin was sensitive to a climate change due to its shallow, epicontinental character and location in mid-latitudes (40–45° N) (Thierry *et al.*, 2000). The constant clumped isotope temperatures evidence; therefore, the long-term stability of the latest Middle Jurassic–Late Jurassic climate. The mean clumped isotope temperature of ca. 21 °C is higher than modern average seawater temperatures of 8.0 °C and 11.4 °C at 100 m depth at 40° N and 45° N, respectively (Locarnini *et al.*, 2013). This may be a result of a warmer and more equable Jurassic climate and the absence of cold bottom water masses. It is worth noting that the calculated clumped isotope temperatures are within the range of previously reported belemnite clumped isotope temperatures (13–19 °C) for the lowermost Cretaceous of the sub-polar Urals (Price & Passey, 2013) (Chapter 3). The constant clumped isotope-derived temperatures of the Middle Russian Sea during the latest Callovian–earliest Late Kimmeridgian, *i.e.*, the Lamberti–Mutabilis Zones (Figure 4.2), challenge the previous interpretation of the carbonate $\delta^{18}O$ signal. Prominent temporal variations in the cylindroteuthid belemnite $\delta^{18}O$ values of the Russian Platform (Figure 4.2) are likely due to changes in $\delta^{18}O_{water}$. In addition, the clumped isotope data suggest that the previously postulated thermal stratification of the Middle Russian Sea (Wierzbowski & Rogov, 2011; Wierzbowski *et al.*, 2013) was apparent and arising from salinity stratification of the water column.

4.4.3. Water $\delta^{18}O$ values

Clumped and oxygen isotope data allow calculation of $\delta^{18}O$ values of water from which calcium carbonate was precipitated. The $\delta^{18}O_{water}$ values of the Middle Russian Sea calculated from the cylindroteuthid data gradually decrease from ca. +2‰ at the Callovian–Oxfordian transition to ca. -2‰ SMOW at the Early–Late Kimmeridgian transition (Figure 4.5). These values fall in the range of modern seawater $\delta^{18}O$ at mid-latitudes (Craig & Gordon, 1965; LeGrande & Schmidt, 2006; Rohling, 2013).

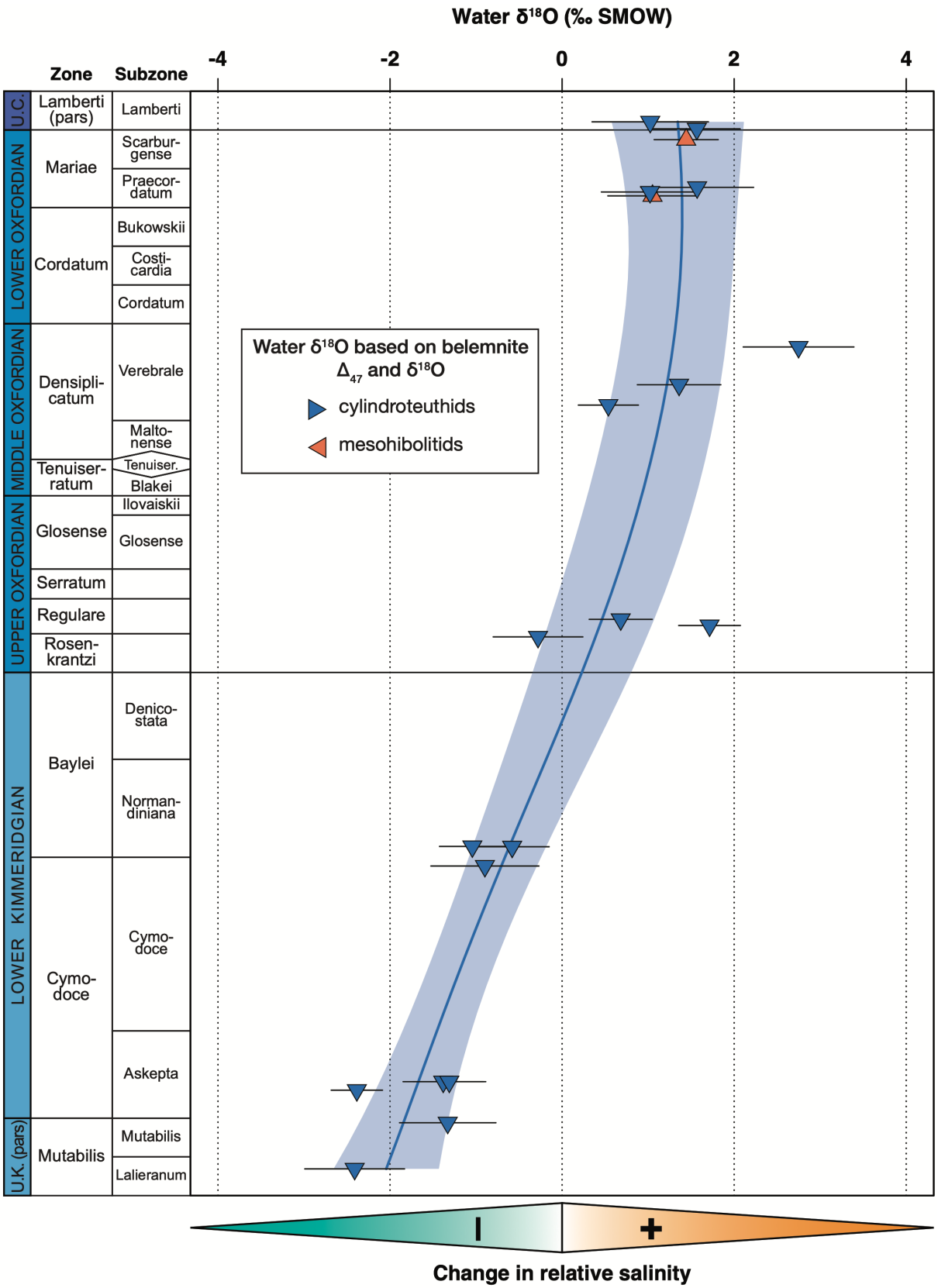

Figure 4.5 | Water $\delta^{18}O$ values of the Middle Russian Sea estimated from the oxygen and clumped isotope compositions of cylindroteuthid belemnites.

The smoothed curve and its 95% confidence interval are calculated using locally weighted linear regression. Note the reversed age axis: oldest samples are on top.

Increased salinities may have characterised the waters of the Middle Russian Sea during the latest Callovian–Middle Oxfordian because of diminished freshwater influx and the presence of saline, subtropical, Tethyan waters. A general decrease in sea level after the worldwide Middle–Late Jurassic transition highstand (Sazonova & Sazonov, 1967; Norris & Hallam, 1995; Hallam, 2001; Wierzbowski *et al.*, 2009; Wierzbowski *et al.*, 2013) may have contributed to the enhanced freshwater runoff and the limitation of oceanic water exchange with the restricted Middle Russian Sea. This probably led to a decrease in salinity and water $\delta^{18}O$ values of this basin. The decrease is likely recorded in $\delta^{18}O$ values of carbonate fossils from the Russian Platform, whose fall was previously interpreted as evidence for the prolonged period of warm Kimmeridgian–Volgian climate (Riboulleau *et al.*, 1998; Price & Rogov, 2009). Coeval oxygen isotope data from other (Sub)Boreal basins, *i.e.,* Scotland, Northern Siberia (Nunn *et al.*, 2009; Nunn & Price, 2010; Žák *et al.*, 2011) suggest that the Kimmeridgian–Volgian decrease in carbonate $\delta^{18}O$ values is a common feature in this palaeobiogeographical province. In addition, clumped isotope data imply that previously postulated thermal stratification of the Middle Russian sea (Wierzbowski & Rogov, 2011; Wierzbowski *et al.*, 2013) was apparent and resulting from salinity and $\delta^{18}O$ value stratification of the water column.

The increasing restriction of the Middle Russian Sea during the Late Oxfordian–earliest Kimmeridgian is substantiated by a fall in $\varepsilon_{Nd\,(t)}$ values of local sediments, which is linked to an increasing rate of neodymium derived from adjacent Precambrian cratons (Dera *et al.*, 2015). Limitation of water circulation and salinity stratification of the Middle Russian Sea may have contributed to the formation of oxygen-depleted bottom layer and the deposition of black shales rich in organic matter that are common in the Russian Platform starting from the Middle–Upper Oxfordian boundary (Hantzpergue *et al.*, 1998; Zakharov *et al.*, 2017). Black shale layers occur in the studied sections of the Russian Platform in the Maltonense Subzone of the Densiplicatum Zone of the uppermost Middle Oxfordian, in the Ilovaiskii Subzone of the Glosense Zone of the lowermost Upper Oxfordian, and in the Lalieranum Subzone of the Mutabilis Zone of the lowermost Upper Kimmeridgian (Głowniak *et al.*, 2010; Wierzbowski *et al.*, 2013; Rogov *et al.*, 2017a; Zakharov *et al.*, 2017). A local organic-rich layer is also found in the lowermost Kimmeridgian (the Densicostata Subzone of the Baylei Zone) of the Kostroma Region of Russia (Zakharov *et al.*, 2017). Interestingly, black shales are even more widespread and thick in the uppermost Kimmeridgian–Volgian of the Russian Platform (Hantzpergue *et*

al., 1998; Shchepetova *et al.*, 2011; Zakharov *et al.*, 2017). Organic-rich strata are also common in the uppermost Oxfordian–Lower Tithonian of NW Europe (Hantzpergue *et al.*, 1998; Morgans-Bell *et al.*, 2001; Smelror *et al.*, 2001) and attributed to restricted water circulation during sea level lowstand (Mutterlose *et al.*, 2003). Weakening of water movement and inflow of freshwaters into Subboreal basins in the Late Jurassic is consistent with postulated models of deposition of the organic-rich beds under permanent or seasonal stratification of the water column (Tyson *et al.*, 1979; Oschmann, 1991) or during a spread of stagnant deep waters in submarine depressions (Wignall & Hallam, 1991).

4.4.4. Changes in cephalopod assemblages

The impact of the decrease in salinity of the Middle Russian sea, as indicated by clumped and oxygen isotope data, on the biota could be noticeable constituting a major reason for periods of occurrences of a mixed Boreal–Mediterranean and endemic Boreal cephalopod faunas in the study area (Głowniak *et al.*, 2010; Wierzbowski & Rogov, 2011). Cephalopods do not tolerate substantial decreases in salinity because of the salt sensitivity of the hemocyanin in their blood (Magnum, 1991). Mangold and Boletzky (1988) show that no modern cephalopod survives at salinities lower than 15‰ or higher than 45‰ although some species are moderately tolerant to salinity variations. For example, *Lolliguncula brevis* occurred at salinities between 17‰ and 38‰ (Zuev & Nesis, 1971) while *Sepia officinalis* is caught in regions marked by fluctuations in salinity from 20‰ to 35.5‰ (Guerra & Castro, 1988). It should be noted that areas characterised either by low or high salinities are poor in cephalopods (Zuev & Nesis, 1971). The response of extinct ammonites to low or high salinity remains unclear, although a general relationship between their diversity and salinities is suggested. Some ammonites, *e.g.,* some Triassic ceratitids, are interpreted to be tolerant to high salinities (Westermann; 1996). Ammonites from the Late Cretaceous Western Interior Seaway of North America are, in turn, understood to have occurred at a wide range of salinities between 20‰ and 35‰ (Cochran *et al.*, 2003). Hallam (1969) argue that reduced salinity in Boreal seas was a key factor responsible for the diversity contrast between Tethyan and Boreal faunas. This view is criticised by Stevens (1971) who suggests climatic zonation as a dominant factor responsible for differentiation of marine faunas.

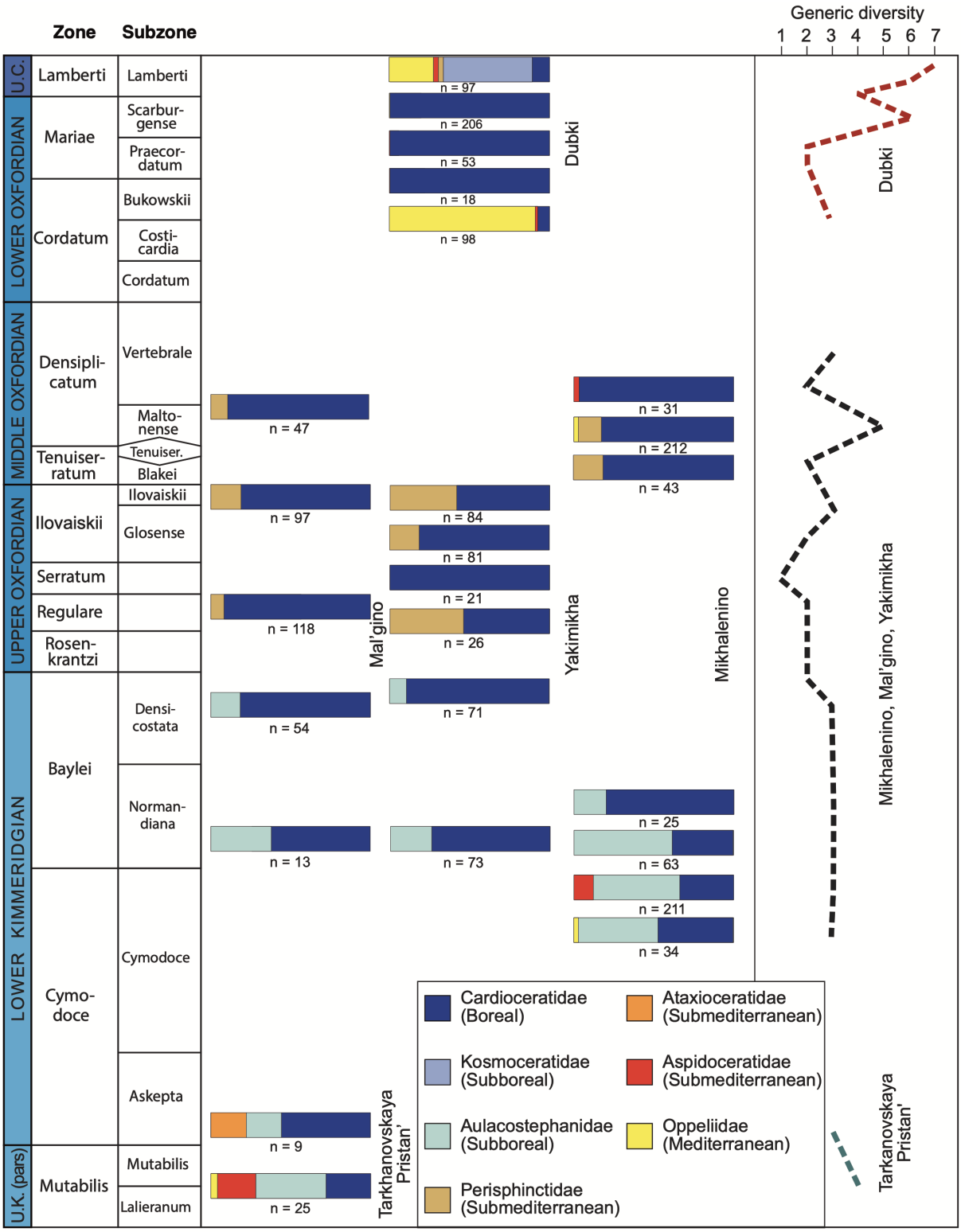

Figure 4.6 | Changes in latest Callovian–earliest Late Kimmeridgian ammonite assemblages of the Russian Platform.

Ammonite diversity is calculated based on number of macroconchiate genera in cases when different genera names are used for micro- and macroconchs of the same ammonite. Note the reversed age axis: oldest samples are on top.

Callovian–Kimmeridgian ammonite faunas of the study areas are characterised by mixed origin and consist of Boreal, Subboreal, Submediterranean and Mediterranean taxa (Zakharov & Rogov, 2003; Głowniak *et al.*, 2010; Wierzbowski & Rogov, 2011; Kiselev *et al.*, 2013). Ammonite assemblages have been studied in sections sampled for clumped isotopes and two additional sections (Mal'gino and Yakimikha) located in the Kostroma Region of Russia (Figure 4.6). Nearly all studied uppermost Callovian–Oxfordian ammonite faunas are dominated by Boreal cardioceratids except for an assemblage of the Bukowskii Subzone of the Cordatum Zone (Lower Oxfordian, the Dubki section), which is crowded by Mediterranean oppeliids (Wierzbowski & Rogov, 2011; Kiselev *et al.*, 2013; Rogov, 2017) (Figure 4.6). Ammonites of the Submediterranean origin occur in the Lower and the Middle Oxfordian. Starting from the Middle–Upper Oxfordian boundary Submediterranean ammonites decline in frequency, and they are missing from the uppermost Oxfordian (Głowniak *et al.*, 2010) (Figure 4.6). Lowermost Kimmeridgian assemblages are dominated by dwarf Boreal *Plasmatites* with the admixture of Subboreal aulacostephanids; only in a short interval near the Baylei–Cymodoce boundary an assemblage with relatively common Submediterranean faunal elements (*Aspidoceras*, *Lingulaticeras*) is recognized (Głowniak *et al.*, 2010; Rogov, 2017) (Figure 4.6). The Lower–Upper Kimmeridgian boundary studied recently in the southern Tatarstan is also characterised by the presence of Submediterranean taxa. They are represented by *Crussoliceras* spp. in the uppermost Cymodoce Zone and by *Aspidoceras* spp. in the Mutabilis Zone (Rogov *et al.*, 2017b) (Figure 4.6). Considering the absence of aspidoceratids in the Mutabilis Subzone of the Subboreal succession of Western Europe, we conclude that these ammonites penetrated in the Middle Russian Sea via a southern strait which connected it with the Caucasian margin of the Tethys.

Ammonite assemblages of the Russian Platform are characterised by a drop of diversity near the Callovian–Oxfordian boundary. The appearance of Submediterranean ammonites at some intervals possibly reflect changes in water circulation (Rogov *et al.*, 2017b). Oscillations in ammonoid assemblages of the Russian Platform are not consistent with palaeotemperature data based on oxygen isotopes (Riboulleau *et al.*, 1998; Dromart *et al.*, 2003; Price & Rogov, 2009; Wierzbowski *et al.*, 2013). Late Oxfordian–Early Kimmeridgian ammonite assemblages of the Russian Platform are strongly dominated by Boreal and Subboreal taxa, which conflicts with a temperature rise postulated previously based on the oxygen isotope composition of carbonate fossils. Observed changes in the

ammonite assemblages are, however, in general agreement with a gradual decrease of salinity detected by present clumped and oxygen isotope analyses.

The Mediterranean mesohibolitid belemnites of the Russian Platform, represented by the genus *Hibolithes*, are very rare north to the Unzha river (Gustomesov, 1976). They are characterised by small size (maximal diameter of ca. 8 mm) compared to the much bigger *Hibolithes* rostra found in Central or Southern Europe (Gustomesov, 1976; Wierzbowski *et al.*, 2013). Occurrences of *Hibolithes* belemnites in the Russian Platform became discontinued at the Middle–Upper Oxfordian boundary, as they disappear entirely in the Upper Oxfordian (Rogov, 2003; Wierzbowski *et al.*, 2013), which is also consistent with postulated restriction and a decrease in salinity of the Middle Russian Sea.

4.4.5. Changes in ostracod and other microfossil assemblages

Uppermost Callovian–Lower Kimmeridgian ostracod fauna of the Russian Platform was studied in detail by Tesakova (2008) and Tesakova *et al.* (2012). Ostracods occur at wide ranges of salinity and cannot be used as an indicator of moderate salinity oscillations. Despite attempts of the reconstruction of variations of seawater temperatures based on the distribution of ostracod faunas (Tesakova, 2014b) there are still problems with interpretation of thermal preferences of cosmopolitan taxa; observed changes in distribution of ostracods may also be affected by sea level fluctuations.

An approach to the reconstruction of relative depth of the basin based on analysis of ostracod communities has been made by Tesakova (2014a). The lower boundary of the upper sublittoral zone (below 50 m), which is penetrated by visible light and grown by seaweeds, is usually inhabited by large-sized benthic ostracods (carapace length of 0.48–1.2 mm). Another small-shelled ostracod assemblage (carapace length 0.25–0.32 mm) is typical for deposit feeders, which occur at all depths but predominate in the middle part of the shelf and deeper environments (Yasuhara *et al.*, 2009; Tesakova, 2014a). The shallow-water environments can; thus, be recognised based on high abundance (70–90%) of large-shelled ostracods.

The Callovian–Kimmeridgian assemblage of large-sized ostracods of the Russian Platform consists of the following genera: *Amphicythere, Balowella, Bythoceratina, Cytherella, Fastigatocythere, Fuhrbergiella, Galliaecytheridea, Klentnicella, Lophocythere, Neurocythere, Patellacythere, Platylophocythere, Progonocythere, Sabacythere and Schuleridea*. Small-sized ostracods are, in turn, represented by *Acrocythere*,

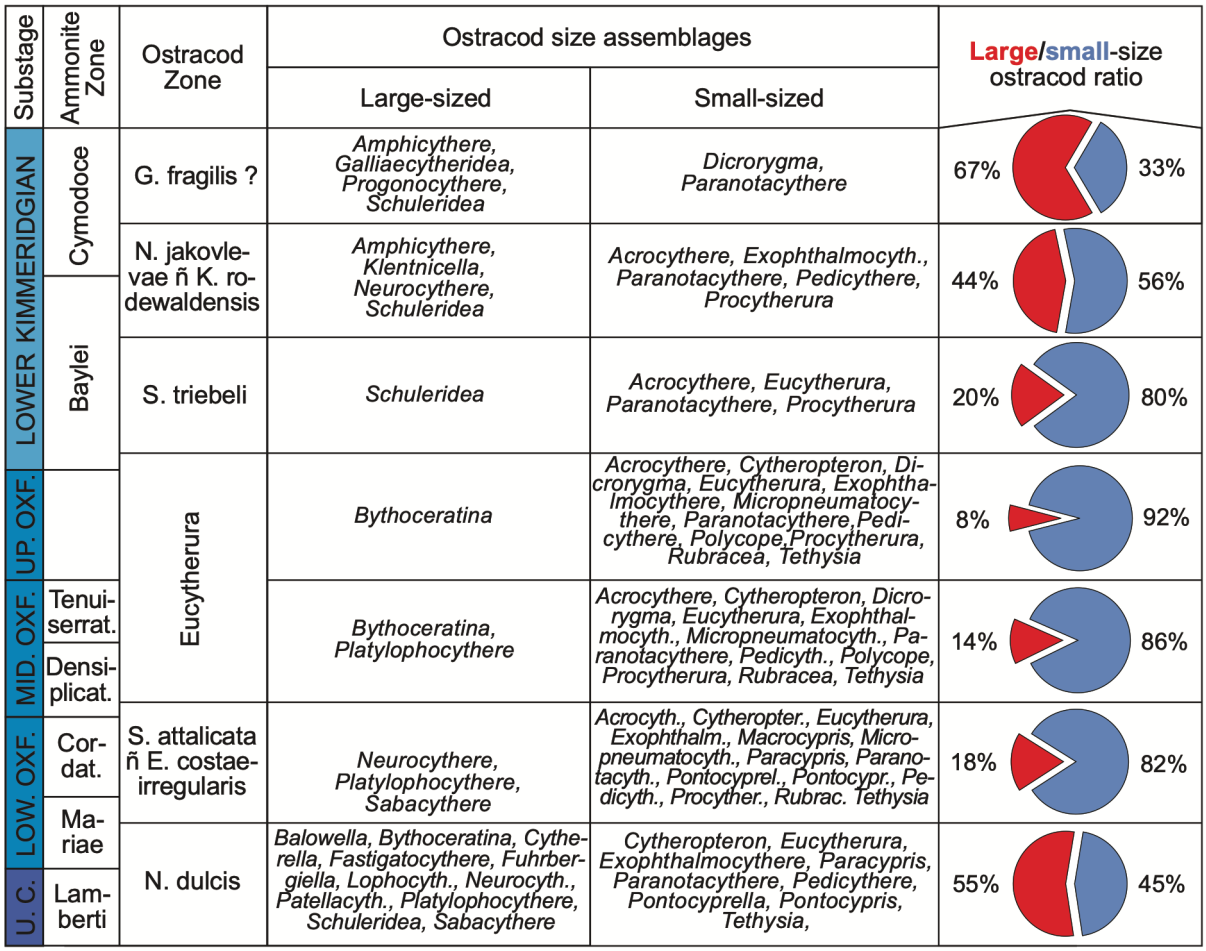

Figure 4.7 | Variations in number of large-sized and small-sized ostracods in the Oxfordian–Lower Kimmeridgian of the Dubki and the Mikhalenino sections.

Cytheropteron, *Dicrorygma* (*Orthorygma*), *Eucytherura*, *Exophthalmocythere*, *Polycope*, *Rubracea*, *Paracypris*, *Pontocypris*, *Pontocyprella*, *Paranotacythere*, *Micropneumatocythere*, *Pedicythere*, *Procytherura* and *Tethysia*. The common Callovian–Kimmeridgian small-sized ostracods including *Cytheropteron*, *Eucytherura* and *Pedicythere* also occur in modern seas being characterised of the lower sublittoral and the deeper zones (Mostafawi *et al.*, 2010).

Variations in relative diversity of small-shelled and large-shelled assemblages studied in the Dubki and the Mikhalenino sections are shown in Figure 4.7. A predominance of the shallow-water environment is inferred for the latest Callovian due to the high abundance of large-sized ostracods in the Lamberti Zone. Since the beginning of the Oxfordian relative diversity of small-sized genera grows drastically. The small-sized ostracods prevail in the Oxfordian and the lowermost Kimmeridgian. It reveals deep-water settings of the studied part of the Middle Russian Sea in this time period. Shallowing, marked by increasing diversity of large-sized ostracods, began in the latest

Baylei Chron and is evident in the Cymodoce Chron of the Early Kimmeridgian. The large-sized ostracods also predominate in the Volgian of the Russian Platform (Tesakova, 2017; Ustinova & Tesakova, 2017). The sea level fall and the restriction of the Middle Russian Sea during the earliest Kimmeridgian are; thus, suggested based on the ostracod fauna.

Worth noting is also the distribution of other microfossils in the Russian Platform. Planktonic foraminifera are documented to be abundant in the Middle and the lowermost Upper Oxfordian of the Makar'ev and Mikhalenino section. They become rare in younger sediments and gradually disappear around the Oxfordian–Kimmeridgian boundary (Ustinova, 2012; Colpaert *et al.*, 2016). Studied assemblages of calcareous nannoplankton from the Moscow region show a general decline in abundance and a noticeable decrease in the number of the cosmopolitian *Watznaueria* spp. in the uppermost Oxfordian (Ustinova, 2009).

Microfossil data substantiate the validity of present interpretations of temporal changes in salinity and circulation of the Middle Russian Sea based on isotopic proxies. They are not consistent with previous views about the existence of a few short-term falls in sea level of the basin during the Oxfordian and the Kimmeridgian, which might have overlapped the long-term period of high sea level (Sahagian *et al.*, 1996).

4.5. Conclusions

Clumped isotope analyses of chemically and thermally well-preserved belemnite rostra and ammonite shells from the Russian Platform have allowed to calculate absolute water temperatures of the Middle Russian Sea and verification of previously presented opinions on the latest Middle–Late Jurassic palaeoenvironmental and palaeoclimatic variations.

The clumped isotope data indicate constant temperatures of water of the Middle Russian Sea of ca. 21(±2) °C in the course of the latest Callovian–earliest Late Kimmeridgian. Our results document the long-term stability of the Late Jurassic climate and challenges previously presented opinions on short-term cooling at the Callovian–Oxfordian transition and pronounced warming during the Late Oxfordian–Early Kimmeridgian. Minor variations in belemnite Mg/Ca ratios and major variations in their Sr/Ca ratios are presently interpreted to reflect secular variations in global seawater chemistry rather than temperatures of belemnite growth.

The clumped and oxygen isotope data derived from cylindroteuthid belemnites, which occur continuously in the studied sediments, enable calculation of variations in

$\delta^{18}O_{water}$ values and estimation of fluctuations in salinity of the Middle Russian Sea around the Middle–Late Jurassic transition. The data show the presence of waters of possibly slightly increased salinities during the latest Callovian–Middle Oxfordian and a gradual decrease in salinity during the Late Oxfordian–earliest Kimmeridgian. The observed change may relate to the inflow of saline, subtropical waters from the Tethys Ocean during the sea level highstand at the Middle–Late Jurassic transition and a subsequent period of progressive isolation of the Middle Russian Sea resulting in freshening of its waters. This is consistent with increasing provincialism of local macro- and microfauna in the Late Oxfordian–Kimmeridgian.

Similar circulation changes probably occurred in all Subboreal basins of Europe. They are manifested by decreases in $\delta^{18}O$ values of carbonate fossils, decreases in $\varepsilon_{Nd\ (t)}$ sediment values, and increasing faunal provincialism. The restriction of epeiric Subboreal basins, diminishing water circulation and freshwater input may have contributed to temporal bottom water anoxia and widespread sedimentation of Upper Jurassic organic-rich facies.

Chapter 5: Precision of Δ_{48} and Δ_{47} data is increased by automated CO_2 purification

Abstract

Precise and accurate temperature reconstruction that is necessary for meaningful palaeoceanography requires precise and accurate clumped isotope data. Δ_{47} and Δ_{48} measurements of carbonate-derived CO_2 are susceptible to sample preparation. The primary sources of poor accuracy and decreased precision of Δ_{47} measurements are widely postulated to be related to the re-equilibration of CO_2 due to the presence of water and contamination of the analyte gas.

Here, we compare Δ_{47} and Δ_{48} measurements of equilibrated gases (1000 °C and 25 °C) that were purified using an offline preparation technique or on an automated line that is directly connected to the mass spectrometer. All gases were analysed on a Thermo Scientific™ 253 Plus™ gas-source mass spectrometer.

We analysed 98 equilibrated gases that were prepared manually and 38 equilibrated gases that were purified using the automated line. Automated gas purification increases the precision of Δ_{47} and Δ_{48}, as expressed by the external 1σ standard deviation. The precision improves from ca. 0.012‰ to ca. 0.008‰ for Δ_{47}, and from ca. 0.049‰ to ca. 0.038‰ for Δ_{48}.

An automated sample preparation line that directly enters the analyte gas into the mass spectrometer after sample purification can decrease external measurement errors because contamination of the analyte CO_2 can be avoided.

Collaborators

Jens Fiebig[1], Niklas Löffler[1,2], Katharina Methner[2], Emilija Krsnik[2], Sven Hofmann[1] — ([1] Goethe University Frankfurt, [2] Senckenberg Biodiversity and Climate Research Centre).

5.1. Introduction

Clumped isotope analyses of carbonates, since its first application (Ghosh *et al.*, 2006), became a widespread method to determine carbonate precipitation temperatures, independent of fluid chemistry. Due to the low natural abundance of the investigated CO_2 isotopologues (mass 47: $^{13}C^{18}O^{16}O$; mass 48: $^{12}C^{18}O^{18}O$), the preparation of the analyte gas for mass spectrometry must be done meticulously. Even a small-scale re-equilibration of CO_2 due to the presence of water (Wacker *et al.*, 2013), or minor amounts of contaminants causing isobaric interferences (Eiler & Schauble, 2004) can bias the accuracy of the measurements.

To achieve Δ_{47} values that can be compared across laboratories, one needs a reference material with a known state of reordering. Huntington *et al.* (2009) proposed that laboratories measure gases equilibrated at low (25 °C) and high (1000 °C) temperatures. With the theoretical Δ_{47} values calculated for these temperatures, each laboratory can determine an empirical transfer function (ETF) for a specific measurement period and use this ETF to scale the measured "raw" Δ_{47} values ($\Delta_{47,\,raw}$) of carbonate-derived CO_2 to a Carbon Dioxide Equilibrium Scale (CDES; "reference frame", RF). Since CO_2 is equilibrated in break seal quartz tubes from which the gases are transferred, the preparation of the equilibrated gases is often done manually, offline from the mass spectrometer.

Here we compare two sample preparation techniques for equilibrated CO_2 gases: manual and automated. Our aim is to show that automation can increase measurement precision.

5.2. Experimental

5.2.1. Preparation of the break-seal quartz tubes

To prepare a break-seal tube for a heated gas (HG, CO_2 gas equilibrated at 1000 °C), first, we bake out a half-sealed quartz tube (ca. 20 cm; GM Associates, USA) on a turbo-pumped high-vacuum line using a propane torch. This step is necessary to remove the structure-bound water from the glass. Afterwards, on the high-vacuum line, we cryogenically purify reference CO_2 gas two times at -80 °C, before freezing it out in the break-seal tube using liquid nitrogen. The top side of the tube is cut and sealed using a propane-oxygen torch, while the bottom half is still submerged in liquid nitrogen.

To prepare break-seal tube for CO_2 gas equilibrated at 25 °C (25G), we first pipette 0.300 mm^3 of water into a half-sealed quartz tube. Then, we connect the tube to a vacuum line pumped with a rotary vane pump and evacuate it. Reference CO_2 gas is frozen out in the break-seal tube using liquid nitrogen. The tube is finally sealed using the propane-oxygen torch.

5.2.2. Manual purification of CO_2

Heated gas break-seal quartz tubes are equilibrated in a muffle oven at 1000 °C for at least 3 hours. After we take the HG tubes out from the oven, we first let it cool down to room temperature, and then insert it into a tube-cracker and connect it to a high-vacuum line pumped with a turbomolecular pump (HiCube Eco 80, Pfeiffer Vacuum, Germany; cryotrap upstream the pump) (Figure A5.1a). When the vacuum reaches a threshold level (8.6×10^{-7} mBar), we crack the finger. The elapsed time between quenching and breaking the break-seal tube is always less than 6 minutes. The CO_2 is led through ethanol slush traps two times, before being frozen out in a glass tube with a manually operated valve on top ("finger"). Afterwards, the finger is attached to a gas chromatographic line, and the overhead space is flushed with helium (purity > 5.0; Alphagaz™ 2 He, Air Liquide, France) for at least five minutes. The gas chromatographic cleaning of the analyte gas is necessary to remove organic and inorganic contaminants that may cause interferences in the mass spectrometer. The CO_2 is then entrained in a helium carrier gas and led through the GC. The GC line consists of an initial ethanol slush trap, the GC column that is cooled down to -15 °C, a second ethanol slush trap, and a final U-trap submerged in liquid nitrogen with a long capillary vent. The purification process takes 50 minutes. The U-trap is then connected to the high-vacuum line where the helium from the overhead space is pumped away. The CO_2 is thawed at -80 °C and led through two ethanol slush traps before being frozen out in a glass tube with a pneumatic diaphragm valve (Swagelok, USA) on top ("autofinger").

The 25G gases are prepared similarly to the heated gases. However, before entering the high vacuum line, the water is scrapped from the 25 °C equilibrated gases on a separate purification line pumped with a rotary vane pump (Figure A5.1b). Immediately after taken out from a water bath, in which the tubes are equilibrated for at least 72 hours at 25 °C, the glass tubes containing both CO_2 and water are submerged into liquid nitrogen. The glass tubes are inserted into a tube cracker and attached to the preparation line. The overhead space is pumped for 10 minutes, and then the CO_2 is thawed in an

ethanol slush. The CO_2 is purified through ethanol slush traps five times before frozen out in a finger. The finger is then attached to the high vacuum line, from which point on the CO_2 is prepared identically to the heated gases. Before the measurement, the autofinger is directly connected to the sample bellow of the mass spectrometer. The vented parts of the inlet system are turbo-pumped for at least 10 minutes before the analyte gas is expanded into the bellow.

5.2.3. Automated purification of CO_2

The first step of gas purification is identical to that of the manually prepared gases. Equilibrated gases are prepared on the high-vacuum line first (Figure A5.1a), but they are frozen out into an autofinger which is then attached to an automated purification line (HAL, Hofmann's Auto Line) connected to the mass spectrometer. The description of HAL is detailed in Chapter 6 (Fiebig *et al.*, in review). Briefly, after the vented inlet ports of the automatization are turbo-pumped for at least one hour, the CO_2 is freed from the autofinger, led through a U-trap kept at -80 °C using ethanol slush, and is immediately frozen out in a subsequent U-trap kept at -196 °C using liquid nitrogen. The automatization lets the CO_2 sublime from the second U-trap while keeping it at -80 °C, so that the water remains frozen out, and freezes the CO_2 out in a consecutive U-trap. The process of CO_2 sublimation is repeated six times altogether. For further purification, the CO_2 gas is entrained into a helium carrier gas and led through a Porapak™ Q column (80-100 mesh, Merck, Germany; packed 2.0 m of 1/8" stainless steel tube), kept at -15 °C, over the time of 45 minutes. Finally, the helium carrier gas is pumped away, and the clean CO_2 gas is expanded into the sample bellow of the mass spectrometer. Parts of the preparation line that are not being used at any time are turbo-pumped. The GC, when not in use, is kept at 150 °C and backwards-flushed with high-purity helium.

5.2.4. Mass spectrometry

Isotopic analyses are carried out on a Thermo Scientific™ 253 Plus™ (Thermo Fisher Scientific, Germany) gas source mass spectrometer equipped with Faraday cups for m/z 44 (3×10^8 Ω), 45 (3×10^{10} Ω), 46, (10^{11} Ω); and m/z 47, 47.5, 48 and 49 (10^{13} Ω). Sample gases are measured against a reference gas (ISO-TOP, Air Liquide, France; $\delta^{18}O_{VSMOW}$ = 25.26‰, $\delta^{13}C_{VPDB}$ = -4.20‰) using the dual inlet system. The measurement capillaries are made of stainless steel with inert fused silica coating inside. Reference and sample gas

intensity on m/z 44 are automatically adjusted to 12000(±100) mV from April 2018 to November 2018 (interval of manual gas preparation), and to 16000(±100) mV from November 2018 onward (interval of automated gas preparation). The total ion integration time for both 12V and 16V measurements was 2000 seconds, *i.e.,* ten cycles with ten acquisitions each. After adding the m/z 47.5 background to the raw intensities in Isodat, the acquisition files are imported into Easotope (release 20190125) (John & Bowen, 2016) that calculates the $\delta^{13}C_{VPDB}$, $\delta^{18}O_{VPDB}$, δ_{45-49}, and $\Delta_{47-49,\,raw}$ values.

5.3. Results

Results of all replicate analyses are documented in Supplementary Data 5.1. To allow for an accurate comparison of the two sample preparation techniques, we slope corrected the $\Delta_{i,\,raw}$ values using the following equation:

(Eq. 5.1) $$\Delta_{i,\,sc} = \Delta_{i,\,raw} - (m \times \delta_i)$$

(i = 47–48) where m is the residual slope, calculated individually for the HG and 25G gases corresponding to each technique, respectively (Figure 5.1). To allow a detailed comparison, "raw" Δ_{47} values are presented in Figure A5.2, and "raw" Δ_{48} values in

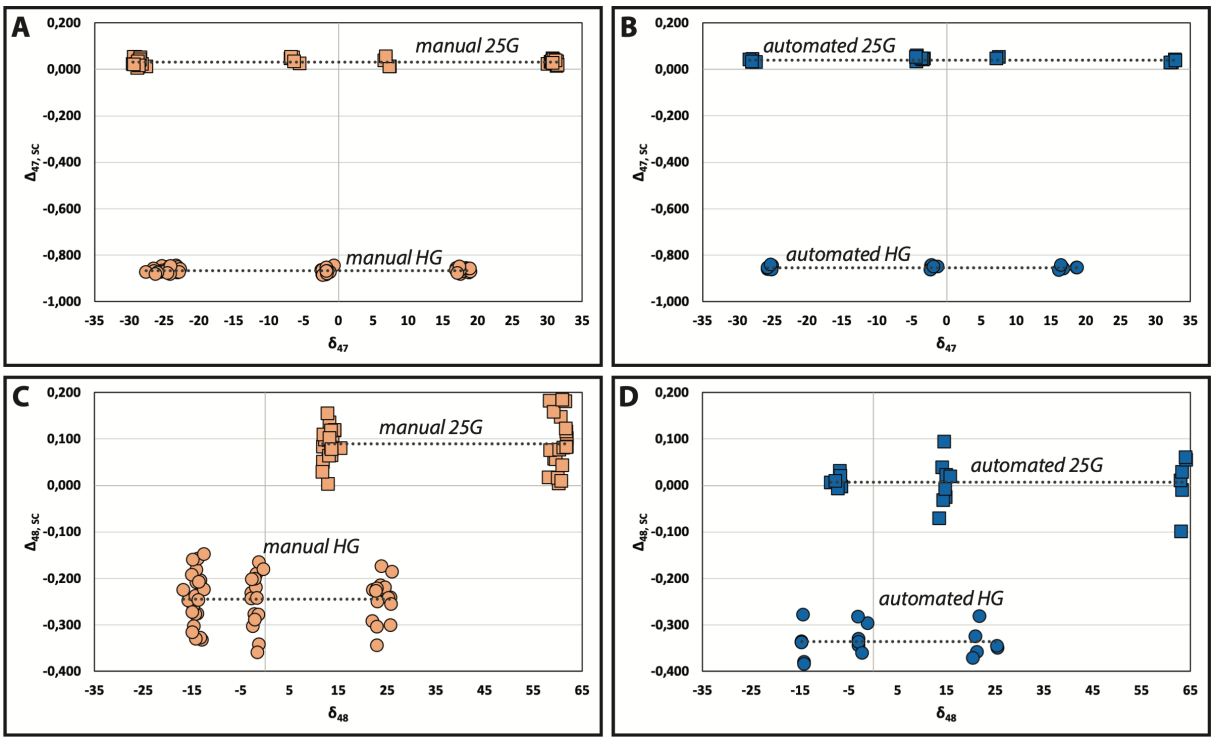

Figure 5.1 | Plots of $\Delta_{i,\,sc}$ *vs.* δ_i for the equilibrated gases (1000 °C and 25 °C) prepared using the manual and the automated technique.
(A) $\Delta_{47,\,sc}$ *vs.* $\delta_{47,\,sc}$ of gases prepared using the manual technique. **(B)** $\Delta_{47,\,sc}$ *vs.* $\delta_{47,\,sc}$ of gases prepared using the automated technique. **(C)** $\Delta_{48,\,sc}$ *vs.* $\delta_{48,\,sc}$ of gases prepared using the manual technique. **(D)** $\Delta_{48,\,sc}$ *vs.* $\delta_{48,\,sc}$ of gases prepared using the automated technique.

Figure A5.3. A concise comparison between the precision of the δ_{47}, δ_{48}, $\Delta_{47,\,sc}$, and $\Delta_{48,\,sc}$ analyses are shown in Table 5.1 and on Figure 5.1.

5.4. Discussion

The internal standard deviations (iSD, 1σ) of the δ_i and Δ_i values are controlled by the number of ions collected over the set integration time; thus, at a higher measurement voltage, the iSD becomes smaller (Merrit & Hayes, 1994). Solely based on ion counting, we can expect a 13.4% decrease in the shot noise limit, *i.e.,* the best attainable performance of the mass spectrometer (Equation 15 of Merrit and Hayes (1994)), for both Δ_{48} and Δ_{47} when changing the m/z 44 measurement voltage from 12 V to 16 V (Supplementary Data 5.1). In our data, the difference in iSD between the 12 V (manual purification) and the 16 V (automated purification, HAL) measurements is ca. 0.004‰ for δ_{47} and Δ_{47} and ca. 0.013 for δ_{48} and Δ_{48} (Figure 5.2 and Table 5.1). This is approximately a 12–13% improvement, analogous to what we expected. An increase in internal precision (iSD) does not directly translate into increased external precision (1σ external standard deviation of the Δ_i values, eSD). After changing from manual to the automated purification technique, the eSD of the $\Delta_{47,\,sc}$ values decrease by ca. 0.004‰, and the eSD of the $\Delta_{48,\,sc}$ values decrease by ca. 0.011‰ (Figure 5.2 and Table 5.1), which correspond to ca. 32% and 23% improvement in precision, respectively.

The reduced eSD of the $\Delta_{i,\,sc}$ data can be related to (1) reduced re-equilibration during sample preparation or (2) decreased contamination. If re-equilibration occurred during sample preparation, that would cause compression for both measured Δ_{47} and Δ_{48} values between the HG and 25G gases. Theoretical Δ_{47} values for CO_2 equilibrated at 25 °C and 1000 °C, are 0.9199‰ and 0.0266‰, respectively (Petersen *et al.*, in review), whereas theoretical Δ_{48} values are 0.345‰ and 0.000‰, respectively (Wang *et al.*, 2004). The difference in Δ_{47} and Δ_{48} intercepts between 25G and HG for the automated technique, *i.e.,* 0.894±0.002 for Δ_{47} (Figures 5.1b and A5.2b,d) and 0.343±0.010 for Δ_{48} (Figures 5.1d

Method	Gas	N	δ_{47} iSD	δ_{48} iSD	Δ_{47} iSD	Δ_{48} iSD	Δ_{47} eSD	Δ_{48} eSD
automated	HG	18	0.026±0.006	0.094±0.025	0.026±0.005	0.094±0.026	0.008	0.032
automated	25G	20	0.023±0.005	0.088±0.026	0.023±0.005	0.086±0.024	0.009	0.043
manual	HG	54	0.027±0.007	0.101±0.026	0.028±0.006	0.101±0.026	0.011	0.053
manual	25G	44	0.028±0.008	0.107±0.026	0.028±0.007	0.104±0.025	0.014	0.046

Table 5.1 | Precision and accuracy of the clumped isotope measurements (δ_{47}, δ_{48}, $\Delta_{47,\,sc}$, $\Delta_{48,\,sc}$) of equilibrated gases (1000 °C and 25 °C).

iSD = mean internal 1σ S.D. of the replicates, eSD = external 1σ S.D. of the replicated values. Errors represent the 1σ S.D. of the corresponding mean values. Data for this table is found in Supplementary Data 5.1.

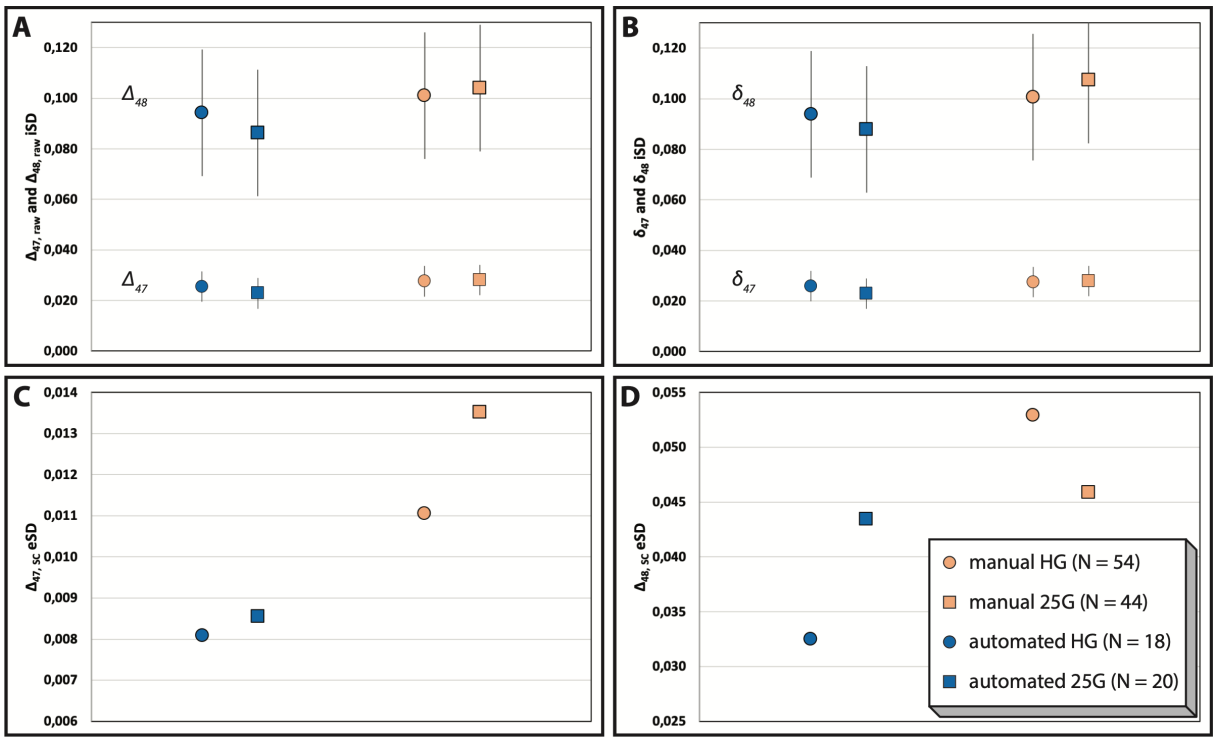

Figure 5.2 | Comparison of the internal and external precision of equilibrated gases (1000 °C and 25 °C) for the manual and the automated sample preparation technique.
(A) Internal precision (iSD) of the $\Delta_{47, raw}$ and $\Delta_{48, raw}$ analyses as expressed by the averages of the internal 1σ standard deviations calculated for the replicates. Error bars represent the 1σ S.D. of the internal 1σ standard deviations. **(B)** Internal precision (iSD) of the δ_{47} and δ_{48} analyses as expressed by the averages of the internal 1σ standard deviations calculated for the replicates. Error bars represent the 1σ S.D. of the internal 1σ standard deviations. **(C)** External precision (eSD) of the $\Delta_{47, SC}$ analyses as expressed by the 1σ standard deviation of the $\Delta_{47, SC}$ values. **(D)** External precision of the $\Delta_{48, SC}$ analyses as expressed by the 1σ standard deviation of the $\Delta_{48, SC}$ values. Since eSD is a standard deviation, no error bars apply.

and A5.3b,d), matches the difference in the theoretically calculated values, *i.e.,* 0.893 for Δ_{47} and 0.345 for Δ_{48}. For the manual preparation technique, the difference is 0.898±0.002 for Δ_{47} (Figures 5.1a and A5.2a,c) and 0.335±0.010 for Δ_{48} (Figures 5.1c and A5.3a,c). A small "positive" compression of Δ_{47} (0.004±0.002) and minor to no compression in Δ_{48} (-0.01±0.01) for the manually prepared gases point to a different factor that decreases the external precision, other than re-equilibration.

Isotopologues of contaminants with m/z 47 and m/z 48 can cause isobaric interferences during mass spectrometric analyses. Contamination can originate either from inefficient sample cleaning or from impure surfaces that the analyte gas encounters. For both the manual and the automated sample preparation techniques, the CO_2 is purified using a GC column. However, for the manual technique, the autofinger containing the analyte CO_2 must be attached to the mass spectrometer through a port that is vented. Although the vented parts of the bellow-inlet system are turbo pumped, contaminants from the ambient air could stick to the stainless-steel surfaces. For the automated

technique contamination of this sort cannot take place because the preparation line is directly connected to the mass spectrometer via a constantly turbo-pumped tubing.

Contaminants with m/z 47 and m/z 48 isotopologues may include hydrocarbons, halocarbons, and nitrogen oxides (Eiler & Schauble, 2004). Contamination with hydrocarbons and halocarbons causes an increase in both measured Δ_{47} and Δ_{48}. Contamination with NO_2 causes coupled decrease in Δ_{47} and increase in Δ_{48}, whereas, contamination with N_2O leads to increased Δ_{47} and no change in Δ_{48} (Eiler & Schauble, 2004). Compared to the automated technique, the Δ_{47} intercepts for the manually prepared HG and 25G gases are shifted by ca. -0.011(±0.002) (Figure A5.2), and the Δ_{48} intercepts are shifted by ca. +0.087(±0.010) (Figure A5.3). A decrease in Δ_{47} and an increase in Δ_{48} points toward contamination by NO_2. The natural abundance ratio of CO_2 m/z 48 to m/z 47 isotopologues is approximately 1:10, whereas the natural abundance ratio of NO_2 m/z 47 to m/z 48 isotopologues is approximately 1:1. Thus, contamination by NO_2 would lead to approximately 10-times larger contamination in Δ_{48} than in Δ_{47}. Interestingly, this corresponds to the ratio between the decrease in Δ_{47} intercepts and the increase in Δ_{48} intercepts for the HG and 25G gases, between the automated and the manual technique, respectively. Nitrogen dioxide may originate from the ambient laboratory air because the room is located on the ground floor of the building near the street. An alternate source of NO_2 could be the O_2 and N_2 molecules of air that, in the source of the mass spectrometer, could scramble and recombine to NO_2.

5.5. Conclusions

Directly entering the analyte gas into the mass spectrometer after sample purification can increase the precision of the Δ_{47} and Δ_{48} measurements. The most likely source of the increased precision is reduced contamination. We suggest that laboratories use a direct inlet system after sample purification for entering the analyte CO_2 to the bellow of the mass spectrometer, as this may reduce contamination.

Chapter 6: High-precision Δ_{48} and Δ_{47} analysis of carbonates

Abstract

High-precision analysis of the excess abundance (relative to the stochastic distribution) of m/z 48 isotopologues in CO_2 evolved from acid digestion of carbonates (Δ_{48}) has recently not been possible due to the relatively low natural abundance of ^{18}O. Here we show that the 253 Plus™ gas source mass spectrometer equipped with Faraday cups and 10^{13} Ω resistors can perform combined Δ_{47} and Δ_{48} analyses on carbonates with external reproducibilities (1SD) of 0.010‰ and 0.030‰, respectively.

Ca. 10 mg aliquots of five carbonate reference materials (ETH1, ETH2, ETH3, ETH4, and Carrara) are digested with phosphoric acid at 90 °C using a common acid bath. The evolved CO_2 is purified using an automated gas preparation system (including cryotraps and a GC) and analysed for its Δ_{47} and Δ_{48} compositions using the dual inlet system of a 253 Plus™ gas source mass spectrometer. Raw Δ_{47} and Δ_{48} values are finally normalized to the Carbon Dioxide Equilibrium Scale (CDES).

In $\Delta_{47\ (CDES\ 90°C)}$ *vs.* $\Delta_{48\ (CDES\ 90°C)}$ space, calcite reference materials Carrara, ETH3 and ETH4 agree with the equilibrium curve for calcite after adding experimentally determined 90°C acid fractionation factors of 0.193‰ (for Δ_{47}) and 0.135‰ (for Δ_{48}) to theoretical Δ_{63} and Δ_{64} data.

Agreement between measured and theoretically expected $\Delta_{48\ (CDES\ 90°C)}$ highlights the accuracy of our high-precision clumped isotope analytical setup. Combined analysis of m/z 47 and 48 isotopologue abundances in CO_2 evolved from acid digestion of natural carbonates has excellent potential for the determination of accurate palaeotemperatures and the identification of rate-limiting biomineralisation processes.

Collaborators

Jens Fiebig[1], Niklas Löffler[1,2], Katharina Methner[2], Emilija Krsnik[2], Andreas Mulch[2], Sven Hofmann[1] — ([1] Goethe University Frankfurt, [2] Senckenberg Biodiversity and Climate Research Centre).

6.1. Introduction

Clumped isotope analysis of the sum of $^{13}C^{18}O^{16}O$ and $^{12}C^{18}O^{17}O$ isotopologues (Δ_{47}) in CO_2 evolved from phosphoric acid digestion of carbonates (Ghosh *et al.*, 2006) has become a now increasingly utilized (palaeo)thermometer (Eiler, 2011) to determine marine (Wierzbowski *et al.*, 2018) and terrestrial (Methner *et al.*, 2016) palaeotemperatures as well as body temperatures of extinct vertebrates (Eagle *et al.*, 2011). Since this type of thermometer is based on the internal fractionation of isotopes amongst carbonate isotopologues, it is independent on the isotopic composition of the water from which the carbonate-bearing phase precipitated. Nonetheless, discrepant Δ_{47}–temperature calibrations have been obtained in different laboratories (Ghosh *et al.*, 2006; Dennis & Schrag, 2010). Accuracy of Δ_{47} calibration data has been shown to be sensitive to the choice of parameters used for the correction of (1) contributions deriving from ^{17}O-bearing CO_2 (Daëron *et al.*, 2016; Schauer *et al.*, 2016), (2) pressure baseline effect (He *et al.*, 2012; Bernasconi *et al.*, 2013; Fiebig *et al.*, 2016), (3) scale compression (Huntington *et al.*, 2009; Dennis *et al.*, 2011), and (4) acid fractionation (Petersen *et al.*, in review). Also, calibration regression lines can be biased if the number of samples and replicates per sample, as well as the investigated temperature range, is relatively low (Fernandez *et al.*, 2017). The observed discrepancy in Δ_{47}–T calibrations is slightly reduced if calibration data from eight experimental and six empirical studies are processed with the IUPAC ^{17}O parameters, recommended by Daëron *et al.* (2016), and with a unique temperature dependence of the acid fractionation factor (see Petersen *et al.* (in review)). However, even for these reprocessed calibrations the absolute spread in Δ_{47} at a given temperature still occurs as large as 0.08‰, with slopes ranging from 0.033 to 0.042 in Δ_{47} *vs.* $1/T^2$ space (Petersen *et al.*, in review). Most recent investigations suggest that much of the observed scatter could be due to kinetics occurring in the solution prior to carbonate precipitation and at the solution-carbonate interface (Bajnai *et al.*, 2018; Daëron *et al.*, 2019). If relevant, kinetic departures from equilibrium would limit the accuracy of the clumped isotope Δ_{47} palaeothermometer.

The second most abundant carbonate isotopologue containing two heavy isotopes is $^{12}C^{18}O^{18}O^{16}O$. CO_2 derived from acid digestion of carbonate contains on average 4.1 ppm of $^{12}C^{18}O^{18}O$ (m/z 48), which is an order of magnitude lower than its $^{13}C^{18}O^{16}O$ (m/z 47) content (Ghosh *et al.*, 2006). Another m/z 48 isotopologue is $^{13}C^{18}O^{17}O$ that has an average natural abundance of 16.7 ppb only. The weighted sum of the excess abundances of these

two m/z 48 isotopologues (relative to their stochastic distributions) is reflected by the Δ_{48} value:

(Eq. 6.1) $$\Delta_{48} = [(R_{48} / R_{48}^* - 1) - 2 \times (R_{46} / R_{46}^* - 1)] \times 1000$$

where Ri and Ri* represent the measured and stochastic* i/44 isotopologue ratios.

Like Δ_{47}, the carbonate Δ_{48} composition does not depend on the oxygen isotopic composition of the water from which the carbonate crystallized. The position of a given carbonate sample in Δ_{47} *vs.* Δ_{48} space is; therefore, determined by its formation temperature and, if kinetics prevailed during formation, by the extent of kinetic departure from equilibrium. Since kinetically induced departures from equilibrium follow for given rate-limiting exchange mechanisms characteristic trajectories in Δ_{47} *vs.* Δ_{48} space, it should be possible to determine accurate carbonate formation temperatures based on measured Δ_{47} *vs.* Δ_{48} compositions even if these were affected by kinetics (Guo & Zhou, 2019).

So far, the precision of Δ_{48} measurements with common gas source mass spectrometers equipped with ≤ 10^{12} Ω amplifiers has been inadequate to permit temperature estimates based on Δ_{48}. Instead, laboratories that analyse Δ_{48} use its magnitude for data quality assurance of Δ_{47} data, *i.e.,* as an indicator of potential isobaric interferences on m/z 47 (Huntington *et al.*, 2009). Here we demonstrate that high-precision Δ_{47} and Δ_{48} analyses of carbonates are possible using a common acid bath and the dual inlet of a Thermo Scientific™ 253 Plus™ gas source mass spectrometer. The external reproducibility for these measurements occurs close to the predicted shot noise limits. Our results imply that internal isotopic equilibrium is closely attained in ETH1, ETH2, ETH3, ETH4, and Carrara.

6.2. Experimental

6.2.1. Samples

Calcite reference materials analysed for this study were an in-house Carrara and the internationally distributed ETH1, ETH2, ETH3, and ETH4 standards. ETH1 and ETH2 represent calcites that were internally equilibrated at 600 °C, whereas the formation temperatures of ETH3 and ETH4 calcites are unknown (Meckler *et al.*, 2014). Bernasconi *et al.* (2018) reported $\Delta_{47\,(CDES\ 25°C)}$ for ETH1, ETH2, ETH3 and ETH4 that were assigned

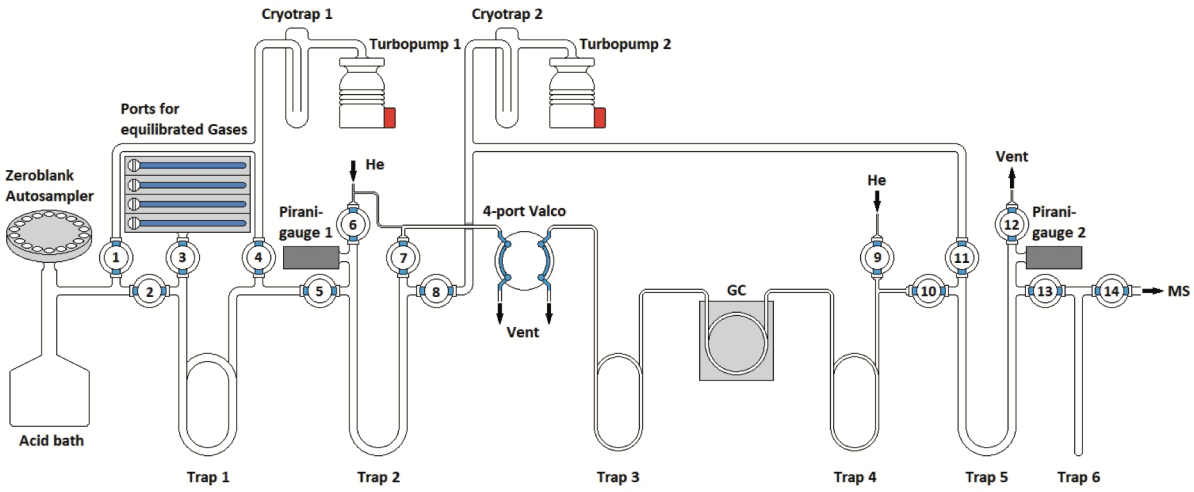

Figure 6.1 | Schematic setup of Hofmann's Auto Line (HAL).
For more detailed explanation see text.

using the dual inlet system for equilibrated gas measurements and a Thermo Scientific™ KIEL IV Carbonate Device for carbonate-derived CO_2 measurements.

6.2.2. Carbonate reaction and gas purification

The setup of the self-constructed automated carbonate acid digestion and gas purification system (Hofmann's Auto Line, HAL) used for sample preparation is displayed in Figure 6.1. It consists of a Zero Blank Autosampler (Costech Analytical Technologies, USA), a common acid bath, several cryotraps and a gas chromatograph (GC; 2.0 m of 1/8" stainless steel tube packed with Porapak™ Q 80-100 mesh, Merck, Germany) and two turbopumps (HiCube 80 Eco, Pfeiffer Vacuum, Germany) with cryogenic water traps upstream of the turbo pumps. One pumps the part of the extraction line in front of the GC, including the autosampler and the common acid bath, the other provides the high vacuum for the two cryotraps in front of and behind the GC. Per replicate, ~10 mg of calcite is loaded into silver capsules (IVA Analysentechnik, Germany). These are then placed into the autosampler, located on top of the common acid bath. Once loading is completed, the autosampler and the common acid bath are turbo-pumped for at least 5 hours. Slight rotation of the autosampler forces a sample-bearing silver capsule to drop down into the phosphoric acid (> 105 wt%). Carbonate samples are routinely reacted for 30 minutes, and the evolving CO_2 is continuously removed at -196 °C in trap 2. Trap 1 is kept at -80 °C to remove water. During the reaction, the pressure is continuously read in at trap 2. After the reaction is complete, traps 2, 3 and 4 are set to -80 °C, while trap 5 is cooled to -196 °C. Helium (purity > 5.0; Alphagaz™ 1 He, Air Liquide, France, gas led through a Supelco® 27600-U, Merk, Germany, helium purifier) enters trap 2 at a flow rate of 15 ml/min and

purges the CO_2 through trap 3, the GC column (kept at -15 °C) and trap 4, before it is frozen out again in trap 5. After 45 minutes, the GC column is purged with He in the reverse flow, heated to 150 °C and kept at this temperature until the next sample is being prepared. Helium is pumped away from trap 5. Afterward, trap 5 is warmed up to -80 °C and trap 6 cooled down to -196 °C. The yield of CO_2 is determined in the volume of trap 5 and the CO_2 then frozen out in trap 6. Once freezing is complete, trap 6 is isolated from trap 5, warmed up to -80 °C and the pure CO_2 introduced into the sample bellow of the mass spectrometer through expansion. LabVIEW (National Instruments, USA) drives the automatization of HAL.

6.2.3. Equilibrated gases and gas purification

CO_2, equilibrated at 1000 °C for at least 2 hours in a quartz break seal tube (GM Associates, USA), is taken off the muffle furnace and quenched to room temperature within 2 minutes. The break seal tube is mounted to a tube cracker that is connected to a high vacuum (water trap upstream the turbopump), manually operated gas extraction line. Within less than 5 minutes after having left the muffle furnace, the break seal tube is cracked, and the CO_2 is passed twice over a water trap kept at -80 °C. The CO_2 is finally quantitatively transferred into a quartz glass with a pneumatic diaphragm valve (Swagelok, USA) at its top ("autofinger"). The same high vacuum line is used to clean CO_2 equilibrated at 25 °C and to transfer it to the autofinger. However, before CO_2 equilibrated at 25 °C is allowed to enter the manually operated high-vacuum gas purification line, liquid water is stripped off on a separate, rotary vane-pumped gas extraction line by passing the CO_2 five times over a cryogenic water trap kept at -80 °C. This way we can avoid that any significant amounts of water enter the high-vacuum gas preparation line.

The autofinger is finally connected to HAL in front of trap 2 (Figure 6.1). There, equilibrated gases follow the same preparation pathway as carbonate-derived CO_2 with the exception that they enter HAL isolated from the common acid bath. Equilibrated gases are prepared in amounts equivalent to the CO_2 derived from carbonates (between 80–100 μmol).

6.2.4. Mass spectrometric measurements

Isotopic analyses are carried out on a Thermo Scientific™ 253 Plus™ (Thermo Fisher Scientific, Germany) gas source mass spectrometer using its dual inlet system. The 253 Plus™ at the Goethe University has Faraday cups for m/z 44, 45, 46, 47, 47.5, 48 and 49.

Cups for m/z 44–46 have 3 x 10^8 Ω, 3 x 10^{10} Ω, and 10^{11} Ω resistors, respectively, while m/z 47–49 cups are amplified by 10^{13} Ω resistors. The m/z 47.5 cup is used to continuously read in the pressure baseline next to m/z 47.

After the sample bellow has been loaded with CO_2, an equivalent amount (80–100 µmol) of reference gas CO_2 (ISO-TOP, Air Liquide; $\delta^{18}O_{VSMOW}$ = 25.26‰, $\delta^{13}C_{VPDB}$ = -4.20‰) is introduced into the reference gas bellow. Reference and sample gas enter the ion source of the 253 Plus™ gas source mass spectrometer through stainless steel capillaries whose inner surface is coated with inert fused silica (Thermo Fisher Scientific; bre 00014684). Reference and sample gas intensity are automatically adjusted to an intensity of 16000(±100) mV on m/z 44. Sample and reference gas are measured in 10 acquisitions, consisting of 10 cycles each. Each cycle considers an integration time of 20 seconds both for the reference and the sample gas, yielding a total integration time of 2000 seconds per replicate. Idle time is set to 16 seconds.

6.2.5. Data processing

The negative background that is read in on m/z 47.5 is directly added to the raw intensities obtained for m/z 47 and m/z 48 in Isodat. Acquisition files are then exported to Easotope (release 20190125) (John & Bowen, 2016) that performs the calculation of $\delta^{13}C_{VPDB}$, $\delta^{18}O_{VPDB}$, δ_{47}, δ_{48}, $\Delta_{47,\,raw}$ and $\Delta_{48,\,raw}$ using the IUPAC parameters (Daëron *et al.*, 2016).

	Carrara		ETH 4		ETH 3		ETH 2		ETH 1	
	$\Delta_{47\ (CDES\ 90°C)}$	$\Delta_{48\ (CDES\ 90°C)}$	$\Delta_{47\ (CDES\ 90°C)}$	$\Delta_{48\ (CDES\ 90°C)}$	$\Delta_{47\ (CDES\ 90°C)}$	$\Delta_{48\ (CDES\ 90°C)}$	$\Delta_{47\ (CDES\ 90°C)}$	$\Delta_{48\ (CDES\ 90°C)}$	$\Delta_{47\ (CDES\ 90°C)}$	$\Delta_{48\ (CDES\ 90°C)}$
	0.313	0.182	0.463	0.258	0.623	0.313	0.227	0.166	0.222	0.102
	0.319	0.132	0.470	0.191	0.630	0.251	0.213	0.131	0.224	0.141
	0.313	0.113	0.465	0.162	0.611	0.293	0.214	0.119	0.218	0.166
	0.320	0.181	0.457	0.221	0.615	0.304	0.215	0.146	0.205	0.168
	0.318	0.136	0.438	0.200	0.629	0.264	0.201	0.115	0.194	0.147
	0.308	0.153	0.448	0.213	0.628	0.220	0.224	0.190	0.203	0.189
	0.305	0.128	0.456	0.234	0.602	0.297	0.204	0.124	0.215	0.115
	0.301	0.113	0.456	0.243	0.627	0.260	0.208	0.130	0.220	0.124
	0.314	0.129	0.460	0.228	0.627	0.212	0.203	0.162	0.213	0.116
	0.312	0.143	0.456	0.249	0.611	0.256	0.203	0.076	0.202	0.115
					0.613	0.283	0.204	0.156	0.199	0.145
									0.214	0.118
avg.	**0.312**	**0.141**	**0.457**	**0.220**	**0.620**	**0.268**	**0.211**	**0.138**	**0.210**	**0.137**
1 SD	0.006	0.025	0.009	0.029	0.010	0.033	0.009	0.031	0.010	0.027
2 SE	0.004	0.018	0.006	0.021	0.006	0.022	0.006	0.021	0.006	0.017
sn	0.003	0.009	0.003	0.009	0.002	0.008	0.002	0.008	0.002	0.002

Table 6.1 | $\Delta_{47\ (CDES\ 90°C)}$ and $\Delta_{48\ (CDES\ 90°C)}$ of carbonate reference materials analysed in this study.
All values are processed using the IUPAC parameters recommended by Daëron *et al.* (2016). 1 SD and 2 SE denote the 1σ standard deviation and the 2σ standard error, respectively. The shot noise limit (sn) represents the best analytical precision that can be obtained. It was calculated from Equation 15 of Merrit and Hayes (1994), considering the total integration time represented by the total number of replicates (2000 seconds x 10–12 replicates).

6.3. Results

A total of 54 carbonate reference samples and 30 equilibrated gases were run within a period of 4 weeks in January 2019. $\delta^{13}C_{VPDB}$, $\delta^{18}O_{VPDB}$, δ_{47}, δ_{48}, $\Delta_{47,\,raw}$ and $\Delta_{48,\,raw}$ of equilibrated gases and carbonate reference materials are listed in Supplementary Data 6.1, and additionally, for the carbonate reference materials, we present a summary table in the manuscript (Table 6.1).

6.4. Discussion

6.4.1. Quality of background correction and scale compression

Figure 6.2 displays the correlation between δ_{47} and $\Delta_{47,\,raw}$ for CO_2 equilibrated at 1000 °C and 25 °C, respectively, as well as for ETH1 and ETH2. The slopes of the corresponding regression lines are almost zero, demonstrating that the m/z 47.5 cup accurately reads in the negative background below m/z 47. However, since there is a slight residual slope for the heated gases that is distinguishable from zero, an additional slope correction of $\Delta_{47,\,raw}$ data needs to be applied. To determine this slope, 1000 °C and 25 °C gas data are merged, adding the difference between intercepts to the heated gas $\Delta_{47,\,raw}$ values. This way, a residual slope of -0.00013 is obtained that exactly matches the residual slope displayed by ETH1 and ETH2 raw data (Figure 6.2). Slope corrected $\Delta_{47,\,sc}$ data is calculated by applying a slope correction to $\Delta_{47,\,raw}$ data:

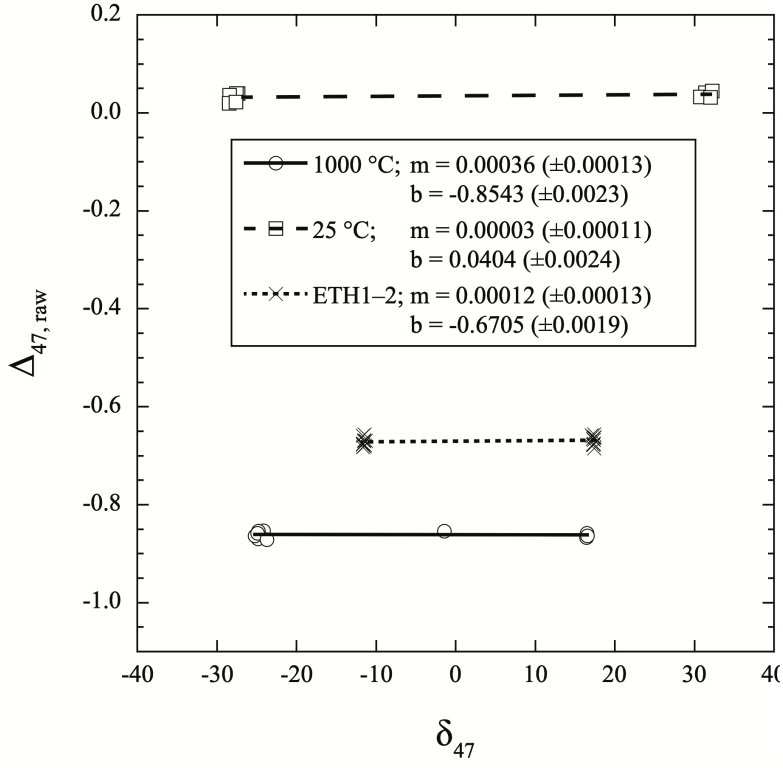

Figure 6.2 | Plot of $\Delta_{47,\,raw}$ *vs.* δ_{47} for CO_2 equilibrated at 1000 °C and 25 °C, respectively, as well as for carbonate reference materials ETH1 and ETH2.
$\Delta_{47,\,raw}$ and δ_{47} values are relative to the working gas composition. Slopes (m) and intercepts (b) of the corresponding regression lines, as well as their errors, are provided for further information.

(Eq. 6.2) $$\Delta_{47,\,sc} = \Delta_{47,\,raw} - (m_{47} \times \delta_{47})$$

where m_{47} is the residual slope, in our case -0.00013.

Correlation plots of $\Delta_{48,\,raw}$, *vs.* δ_{48}; however, yield significant steeper residual negative slopes (Figure 6.3). In addition, the slopes vary slightly between -0.01454 for 25 °C gases, -0.01515 for ETH1 and ETH2 and -0.01595 for heated gases. These residual slopes result from an overcorrection of the negative background occurring below m/z 48 when using the intensity read in by the m/z 47.5 cup. CO_2 equilibrated at 25 °C describes a much larger variation in δ_{48} than carbonate-derived CO_2 and heated gases. If 25 °C gases with extraordinarily high δ_{48} are excluded all slopes become indistinguishable from each other within errors. Considering that ETH1 and ETH2 yield identical $\Delta_{47\,(CDES\ 90°C)}$ (see below), there is no reason to assume that there is any significant difference in their $\Delta_{48\,(CDES\ 90°C)}$ compositions. We; therefore, used the intermediate slope obtained from the ETH1 and ETH2 data (Figure 6.3) to correct all sample $\Delta_{48,\,raw}$ data for the overcorrection induced by the m/z 47.5 intensity:

(Eq. 6.3) $$\Delta_{48,\,sc} = \Delta_{48,\,raw} - (m_{48} \times \delta_{48})$$

where m_{48} is the residual slope, in this study -0.01515.

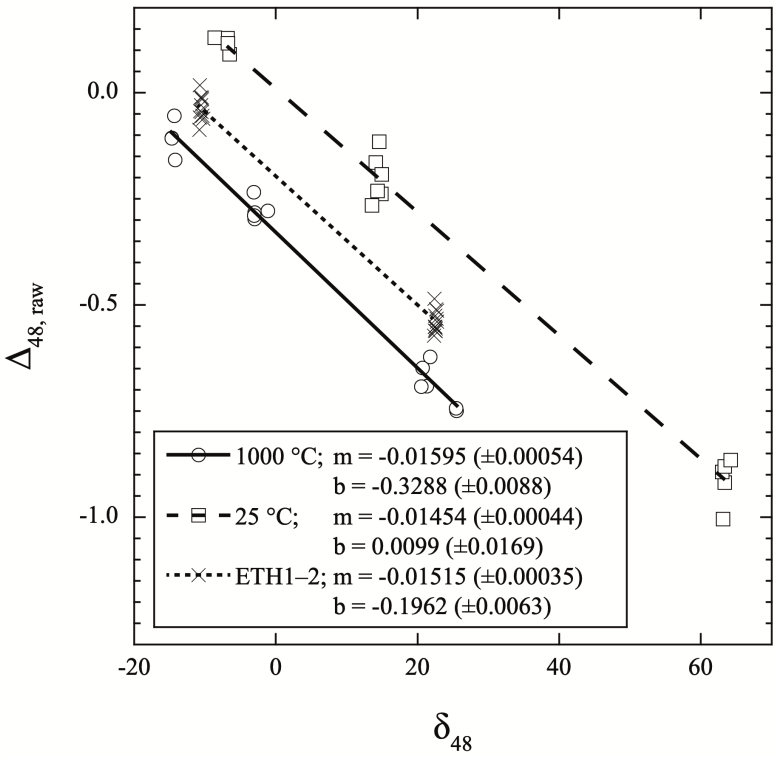

Figure 6.3 | Plot of $\Delta_{48,\,raw}$ *vs.* δ_{48} for CO_2 equilibrated at 1000 °C and 25 °C, respectively, as well as for carbonate reference materials ETH1 and ETH2.
$\Delta_{48,\,raw}$ and δ_{48} values are relative to the working gas composition. Slopes (m) and intercepts (b) of the corresponding linear regression lines, as well as their errors, are provided for further information. If gases with extraordinarily high δ_{48} are excluded, for CO_2 equilibrated at 25 °C, the slope of the regression line becomes m = -0.01464 (±0.00139) and; hence, within errors indistinguishable from that characteristic for heated gases (1000 °C) and ETH1 & ETH2, respectively.

6.4.2. Projecting measured $\Delta_{47,\,raw}$ and $\Delta_{48,\,sc}$ values to the CO_2 equilibrium scale

Empirical transfer functions for the projection of $\Delta_{47,\,raw}$ and $\Delta_{48,\,sc}$ values onto the CDES can be derived plotting $\Delta_{47,\,raw}$ and $\Delta_{48,\,sc}$ values of equilibrated gases against their corresponding theoretical values. Theoretical $\Delta_{48,\,1000°C}$ and $\Delta_{48,\,25°C}$ values are not directly available but can be computed from the data provided by Wang *et al.* (2004), who calculated the temperature dependence of $\Delta_{12C18O18O}$ and $\Delta_{13C18O17O}$ as a function of temperature. Considering that $^{12}C^{18}O^{18}O$ contributes 99.6% and $^{13}C^{18}O^{17}O$ 0.4‰ to m/z 48, theoretical Δ_{48} values at any temperature can be computed according to:

(Eq. 6.4) $$\Delta_{48,\,CO2} = 0.996 \times \Delta_{12C18O18O} + 0.004 \times \Delta_{13C18O17O}$$

After processing the data of Wang *et al.* (2004) (their Table 4(I)) through Equation 6.4, a best fit polynomial regression yields:

(Eq. 6.5) $$\Delta_{48,\,CO2} = \text{-}1.0345 \text{ x } 10^{-4} \times (10^6 / T^2)^3 + 4.22629 \times 10^{-3} \times (10^6 / T^2)^2 - 3.76112 \times 10^{-3} \times (10^6 / T^2)$$

According to Equation 6.5, the theoretical Δ_{48} should be 0.345‰ and 0.000‰ for CO_2 at temperatures of 25 °C and 1000 °C, respectively. At these temperatures, the corresponding theoretical Δ_{47} values are 0.9252‰ and 0.0266‰, respectively (Dennis *et al.*, 2011).

In $\Delta_{47,\,raw}$ *vs.* δ_{47} space, the difference in intercepts between 1000 °C and 25 °C CO_2 exactly matches the theoretical difference of 0.90 (Figure 6.2). The 253 Plus™ installed at the joint Goethe University – Senckenberg BIK-F stable isotope facility is devoid of any significant scale compression for Δ_{47}, contrary to the MAT 253™ that was run in the same laboratory using electropolished nickel capillaries (Fiebig *et al.*, 2016). For the determination of $\Delta_{47\,(CDES\,90°C)}$ the following empirical transfer function is obtained:

(Eq. 6.6) $$\Delta_{47\,(CDES\,90°C)} = 1.0044 \times \Delta_{47,\,sc} + 0.8846$$

After correcting equilibrated gas $\Delta_{48,\,raw}$ data using a slope of -0.01515, intercepts of -0.3355 and 0.0104 are obtained for CO_2 equilibrated at 1000 °C and 25 °C, respectively (Figure 6.4). The difference between the two intercepts is in perfect agreement with the theoretically expected value of 0.345‰. The hypothesis that the 253 Plus™ installed in our laboratory is not affected by any significant scale compression is; therefore, confirmed by Δ_{48} data of equilibrated gases. It follows:

(Eq. 6.7) $$\Delta_{48\,(CDES\,90°C)} = 0.9974 \times \Delta_{48,\,sc} + 0.3346$$

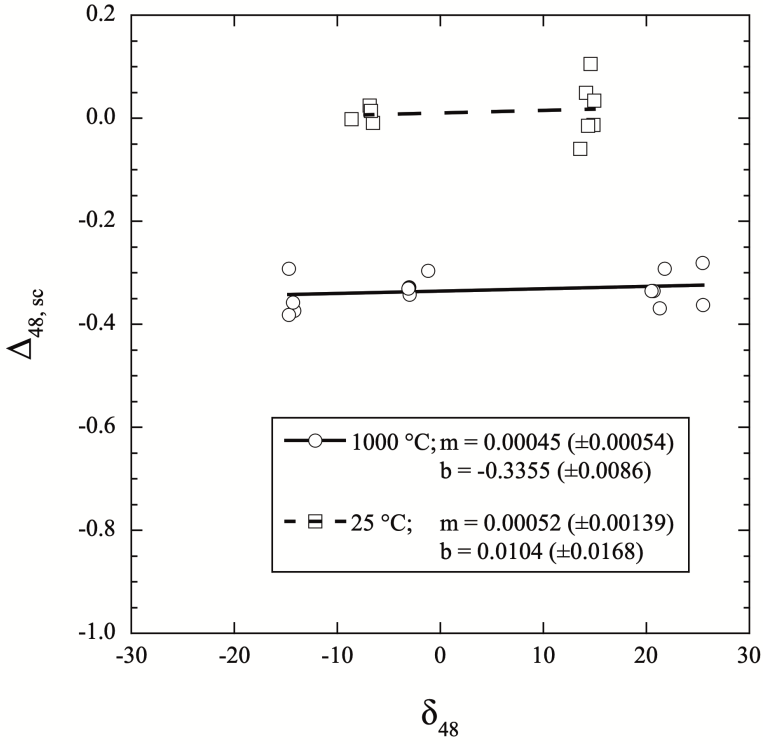

Figure 6.4 | Plot of $\Delta_{48,\,sc}$ *vs.* δ_{48} for CO_2 equilibrated at 1000 °C and 25 °C, respectively.
$\Delta_{48,\,sc}$ is derived from Equation 6.3, after correcting $\Delta_{48,\,raw}$ for the slope displayed by ETH1 and ETH2 data (Figure 6.3). Gases with extraordinary high δ_{48} were excluded as these are far outside the range characteristic for carbonates. Note that the equilibrated slopes become, within errors, indistinguishable from zero.

$\Delta_{47\,(CDES\ 90°C)}$ and $\Delta_{48\,(CDES\ 90°C)}$ computed for carbonate reference materials ETH1, ETH2, ETH3, ETH4 and Carrara are listed in Table 6.1. For these, it becomes obvious that $\Delta_{48\,(CDES\ 90°C)}$ increases with $\Delta_{47\,(CDES\ 90°C)}$. Such behavior is expected if both compositions are largely controlled by temperature. External reproducibilities (expressed as 1σ standard deviation, 1SD) range from ±0.006‰ to ±0.010‰ for $\Delta_{47\,(CDES\ 90°C)}$ and from ±0.025 to ±0.033‰ for $\Delta_{48\,(CDES\ 90°C)}$ (Table 6.1). The corresponding mean values of 0.009‰ and 0.029‰ are only slightly higher than the predicted shot noise limits of 0.008‰ and 0.027‰, respectively, which represent the best attainable precision for the chosen analytical conditions of 2000 seconds integration time per replicate (Merrit & Hayes, 1994). Compared to the MAT 253™ (1SD of 11–16 ppm, see Fiebig *et al.* (2016)), the external reproducibility for dual inlet-based Δ_{47} measurements with the high-ohmic 253 Plus™ is improved by a factor of 2.

6.4.3. $\Delta_{47\,(CDES\ 25°C)}$ of ETH carbonate reference materials

Addition of a 25–90 °C acid fractionation factor of 0.088‰ (Petersen *et al.*, in review) to the $\Delta_{47\,(CDES\ 90°C)}$ values reported in Table 6.1 yields $\Delta_{47\,(CDES\ 25°C)}$ values (±1SD) of 0.298(±0.010)‰ for ETH1, 0.299(±0.009)‰ for ETH2, 0.708(±0.010)‰ for ETH3, and 0.545(±0.009)‰ for ETH4. These values are significantly different from those reported in Bernasconi *et al.* (2018), even if 0.006‰ are added to the latter data to account for the unique temperature dependence of the acid fractionation factor (Petersen *et al.*, in

review). We speculate that the observed differences may arise from the circumstance that in the analytical setup used by Meckler *et al.* (2014) and Bernasconi *et al.* (2018) CO_2 gas derived from the ETH standards did not enter the ion source of the gas source mass spectrometer through the same stainless steel capillary as the equilibrated gases. If small amounts of water were adsorbed at the inner surface of the sample gas capillary, partial re-equilibration of CO_2 at lower ambient temperature may happen while the CO_2 passes through the capillary, finally introducing a compression of the Δ_{47}-scale. Partial re-equilibration may attain a steady state as long as the water content and the gas flux through the capillary are constant. Under such conditions, sample-derived CO_2 can still be accurately projected onto the CDES if the equilibrated gases enter the ion source through the same capillary as the sample gases. However, the same correction procedure would deliver inaccurate results if two different capillaries with distinct water contents and fluxes were used.

6.4.4. Comparing measured $\Delta_{47\ (CDES\ 90°C)}$ and $\Delta_{48\ (CDES\ 90°C)}$ with predicted equilibrium values

According to Hill *et al.* (2014), the B3LYP (6-311++G(2d,2p) supramolecular cluster model describes the temperature dependence of equilibrium clumping in calcite most reliably. To make measured $\Delta_{47\ (CDES\ 90°C)}$ and $\Delta_{48\ (CDES\ 90°C)}$ comparable with equilibrium Δ_{63} and Δ_{64} values, the acid fractionation factors $\Delta^*_{47\text{-}63}$ and $\Delta^*_{48\text{-}64}$, characteristic for a reaction at 90 °C, have to be added to the Δ_{63} and Δ_{64} values, respectively. These can be constrained from measured and theoretical data. For ETH1 and ETH2, we obtain mean $\Delta_{47\ (CDES\ 90°C)}$ and $\Delta_{48\ (CDES\ 90°C)}$ values of 0.211(±0.009)‰ and 0.137(±0.029)‰, respectively (Table 6.1). According to Hill *et al.* (2014), a Δ_{63} value of 0.018‰ and a Δ_{64} value of 0.002‰ is predicted for calcite at 600 °C, *i.e.,* the temperature at which ETH1 and ETH2 were prepared. Subtracting these values from the mean $\Delta_{47\ (CDES\ 90°C)}$ and $\Delta_{48\ (CDES\ 90°C)}$ values obtained for ETH1 and ETH2 yields $\Delta^*_{47\text{-}63}$ and $\Delta^*_{48\text{-}64}$ acid fractionation factors of 0.193‰ and 0.135‰, respectively. Theoretically expected $\Delta_{47\ (CDES\ 90°C)}$ and $\Delta_{48\ (CDES\ 90°C)}$ values for CO_2 derived from acid digestion of equilibrated calcite may now be computed adding $\Delta^*_{47\text{-}63}$ and $\Delta^*_{48\text{-}64}$ to the theoretical Δ_{63} and Δ_{64} values of Hill *et al.* (2014) at any temperature.

Figure 6.5 provides a comparison of theoretical equilibrium with measured values in $\Delta_{47\ (CDES\ 90°C)}$ *vs.* $\Delta_{48\ (CDES\ 90°C)}$ space. Generally, measured $\Delta_{48\ (CDES\ 90°C)}$ for ETH3, ETH4 and Carrara confirm measured $\Delta_{47\ (CDES\ 90°C)}$ values in that $\Delta_{48\ (CDES\ 90°C)}$ increases with $\Delta_{47\ (CDES\ 90°C)}$. This is expected if both $\Delta_{48\ (CDES\ 90°C)}$ and $\Delta_{47\ (CDES\ 90°C)}$ are primarily controlled by

temperature. Moreover, within errors, measured $\Delta_{47\ (CDES\ 90°C)}$ and $\Delta_{48\ (CDES\ 90°C)}$ values agree with theoretical equilibrium implying that internal isotopic equilibrium may have been attained in all investigated carbonates. We would not expect such a systematic correlation between $\Delta_{47\ (CDES\ 90°C)}$ and $\Delta_{48\ (CDES\ 90°C)}$ for these three carbonates if isobaric interferences on m/z 47 and m/z 48 were of importance.

Should equilibrium really have been attained in ETH3, ETH4 and Carrara, it would have been established at temperatures of 13(±2) °C, 84(±4) °C, and 209(±6) °C, respectively, as reflected from measured $\Delta_{47\ (CDES\ 90°C)}$ values (Figure 6.5). However, considering the error in $\Delta_{48\ (CDES\ 90°C)}$, we alternatively cannot rule out that the true $\Delta_{47\ (CDES\ 90°C)}$ and $\Delta_{48\ (CDES\ 90°C)}$ compositions of Carrara and ETH4 plot below and above the equilibrium line, respectively (Figure 6.5). Generally, departures from equilibrium would be introduced by rate-limiting kinetic effects. It has recently been shown that the most prominent rate-limiting processes involved in carbonate precipitation, CO_2 absorption and CO_2 degassing, follow their specific trajectories in $\Delta_{47\ (CDES\ 90°C)}$ *vs.* $\Delta_{48\ (CDES\ 90°C)}$ space (Guo & Zhou, 2019). Hence, even if kinetics were of any importance during carbonate mineralisation, it could be possible to determine accurate formation temperatures, along with the rate-limiting step governing isotopic exchange, solely based on the position of measured data in $\Delta_{47\ (CDES\ 90°C)}$ *vs.* $\Delta_{48\ (CDES\ 90°C)}$ space (Guo & Zhou, 2019).

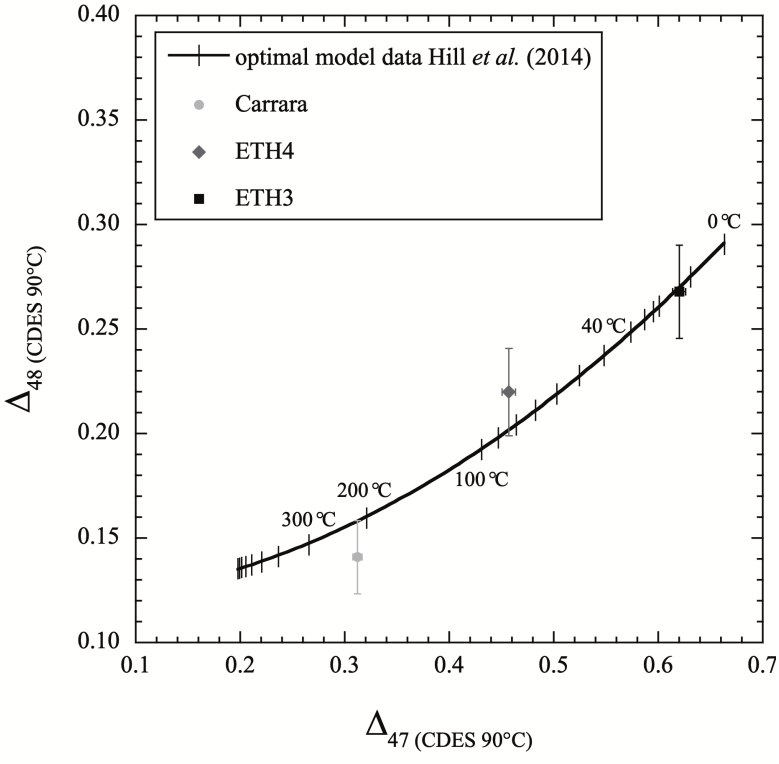

Figure 6.5 | Plot of $\Delta_{48\ (CDES\ 90°C)}$ *vs.* $\Delta_{47\ (CDES\ 90°C)}$ for ETH3, ETH4, and Carrara.
Within errors (2σ S.E.), all data points agree with the theoretical equilibrium curve after adding the experimentally determined phosphoric acid fractionation factors of 0.135‰ and 0.193‰, respectively, to the theoretical Δ_{64} and Δ_{63} values for calcite (Hill *et al.*, 2014).

6.5. Conclusions

We describe an analytical setup that allows accurate and precise determination of Δ_{48} along with Δ_{47} in CO_2 evolved from phosphoric acid digestion of carbonates. External reproducibilities for Δ_{48} and Δ_{47} analyses occur close to the corresponding shot-noise limits. There is no indication that the chosen setup introduces any significant artificial biases in the measured abundances of m/z 47 and m/z 48 CO_2 isotopologues.

Chapter 7: Summary and Outlook

For a long time, the stable oxygen isotope composition of the carbonate remains of marine calcifiers served as one of the most reliable and most widely used palaeoseawater-temperature proxy. However, the $\delta^{18}O$-thermometer have limitations. First, to reconstruct seawater temperatures, one must assume the oxygen isotope composition of the seawater ($\delta^{18}O_{sw}$) since it cannot be independently determined. It is debated if the $\delta^{18}O_{sw}$ changed significantly (> 6‰) over geological timescales (Veizer & Prokoph, 2015; Coogan *et al.*, 2019). High temperature (> 350 °C) rock-water interactions at seafloor hydrothermal systems lead to an ^{18}O enrichment in the seawater, while oxygen isotope exchange between silicates and water below 350 °C lead to an ^{18}O depletion. In explanation to the unreasonably warm $\delta^{18}O$-based Palaeozoic temperatures, it was postulated that the ratio of hot/cold rock-water interactions changed in deep-time due to, *e.g.,* lower sea level leading to reduced water penetration, shallower mid-ocean ridge depth, or reduced thickness of biogenic sediment cover (Veizer & Prokoph, 2015). Even in modern oceans, there is a substantial (up to 4‰) variation in $\delta^{18}O_{sw}$ across latitudes and different marine settings mostly due to Rayleigh fractionation*, i.e.,* ^{18}O depletion during evaporation and precipitation, and to variable continental freshwater influx (LeGrande & Schmidt, 2006). In contrast to the $\delta^{18}O$ thermometer, the clumped isotope thermometer is independent of fluid chemistry as it addresses the fractionation of isotopes within a single carbonate phase and; thus, has a great potential to reconstruct ancient oceanic temperatures (Eiler, 2011).

Another limitation of the $\delta^{18}O$-thermometer is that kinetic effects (vital effects) occurring during biomineralisation influence the isotopic composition of the carbonates. Growth rate or pH-related vital effects on $\delta^{18}O$ were recognised, among others calcifiers, in brachiopods (Lowenstam, 1961), and corals (McConnaughey, 1989a). Recent studies observed kinetic effects affecting the clumped isotope composition (Δ_{47}) of corals, certain foraminifera, and echinoderms (Tripati *et al.*, 2010; Thiagarajan *et al.*, 2011; Saenger *et al.*, 2012; Spooner *et al.*, 2016; Davies & John, 2019). Since brachiopods are the most widely used archive for deep-time palaeoceanography, due to their frequent occurrence in sedimentary deposits and generally good preservation, it is essential that the nature and extent of kinetic effects influencing Δ_{47} are studied in them. In **Chapter 2** of this thesis, I investigated if we can observe systematic trends in the $\delta^{18}O$ and Δ_{47} of brachiopods shells by analysing 18 modern specimens for which growth temperature and $\delta^{18}O_{sw}$ were

independently known. I found that in offset Δ_{47} *vs.* offset $\delta^{18}O$ space, where offset represents the difference from expected equilibrium, there is a significant negative correlation between our data (**Figure 2.2 on page 23**). Such a trend indicates kinetic effects due to Knudsen diffusion or incomplete $CO_{2\,(aq)}$ hydration and hydroxylation reactions. Correlations between shell growth rates and offset isotope values (**Figure 2.4 on page 28**), as well as between shell $\delta^{18}O$ and $\delta^{13}C$ provide further arguments for the presence of kinetics.

In brachiopods, the magnitude of the kinetic effects on Δ_{47} and $\delta^{18}O$ depends on the shell growth rate. Since it is difficult to determine the growth rate of extinct brachiopods, they may not be the most reliable archive of deep-time seawater temperatures. In **Chapters 3 and 4**, I turn to fossil belemnites to reconstruct Mesozoic seawater temperatures. Generally, in sections where both belemnites and brachiopods were concurrently investigated, belemnites give colder $\delta^{18}O$-based temperature estimates (Voigt *et al.*, 2003; Alberti *et al.*, 2012a; Veizer & Prokoph, 2015). However, as I pointed out in **Chapter 2**, brachiopods are biased towards warmer temperature estimates. Compared to brachiopods, belemnites may precipitate closer to equilibrium and allow a more accurate temperature reconstruction. Near-equilibrium precipitation warrants the use of the Coplen (2007) equation with the $\delta^{18}O$ proxy, instead of the Kim and O'Neil (1997) equation.

Altogether, I have investigated 56 Jurassic to Cretaceous (ca. 160–125 million years ago) belemnite rostra for Δ_{47} (Figure 7.1). Latest Jurassic to Early Cretaceous belemnites from DSDP Site 511 yield balmy (25±4 °C) southern high-latitude seawater temperatures, which are within the range of TEX_{86}^{H} temperatures acquired from the same site (Jenkyns *et al.*, 2012) (**Figure 3.2 on page 42**). In comparison, the $\delta^{18}O$-thermometer for the same rostra, assuming a $\delta^{18}O_{sw}$ of -1‰ SMOW and using the Kim and O'Neil (1997) equation yield ca. 10 °C colder temperature estimates. Additionally, I investigated Valanginian (Early Cretaceous, ca. 135 million years ago) belemnites from northern hemisphere mid-latitudes and northern high-latitudes, collected from four locations in Spain, the UK, and Russia. The Δ_{47} sea surface temperature estimates (21±5 °C to 31±6 °C) are consistently warmer than modern equivalents and produce a shallow latitudinal gradient (**Figure 3.3 on page 45**). The balmy northern and southern high latitude

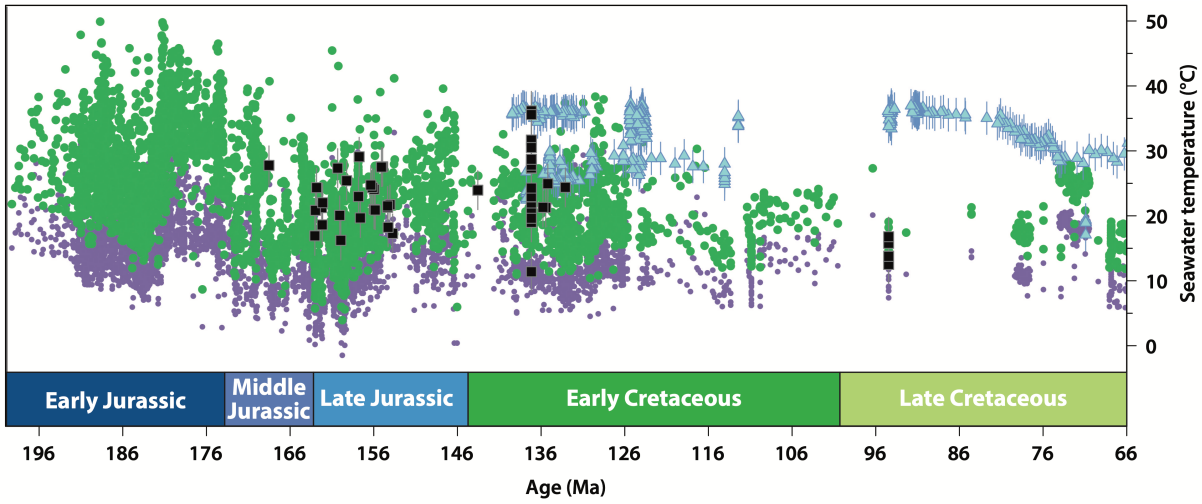

Figure 7.1 | The temperature evolution of Jurassic and Cretaceous seas, as inferred from belemnite $\delta^{18}O$ and Δ_{47}, and TEX_{86} analyses.
The 56 belemnite Δ_{47}-based temperature estimates from this study (black squares), are shown together with TEX_{86}^{H} temperatures (blue triangles), belemnite $\delta^{18}O$ based temperatures calculated using the "traditional" Kim and O'Neil (1997) equation and a constant $\delta^{18}O_{sw}$ of -1‰ SMOW (small purple circles), and the suggested Coplen (2007) equation with a constant $\delta^{18}O_{sw}$ of 0.5‰ SMOW (Valanginian northern hemisphere average from this study; large green circles). Belemnite $\delta^{18}O$-based temperature estimates converge with the Δ_{47} and TEX_{86} estimates if the Coplen (2007) equation and a modern-like $\delta^{18}O_{sw}$ is used. On the contrary, using the Kim and O'Neil (1997) equation and a $\delta^{18}O_{sw}$ of -1‰ SMOW results in underestimated seawater temperatures. The variation in $\delta^{18}O$-based temperatures is presumably related to a non-homogeneous $\delta^{18}O_{sw}$ across latitudes and ocean basins (**Chapter 3**). References for $\delta^{18}O$ and TEX_{86}, as well as all the values used for this plot, are in Supplementary Data 7.1. Cenomanian belemnite Δ_{47} values, not discussed elsewhere in this work, are presented in Supplementary Data 7.2.

temperatures presented in **Chapter 3** inhibit extended polar ice (Grasby *et al.*, 2017) and provide an additional argument for the significance of polar amplification in a high pCO_2 world (Sagoo *et al.*, 2013). From the calcite $\delta^{18}O$ and the measured Δ_{47} temperatures, it was possible to infer $\delta^{18}O_{sw}$ values that are more positive than expected (Valanginian mean: 0.5‰ SMOW) and are in the range of modern values (**Figure 3.4 on page 50**). Seawater $\delta^{18}O$ was likely not homogenous across ocean basins, and evaporation and continental freshwater influx played a significant role in determining its value. In **Chapter 4**, I turn to a composite Middle–Late Jurassic section in Russia, where assuming a constant $\delta^{18}O_{sw}$ for the entire period, carbonate oxygen isotope thermometry inferred a ca. 10 °C warming (Wierzbowski *et al.*, 2013; Wierzbowski, 2015). Contrary, belemnite Δ_{47} suggests constant seawater temperatures of ca. 21(±2) °C (**Figure 4.2 on page 63**). A decreasing trend in $\delta^{18}O_{sw}$, *i.e.,* freshening, may resolve the discrepancy between the two records. A drop in εNd values and changes in ammonite and ostracod bioassemblages are consistent with an elevated freshwater input to the basin. A sea level decrease starting

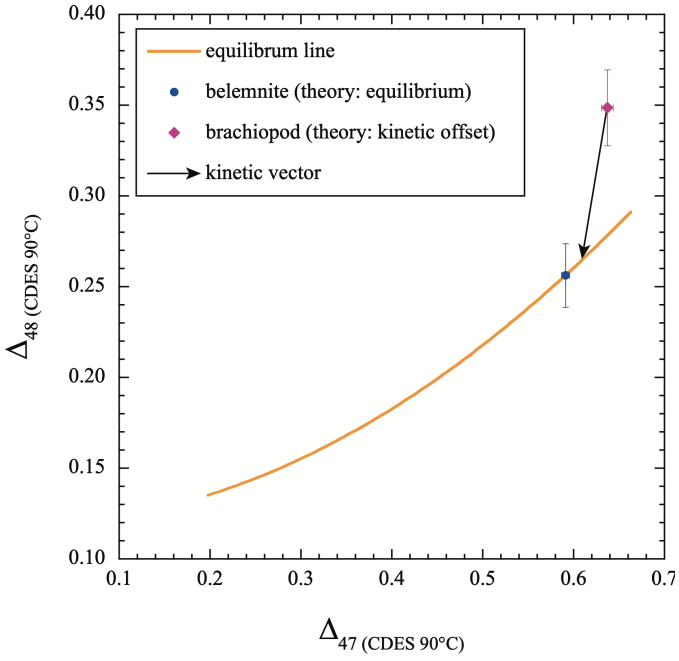

Figure 7.2 | Correction for kinetic effects in Δ_{48} *vs.* Δ_{47} space.
Theoretical brachiopod and belemnite data are plotted in Δ_{48} *vs.* Δ_{47} space, with error bars commonly achieved by ten replicate analyses (see **Figure 6.5 on page 97** for more detail). In **Chapter 2**, I show that brachiopod Δ_{47} is affected by kinetics that may also cause an offset from theoretical Δ_{48}. However, knowing the slope of the kinetic vector corresponding to the rate-limiting process, in the case of brachiopods incomplete $CO_{2\,(aq)}$ hydration and hydroxylation or diffusion, it is possible to project the "kinetic point" to the equilibrium line and estimate the "true" growth temperature. In contrast, if belemnites precipitated in equilibrium, they would plot on the equilibrium line.

from the Lower Oxfordian may have led to a restricted Middle Russian Sea, limiting seawater exchange with the open ocean.

Belemnites seem to provide a good geochemical archive for palaeothermometry. However, since they went extinct, we cannot investigate modern specimen and exclude vital effects. A new method is necessary to independently determine the extent and nature of kinetic effects in biogenic carbonates that don't have modern analogues, and for which water chemistry cannot be independently determined. In **Chapters 5 and 6**, I show that first in the world at the Goethe University we can simultaneously conduct high-accuracy and precision carbonate Δ_{47} and Δ_{48} analyses (**Figure 6.5 on page 97**). The Δ_{48} of a carbonate is, like the Δ_{47}, independent of fluid chemistry. In Δ_{48} *vs.* Δ_{47} space, the position of a carbonate, if precipitated in thermodynamic equilibrium, is determined by its formation temperature. A recent study has shown that kinetic effects result in a systematic shift from the Δ_{48}–Δ_{47} equilibrium line (Guo & Zhou, 2019): for example, brachiopods are expected to plot below or above the equilibrium line (Figure 7.2). Their "true" precipitation temperatures could be acquired if the "kinetic" point is projected onto the equilibrium line using a slope representative to the kinetics involved. Belemnites, or other biogenic calcites, if precipitated in thermodynamic equilibrium, would plot on the equilibrium line in Δ_{48} *vs.* Δ_{47} space. Paired clumped isotope (Δ_{48} and Δ_{47}) analysis of carbonates is a promising tool for palaeothermometry and future research delving into the nature and extent of kinetic effects in carbonates.

References

Abbink, O., Targarona, J., Brinkhuis, H., & Visscher, H. (2001). Late Jurassic to earliest Cretaceous palaeoclimatic evolution of the southern North Sea. *Global and Planetary Change, 30*(3-4), 231-256.

Adkins, J. F., Boyle, E. A., Curry, W. B., & Lutringer, A. (2003). Stable isotopes in deep-sea corals and a new mechanism for "vital effects". *Geochimica et Cosmochimica Acta, 67*(6), 1129-1143.

Aguado, R., Company, M., & Tavera, J. M. (2000). The Berriasian/Valanginian boundary in the Mediterranean region: New data from the Caravaca and Cehegín sections, SE Spain. *Cretaceous Research, 21*(1), 1-21.

Alberti, M., Fürsich, F. T., & Pandey, D. K. (2012a). The Oxfordian stable isotope record ($\delta^{18}O$, $\delta^{13}C$) of belemnites, brachiopods, and oysters from the Kachchh Basin (western India) and its potential for palaeoecologic, palaeoclimatic, and palaeogeographic reconstructions. *Palaeogeography, Palaeoclimatology, Palaeoecology, 344-345*, 49-68.

Alberti, M., Fürsich, F. T., Pandey, D. K., & Ramkumar, M. (2012b). Stable isotope analyses of belemnites from the Kachchh Basin, western India: paleoclimatic implications for the Middle to Late Jurassic transition. *Facies, 58*(2), 261-278.

Anderson, T. F., Popp, B. N., Williams, A. C., Ho, L. Z., & Hudson, J. D. (1994). The stable isotopic records of fossils from the Peterborough Member, Oxford Clay Formation (Jurassic), UK: Palaeoenvironmental implications. *Journal of the Geological Society, 151*(1), 125-138.

Arabas, A. (2016). Middle–Upper Jurassic stable isotope records and seawater temperature variations: New palaeoclimate data from marine carbonate and belemnite rostra (Pieniny Klippen Belt, Carpathians). *Palaeogeography, Palaeoclimatology, Palaeoecology, 446*, 284-294.

Armendáriz, M., Rosales, I., Bádenas, B., Piñuela, L., Aurell, M., & García-Ramos, J. C. (2013). An approach to estimate Lower Jurassic seawater oxygen-isotope composition using $\delta^{18}O$ and Mg/Ca ratios of belemnite calcites (Early Pliensbachian, northern Spain). *Terra Nova, 25*(6), 439-445.

Assonov, S. S., & Brenninkmeijer, C. A. (2003). A redetermination of absolute values for $^{17}R_{VPDB\text{-}CO2}$ and $^{17}R_{VSMOW}$. *Rapid Communications in Mass Spectrometry, 17*(10), 1017-1029.

Auclair, A.-C., Joachimski, M. M., & Lécuyer, C. (2003). Deciphering kinetic, metabolic and environmental controls on stable isotope fractionations between seawater and the shell of *Terebratalia transversa* (Brachiopoda). *Chemical Geology, 202*(1-2), 59-78.

Baertschi, P. (1976). Absolute ^{18}O content of Standard Mean Ocean Water. *Earth and Planetary Science Letters, 31*(3), 341-344.

Bailey, T. R., Rosenthal, Y., McArthur, J. M., van de Schootbrugge, B., & Thirlwall, M. F. (2003). Paleoceanographic changes of the Late Pliensbachian-Early Toarcian interval: a possible link to the genesis of an Oceanic Anoxic Event. *Earth and Planetary Science Letters, 212*(3-4), 307-320.

Baird, M. J., Lee, D. E., & Lamare, M. D. (2013). Reproduction and growth of the terebratulid brachiopod *Liothyrella neozelanica* Thomson, 1918 From Doubtful Sound, New Zealand. *Biological Bulletin, 225*(3), 125-136.

Bajnai, D., Fiebig, J., Tomašových, A., Milner Garcia, S., Rollion-Bard, C., Raddatz, J., Löffler, N., Primo-Ramos, C., & Brand, U. (2018). Assessing kinetic fractionation in brachiopod calcite using clumped isotopes. *Scientific Reports, 8*(1), 1-12.

Baraboshkin, E. J. (2007). Stratigraphy and Boreal-Tethyan correlation of marine Lower Hauterivian of Russia and CIS. In E. M. Pervushov (Ed.), *Selected Papers of the Third All-Russia Meeting 'Cretaceous System of Russia and Near Overseas: Problems of Stratigraphy and Paleogeography*. Saratov, RUS: Publishing House of Saratov State University.

Barkan, E., & Luz, B. (2005). High precision measurements of $^{17}O/^{16}O$ and $^{18}O/^{16}O$ ratios in H_2O. *Rapid Communications in Mass Spectrometry, 19*(24), 3737-3742.

Barron, E. J. (1983). A warm, equable Cretaceous: The nature of the problem. *Earth-Science Reviews, 19*(4), 305-338.

Barron, E. J., & Washington, W. M. (1982). Cretaceous climate: A comparison of atmospheric simulations with the geologic record. *Palaeogeography Palaeoclimatology Palaeoecology, 40*(1-3), 103-133.

Basov, I. A., & Krasheninnikov, V. A. (1983). Benthic foraminifers in Mesozoic and Cenozoic sediments of the southwestern Atlantic as an indicator of paleoenvironment, Deep Sea Drilling Project leg 71. *Initial Reports of the Deep Sea Drilling Project, 71*, 739-787.

Baumgarten, S., Laudien, J., Jantzen, C., Häussermann, V., & Försterra, G. (2014). Population structure, growth and production of a recent brachiopod from the Chilean fjord region. *Marine Ecology, 35*(4), 401-413.

Bazhenova, T. K. (2008). Problem of petroleum potential of basal horizons in the basins of ancient platforms in aspect of their katagenetic evolution. *Petroleum Geology – Theoretical and Applied Studies, 3*, 1-21.

Beck, W. C., Grossman, E. L., & Morse, J. W. (2005). Experimental studies of oxygen isotope fractionation in the carbonic acid system at 15°, 25°, and 40°C. *Geochimica et Cosmochimica Acta, 69*(14), 3493-3503.

Benito, M. I., Reolid, M., & Viedma, C. (2016). On the microstructure, growth pattern and original porosity of belemnite rostra: insights from calcitic Jurassic belemnites. *Journal of Iberian Geology, 42*(2), 201-226.

Bernard, S., Daval, D., Ackerer, P., Pont, S., & Meibom, A. (2017). Burial-induced oxygen-isotope re-equilibration of fossil foraminifera explains ocean paleotemperature paradoxes. *Nature Communications, 8*(1134), 1-10.

Bernasconi, S. M., Hu, B., Wacker, U., Fiebig, J., Breitenbach, S. F., & Rutz, T. (2013). Background effects on Faraday collectors in gas-source mass spectrometry and implications for clumped isotope measurements. *Rapid Communications in Mass Spectrometry, 27*(5), 603-612.

Bernasconi, S. M., Müller, I. A., Bergmann, K. D., Breitenbach, S. F. M., Fernandez, A., Hodell, D. A., Jaggi, M., Meckler, A. N., Millan, I., & Ziegler, M. (2018). Reducing uncertainties in carbonate clumped isotope analysis through consistent carbonate-based standardization. *Geochemistry, Geophysics, Geosystems, 19*(9), 2895-2914.

Berner, R. A., & Kothavala, Z. (2001). GEOCARB III: A revised model of atmospheric CO_2 over phanerozoic time. *American Journal of Science, 301*(2), 182-204.

Bice, K. L., Huber, B. T., & Norris, R. D. (2003). Extreme polar warmth during the Cretaceous greenhouse? Paradox of the late Turonian $\delta^{18}O$ record at Deep Sea Drilling Project Site 511. *Paleoceanography, 18*(2), 1-7.

Bigeleisen, J. (1955). Statistical Mechanics of Isotopic Systems with Small Quantum Corrections. I. General Considerations and the Rule of the Geometric Mean. *The Journal of Chemical Physics, 23*(12), 2264-2267.

Bigeleisen, J. (1965). Chemistry of Isotopes - Isotope chemistry has opened new areas of chemical physics, geochemistry, and molecular biology. *Science, 147*(3657), 463-471.

Bigeleisen, J., & Mayer, M. G. (1947). Calculation of equilibrium constants for isotopic exchange reactions. *The Journal of Chemical Physics, 15*(5), 261-267.

Bischoff, J. L. (1969). Temperature controls on aragonite-calcite transformation in aqueous solution. *The American Mineralogist, 54*, 149-155.

Bodin, S., Fiet, N., Godet, A., Matera, V., Westermann, S., Clément, A., Janssen, N. M. M., Stille, P., & Föllmi, K. B. (2009). Early Cretaceous (late Berriasian to early Aptian) palaeoceanographic change along the northwestern Tethyan margin (Vocontian Trough, southeastern France): $\delta^{13}C$, $\delta^{18}O$ and Sr-isotope belemnite and whole-rock records. *Cretaceous Research, 30*(5), 1247-1262.

Bonifacie, M., Calmels, D., Eiler, J. M., Horita, J., Chaduteau, C., Vasconcelos, C., Agrinier, P., Katz, A., Passey, B. H., Ferry, J. M.*, et al.* (2017). Calibration of the dolomite clumped isotope thermometer from 25 to 350 °C, and implications for a universal calibration for all (Ca, Mg, Fe)CO_3 carbonates. *Geochimica et Cosmochimica Acta, 200*, 255-279.

Brand, U. (1989). Aragonite-calcite transformation based on Pennsylvanian molluscs. *Geological Society of America Bulletin, 101*(3), 377-390.

Brand, U., Azmy, K., Bitner, M. A., Logan, A., Zuschin, M., Came, R., & Ruggiero, E. (2013). Oxygen isotopes and $MgCO_3$ in brachiopod calcite and a new paleotemperature equation. *Chemical Geology, 359*, 23-31.

Brand, U., Azmy, K., Griesshaber, E., Bitner, M. A., Logan, A., Zuschin, M., Ruggiero, E., & Colin, P. L. (2015). Carbon isotope composition in modern brachiopod calcite: A case of equilibrium with seawater? *Chemical Geology, 411*, 81-96.

Brand, U., Came, R. E., Affek, H., Azmy, K., Mooi, R., & Layton, K. (2014). Climate-forced change in Hudson Bay seawater composition and temperature, Arctic Canada. *Chemical Geology, 388*, 78-86.

Brand, U., & Veizer, J. (1980). Chemical diagenesis of a multicomponent carbonate system – 1: Trace Elements. *Journal of Sedimentary Petrology, 50*(4), 1219-1236.

Brand, U., Webster, G. D., Azmy, K., & Logan, A. (2007). Bathymetry and productivity of the southern Great Basin seaway, Nevada, USA: An evaluation of isotope and trace element chemistry in mid-Carboniferous and modern brachiopods. *Palaeogeography, Palaeoclimatology, Palaeoecology, 256*(3-4), 273-297.

Brand, W. A., Assonov, S. S., & Coplen, T. B. (2010). Correction for the ^{17}O interference in $\delta(^{13}C)$ measurements when analyzing CO_2 with stable isotope mass spectrometry (IUPAC Technical Report). *Pure and Applied Chemistry, 82*(8), 1719-1733.

Brenner, D. C., Passey, B. H., & Stolper, D. A. (2018). Influence of water on clumped-isotope bond reordering kinetics in calcite. *Geochimica et Cosmochimica Acta, 224*, 42-63.

Brey, T., Peck, L. S., Gutt, J., Hain, S., & Arntz, W. E. (1995). Population dynamics of *Magellania fragilis,* a brachiopod dominating a mixed-bottom macrobenthic assemblage on the Antarctic shelf. *Journal of the Marine Biological Association of the United Kingdom, 75*(4), 857-869.

Brigaud, B., Pucéat, E., Pellenard, P., Vincent, B., & Joachimski, M. M. (2008). Climatic fluctuations and seasonality during the Late Jurassic (Oxfordian–Early Kimmeridgian) inferred from $\delta^{18}O$ of Paris Basin oyster shells. *Earth and Planetary Science Letters, 273*(1-2), 58-67.

Brock, T., D. (1967). Life at high temperatures. *Science, 158*(3804), 1012-1019.

Burgener, L., Hyland, E., Huntington, K. W., Kelson, J. R., & Sewall, J. O. (2019). Revisiting the equable climate problem during the Late Cretaceous greenhouse using paleosol carbonate clumped isotope temperatures from the Campanian of the Western Interior Basin, USA. *Palaeogeography, Palaeoclimatology, Palaeoecology, 516*, 244-267.

Bushnev, D. A., Shchepetova, E. V., & Lyyurov, S. V. (2006). Organic geochemistry of Oxfordian carbon-rich sedimentary rocks of the Russian plate. *Lithology and Mineral Resources, 41*(5), 423-434.

Butler, S., Bailey, T. R., Lear, C. H., Curry, G. B., Cherns, L., & McDonald, I. (2015). The Mg/Ca–temperature relationship in brachiopod shells: Calibrating a potential palaeoseasonality proxy. *Chemical Geology, 397*, 106-117.

Came, R. E., Brand, U., & Affek, H. P. (2014). Clumped isotope signatures in modern brachiopod carbonate. *Chemical Geology, 377*, 20-30.

Came, R. E., Eiler, J. M., Veizer, J., Azmy, K., Brand, U., & Weidman, C. R. (2007). Coupling of surface temperatures and atmospheric CO_2 concentrations during the Palaeozoic era. *Nature, 449*(7159), 198-201.

Cantrill, D. J. (1998). Early Cretaceous fern foliage from President Head, Snow Island, Antarctica. *Alcheringa: An Australasian Journal of Palaeontology, 22*(3), 241-258.

Carpenter, S. J., & Lohmann, K. C. (1995). $\delta^{18}O$ and $\delta^{13}C$ values of modern brachiopod shells. *Geochimica et Cosmochimica Acta, 59*(18), 3749-3764.

Chang, T. L., & Li, W. J. (1990). A calibrated measurement of the atomic weight of carbon. *Chinese Science Bulletin, 35*(4), 290-296.

Chaudhuri, P., & Marron, J. S. (1999). SiZer for exploration of structures in curves. *Journal of the American Statistical Association, 94*(447), 807-823.

Chen, S., Gagnon, A. C., & Adkins, J. F. (2018). Carbonic anhydrase, coral calcification and a new model of stable isotope vital effects. *Geochimica et Cosmochimica Acta*.

Cochran, J. K., Kallenberg, K., Landman, N. H., Harries, P. J., Weinreb, D., Turekian, K. K., Beck, A., & Cobban, W. A. (2010). Effect of diagenesis on the Sr, O, and C Isotope composition of Late Cretaceous mollusks from the Western Interior Seaway of North America. *American Journal of Science, 310*(2), 69-88.

Cochran, J. K., Landman, N. H., Turekian, K. K., Michard, A., & Schrag, D. P. (2003). Paleoceanography of the Late Cretaceous (Maastrichtian) Western Interior Seaway of North America: evidence from Sr and O isotopes. *Palaeogeography, Palaeoclimatology, Palaeoecology, 191*(1), 45-64.

Colpaert, C., Nikitenko, B., Khafaeva, S., & Wall, A. F. (2016). The evolution of Late Callovian to Early Kimmeridgian foraminiferal associations from the central part of the Russian Sea (Makar'yev section, Volga River Basin, Russia). *Palaeogeography, Palaeoclimatology, Palaeoecology, 451*, 97-109.

Company, M., & Tavera, J. M. (2015). Lower Valanginian ammonite biostratigraphy in the Subbetic Domain (Betic Cordillera, southeastern Spain). *Carnets de Géologie, 15*(8), 71-88.

Coogan, L. A., Daëron, M., & Gillis, K. M. (2019). Seafloor weathering and the oxygen isotope ratio in seawater: Insight from whole-rock $\delta^{18}O$ and carbonate $\delta^{18}O$ and Δ_{47} from the Troodos ophiolite. *Earth and Planetary Science Letters, 508*, 41-50.

Coplen, T. B. (2007). Calibration of the calcite–water oxygen-isotope geothermometer at Devils Hole, Nevada, a natural laboratory. *Geochimica et Cosmochimica Acta, 71*(16), 3948–3957.

Coplen, T. B., Kendall, C., & Hopple, J. (1983). Comparison of stable isotope reference samples. *Nature, 302*(5905), 236-238.

Craig, H., & Gordon, L. I. (1965). Deuterium and oxygen 18 variations in the ocean and the marine atmosphere. In E. Tongiorgi (Ed.), *Proceedings of the Spoleto Conference on Stable Isotopes in Oceanographic Studies and Paleotemperatures* (pp. 9-130). Pisa: Consiglio Nazionale delle Ricerche, Laboratorio de Geologia Nucleare.

Cummins, R. C., Finnegan, S., Fike, D. A., Eiler, J. M., & Fischer, W. W. (2014). Carbonate clumped isotope constraints on Silurian ocean temperature and seawater $\delta^{18}O$. *Geochimica et Cosmochimica Acta, 140*, 241-258.

Curry, G. B., & Brunton, C. H. C. (2007). Stratigraphic distribution of brachiopods. In P. A. Selden (Ed.), *Treatise on Invertebrate Paleontology. Part H, Brachiopoda (Revised)* (pp. 2901-3081). Boulder, CO, USA and Lawrence, KS, USA: Geological Society of America, University of Kansas.

Cusack, M., Huerta, A. P., & EIMF. (2012). Brachiopods recording seawater temperature - A matter of class or maturation? *Chemical Geology, 334*, 139-143.

Daëron, M., Blamart, D., Peral, M., & Affek, H. P. (2016). Absolute isotopic abundance ratios and the accuracy of Δ_{47} measurements. *Chemical Geology, 442*, 83-96.

Daëron, M., Drysdale, R. N., Peral, M., Huyghe, D., Blamart, D., Coplen, T. B., Lartaud, F., & Zanchetta, G. (2019). Most Earth-surface calcites precipitate out of isotopic equilibrium. *Nature Communications, 10*(429), 1-7.

Dauphin, Y., & Denis, A. (1990). Analyse microstructurale des tests de mollusques du Callovien de Lukow (Pologne) – Comparaison de l'etat de conservation de quelques types structuraux majeurs. *Revue de Paléobiologie, 9*, 27-36.

Davies, A. J., & John, C. M. (2019). The clumped (^{13}C-^{18}O) isotope composition of echinoid calcite: further evidence for "vital effects" in the clumped isotope proxy. *Geochimica et Cosmochimica Acta, 245*, 172-189.

de Bar, M. W., de Nooijer, L. J., Schouten, S., Ziegler, M., Sluijs, A., & Reichart, G. J. (2019). Comparing sea water temperature proxy records for the past 90 Myrs from the shallow shelf record Bass River, New Jersey. *Paleoceanography and Paleoclimatology*.

DeConto, R. M., & Pollard, D. (2003). Rapid Cenozoic glaciation of Antarctica induced by declining atmospheric CO_2. *Nature, 421*(6920), 245-249.

Defliese, W. F., Hren, M. T., & Lohmann, K. C. (2015). Compositional and temperature effects of phosphoric acid fractionation on Δ_{47} analysis and implications for discrepant calibrations. *Chemical Geology, 396*, 51-60.

Defliese, W. F., & Lohmann, K. C. (2015). Non-linear mixing effects on mass-47 CO_2 clumped isotope thermometry: Patterns and implications. *Rapid Communications in Mass Spectrometry, 29*(9), 901-909.

Dennis, K. J., Affek, H. P., Passey, B. H., Schrag, D. P., & Eiler, J. M. (2011). Defining an absolute reference frame for 'clumped' isotope studies of CO_2. *Geochimica et Cosmochimica Acta, 75*(22), 7117-7131.

Dennis, K. J., & Schrag, D. P. (2010). Clumped isotope thermometry of carbonatites as an indicator of diagenetic alteration. *Geochimica et Cosmochimica Acta, 74*(14), 4110-4122.

DePaolo, D. J. (2011). Surface kinetic model for isotopic and trace element fractionation during precipitation of calcite from aqueous solutions. *Geochimica et Cosmochimica Acta, 75*(4), 1039-1056.

Dera, G., Brigaud, B., Monna, F., Laffont, R., Puceat, E., Deconinck, J. F., Pellenard, P., Joachimski, M. M., & Durlet, C. (2011). Climatic ups and downs in a disturbed Jurassic world. *Geology, 39*(3), 215-218.

Dera, G., Prunier, J., Smith, P. L., Haggart, J. W., Popov, E., Guzhov, A., Rogov, M., Delsate, D., Thies, D., Cuny, G., *et al.* (2015). Nd isotope constraints on ocean circulation,

paleoclimate, and continental drainage during the Jurassic breakup of Pangea. *Gondwana Research, 27*(4), 1599-1615.

Dercourt, J., Gaetani, M., & Vrielynck, B. (Eds.). (2000). *Atlas Peri-Tethys Palaeogeographical Maps*: CCGM.

Devriendt, L. S., Watkins, J. M., & McGregor, H. V. (2017). Oxygen isotope fractionation in the $CaCO_3$–DIC–H_2O system. *Geochimica et Cosmochimica Acta, 214*, 115-142.

Dickson, J. A. D. (2004). Echinoderm skeletal preservation: Calcite-aragonite seas and the Mg/Ca ratio of Phanerozoic oceans. *Journal of Sedimentary Research, 74*(3), 355-365.

Dietzel, M., Tang, J. W., Leis, A., & Kohler, S. J. (2009). Oxygen isotopic fractionation during inorganic calcite precipitation - Effects of temperature, precipitation rate and pH. *Chemical Geology, 268*(1-2), 107-115.

Ditchfield, P. W. (1997). High northern palaeolatitude Jurassic-Cretaceous palaeotemperature variation: new data from Kong Karls Land, Svalbard. *Palaeogeography, Palaeoclimatology, Palaeoecology, 130*(1-4), 163-175.

Dobretsov, N. L., Polyansky, O. P., Reverdatto, V. V., & Babichev, A. V. (2013). Dynamics of the Arctic and adjacent petroleum basins: a record of plume and rifting activity. *Russian Geology and Geophysics, 54*(8), 888-902.

Dodd, J. R., & Crisp, E. L. (1982). Non-linear variation with salinity of Sr/Ca and Mg/Ca ratios in water and aragonitic bivalve shells and implications for paleosalinity studies. *Palaeogeography, Palaeoclimatology, Palaeoecology, 38*(1-2), 45-56.

Doherty, P. J. (1979). Demographic study of a subtidal population of the New Zealand articulate brachiopod *Terebratella inconspicua*. *Marine Biology, 52*(4), 331-342.

Donnadieu, Y., Puceat, E., Moiroud, M., Guillocheau, F., & Deconinck, J. F. (2016). A better-ventilated ocean triggered by Late Cretaceous changes in continental configuration. *Nature Communications, 7*(10316), 1-12.

Douglas, J. G., & Williams, G. E. (1982). Southern polar forests: The Early Cretaceous floras of Victoria and their palaeoclimatic significance. *Palaeogeography, Palaeoclimatology, Palaeoecology, 39*(3-4), 171-185.

Dromart, G., Garcia, J. P., Gaumet, F., Picard, S., Rousseau, M., Atrops, F., Lecuyer, C., & Sheppard, S. M. F. (2003). Perturbation of the carbon cycle at the Middle/Late Jurassic transition: Geological and geochemical evidence. *American Journal of Science, 303*(8), 667-707.

Eagle, R. A., Tütken, T., Martin, T. S., Tripati, A. K., Fricke, H. C., Connely, M., Cifelli, R. L., & Eiler, J. M. (2011). Dinosaur body temperatures determined from isotopic (13C-18O) ordering in fossil biominerals. *Science, 333*(6041), 443-445.

Eiler, J. M. (2007). “Clumped-isotope” geochemistry—The study of naturally-occurring, multiply-substituted isotopologues. *Earth and Planetary Science Letters, 262*(3-4), 309-327.

Eiler, J. M. (2011). Paleoclimate reconstruction using carbonate clumped isotope thermometry. *Quaternary Science Reviews, 30*(25-26), 3575-3588.

Eiler, J. M., & Schauble, E. (2004). $^{18}O^{13}C^{16}O$ in Earth’s atmosphere. *Geochimica et Cosmochimica Acta, 68*(23), 4767-4777.

Epstein, S., Buchsbaum, R., Lowenstam, H., & Urey, H. C. (1951). Carbonate-water isotopic temperature scale. *Geological Society of America Bulletin, 62*(4), 417-426.

Epstein, S., Buchsbaum, R., Lowenstam, H. A., & Urey, H. C. (1953). Revised carbonate-water isotopic temperature scale. *Geological Society of America Bulletin, 64*(11), 1315-1326.

Erbacher, J., Friedrich, O., Wilson, P. A., Lehmann, J., & Weiss, W. (2011). Short-term warming events during the boreal Albian (mid-Cretaceous). *Geology, 39*(3), 223-226.

Evans, D., Sagoo, N., Renema, W., Cotton, L. J., Müller, W., Todd, J. A., Saraswati, P. K., Stassen, P., Ziegler, M., Pearson, P. N., *et al.* (2018). Eocene greenhouse climate revealed by coupled clumped isotope-Mg/Ca thermometry. *Proceedings of the National Academy of Sciences of the United States of America, 115*(6), 1174-1179.

Fernandez, A., Müller, I. A., Rodríguez-Sanz, L., van Dijk, J., Looser, N., & Bernasconi, S. M. (2017). A reassessment of the precision of carbonate clumped isotope measurements: Implications for calibrations and paleoclimate reconstructions. *Geochemistry, Geophysics, Geosystems, 18*, 1-12.

Fiebig, J., Bajnai, D., Löffler, N., Methner, K., Krsnik, E., Mulch, A., & Hofmann, S. (in review). High-precision Δ_{48} and Δ_{47} analysis of carbonates using a Thermo Scientific™ 253 Plus™ gas source mass spectrometer. *Chemical Geology*.

Fiebig, J., Hofmann, S., Niklas, L., Lüdecke, T., Methner, K., & Wacker, U. (2016). Slight pressure imbalances can affect accuracy and precision of dual inlet-based clumped isotope analysis. *Isotopes in Environmental and Health Studies, 52*(1-2), 12-28.

Foster, G. L., Royer, D. L., & Lunt, D. J. (2017). Future climate forcing potentially without precedent in the last 420 million years. *Nature Communications, 8*(14845), 1-8.

Föllmi, K. B. (2012). Early Cretaceous life, climate and anoxia. *Cretaceous Research, 35*, 230-257.

Frakes, L. A. (1979). *Climates throughout geologic time*. Amsterdam: Elsevier.

Frakes, L. A., & Francis, J. E. (1988). A guide to Phanerozoic cold polar climates from high-latitude ice-rafting in the Cretaceous. *Nature, 333*(6173), 547-549.

Francis, J. E., & Poole, I. (2002). Cretaceous and early Tertiary climates of Antarctica: Evidence from fossil wood. *Palaeogeography, Palaeoclimatology, Palaeoecology, 182*(1-2), 47-64.

Freitas, P. S., Clarke, L. J., Kennedy, H., & Richardson, C. A. (2012). The potential of combined Mg/Ca and $\delta^{18}O$ measurements within the shell of the bivalve *Pecten maximus* to estimate seawater $\delta^{18}O$ composition. *Chemical Geology, 291*, 286-293.

Friedman, I., & O'Neil, J. R. (1977). Compilation of stable isotope fractionation factors of geochemical interest *Geochemical Survey Professional Paper* (6th ed., Vol. 440-KK, pp. KK1-KK12).

Galeotti, S., Rusciadelli, G., Sprovieri, M., Lanci, L., Gaudio, A., & Pekar, S. (2009). Sea-level control on facies architecture in the Cenomanian–Coniacian Apulian margin (Western Tethys): A record of glacio-eustatic fluctuations during the Cretaceous greenhouse? *Palaeogeography, Palaeoclimatology, Palaeoecology, 276*(1-4), 196-205.

Ghosh, P., Adkins, J., Affek, H., Balta, B., Guo, W., Schauble, E. A., Schrag, D., & Eiler, J. M. (2006). ^{13}C–^{18}O bonds in carbonate minerals: A new kind of paleothermometer. *Geochimica et Cosmochimica Acta, 70*(6), 1439-1456.

Głowniak, E., Kiselev, D. N., Rogov, M., Wierzbowski, A., & Wright, J. K. (2010). The Middle Oxfordian to lowermost Kimmeridgian ammonite succession at Mikhalenino (Kostroma District) of the Russian Platform, and its stratigraphical and palaeobiogeographical importance. *Volumina Jurassica, 8*(1), 5-48.

Gómez Dacal, A. R., Richiano, S. M., Gómez Peral, L. E., Spalletti, L. A., Sial, A. N., & Poiré, D. G. (2019). Evidence of warm seas in high latitudes of southern South America during the Early Cretaceous. *Cretaceous Research, 95*, 8-20.

Grasby, S. E., McCune, G. E., Beauchamp, B., & Galloway, J. M. (2017). Lower Cretaceous cold snaps led to widespread glendonite occurrences in the Sverdrup Basin, Canadian High Arctic. *Geological Society of America Bulletin, 129*(7-8), 771-787.

Grauel, A.-L., Schmid, T. W., Hu, B., Bergami, C., Capotondi, L., Zhou, L., & Bernasconi, S. M. (2013). Calibration and application of the 'clumped isotope' thermometer to foraminifera for high-resolution climate reconstructions. *Geochimica et Cosmochimica Acta, 108*, 125-140.

Grossman, E. L. (1987). Stable isotopes in modern benthic foraminifera; a study of vital effect. *Journal of Foraminiferal Research, 17*(1), 48-61.

Grossman, E. L., & Ku, T. L. (1986). Oxygen and carbon isotope fractionation in biogenic aragonite: Temperature effects. *Chemical Geology, 59*(1), 59-74.

Guerra, A., & Castro, B. G. (1988). On the life cycle of *Sepia officinalis* (Cephalopoda, Sepioidea) in the ria de Vigo (NW Spain). *Cahiers de Biologie Marine, 29*, 395-405.

Guo, W., Kim, S., Thiagarajan, N., Adkins, J. F., & Eiler, J. M. (2009). *Mechanisms for "vital effects" in biogenic carbonates: New perspectives based on abundances of ^{13}C–^{18}O bonds*. Paper presented at the American Geophysical Union Fall Meeting.

Guo, W., & Zhou, C. (2019). *Δ_{48} fractionation in carbonates and its implications for clumped isotope thermometry*. Paper presented at the 7th International Clumped Isotope Workshop, Queen Mary, Long Beach, CA, USA.

Gustomesov, V. A. (1976). O pozdneyurskikh belemnitakh roda *Hibolithes* Russkoy Platformy [in Russian]. *Paleontologicheskii Zhurnal, 4*, 51-60.

Hallam, A. (1969). Faunal realms and facies in the Jurassic. *Palaeontology, 12*(1), 1-18.

Hallam, A. (2001). A review of the broad pattern of Jurassic sea-level changes and their possible causes in the light of current knowledge. *Palaeogeography, Palaeoclimatology, Palaeoecology, 167*(1-2), 23-37.

Hantzpergue, P., Baudin, F., Mitta, V., Olferiev, A., & Zakharov, V. (1998). The Upper Jurassic of the Volga basin: ammonite biostratigraphy and occurrence of organic-carbon rich facies. Correlations between boreal-subboreal and submediterranesn provinces. In S. Crasquin-Soleau & E. Barrier (Eds.), *Peri-Tethys Memoir 4. Epicratonic basins of Peri-Tethyan Platforms* (pp. 9-33).

Hardie, L. A. (1996). Secular variation in seawater chemistry: An explanation for the coupled secular variation in the mineralogies of marine limestones and potash evaporites over the past 600 m.y. *Geology, 24*(3), 279-283.

Hay, W. W., Migdisov, A., Balukhovsky, A. N., Wold, C. N., Flögel, S., & Söding, E. (2006). Evaporites and the salinity of the ocean during the Phanerozoic: Implications for climate, ocean circulation and life. *Palaeogeography, Palaeoclimatology, Palaeoecology, 240*(1-2), 3-46.

He, B., Olack, G. A., & Colman, A. S. (2012). Pressure baseline correction and high-precision CO_2 clumped-isotope (Δ_{47}) measurements in bellows and micro-volume modes. *Rapid Communications in Mass Spectrometry, 26*(24), 2837-2853.

Henkes, G. A., Passey, B. H., Grossman, E. L., Shenton, B. J., Perez-Huerta, A., & Yancey, T. E. (2014). Temperature limits for preservation of primary calcite clumped isotope paleotemperatures. *Geochimica et Cosmochimica Acta, 139*, 362-382.

Henkes, G. A., Passey, B. H., Grossman, E. L., Shenton, B. J., Yancey, T. E., & Pérez-Huerta, A. (2018). Temperature evolution and the oxygen isotope composition of Phanerozoic

oceans from carbonate clumped isotope thermometry. *Earth and Planetary Science Letters, 490*, 40-50.

Henkes, G. A., Passey, B. H., Wanamaker, A. D., Grossman, E. L., Ambrose, W. G., & Carroll, M. L. (2013). Carbonate clumped isotope compositions of modern marine mollusk and brachiopod shells. *Geochimica et Cosmochimica Acta, 106*, 307-325.

Hermoso, M., Horner, T. J., Minoletti, F., & Rickaby, R. E. M. (2014). Constraints on the vital effect in coccolithophore and dinoflagellate calcite by oxygen isotopic modification of seawater. *Geochimica et Cosmochimica Acta, 141*, 612-627.

Hill, P. S., Tripati, A. K., & Schauble, E. A. (2014). Theoretical constraints on the effects of pH, salinity, and temperature on clumped isotope signatures of dissolved inorganic carbon species and precipitating carbonate minerals. *Geochimica et Cosmochimica Acta, 125*, 610-652.

Hoffmann, R., Richter, D. K., Neuser, R. D., Jöns, N., Linzmeier, B. J., Lemanis, R. E., Fusseis, F., Xiao, X., & Immenhauser, A. (2016). Evidence for a composite organic–inorganic fabric of belemnite rostra: Implications for palaeoceanography and palaeoecology. *Sedimentary Geology, 341*, 203-215.

Holliday, D. W. (1999). Palaeotemperatures, thermal modelling and depth of burial studies in northern and eastern England. *Proceedings of the Yorkshire Geological Society, 52*, 337-352.

Hollis, C. J., Handley, L., Crouch, E. M., Morgans, H. E. G., Baker, J. A., Creech, J., Collins, K. S., Gibbs, S. J., Huber, M., Schouten, S.*, et al.* (2009). Tropical sea temperatures in the high-latitude South Pacific during the Eocene. *Geology, 37*(2), 99-102.

Hollis, C. J., Taylor, K. W. R., Handley, L., Pancost, R. D., Huber, M., Creech, J. B., Hines, B. R., Crouch, E. M., Morgans, H. E. G., Crampton, J. S.*, et al.* (2012). Early Paleogene temperature history of the Southwest Pacific Ocean: Reconciling proxies and models. *Earth and Planetary Science Letters, 349-350*, 53-66.

Hotinski, R. M., & Toggweiler, J. R. (2003). Impact of a Tethyan circumglobal passage on ocean heat transport and "equable" climates. *Paleoceanography, 18*(1), 1-15.

Huber, B. T., Hodell, D. A., & Hamilton, C. P. (1995). Middle-Late Cretaceous climate of the southern high latitudes: Stable isotopic evidence for minimal equator-to-pole thermal gradients. *Geological Society of America Bulletin, 107*(10), 1164-1191.

Huber, M., & Caballero, R. (2011). The early Eocene equable climate problem revisited. *Climate of the Past, 7*(2), 603-633.

Hughes, W. W., Rosenberg, G. D., & Tkachuck, R. D. (1988). Growth increments in the shell of the living brachiopod *Terebratalia transversa*. *Marine Biology, 98*(4), 511-518.

Huntington, K. W., Eiler, J. M., Affek, H. P., Guo, W., Bonifacie, M., Yeung, L. Y., Thiagarajan, N., Passey, B., Tripati, A., Daeron, M., *et al.* (2009). Methods and limitations of 'clumped' CO_2 isotope (Δ_{47}) analysis by gas-source isotope ratio mass spectrometry. *Journal of Mass Spectrometry, 44*(9), 1318-1329.

Hurum, J. H., Milan, J., Hammer, O., Midtkandal, I., Amundsen, H., & Saether, B. (2006). Tracking polar dinosaurs - new finds from the Lower Cretaceous of Svalbard. *Norwegian Journal of Geology, 86*(4), 397-402.

Imai, N., Terashima, S., Itoh, S., & Ando, A. (1996). 1996 compilation of analytical data on nine GSJ geochemical reference samples, "Sedimentary rock series". *Geostandards Newsletter, 20*(2), 165-216.

Jackson, D. J., Mann, K., Haussermann, V., Schilhabel, M. B., Luter, C., Griesshaber, E., Schmahl, W., & Worheide, G. (2015). The *Magellania venosa* biomineralizing proteome: A window into brachiopod shell evolution. *Genome Biology and Evolution, 7*(5), 1349-1362.

Jaffrés, J. B. D., Shields, G. A., & Wallmann, K. (2007). The oxygen isotope evolution of seawater: A critical review of a long-standing controversy and an improved geological water cycle model for the past 3.4 billion years. *Earth-Science Reviews, 83*(1-2), 83-122.

Janssen, N. M. M. (2003). Mediterranean Neocomian belemnites, part 2: The Berriasian-Valanginian boundary in southeast Spain (Río Argos, Cañada Lengua and Tornajo). *Scripta Geologica, 126*, 121-183.

Jean, C. B., Kyser, T. K., James, N. P., & Stokes, M. D. (2015). The Antarctic brachiopod *Liothyrella uva* as a proxy for ambient oceanographic conditions at McMurdo Sound. *Journal of Sedimentary Research, 85*(12), 1492-1509.

Jeletzky, J. A. (1983). Macroinvertebrate paleontology, biochronology, and paleoenvironments of Lower Cretaceous and Upper Jurassic rocks Deep Sea Drilling Hole 511, eastern Falkland Plateau. *Initial Reports of the Deep Sea Drilling Project, 71*(Part F: Paleontology), 951-975.

Jenkyns, H. C., Forster, A., Schouten, S., & Sinninghe Damsté, J. S. (2004). High temperatures in the late Cretaceous Arctic Ocean. *Nature, 432*(7019), 888-892.

Jenkyns, H. C., Schouten-Huibers, L., Schouten, S., & Sinninghe Damsté, J. S. (2012). Warm Middle Jurassic–Early Cretaceous high-latitude sea-surface temperatures from the Southern Ocean. *Climate of the Past, 8*(1), 215-226.

Jiménez-López, C., Romanek, C. S., Huertas, F. J., Ohmoto, H., & Caballero, E. (2004). Oxygen isotope fractionation in synthetic magnesian calcite. *Geochimica et Cosmochimica Acta, 68*(16), 3367-3377.

John, C. M., & Bowen, D. (2016). Community software for challenging isotope analysis: First applications of 'Easotope' to clumped isotopes. *Rapid Communications in Mass Spectrometry, 30*(21), 2285-2300.

Johnson, K. S. (1982). Carbon dioxide hydration and dehydration kinetics in seawater. *Limnology and Oceanography, 27*(5), 894-855.

Keith, M. L., & Weber, J. N. (1965). Systematic relationships between carbon and oxygen isotopes in carbonates deposited by modern corals and algae. *Science, 150*(3695), 498-501.

Kele, S., & Bajnai, D. (2017). Kapcsolt izotópok (clumped isotopes) a földtudományi kutatásokban *[Clumped isotopes in geoscience research]*. *Földtani Közlöny, 147*(2), 177-194.

Kele, S., Breitenbach, S. F. M., Capezzuoli, E., Nele Meckler, A., Ziegler, M., Millan, I. M., Kluge, T., Deák, J., Hanselmann, K., John, C. M.*, et al.* (2015). Temperature dependence of oxygen- and clumped isotope fractionation in carbonates: a study of travertines and tufas in the 6–95 °C temperature range. *Geochimica et Cosmochimica Acta, 168*, 172-192.

Kelson, J. R., Huntington, K. W., Schauer, A. J., Saenger, C., & Lechler, A. R. (2017). Toward a universal carbonate clumped isotope calibration: Diverse synthesis and preparatory methods suggest a single temperature relationship. *Geochimica et Cosmochimica Acta, 197*, 104-131.

Kiehl, J. T., & Shields, C. A. (2013). Sensitivity of the Palaeocene-Eocene Thermal Maximum climate to cloud properties. *Philos Trans A Math Phys Eng Sci, 371*(2001), 20130093.

Kim, J.-H., Romero, O. E., Lohmann, G., Donner, B., Laepple, T., Haam, E., & Sinninghe Damsté, J. S. (2012). Pronounced subsurface cooling of North Atlantic waters off Northwest Africa during Dansgaard–Oeschger interstadials. *Earth and Planetary Science Letters, 339-340*, 95-102.

Kim, J.-H., van der Meer, J., Schouten, S., Helmke, P., Willmott, V., Sangiorgi, F., Koç, N., Hopmans, E. C., & Damsté, J. S. S. (2010). New indices and calibrations derived from the distribution of crenarchaeal isoprenoid tetraether lipids: Implications for past sea surface temperature reconstructions. *Geochimica et Cosmochimica Acta, 74*(16), 4639-4654.

Kim, S.-T., Mucci, A., & Taylor, B. E. (2007). Phosphoric acid fractionation factors for calcite and aragonite between 25 and 75 °C: Revisited. *Chemical Geology, 246*(3-4), 135-146.

Kim, S.-T., & O'Neil, J. R. (1997). Equilibrium and nonequilibrium oxygen isotope effects in synthetic carbonates. *Geochimica et Cosmochimica Acta, 61*(16), 3461-3475.

Kimball, J., Eagle, R., & Dunbar, R. (2016). Carbonate "clumped" isotope signatures in aragonitic scleractinian and calcitic gorgonian deep-sea corals. *Biogeosciences, 13*(23), 6487-6505.

Kısakürek, B., Eisenhauer, A., Böhm, F., Garbe-Schönberg, D., & Erez, J. (2008). Controls on shell Mg/Ca and Sr/Ca in cultured planktonic foraminiferan, *Globigerinoides ruber* (white). *Earth and Planetary Science Letters, 273*(3-4), 260-269.

Kiselev, D., Rogov, M., Glinskikh, L., Guzhikov, A., Pimenov, M., Mikhailov, A., Dzyuba, O., Matveev, A., & Tesakova, E. (2013). Integrated stratigraphy of the reference sections for the Callovian-Oxfordian boundary in European Russia. *Volumina Jurassica, 11*, 59–96.

Klett, T. R., Wandrey, C. J., & Pitman, J. K. (2011). Geology and petroleum potential of the north and east margins of the Siberian Craton, north of the Arctic Circle. *Arctic Petroleum Geology, 35*, 413-431.

Klug, C., Schweigert, G., Fuchs, D., Kruta, I., & Tischlinger, H. (2016). Adaptations to squid-style high-speed swimming in Jurassic belemnitids. *Biology Letters, 12*(20150877), 1-5.

Korte, C., Hesselbo, S. P., Ullmann, C. V., Dietl, G., Ruhl, M., Schweigert, G., & Thibault, N. (2015). Jurassic climate mode governed by ocean gateway. *Nature Communications, 6*(10015), 1-7.

Kump, L. R., & Pollard, D. (2008). Amplification of Cretaceous warmth by biological cloud feedbacks. *Science, 320*(5873), 195.

Langseth, M. G., & Ludwig, W. J. (1983). A heat flow measurement on the Falkland Plateau. *Deep Sea Drilling Project Initial Reports, 71*, 299-303.

Lea, D. W., Mashiotta, T. A., & Spero, H. J. (1999). Controls on magnesium and strontium uptake in planktonic foraminifera determined by live culturing. *Geochimica et Cosmochimica Acta, 63*(16), 2369-2379.

Lécuyer, C., Picard, S., Garcia, J.-P., Sheppard, S. M. F., Grandjean, P., & Dromart, G. (2003). Thermal evolution of Tethyan surface waters during the Middle-Late Jurassic: Evidence from $\delta^{18}O$ values of marine fish teeth. *Paleoceanography, 18*(3), 1-16.

Lee, D. E., Robinson, J. H., Witman, J. D., Copeland, S. E., Harper, E. M., Smith, F., & Lamare, M. D. (2010). Observations on recruitment, growth and ecology in a diverse living

brachiopod community, Doubtful Sound, Fiordland, New Zealand. *Special Papers in Palaeontology, 84*, 177-191.

LeGrande, A. N., & Schmidt, G. A. (2006). Global gridded data set of the oxygen isotopic composition in seawater. *Geophysical Research Letters, 33*(12), 1-5.

Leider, A., Hinrichs, K.-U., Mollenhauer, G., & Versteegh, G. J. M. (2010). Core-top calibration of the lipid-based $U_{37}^{K'}$ and TEX_{86} temperature proxies on the southern Italian shelf (SW Adriatic Sea, Gulf of Taranto). *Earth and Planetary Science Letters, 300*(1-2), 112-124.

Levitt, N. P., Eiler, J. M., Romanek, C. S., Beard, B. L., Xu, H., & Johnson, C. M. (2018). Near equilibrium ^{13}C-^{18}O bonding during inorganic calcite precipitation under chemo-stat conditions. *Geochemistry, Geophysics, Geosystems, 19*(3), 901-920.

Lindquist, S. J. (1999). The Timan-Pechora Basin province of northwest Arctic Russia; Domanik, Paleozoic total petroleum system. *USGS Open-File Report, 99-50*, 1-24.

Littler, K., Robinson, S. A., Bown, P. R., Nederbragt, A. J., & Pancost, R. D. (2011). High sea-surface temperatures during the Early Cretaceous Epoch. *Nature Geoscience, 4*(3), 169-172.

Locarnini, R. A., Mishonov, A. V., Antonov, J. I., Boyer, T. P., Garcia, H. E., Baranova, O. K., Zweng, M. M., Paver, C. R., Reagan, J. R., Johnson, D. R., *et al.* (2013). *World Ocean Atlas 2013, Volume 1: Temperature*.

Lorrain, A., Gillikin, D. P., Paulet, Y.-M., Chauvaud, L., Mercier, A. L., Navez, J., & André, L. (2005). Strong kinetic effects on Sr/Ca ratios in the calcitic bivalve *Pecten maximus*. *Geology, 33*(12), 965-968.

Lowenstam, H. A. (1961). Mineralogy, O^{18}/O^{16} ratios, and strontium and magnesium contents of recent and fossil brachiopods and their bearing on the history of the oceans. *The Journal of Geology, 69*(3), 241-260.

Loyd, S. J., Sample, J., Tripati, R. E., Defliese, W. F., Brooks, K., Hovland, M., Torres, M., Marlow, J., Hancock, L. G., Martin, R., *et al.* (2016). Methane seep carbonates yield clumped isotope signatures out of equilibrium with formation temperatures. *Nature Communications, 7*(12274), 1-12.

Löffler, N., Fiebig, J., Mulch, A., Tütken, T., Schmidt, B. C., Bajnai, D., Conrad, A. C., Wacker, U., & Böttcher, M. E. (2019). Refining the temperature dependence of the oxygen and clumped isotopic compositions of structurally bound carbonate in apatite. *Geochimica et Cosmochimica Acta, 253*, 19-38.

Lukeneder, A. (2005). First nearly complete skeleton of the Cretaceous duvaliid belemnite Conobelus. *Acta Geologica Polonica, 55*(2), 147-162.

Lunt, D. J., Farnsworth, A., Loptson, C., Foster, G. L., Markwick, P., apos, Brien, C. L., Pancost, R. D., Robinson, S. A., & Wrobel, N. (2016). Palaeogeographic controls on climate and proxy interpretation. *Climate of the Past, 12*(5), 1181-1198.

Lyyurov, S. V. (1996). *Yurskie otlozheniya severa Russkoy plity [Jurassic deposits north to the Russian plate]*. Yekaterinburg, Russia: UrO RAN.

Magnum, C. P. (1991). Salt sensitivity of the hemocyanin of eury- and stenohaline squids. *Comparative Biochemistry and Physiology Part A: Physiology, 99*(1-2), 159-161.

Malkoč, M., & Mutterlose, J. (2010). The Early Barremian warm pulse and the Late Barremian cooling: A high-resolution geochemical record of the Boreal realm. *Palaios, 25*(1), 14-23.

Mangold, K., & Boletzky, S. (1988). Mediterranean Cephalopod Fauna. In E. R. Trueman & M. R. Clarke (Eds.), *Paleontology and Neontology of Cephalopods* (Vol. 12, pp. 315-330): Elsevier.

Marshall, J. D. (1992). Climatic and oceanographic isotopic signals from the carbonate rock record and their preservation. *Geological Magazine, 129*(2), 143-160.

Matyja, B. A., & Wierzbowski, A. (1995). Biogeographic differentiation of the Oxfordian and Early Kimmeridgian ammonite faunas of Europe, and its stratigraphic consequences. *Acta Geologica Polonica, 45*(1-2), 1-8.

Matyja, B. A., & Wierzbowski, A. (2000). Biostratigraphical correlations between the subboreal Mutabilis Zone and the submediterranean Upper Hypselocyclum – Divisum Zones of the Kimmeridgian: new data from northern Poland. In R. L. Hall & P. L. Smith (Eds.), *Advances in Jurassic Research 2000* (Vol. 6, pp. 129-136): Trans Tech Publications.

McArthur, J. M., Donovan, D. T., Thirlwall, M. F., Fouke, B. W., & Mattey, D. (2000). Strontium isotope profile of the Early Toarcian (Jurassic) Oceanic Anoxic Event, the duration of ammonite biozones, and belemnite paleotemperatures. *Earth and Planetary Science Letters, 179*, 269-285.

McArthur, J. M., Doyle, P., Leng, M. J., Reeves, K., Williams, C. T., Garcia-Sanchez, R., & Howarth, R. J. (2007a). Testing palaeo-environmental proxies in Jurassic belemnites: Mg/Ca, Sr/Ca, Na/Ca, $\delta^{18}O$ and $\delta^{13}C$. *Palaeogeography, Palaeoclimatology, Palaeoecology, 252*(3-4), 464-480.

McArthur, J. M., Janssen, N. M. M., Reboulet, S., Leng, M. J., Thirlwall, M. F., & van de Schootbrugge, B. (2007b). Palaeotemperatures, polar ice-volume, and isotope stratigraphy (Mg/Ca, $\delta^{18}O$, $\delta^{13}C$, $^{87}Sr/^{86}Sr$): The Early Cretaceous (Berriasian,

Valanginian, Hauterivian). *Palaeogeography, Palaeoclimatology, Palaeoecology, 248*(3–4), 391-430.

McArthur, J. M., Mutterlose, J., Price, G. D., Rawson, P. F., Ruffell, A., & Thirlwall, M. F. (2004). Belemnites of Valanginian, Hauterivian and Barremian age: Sr-isotope stratigraphy, composition ($^{87}Sr/^{86}Sr$, $\delta^{13}C$, $\delta^{18}O$, Na, Sr, Mg), and palaeo-oceanography. *Palaeogeography, Palaeoclimatology, Palaeoecology, 202*(3-4), 253-272.

McConnaughey, T. (1989a). ^{13}C and ^{18}O isotopic disequilibrium in biological carbonates: I. Patterns. *Geochimica et Cosmochimica Acta, 53*, 151-162.

McConnaughey, T. (1989b). ^{13}C and ^{18}O isotopic disequilibrium in biological carbonates: II. In vitro simulation of kinetic isotope effects. *Geochimica et Cosmochimica Acta, 53*, 163-171.

McCrea, J. M. (1950). On the isotopic chemistry of carbonates and a paleotemperature scale. *The Journal of Chemical Physics, 18*(6), 849-857.

Meckler, A. N., Ziegler, M., Millan, M. I., Breitenbach, S. F., & Bernasconi, S. M. (2014). Long-term performance of the KIEL Carbonate Device with a new correction scheme for clumped isotope measurements. *Rapid Communications in Mass Spectrometry, 28*(15), 1705-1715.

Merrit, D. A., & Hayes, J. M. (1994). Factors controlling precision and accuracy in isotope-ratio-monrtoring mass spectrometry. *Analytical Chemistry, 66*, 2336-2347.

Methner, K., Mulch, A., Fiebig, J., Wacker, U., Gerdes, A., Graham, S. A., & Chamberlain, C. P. (2016). Rapid Middle Eocene temperature change in western North America. *Earth and Planetary Science Letters, 450*, 132-139.

Meyer, K. W., Petersen, S. V., Lohmann, K. C., & Winkelstern, I. Z. (2018). Climate of the Late Cretaceous North American Gulf and Atlantic Coasts. *Cretaceous Research, 89*, 160-173.

Miller, K. G. (2009). Broken greenhouse windows. *Nature Geoscience, 2*(7), 465-466.

Monks, N., Hardwick, J. D., & Gale, A. S. (1996). The function of the belemnite guard. *Paläontologische Zeitschrift, 70*(3-4), 425-431.

Morgans-Bell, H. S., Coe, A. L., Hesselbo, S. P., Jenkyns, H. C., Weedon, G. P., Marshall, J. E. A., Tyson, R. V., & Williams, C. J. (2001). Integrated stratigraphy of the Kimmeridge Clay Formation (Upper Jurassic) based on exposures and boreholes in south Dorset, UK. *Geological Magazine, 138*(5), 511-539.

Mostafawi, N., Nabavi, S. M. B., & Moghaddasi, B. (2010). Ostracods from the Strait of Hormuz and Gulf of Oman, Northern Arabian Sea. *Revista Española de Micropaleontología, 42*(2), 243–265.

Mutterlose, J., Brumsack, H., Flögel, S., Hay, W., Klein, C., Langrock, U., Lipinski, M., Ricken, W., Söding, E., Stein, R.*, et al.* (2003). The Greenland-Norwegian Seaway: A key area for understanding Late Jurassic to Early Cretaceous paleoenvironments. *Paleoceanography, 18*(1), 1-26.

Mutterlose, J., Malkoc, M., Schouten, S., Sinninghe Damsté, J. S., & Forster, A. (2010). TEX_{86} and stable $\delta^{18}O$ paleothermometry of early Cretaceous sediments: Implications for belemnite ecology and paleotemperature proxy application. *Earth and Planetary Science Letters, 298*(3-4), 286–298.

Naafs, B. D. A., & Pancost, R. D. (2016). Sea-surface temperature evolution across Aptian Oceanic Anoxic Event 1a. *Geology, 44*(11), 959-962.

Norris, M. S., & Hallam, A. (1995). Facies variations across the Middle-Upper Jurassic boundary in Western Europe and the relationship to sea-level changes. *Palaeogeography, Palaeoclimatology, Palaeoecology, 116*(3-4), 189-245.

Nunn, E. V., & Price, G. D. (2010). Late Jurassic (Kimmeridgian–Tithonian) stable isotopes ($\delta^{18}O$, $\delta^{13}C$) and Mg/Ca ratios: New palaeoclimate data from Helmsdale, northeast Scotland. *Palaeogeography, Palaeoclimatology, Palaeoecology, 292*(1-2), 325-335.

Nunn, E. V., Price, G. D., Gröcke, D. R., Baraboshkin, E. Y., Leng, M. J., & Hart, M. B. (2010). The Valanginian positive carbon isotope event in Arctic Russia: Evidence from terrestrial and marine isotope records and implications for global carbon cycling. *Cretaceous Research, 31*(6), 577-592.

Nunn, E. V., Price, G. D., Hart, M. B., Page, K. N., & Leng, M. J. (2009). Isotopic signals from Callovian-Kimmeridgian (Middle-Upper Jurassic) belemnites and bulk organic carbon, Staffin Bay, Isle of Skye, Scotland. *Journal of the Geological Society, 166*(4), 633-641.

O'Brien, C. L., Robinson, S. A., Pancost, R. D., Sinninghe Damsté, J. S., Schouten, S., Lunt, D. J., Alsenz, H., Bornemann, A., Bottini, C., Brassell, S. C.*, et al.* (2017). Cretaceous sea-surface temperature evolution: Constraints from TEX_{86} and planktonic foraminiferal oxygen isotopes. *Earth-Science Reviews, 172*, 224-247.

O'Connor, L. K., Robinson, S. A., Naafs, B. D. A., Jenkyns, H. C., Henson, S., Clarke, M., & Pancost, R. D. (2019). Late Cretaceous temperature evolution of the southern high latitudes: a TEX_{86} perspective. *Paleoceanography and Paleoclimatology*.

Ogg, J. G., Ogg, G. M., & Gradstein, F. M. (2016). *A Concise Geologic Time Scale*: Elsevier.

Oschmann, W. (1991). Distribution, dynamics and palaeoecology of Kimmeridgian (Upper Jurassic) shelf anoxia in western Europe. *Geological Society, London, Special Publications, 58*, 381-395.

Ostrow, D. G. (2004). *Larval dispersal and population genetic structure of brachiopods in the New Zealand fjords.* (PhD), University of Otago, Dunedin, New Zealand.

Otto-Bliesner, B. L., & Upchurch, G. R. (1997). Vegetation-induced warming of high-latitude regions during the late Cretaceous period. *Nature, 385*(6619), 804-807.

Paine, R. T. (1969). Growth and size distribution of the brachiopod Terebratalia transversa Sowerby. *Pacific Science, 23*(3), 337-343.

Pakhnevich, A. V. (2010). Reasons of micromorphism in modern or fossil brachiopods. *Paleontological Journal, 43*(11), 1458-1468.

Parkinson, D., Curry, G. B., Cusack, M., & Fallick, A. E. (2005). Shell structure, patterns and trends of oxygen and carbon stable isotopes in modern brachiopod shells. *Chemical Geology, 219*(1-4), 193-235.

Passey, B. H., & Henkes, G. A. (2012). Carbonate clumped isotope bond reordering and geospeedometry. *Earth and Planetary Science Letters, 351-352*, 223-236.

Pekar, S. F., & DeConto, R. M. (2006). High-resolution ice-volume estimates for the early Miocene: Evidence for a dynamic ice sheet in Antarctica. *Palaeogeography, Palaeoclimatology, Palaeoecology, 231*(1-2), 101-109.

Penman, D. E., Hönisch, B., Rasbury, E. T., Hemming, N. G., & Spero, H. J. (2013). Boron, carbon, and oxygen isotopic composition of brachiopod shells: Intra-shell variability, controls, and potential as a paleo-pH recorder. *Chemical Geology, 340*, 32-39.

Petersen, S. V., Defliese, W. F., Saenger, C., Daëron, M., Huntington, K. W., John, C. M., Kelson, J. R., Coleman, A. S., Kluge, T., Olack, G. A*., et al.* (in review). Effects of improved ^{17}O correction on inter-laboratory agreement in clumped isotope calibrations, estimates of mineral-specific offsets, and acid fractionation factor temperature dependence. *Geochemistry, Geophysics, Geosystems*.

Petersen, S. V., Tabor, C. R., Lohmann, K. C., Poulsen, C. J., Meyer, K. W., Carpenter, S. J., Erickson, J. M., Matsunaga, K. K. S., Smith, S. Y., & Sheldon, N. D. (2016). Temperature and salinity of the Late Cretaceous Western Interior Seaway. *Geology, 44*(11), 903-906.

Poulsen, C. J. (2004). A balmy Arctic. *Nature, 432*, 814–815.

Poulsen, C. J., Pollard, D., & White, T. S. (2007). General circulation model simulation of the $\delta^{18}O$ content of continental precipitation in the middle Cretaceous: A model-proxy comparison. *Geology, 35*(3), 199-202.

Price, G. D. (1999). The evidence and implications of polar ice during the Mesozoic. *Earth-Science Reviews, 48*(3), 183-210.

Price, G. D., Bajnai, D., & Fiebig, J. (in review). Latitudinal temperature gradient of Early Cretaceous seawater inferred from belemnite clumped isotope measurements. *Proceedings of the National Academy of Sciences of the United States of America*.

Price, G. D., & Gröcke, D. R. (2002). Strontium-isotope stratigraphy and oxygen- and carbon-isotope variation during the Middle Jurassic–Early Cretaceous of the Falkland Plateau, South Atlantic. *Palaeogeography, Palaeoclimatology, Palaeoecology, 183*(3-4), 209-222.

Price, G. D., Hart, M. B., Wilby, P. R., & Page, K. N. (2015). Isotopic analysis of Jurassic (Callovian) mollusks from the Christian Malford lagerstätte (UK): Implications for ocean water temperature estimates based on belemnoids. *Palaios, 30*(9), 645-654.

Price, G. D., Janssen, N. M. M., Martinez, M., Company, M., Vandevelde, J. H., & Grimes, S. T. (2018). A high-resolution belemnite geochemical analysis of Early Cretaceous (Valanginian-Hauterivian) environmental and climatic perturbations. *Geochemistry, Geophysics, Geosystems, 19*(10), 3832-3843.

Price, G. D., & Nunn, E. V. (2010). Valanginian isotope variation in glendonites and belemnites from Arctic Svalbard: Transient glacial temperatures during the Cretaceous greenhouse. *Geology, 38*(3), 251-254.

Price, G. D., & Passey, B. H. (2013). Dynamic polar climates in a greenhouse world: Evidence from clumped isotope thermometry of Early Cretaceous belemnites. *Geology, 41*(8), 923-926.

Price, G. D., & Rogov, M. A. (2009). An isotopic appraisal of the Late Jurassic greenhouse phase in the Russian Platform. *Palaeogeography, Palaeoclimatology, Palaeoecology, 273*(1-2), 41-49.

Price, G. D., & Sellwood, B. W. (1997). "Warm" palaeotemperatures from high Late Jurassic palaeolatitudes (Falkland Plateau): Ecological, environmental or diagenetic controls? *Palaeogeography, Palaeoclimatology, Palaeoecology, 129*(3-4), 315-327.

Price, G. D., & Teece, C. (2010). Reconstruction of Jurassic (Bathonian) palaeosalinity using stable isotopes and faunal associations. *Journal of the Geological Society, 167*(6), 1199-1208.

Price, G. D., Twitchett, R. J., Wheeley, J. R., & Buono, G. (2013). Isotopic evidence for long term warmth in the Mesozoic. *Scientific Reports, 3*(1438), 1-5.

Pucéat, E., Lecuyer, C., Sheppard, S. M. F., Dromart, G., Reboulet, S., & Grandjean, P. (2003). Thermal evolution of Cretaceous Tethyan marine waters inferred from oxygen isotope composition of fish tooth enamels. *Paleoceanography, 18*(2), 1-12.

Railsback, L. B., Anderson, T. F., Ackerly, S. C., & Cisne, J. L. (1989). Paleoceanographic modeling of temperature-salinity profiles from stable isotopic data. *Paleoceanography, 4*(5), 585-591.

Reicherter, K., Wiedmann, J., & Herbin, J. P. (1996). Distribution of organic-rich sediments in Subbetic sections during the Aptian-Turonian (Betic Cordillera, Southern Spain). *Rev. Soc. Geol. Espana, 9*(1-2), 75-88.

Riboulleau, A., Baudin, F., Daux, V., Hantzpergue, P., Renard, M., & Zakharov, V. (1998). Sea surface paleotemperature evolution of the Russian Platform during the Upper Jurassic. *Comptes Rendus De L Academie Des Sciences Serie Ii Fascicule a-Sciences De La Terre Et Des Planetes, 326*(4), 239-246.

Ritter, A.-C., Mavromatis, V., Dietzel, M., Kwiecien, O., Wiethoff, F., Griesshaber, E., Casella, L. A., Schmahl, W. W., Koelen, J., Neuser, R. D.*, et al.* (2017). Exploring the impact of diagenesis on (isotope) geochemical and microstructural alteration features in biogenic aragonite. *Sedimentology, 64*, 1354-1380.

Rogov, M. A. (2003). Upper Jurassic Ochetoceratinae (Oppeliidae, Ammonoidea) of Central Russia [in Russian]. *Bulletin of Moscow Society of Naturalists, Geological Series, 78*(38–52).

Rogov, M. A. (2017). Ammonites and infrazonal stratigraphy of the Kimmeridgian and Volgian Stages of southern part of the Moscow Syneclise [in Russian]. *Trans. Geol. Inst., 615*, 7-160.

Rogov, M. A., Ershova, V. B., Shchepetova, E. V., Zakharov, V. A., Pokrovsky, B. G., & Khudoley, A. K. (2017a). Earliest Cretaceous (late Berriasian) glendonites from Northeast Siberia revise the timing of initiation of transient Early Cretaceous cooling in the high latitudes. *Cretaceous Research, 71*, 102-112.

Rogov, M. A., Wierzbowski, A., & Shchepetova, E. (2017b). Ammonite assemblages in the Lower to Upper Kimmeridgian boundary interval (Cymodoce to Mutabilis zones) of Tatarstan (central European Russia) and their correlation importance. *Neues Jahrbuch für Geologie und Paläontologie - Abhandlungen, 285*(2), 161-185.

Rohling, E. J. (2013). Oxygen isotope composition of seawater. In S. A. Elias (Ed.), *The Encyclopedia of Quaternary Science* (Vol. 2, pp. 915–922): Elsevier.

Rollion-Bard, C., Mangin, D., & Champenois, M. (2007). Development and application of oxygen and carbon isotopic measurements of biogenic carbonates by ion microprobe. *Geostandards and Geoanalytical Research, 31*(1), 39-50.

Rollion-Bard, C., & Marin-Carbonne, J. (2011). Determination of SIMS matrix effects on oxygen isotopic compositions in carbonates. *Journal of Analytical Atomic Spectrometry, 26*(6), 1285-1289.

Rollion-Bard, C., Saulnier, S., Vigier, N., Schumacher, A., Chaussidon, M., & Lécuyer, C. (2016). Variability in magnesium, carbon and oxygen isotope compositions of brachiopod shells: Implications for paleoceanographic studies. *Chemical Geology, 423*, 49-60.

Rosales, I., Robles, S., & Quesada, S. (2004). Elemental and oxygen isotope composition of Early Jurassic belemnites: Salinity vs. temperature signals. *Journal of Sedimentary Research, 74*(3), 342-354.

Ryb, U., & Eiler, J. M. (2018). Oxygen isotope composition of the Phanerozoic ocean and a possible solution to the dolomite problem. *Proceedings of the National Academy of Sciences of the United States of America, 115*(26), 6602-6607.

Sælen, G. (1989). Diagenesis and construction of the belemnite rostrum. *Palaeontology, 32*(4), 765-797.

Saenger, C., Affek, H. P., Felis, T., Thiagarajan, N., Lough, J. M., & Holcomb, M. (2012). Carbonate clumped isotope variability in shallow water corals: Temperature dependence and growth-related vital effects. *Geochimica et Cosmochimica Acta, 99*, 224-242.

Sagoo, N., Valdes, P., Flecker, R., & Gregoire, L. J. (2013). The Early Eocene equable climate problem: Can perturbations of climate model parameters identify possible solutions? *Philosophical Transactions of the Royal Society A, 371*(2001), 1-35.

Sahagian, D., Pinous, O., Olferiev, A., & Zakharov, V. (1996). Eustatic curve for the Middle Jurassic-Cretaceous based on Russian platform and Siberian stratigraphy: Zonal resolution. *American Association of Petroleum Geologists Bulletin, 80*(9), 1433-1458.

Savard, M. M., Veizer, J., & Hinton, R. (1995). Cathodoluminescene at low Fe and Mn concentrations; a SIMS study of zones in natural calcites. *Journal of Sedimentary Research, 65*(1a), 208-213.

Sazonova, I. G., & Sazonov, N. T. (1967). *Paleogeografiya Russkoi platformy v yurskoe i rannemelovoe vremya [Paleogeography of the Russian Platform in the Jurassic and Early Cretaceous]*. Leningrad, USSR: Nedra.

Schauble, E. A., Ghosh, P., & Eiler, J. M. (2006). Preferential formation of $^{13}C–^{18}O$ bonds in carbonate minerals, estimated using first-principles lattice dynamics. *Geochimica et Cosmochimica Acta, 70*(10), 2510-2529.

Schauer, A. J., Kelson, J., Saenger, C., & Huntington, K. W. (2016). Choice of ^{17}O correction affects clumped isotope (Δ_{47}) values of CO_2 measured with mass spectrometry. *Rapid Communications in Mass Spectrometry, 30*(24), 2607-2616.

Scherzinger, A., Schweigert, G., & Főzy, I. (2016). First record of the Mediterranean zonal index Mesosimoceras cavouri (Gemmellaro, 1872) in the Upper Jurassic (Pseudomutabilis Zone, semicostatum γ horizon) of SW Germany and its stratigraphical significance. *Volumina Jurassica, 14*, 145-154.

Schmidt, G. A., & Mysak, L. A. (1996). Can increased poleward oceanic heat flux explain the warm Cretaceous climate? *Paleoceanography, 11*(5), 579-593.

Schouten, S., Hopmans, E. C., & Sinninghe Damsté, J. S. (2013). The organic geochemistry of glycerol dialkyl glycerol tetraether lipids: A review. *Organic Geochemistry, 54*, 19-61.

Shackleton, N. J., & Kennett, J. P. (1975). Paleotemperature history of the Cenozoic and the initiation of antarctic glaciation: oxygen and carbon isotope analyses in DSDP sites 277, 279, and 281. *Deep Sea Drilling Project Initial Reports, 29*, 743-755.

Shchepetova, E. V., Gavrilov, Y., Baraboshkin, E. Y., Rogov, M. A., & Shcherbinina, E. (2011). The main organic rich shale sequences in the Upper Jurassic and Lower Cretaceous of the Russian Platform: sedimentology, geochemistry and paleoenvironmental models. In B. A. Matyja, A. Wierzbowski, & P. Ziółkowski (Eds.), *Jurassica IX, Małogoszcz, 06-08 września 2011, Materiały Konferencyjne, Polskie Towarzystwo Geologiczne, Polska Grupa Robocza Systemu Jurajskiego* (pp. 58-63).

Shchepetova, E. V., & Rogov, M. A. (2013). Organic carbon-rich horizons in the Upper Kimmeridgian of the northern part of Ulyanovsk-Saratov trough (Russian Platform): biostratigraphy, sedimentology, geochemistry. In V. A. Zakharov, M. A. Rogov, & A. P. Ippolitov (Eds.), *Jurassic System of Russia: Problems of stratigraphy and paleogeography* (pp. 249-252).

Shulgina, N. I., Burdykina, M. D., Basov, V. A., & Arhus, N. (1994). Distribution of ammonites, foraminifera and dinoflagellate cysts in the Lower Cretaceous reference sections of the Khatanga Basin, and Boreal Valanginian biogeography. *Cretaceous Research, 15*(1), 1-16.

Simkiss, K., & Wilbur, K. M. (1989). *Biomineralization - Cell biology and mineral deposition*. San Diego, CA, USA: Academic Press.

Smelror, M., Mørk, A., Mørk, M. B. E., Weiss, H. M., & Løseth, H. (2001). Middle Jurassic–Lower Cretaceous transgressive–regressive sequences and facies distribution off northern Nordland and Troms, Norway. In O. J. Martinsen & T. Dreyer (Eds.), *Sedimentary Environments Offshore Norway – Palaeozoic to Recent* (Vol. 10, pp. 211-232): Elsevier Science B.V.

Spero, H. J., Bijma, J., Lea, D. W., & Bemis, B. E. (1997). Effect of seawater carbonate concentration on foraminiferal carbon and oxygen isotopes. *Nature, 390*(6659), 497-500.

Spicer, R. A., Ahlberg, A., Herman, A. B., Hofmann, C.-C., Raikevich, M., Valdes, P. J., & Markwick, P. J. (2008). The Late Cretaceous continental interior of Siberia: A challenge for climate models. *Earth and Planetary Science Letters, 267*(1-2), 228-235.

Spicer, R. A., & Herman, A. B. (2010). The Late Cretaceous environment of the Arctic: A quantitative reassessment based on plant fossils. *Palaeogeography, Palaeoclimatology, Palaeoecology, 295*(3-4), 423-442.

Spooner, P. T., Guo, W., Robinson, L. F., Thiagarajan, N., Hendry, K. R., Rosenheim, B. E., & Leng, M. J. (2016). Clumped isotope composition of cold-water corals: A role for vital effects? *Geochimica et Cosmochimica Acta, 179*, 123-141.

Stevens, G. R. (1963). Faunal realms in Jurassic and Cretaceous belemnites. *Geological Magazine, 100*(6), 481-497.

Stevens, G. R. (1971). Relationship of isotopic temperatures and faunal realms to Jurassic–Cretaceous paleogeography, particularly of the south-west Pacific. *Journal of the Royal Society of New Zealand, 1*(2), 145-158.

Stevens, K., Griesshaber, E., Schmahl, W., Casella, L. A., Iba, Y., & Mutterlose, J. (2017). Belemnite biomineralization, development, and geochemistry: The complex rostrum of Neohibolites minimus. *Palaeogeography, Palaeoclimatology, Palaeoecology, 468*, 388-402.

Stevens, K., Mutterlose, J., & Schweigert, G. (2014). Belemnite ecology and the environment of the Nusplingen Plattenkalk (Late Jurassic, southern Germany): Evidence from stable isotope data. *Lethaia, 47*(4), 512-523.

Stevens, K., Mutterlose, J., & Wiedenroth, K. (2015). Stable isotope data ($\delta^{18}O$, $\delta^{13}C$) of the ammonite genus *Simbirskites* — implications for habitat reconstructions of extinct cephalopods. *Palaeogeography, Palaeoclimatology, Palaeoecology, 417*, 164-175.

Super, J. R., Chin, K., Pagani, M., Li, H., Tabor, C., Harwood, D. M., & Hull, P. M. (2018). Late Cretaceous climate in the Canadian Arctic: Multi-proxy constraints from Devon Island. *Palaeogeography, Palaeoclimatology, Palaeoecology, 504*, 1-22.

Surge, D., & Lohmann, K. C. (2008). Evaluating Mg/Ca ratios as a temperature proxy in the estuarine oyster, *Crassostrea virginica*. *Journal of Geophysical Research: Biogeosciences, 113*(G2001), 1-9.

Surge, D., Lohmann, K. C., & Dettman, D. L. (2001). Controls on isotopic chemistry of the American oyster, *Crassostrea virginica* : implications for growth patterns. *Palaeogeography, Palaeoclimatology, Palaeoecology, 172*(3-4), 283-296.

Surge, D. M., Lohmann, K. C., & Goodfriend, G. A. (2003). Reconstructing estuarine conditions: oyster shells as recorders of environmental change, Southwest Florida. *Estuarine, Coastal and Shelf Science, 57*(5-6), 737-756.

Swart, P. K., Price, R. M., & Greer, L. (2001). The relationship between stable isotopic variations (O, H, and C) and salinity in waters and corals from environments in South Florida: implications for reading the paleoenvironmental record. In B. R. Wardlaw (Ed.), *Paleoecological studies in South Florida* (Vol. 361).

Takayanagi, H., Asami, R., Abe, O., Miyajima, T., Kitagawa, H., Sasaki, K., & Iryu, Y. (2013). Intraspecific variations in carbon-isotope and oxygen-isotope compositions of a brachiopod *Basiliola lucida* collected off Okinawa-jima, southwestern Japan. *Geochimica et Cosmochimica Acta, 115*, 115-136.

Takayanagi, H., Asami, R., Otake, T., Abe, O., Miyajima, T., Kitagawa, H., & Iryu, Y. (2015). Quantitative analysis of intraspecific variations in the carbon and oxygen isotope compositions of the modern cool-temperate brachiopod *Terebratulina crossei*. *Geochimica et Cosmochimica Acta, 170*, 301-320.

Tang, J., Dietzel, M., Fernandez, A., Tripati, A. K., & Rosenheim, B. E. (2014). Evaluation of kinetic effects on clumped isotope fractionation (Δ_{47}) during inorganic calcite precipitation. *Geochimica et Cosmochimica Acta, 134*, 120-136.

Tarduno, J. A., Brinkman, D. B., Renne, P. R., Cottrell, R. D., Scher, H., & Castillo, P. (1998). Evidence for extreme climatic warmth from Late Cretaceous Arctic vertebrates. *Science, 282*(5397), 2241-2244.

Taylor, K. W. R., Huber, M., Hollis, C. J., Hernandez-Sanchez, M. T., & Pancost, R. D. (2013). Re-evaluating modern and Palaeogene GDGT distributions: Implications for SST reconstructions. *Global and Planetary Change, 108*, 158-174.

Tesakova, E. (2008). Late Callovian and Early Oxfordian ostracods from the Dubki section (Saratov area, Russia): implications for stratigraphy, paleoecology, eustatic cycles and palaeobiogeography. *Neues Jahrbuch für Geologie und Paläontologie - Abhandlungen, 249*(1), 25-45.

Tesakova, E. M. (2014a). *Jurassic ostracods of the Russian plate: stratigraphic implications, paleoecology and paleogeography [in Russian].* (PhD).

Tesakova, E. M. (2014b). Palaeotemperature reconstruction of the Middle Russian Sea during the Middle and Late Jurassic by ostracods [in Russian]. In A. V. Ivanov (Ed.), *Problems of Paleoecology and Historical Geoecology. Collection of Papers of All-Russian V.G. Ochev Scientific Conference* (pp. 133–147). Saratov.

Tesakova, E. M. (2017). Ostracods of the Virgatites virgatus Zone from Moscow sections. In M. A. Rogov, A. A. Mironenko, A. V. Guzhov, E. M. Tesakova, M. A. Ustinova, Y. A. Shurupova, N. G. Zverkov, M. S. Archangelsky, A. S. Shmakov, & E. E. Baraboshkin (Eds.), *Jurassic Deposits if the Southern Part of the Moscow Syneclyse and Their Fauna* (Vol. 615, pp. 301-310).

Tesakova, E. M., Demidov, S. M., Guzhov, A. V., Rogov, M. A., & Kiselev, D. N. (2012). Middle Oxfordian – Lower Kimmeridgian ostracod zones from the Mikhalenino section (Kostroma region) and their comparison with synchronous strata of the Eastern and Western Europe. *Neues Jahrbuch für Geologie und Paläontologie - Abhandlungen, 266*(3), 239-249.

Thiagarajan, N., Adkins, J., & Eiler, J. (2011). Carbonate clumped isotope thermometry of deep-sea corals and implications for vital effects. *Geochimica et Cosmochimica Acta, 75*(16), 4416-4425.

Thierry, J., Abbate, E., Alekseev, A. S., Ait-Ouali, R., Ait-Salem, H., Bouaziz, S., Canerot, J., Georgiev, G., Guiraud, R., Hirsch, F.*, et al.* (2000). Early Kimmeridgian (146–144 Ma). In J. Dercourt, M. Gaetani, B. Vrielynck, E. Barrier, B. Biju-Duval, M. F. Brunet, J. P. Cadet, S. Crasquin, & M. Sandulescu (Eds.), *Atlas Peri-Tethys, Palaeogeographical Maps*: CGMW.

Tierney, J. E., & Tingley, M. P. (2015). A TEX_{86} surface sediment database and extended Bayesian calibration. *Scientific Data, 2*, 150029.

Tripati, A. K., Eagle, R. A., Thiagarajan, N., Gagnon, A. C., Bauch, H., Halloran, P. R., & Eiler, J. M. (2010). $^{13}C–^{18}O$ isotope signatures and 'clumped isotope' thermometry in foraminifera and coccoliths. *Geochimica et Cosmochimica Acta, 74*(20), 5697-5717.

Tripati, A. K., Hill, P. S., Eagle, R. A., Mosenfelder, J. L., Tang, J., Schauble, E. A., Eiler, J. M., Zeebe, R. E., Uchikawa, J., Coplen, T. B.*, et al.* (2015). Beyond temperature: Clumped isotope signatures in dissolved inorganic carbon species and the influence of solution chemistry on carbonate mineral composition. *Geochimica et Cosmochimica Acta, 166*, 344-371.

Tyson, R. V., Wilson, R. C. L., & Downie, C. (1979). A stratified water column environmental model for the type Kimmeridge Clay. *Nature, 277*(5695), 377-380.

Uchikawa, J., & Zeebe, R. E. (2012). The effect of carbonic anhydrase on the kinetics and equilibrium of the oxygen isotope exchange in the CO_2–H_2O system: Implications for $\delta^{18}O$ vital effects in biogenic carbonates. *Geochimica et Cosmochimica Acta, 95*, 15-34.

Ullmann, C. V., Frei, R., Korte, C., & Hesselbo, S. P. (2015). Chemical and isotopic architecture of the belemnite rostrum. *Geochimica et Cosmochimica Acta, 159*, 231-243.

Ullmann, C. V., Frei, R., Korte, C., & Lüter, C. (2017). Element/Ca, C and O isotope ratios in modern brachiopods: Species-specific signals of biomineralization. *Chemical Geology, 460*, 15-24.

Ullmann, C. V., Hesselbo, S. P., & Korte, C. (2013). Tectonic forcing of Early to Middle Jurassic seawater Sr/Ca. *Geology, 41*(12), 1211-1214.

Ullmann, C. V., & Korte, C. (2015). Diagenetic alteration in low-Mg calcite from macrofossils: a review. *Geological Quarterly, 59*(1), 3-20.

Ullmann, C. V., & Pogge von Strandmann, P. A. E. (2017). The effect of shell secretion rate on Mg/Ca and Sr/Ca ratios in biogenic calcite as observed in a belemnite rostrum. *Biogeosciences, 14*(1), 89-97.

Urey, H. C. (1947). The thermodynamic properties of isotopic substances. *Journal of the Chemical Society, 0*, 562-581.

Usdowski, W., & Hoefs, J. (1993). Oxygen isotope exchange between carbonic acid, bicarbonate, carbonate, and water: A re-examination of the data of McCrea (1950) and an expression for the overall partitioning of oxygen isotopes between the carbonate species and water. *Geochimica et Cosmochimica Acta, 57*(15), 3815-3818.

Ustinova, M. A. (2009). The distribution of calcareous nannofossils and foraminifers in the Callovian, Oxfordian, and Volgian deposits in the southwest of Moscow. *Stratigraphy and Geological Correlation, 17*(2), 204-217.

Ustinova, M. A. (2012). Foraminifers and stratigraphy of Middle Oxfordian – Lower Kimmeridgian of Kostroma Region (Mikhalenino section) [in Russian]. *Bulletin of Moscow Society of Naturalists, Geological Series, 87*, 43–52.

Ustinova, M. A., & Tesakova, E. M. (2017). New data on microbiota of the Middle Volgian substage in the Loino Section (Kirov oblast). *Stratigraphy and Geological Correlation, 25*(3), 296-306.

Veizer, J. (1974). Chemical diagenesis belemnite shells possible consequences for paleotemperature determinations. *Neues Jahrbuch für Geologie und Paläontologie - Abhandlungen, 147*(1), 91-111.

Veizer, J. (1983). Chemical diagenesis of carbonates: theory and trace element technique. In M. A. Arthur, T. F. Anderson, I. R. Kaplan, J. Veizer, & L. S. Land (Eds.), *Stable Isotopes in Sedimentary Geology* (Vol. 10, pp. 3.1-3.100): SEPM Society for Sedimentary Geology.

Veizer, J., & Prokoph, A. (2015). Temperatures and oxygen isotopic composition of Phanerozoic oceans. *Earth-Science Reviews, 146*, 92-104.

Vickers, M., Bajnai, D., Price, G. D., Linckens, J., & Fiebig, J. (in review). Southern high latitude warmth during Jurassic–Cretaceous: new evidence from clumped isotope thermometry. *Geology*.

Vickers, M. L., Price, G. D., Jerrett, R. M., & Watkinson, M. (2016). Stratigraphic and geochemical expression of Barremian–Aptian global climate change in Arctic Svalbard. *Geosphere, 12*(5), 1594-1605.

Voigt, S., Gale, A. S., & Voigt, T. (2006). Sea-level change, carbon cycling and palaeoclimate during the Late Cenomanian of northwest Europe; an integrated palaeoenvironmental analysis. *Cretaceous Research, 27*(6), 836-858.

Voigt, S., Wilmsen, M., Mortimore, R. N., & Voigt, T. (2003). Cenomanian palaeotemperatures derived from the oxygen isotopic composition of brachiopods and belemnites: evaluation of Cretaceous palaeotemperature proxies. *International Journal of Earth Sciences, 92*(2), 285-299.

von Allmen, K., Nägler, T. F., Pettke, T., Hippler, D., Griesshaber, E., Logan, A., Eisenhauer, A., & Samankassou, E. (2010). Stable isotope profiles (Ca, O, C) through modern brachiopod shells of *T. septentrionalis* and *G. vitreus*: Implications for calcium isotope paleo-ocean chemistry. *Chemical Geology, 269*(3-4), 210-219.

Wacker, U., Fiebig, J., & Schoene, B. R. (2013). Clumped isotope analysis of carbonates: comparison of two different acid digestion techniques. *Rapid Communications in Mass Spectrometry, 27*(14), 1631-1642.

Wacker, U., Fiebig, J., Tödter, J., Schöne, B. R., Bahr, A., Friedrich, O., Tütken, T., Gischler, E., & Joachimski, M. M. (2014). Empirical calibration of the clumped isotope paleothermometer using calcites of various origins. *Geochimica et Cosmochimica Acta, 141*, 127-144.

Wacker, U., Rutz, T., Löffler, N., Conrad, A. C., Tütken, T., Böttcher, M. E., & Fiebig, J. (2016). Clumped isotope thermometry of carbonate-bearing apatite: Revised sample pre-

treatment, acid digestion, and temperature calibration. *Chemical Geology, 443*, 97-110.

Wanamaker, A. D. J., Kreutz, K. J., Wilson, T., Borns Jr, H. W., Introne, D. S., & Feindel, S. (2008). Experimentally determined Mg/Ca and Sr/Ca ratios in juvenile bivalve calcite for *Mytilus edulis*: Implications for paleotemperature reconstructions. *Geo-Marine Letters, 28*(5-6), 359-368.

Wang, Y., Huang, C., Sun, B., Quan, C., Wu, J., & Lin, Z. (2014). Paleo-CO_2 variation trends and the Cretaceous greenhouse climate. *Earth-Science Reviews, 129*, 136-147.

Wang, Z., Schauble, E. A., & Eiler, J. M. (2004). Equilibrium thermodynamics of multiply substituted isotopologues of molecular gases. *Geochimica et Cosmochimica Acta, 68*(23), 4779-4797.

Watkins, J. M., & Hunt, J. D. (2015). A process-based model for non-equilibrium clumped isotope effects in carbonates. *Earth and Planetary Science Letters, 432*, 152-165.

Watkins, J. M., Hunt, J. D., Ryerson, F. J., & DePaolo, D. J. (2014). The influence of temperature, pH, and growth rate on the $\delta^{18}O$ composition of inorganically precipitated calcite. *Earth and Planetary Science Letters, 404*, 332-343.

Watkins, J. M., Nielsen, L. C., Ryerson, F. J., & DePaolo, D. J. (2013). The influence of kinetics on the oxygen isotope composition of calcium carbonate. *Earth and Planetary Science Letters, 375*, 349-360.

Watson, E. B. (2004). A conceptual model for near-surface kinetic controls on the trace-element and stable isotope composition of abiogenic calcite crystals 1 1Associate editor: R.H. Byrne. *Geochimica et Cosmochimica Acta, 68*(7), 1473-1488.

White, T., Gonzalez, L., Ludvigson, G., & Poulsen, C. (2001). Middle Cretaceous greenhouse hydrologic cycle of North America. *Geology, 29*(4), 363-366.

Wierzbowski, A., & Matyja, B. A. (2014). Ammonite biostratigraphy in the Polish Jura sections (central Poland) as a clue for recognition of the uniform base of the Kimmeridgian Stage. *Volumina Jurassica, 12*(1), 45-98.

Wierzbowski, A., Smoleń, J., & Iwańczuk, J. (2015). The Oxfordian and Lower Kimmeridgian of the Peri-Baltic Syneclise (north-eastern Poland): Stratigraphy, ammonites, microfossils (foraminifers, radiolarians), facies, and palaeogeographical implications. *Neues Jahrbuch für Geologie und Paläontologie - Abhandlungen, 277*(1), 63-104.

Wierzbowski, H. (2015). Seawater temperatures and carbon isotope variations in central European basins at the Middle–Late Jurassic transition (Late Callovian–Early Kimmeridgian). *Palaeogeography, Palaeoclimatology, Palaeoecology, 440*, 506-523.

Wierzbowski, H., Anczkiewicz, R., Pawlak, J., Rogov, M. A., & Kuznetsov, A. B. (2017). Revised Middle–Upper Jurassic strontium isotope stratigraphy. *Chemical Geology, 466*, 239-255.

Wierzbowski, H., Bajnai, D., Wacker, U., Rogov, M. A., Fiebig, J., & Tesakova, E. M. (2018). Clumped isotope record of salinity variations in the Subboreal Province at the middle–late Jurassic transition. *Global and Planetary Change, 167*, 172-189.

Wierzbowski, H., Dembicz, K., & Praszkier, T. (2009). Oxygen and carbon isotope composition of Callovian–Lower Oxfordian (Middle–Upper Jurassic) belemnite rostra from central Poland: A record of a Late Callovian global sea-level rise? *Palaeogeography, Palaeoclimatology, Palaeoecology, 283*(3-4), 182-194.

Wierzbowski, H., & Joachimski, M. (2007). Reconstruction of late Bajocian–Bathonian marine palaeoenvironments using carbon and oxygen isotope ratios of calcareous fossils from the Polish Jura Chain (central Poland). *Palaeogeography, Palaeoclimatology, Palaeoecology, 254*(3-4), 523-540.

Wierzbowski, H., & Joachimski, M. M. (2009). Stable isotopes, elemental distribution, and growth rings of belemnopsid belemnite rostra: Proxies for belemnite life habitat. *Palaios, 24*(6), 377-386.

Wierzbowski, H., & Rogov, M. (2011). Reconstructing the palaeoenvironment of the Middle Russian Sea during the Middle–Late Jurassic transition using stable isotope ratios of cephalopod shells and variations in faunal assemblages. *Palaeogeography, Palaeoclimatology, Palaeoecology, 299*(1-2), 250-264.

Wierzbowski, H., Rogov, M. A., Matyja, B. A., Kiselev, D., & Ippolitov, A. (2013). Middle–Upper Jurassic (Upper Callovian–Lower Kimmeridgian) stable isotope and elemental records of the Russian Platform: Indices of oceanographic and climatic changes. *Global and Planetary Change, 107*, 196-212.

Wignall, P. B., & Hallam, A. (1991). Biofacies, stratigraphic distribution and depositional models of British onshore Jurassic black shales. *Geological Society, London, Special Publications, 58*, 291–309.

Williams, A. (1977). Differentiation and growth of the brachiopod mantle. *American Zoologist, 17*(1), 107-120.

Wolthers, M., Nehrke, G., Gustafsson, J. P., & Van Cappellen, P. (2012). Calcite growth kinetics: Modeling the effect of solution stoichiometry. *Geochimica et Cosmochimica Acta, 77*, 121-134.

Yamamoto, K., Asami, R., & Iryu, Y. (2010a). Carbon and oxygen isotopic compositions of modern brachiopod shells from a warm-temperate shelf environment, Sagami Bay,

central Japan. *Palaeogeography, Palaeoclimatology, Palaeoecology, 291*(3-4), 348-359.

Yamamoto, K., Asami, R., & Iryu, Y. (2010b). Within-shell variations in carbon and oxygen isotope compositions of two modern brachiopods from a subtropical shelf environment off Amami-o-shima, southwestern Japan. *Geochemistry, Geophysics, Geosystems, 11*(10), 1-16.

Yamamoto, K., Asami, R., & Iryu, Y. (2013). Correlative relationships between carbon- and oxygen-isotope records in two cool-temperate brachiopod species off Otsuchi Bay, northeastern Japan. *Paleontological Research, 17*(1), 12-26.

Yasuhara, M., Okahashi, H., & Cronin, T. M. (2009). Taxonomy of Quaternary Deep-Sea Ostracods from the Western North Atlantic Ocean. *Palaeontology, 52*(4), 879-931.

York, D., Evensen, N. M., Martínez, M. L., & De Basabe Delgado, J. (2004). Unified equations for the slope, intercept, and standard errors of the best straight line. *American Journal of Physics, 72*(3), 367-375.

Yoshioka, S., & Kitano, Y. (1985). Transformation of Aragonite to Calcite through Heating. *Geochemical Journal, 19*(4), 245-249.

Young, A., Flament, N., Maloney, K., Williams, S., Matthews, K., Zahirovic, S., & Müller, R. D. (2018). Global kinematics of tectonic plates and subduction zones since the late Paleozoic Era. *Geoscience Frontiers*.

Zaarur, S., Affek, H. P., & Brandon, M. T. (2013). A revised calibration of the clumped isotope thermometer. *Earth and Planetary Science Letters, 382*, 47-57.

Zachos, J., Stott, L. D., & Lohmann, K. C. (1994). Evolution of Early Cenozoic marine temperatures. *Paleoceanography, 9*(2), 353-387.

Žák, K., Košťák, M., Man, O., Zakharov, V. A., Rogov, M. A., Pruner, P., Rohovec, J., Dzyuba, O. S., & Mazuch, M. (2011). Comparison of carbonate C and O stable isotope records across the Jurassic/Cretaceous boundary in the Tethyan and Boreal Realms. *Palaeogeography, Palaeoclimatology, Palaeoecology, 299*(1-2), 83-96.

Zakharov, V. A., & Rogov, M. A. (2003). Boreal-Tethyan mollusk migrations at the Jurassic-Cretaceous boundary time and biogeographic ecotone position in the northern hemisphere. *Stratigraphy and Geological Correlation, 11*(2), 152-171.

Zakharov, V. A., Rogov, M. A., & Shchepetova, E. V. (2017). *Black shale events in the Late Jurassic–earliest Cretaceous of Central Russia [in Russian]*. Paper presented at the Jurassic System of Russia: Problems of stratigraphy and paleogeography, Moscow, Russia.

Zeebe, R. E. (1999). An explanation of the effect of seawater carbonate concentration on foraminiferal oxygen isotopes. *Geochimica et Cosmochimica Acta, 63*(13-14), 2001-2007.

Zeebe, R. E., & Wolf-Gladrow, D. A. (Eds.). (2001). *CO_2 in Seawater: Equilibrium, Kinetics, Isotopes* (Vol. 65): Elsevier.

Zhou, J., Poulsen, C. J., Pollard, D., & White, T. S. (2008). Simulation of modern and middle Cretaceous marine $\delta^{18}O$ with an ocean-atmosphere general circulation model. *Paleoceanography, 23*(PA3223), 1-11.

Zuev, G. V., & Nesis, K. N. (1971). *Kal'mary (Biologiya i Promysel) [in Russian]*: Pishchevaya Promyshlennost'.

Appendix Chapter 2

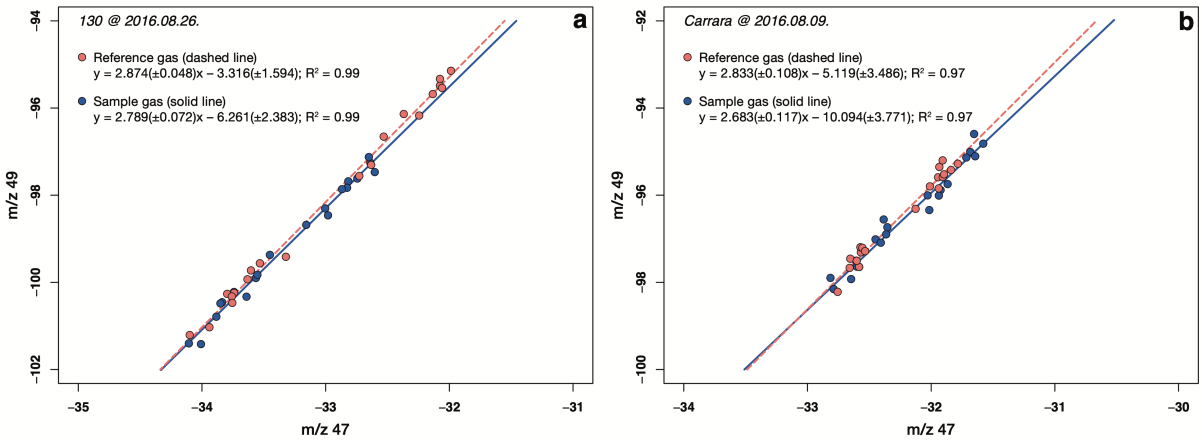

Figure A2.1 | Background correction.
(A) Correlation between intensity of the on-peak m/z 49 ion beam and the corresponding off-peak m/z 47 background for a replicate analysis of the sample that shows the highest Δ_{47} offset with respect to Passey and Henkes (2012). **(B)** Correlation between intensity of the on-peak m/z 49 ion beam and the corresponding off-peak m/z 47 background for a replicate analysis of a Carrara standard. If the sample gas would contain more m/z 49 interferences than the reference gas, the two regression lines would become distinguishable from each other. In this case, the sample gas regression line would shift to the right relative to the reference gas regression line (Bernasconi *et al.*, 2013; Fiebig *et al.*, 2016). Note that in both cases the slope and intercept of reference gas and sample gas measurements agree within errors. As such there are no indications for isobaric interferences on m/z 49.

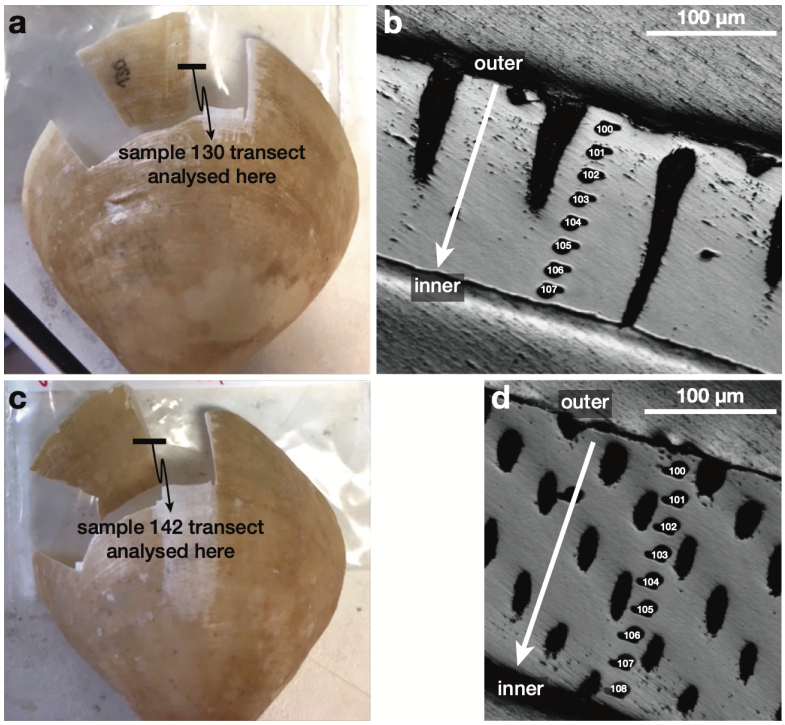

Figure A2.2 | Location of the ion probe measurements on the two analysed *M. venosa* shells.
(A,B) Sample 130. **(C,D)** Sample 142. In both cases, the ventral valves were analysed.

Figure A2.3 | Effect of the magnesium concentration on the $\delta^{18}O$ values.
(A) Magnesium concentrations of the brachiopod shells analysed in this study plotted against the corresponding brachiopod growth temperatures. Our results are consistent with the expected range of modern brachiopod calcite and fall along the Global Brachiopod Mg Line (Brand *et al.*, 2013). **(B,C)** Same as Figures 2.2b,c but the offset $\delta^{18}O$ values are calculated according to Brand *et al.* (2013) that includes a correction for the Mg-effect, which accounts for a 0.17‰ change per mol% $MgCO_3$ (Jiménez-López *et al.*, 2004). The range of the offset $\delta^{18}O$ values become larger, compared to those calculated according to Kim and O'Neil (1997), if the Mg-effect is considered (Figures 2.2b,c). This suggests that the Mg-content of the brachiopod shells cannot account for the observed deviations from apparent oxygen isotope equilibrium. For all plots: linear regression lines fitted to our data consider the errors. Corresponding two-tailed *p*-values are computed using a t-test. Error bars for the offset $\delta^{18}O$ values indicate the mean deviation from oxygen isotope equilibrium calculated using the minimum and the maximum temperature estimates. Error bars for the offset Δ_{47} values indicate the 1σ S.E. of the replicate measurements.

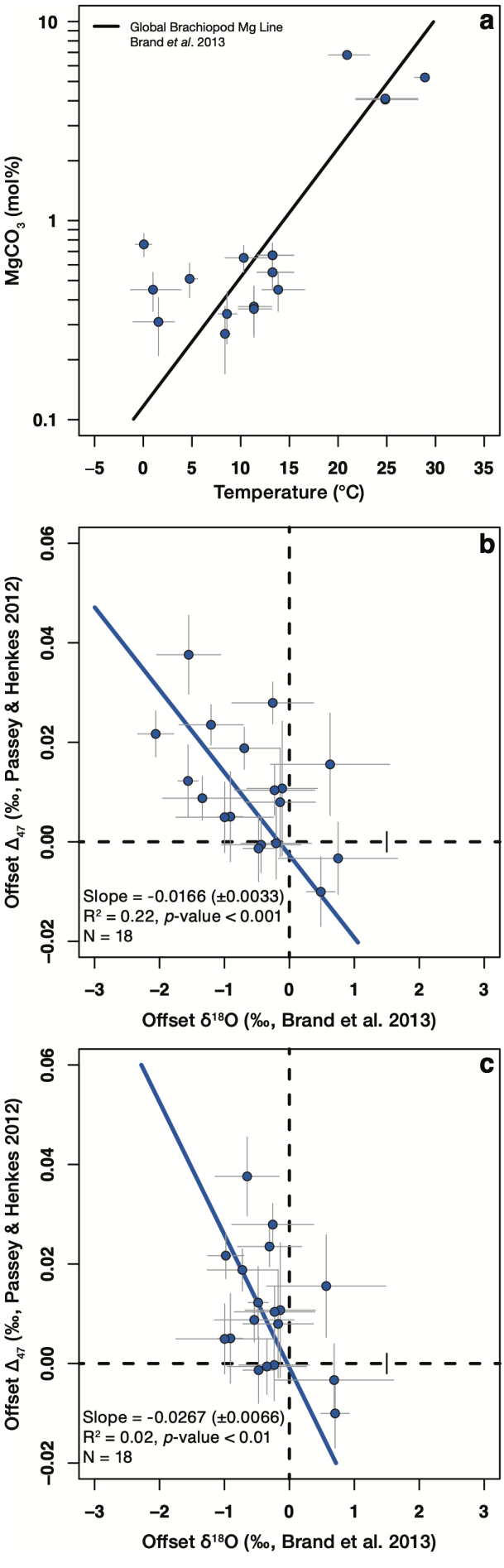

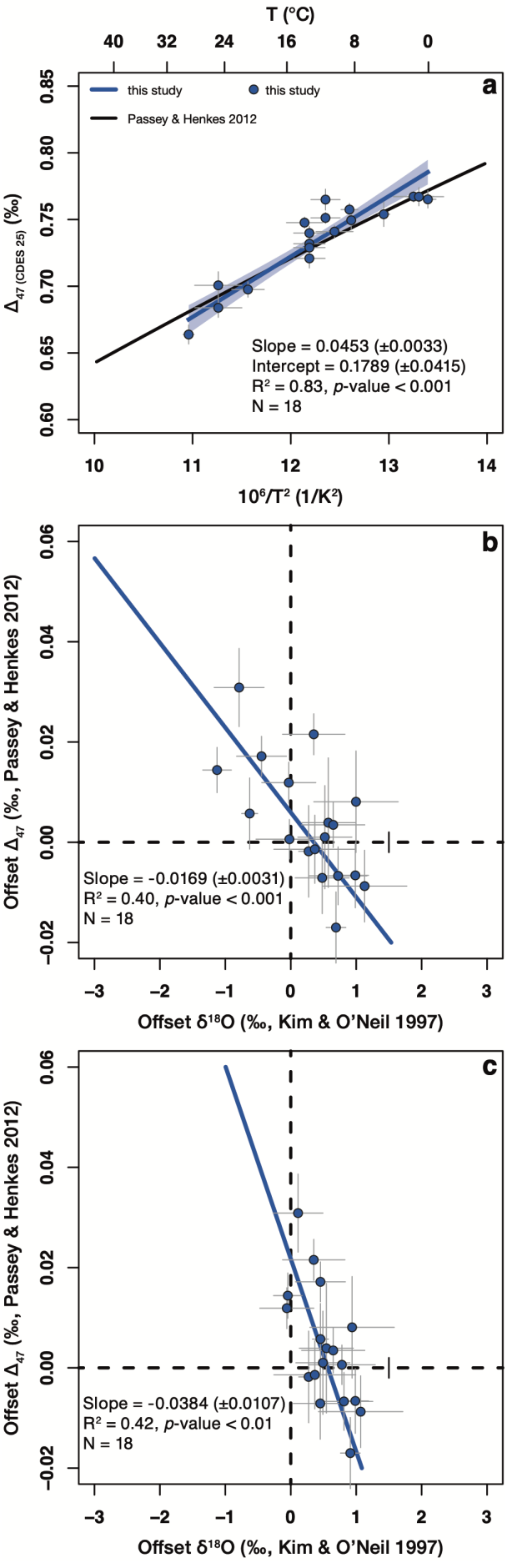

Figure A2.4 | Brachiopods show an offset from equilibrium Δ_{47} and $\delta^{18}O$ values.
Same as Figure 2.2 but all values were calculated using the [*Brand*]/IUPAC set of isotopic parameters (Daëron *et al.*, 2016). **(A)** Δ_{47}–temperature dependence derived from the eighteen modern brachiopods analysed in this study. **(B)** The offset $\delta^{18}O$ and offset Δ_{47} values show a significant negative correlation. Seawater $\delta^{18}O$ values were acquired from the Global Seawater Oxygen-18 Database (LeGrande & Schmidt, 2006). **(C)** The correlation between offset $\delta^{18}O$ and offset Δ_{47} values is still present if, where available, the directly measured seawater $\delta^{18}O$ values (Table A2.1) were used for the calculations. For all plots: linear regression lines fitted to our data consider the errors. Corresponding two-tailed *p*-values are computed using a t-test. Error bars for the offset $\delta^{18}O$ values indicate the mean deviation from oxygen isotope equilibrium calculated using the minimum and the maximum temperature estimates (Table A2.1). Error bars for the offset Δ_{47} values indicate the 1σ S.E. of the replicate measurements.

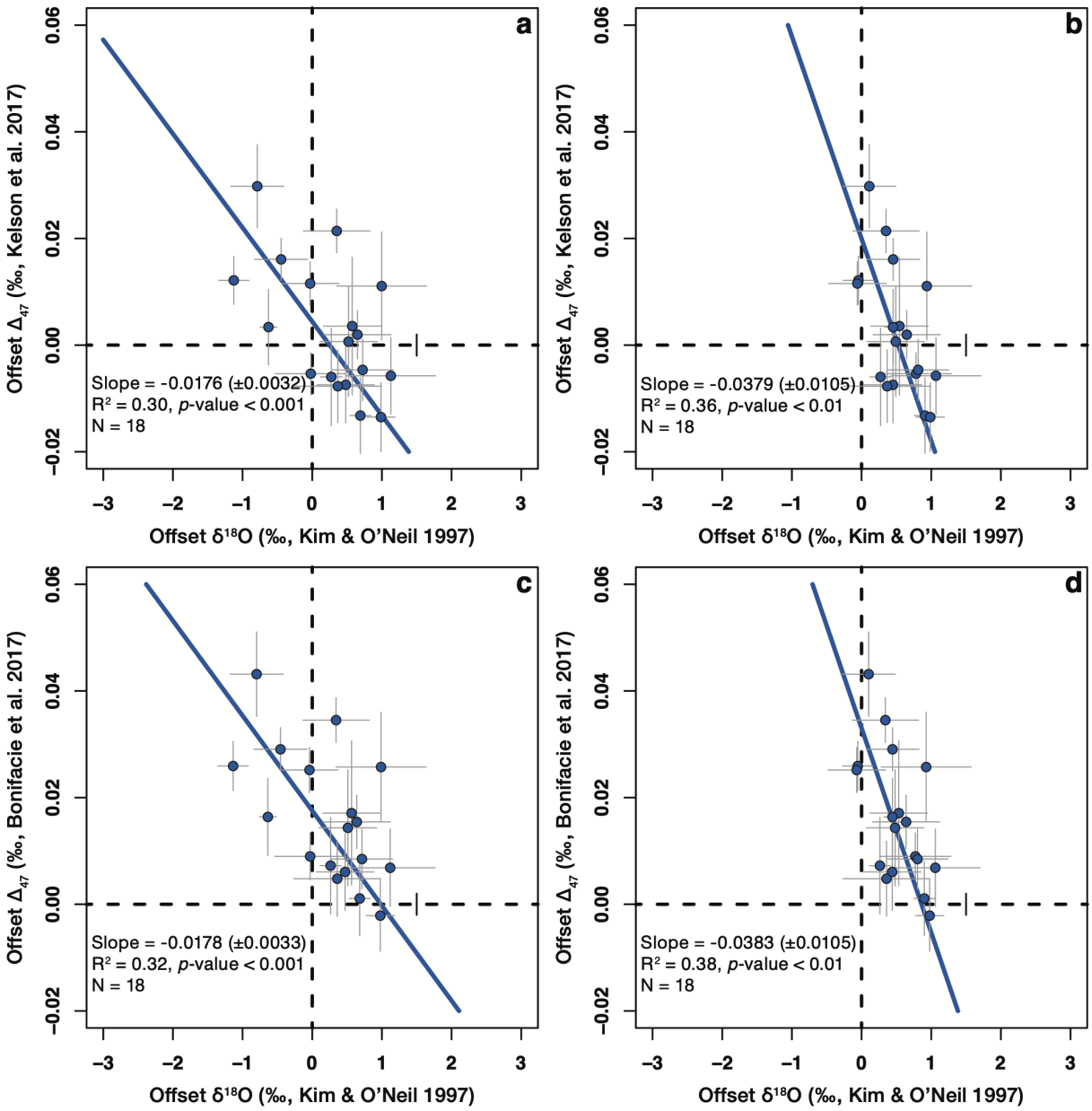

Figure A2.5 | Brachiopods show an offset from equilibrium Δ_{47} and $\delta^{18}O$ values irrespective of the calibration characteristic of clumped isotope equilibrium.

The offset $\delta^{18}O$ and the offset Δ_{47} values show a significant negative correlation even if clumped isotope equilibrium is assumed to be represented by the experimental calibrations of Bonifacie *et al.* (2017), *i.e.,* their eq. 3, or Kelson *et al.* (2017), *i.e.,* their Equation 1. The dataset of Kelson *et al.* (2017) represents the first calibration where raw data was processed using the [*Brand*]/IUPAC set of isotopic parameters (Daëron *et al.*, 2016). **(A,C)** All seawater $\delta^{18}O$ values were acquired from the Global Seawater Oxygen-18 Database (LeGrande & Schmidt, 2006). **(B,D)** Where available, the directly measured seawater $\delta^{18}O$ values were used for the calculations (Brand *et al.*, 2013). For all plots: linear regression lines fitted to our data consider the errors. Corresponding two-tailed *p*-values are computed using a t-test. Error bars for the offset $\delta^{18}O$ values indicate the mean deviation from oxygen isotope equilibrium calculated using the minimum and the maximum temperature estimates. Error bars for the offset Δ_{47} values indicate the 1σ S.E. of the replicate measurements.

Table A2.1 | Environmental and growth parameters of the modern brachiopods investigated in this study. Ambient habitat temperatures for the studied brachiopods were acquired from the World Ocean Atlas 2013 (Locarnini et al., 2013). Mean temperatures depict the yearly average temperatures, while the minimum and maximum estimates are the mean monthly temperature of the coldest and the warmest month, respectively. Seawater $\delta^{18}O$ values were acquired either from the Global Seawater Oxygen-18 Database (LeGrande & Schmidt, 2006) or were measured directly (Brand et al., 2013) (marked with an asterisk*).

Sample	Species	Location (Lat., Long.)	Water depth (m)	$\delta^{18}O_{water}$ (‰, SMOW)	Temperature (°C, annual)	Temperature (°C, max.)	Temperature (°C, min.)	Growth rate (mm/yr, max.)	Growth rate (mm/yr, min.)	Valve length (mm, ventral)
130	*Magellania venosa*	Lilliguapi, Chile -42.162030, -72.598580	18	-0.31 -1.21*	11.36	13.19	9.77	17.3	3.8	64.7
143	*Magellania venosa*	Punta Gruesa, Chile -42.409833, -72.424333	20	-0.31 -1.21*	11.36	13.19	9.77	17.3	3.8	55.9
ChHP1	*Hemithiris psittacea*	Churchill, Canada 58.786867, -94.175450	20	-2.55 -3.35*	1.56	3.20	-1.05	-	-	16.8
D487L	*Terebratalia transversa*	San Juan Is., WA, USA 48.4965, -122.947	64	-0.76 -1.84*	8.59	9.62	7.70	16.7	2.9	21.8
DA5.25.1	*Argyrotheca* sp.	Dahab, Egypt 28.51, 34.52	10	1.80 1.86*	24.84	28.19	21.83	1.2	0.5	< 1
DA5.25.2	*Megerlia* sp.	Dahab, Egypt 28.51, 34.52	9	1.80 1.86*	24.84	28.19	21.83	1.2	0.5	< 1
DS288L	*Magasella sanguinea*	Doubtful Sound, NZ -45.349, 167.0506	20	0.27 0.30*	13.27	15.44	11.68	9.3	1.6	33.4
DS420L	*Calloria inconspicua*	Doubtful Sound, NZ -45.349, 167.0506	20	0.27 0.30*	13.27	15.44	11.68	5.9	1.6	21.4
DS430L	*Liothyrella neozelanica*	Doubtful Sound, NZ -45.349, 167.0506	20	0.27 0.30*	13.27	15.44	11.68	6.9	1.8	51.5
DS431L	*Liothyrella neozelanica*	Doubtful Sound, NZ -45.349, 167.0506	20	0.27 0.30*	13.27	15.44	11.68	6.9	1.8	45.8
FTD1	*Terebratella dorsata*	Falkland Islands -53.0, -60.0	50-400	-0.17	4.76	5.59	4.29	-	-	26.3
GS183L	*Magasella sanguinea*	George Sound, NZ -44.85, 167.35	18	0.31	13.85	16.57	12.20	9.3	1.6	29.6
NN2V	*Notosaria nigricans*	Kaka Point, NZ -46.3866, 169.7823	2-15	0.10	10.31	12.72	8.41	8.0	-	14.5
PA.01	*Pajaudina atlantica*	La Palma, Canary Is. 28.455783, -17.846747	14	1.16 1.07*	20.92	23.24	19.01	1.2	0.5	2–6
S006L	*Terebratalia transversa*	San Juan Is., WA, USA 48.4919, -122.94945	73	-0.76 -1.84*	8.39	8.94	7.87	16.7	2.9	32.8
SAMID10116	*Glaciarcula spitzbergensis*	Svalbard, Norway 79.911, 15.812	46	-0.34	1.00	3.89	-1.32	-	-	10.2
TC.01	*Thecidellina congregata*	Rock Islands, Palau 7.272167, 134.380667	2	0.09 -0.13*	28.91	29.37	27.85	1.2	0.5	2–3
WMF1	*Magellania fragilis*	Weddell Sea, Antarctica -69.950000,-11.816667	215	-0.39	0.06	0.87	-0.80	1.2	0.5	–

Table A2.2 | Results of the stable isotope and trace element analyses.

The Δ_{47} values are reported on the carbon dioxide equilibrium scale and normalised to an acid digestion temperature of 25 °C from the original acid digestion temperature of 90 °C, using an acid fractionation factor of 0.081‰ (Passey & Henkes, 2012). The difference between the [*Gonfiantini/Santrock*] and the [*Brand*]/IUPAC $\delta^{13}C$ and $\delta^{18}O$ values are around 0.01‰ (see Supplementary Data 2.1). Standard errors (in brackets) for the isotope analyses are calculated on the 1σ level and for the trace element analyses on the 2σ level.

Sample	N	$MgCO_3$ (mol%)	Δ_{47} [Gonfiantini] (‰, CDES 25)	Δ_{47} [Brand]/IUPAC (‰, CDES 25)	$\delta^{18}O_{shell}$ (‰, VPDB)	$\delta^{13}C_{shell}$ (‰, VPDB)
130	10	0.37 (±0.1)	0.772 (±0.008)	0.765 (±0.008)	-0.40 (±0.06)	-0.65 (±0.02)
143	10	0.36 (±0.1)	0.758 (±0.004)	0.751 (±0.004)	-0.06 (±0.04)	-0.32 (±0.01)
ChHP1	5	0.31 (±0.1)	0.775 (±0.004)	0.767 (±0.004)	0.38 (±0.01)	1.73 (±0.01)
D487L	6	0.34 (±0.1)	0.765 (±0.005)	0.757 (±0.005)	-0.57 (±0.02)	-0.88 (±0.02)
DA5.25.1	5	4.06 (±0.1)	0.708 (±0.010)	0.701 (±0.010)	0.62 (±0.03)	2.06 (±0.01)
DA5.25.2	4	4.11 (±0.1)	0.689 (±0.007)	0.684 (±0.007)	0.75 (±0.03)	1.76 (±0.02)
DS288L	6	0.67 (±0.1)	0.739 (±0.014)	0.732 (±0.013)	1.12 (±0.02)	1.77 (±0.01)
DS420L	6	0.55 (±0.1)	0.747 (±0.004)	0.740 (±0.004)	0.51 (±0.01)	0.75 (±0.01)
DS430L	6	0.67 (±0.1)	0.728 (±0.007)	0.721 (±0.007)	1.02 (±0.03)	2.17 (±0.02)
DS431L	6	0.55 (±0.1)	0.736 (±0.011)	0.729 (±0.010)	1.06 (±0.03)	2.14 (±0.01)
FTD1	4	0.51 (±0.1)	0.761 (±0.009)	0.754 (±0.009)	2.30 (±0.01)	2.01 (±0.01)
GS183L	5	0.45 (±0.1)	0.754 (±0.004)	0.748 (±0.004)	0.81 (±0.07)	1.17 (±0.01)
NN2V	6	0.65 (±0.1)	0.748 (±0.005)	0.741 (±0.005)	1.68 (±0.02)	2.44 (±0.00)
PA.01	5	6.80 (±0.1)	0.704 (±0.006)	0.698 (±0.006)	0.52 (±0.01)	1.51 (±0.01)
S006L	10	0.27 (±0.1)	0.756 (±0.007)	0.749 (±0.007)	-0.03 (±0.04)	0.09 (±0.03)
SAMID10116	4	0.45 (±0.1)	0.773 (±0.007)	0.767 (±0.007)	3.12 (±0.03)	1.46 (±0.01)
TC.01	5	5.24 (±0.1)	0.671 (±0.007)	0.664 (±0.007)	-2.20 (±0.02)	0.82 (±0.01)
WMF1	5	0.76 (±0.1)	0.770 (±0.007)	0.765 (±0.006)	3.92 (±0.02)	1.72 (±0.01)

Appendix Chapter 3

Table A3.1 | Clumped and bulk isotope composition of Late Jurassic–Early Cretaceous belemnites.
The Δ_{47} values are reported on the reference frame considering a 25–90 °C acid fractionation factor of 0.088‰ (Petersen *et al.*, in review). Seawater temperatures are calculated using the recalculated calibration of Wacker *et al.* (2014) (Equation 1.9). Seawater $\delta^{18}O$ values are calculated using the equation of Coplen (2007). The 1σ S.E. of the carbonate $\delta^{13}C$ and $\delta^{18}O$ values is 0.01‰. The ± uncertainty in the $\Delta_{47\ (RFAC)}$ values represent the external 1σ S.E. (including the *t*-value) of 2–7 replicate analyses (N). The error in the calculated temperatures and $\delta^{18}O_{sw}$ correspond to the 1σ S.E. of the $\Delta_{47\ (RFAC)}$. An extended table with all clumped isotope replicate measurements along with the ETFs are presented in Supplementary Data 3.1 and 3.2. Table 3.1 is a summary version of this table for each location. Palaeolatitudes from Young *et al.* (2018).

Sample	Location (palaeolatitude)	N	$\delta^{13}C$ (‰, VPDB)	$\delta^{18}O$ (‰, VPDB)	Δ_{47} (‰, RFAC)	Temp. (°C)	$\delta^{18}O_{sw}$ (‰, SMOW)
KH181050	Boyarka (74° N)	5	0.22	-1.55	0.707 (±0.005)	21 (±2)	-1.6 (±0.3)
KH181120	Boyarka (74° N)	5	1.12	-0.48	0.701 (±0.006)	23 (±2)	-0.1 (±0.5)
KH1827	Boyarka (74° N)	6	0.96	0.03	0.713 (±0.006)	19 (±2)	-0.5 (±0.4)
KH18285	Boyarka (74° N)	5	0.38	0.07	0.699 (±0.009)	24 (±3)	0.6 (±0.7)
KH18710	Boyarka (74° N)	5	0.60	-2.19	0.709 (±0.007)	20 (±3)	-2.4 (±0.5)
YCL214.031	Caravaca (24° N)	6	-1.25	-0.57	0.670 (±0.012)	36 (±5)	2.2 (±1.0)
YG015	Caravaca (24° N)	3	0.59	0.24	0.671 (±0.007)	36 (±3)	2.9 (±0.6)
YP14.5	Caravaca (24° N)	5	1.74	-0.41	0.691 (±0.013)	27 (±5)	0.7 (±1.0)
YP14001	Caravaca (24° N)	6	-0.29	-0.50	0.690 (±0.009)	28 (±4)	0.7 (±0.7)
YP1414	Caravaca (24° N)	4	0.95	-0.27	0.691 (±0.009)	27 (±3)	0.9 (±0.7)
PC7B1	Izhma (59° N)	7	-0.49	0.21	0.735 (±0.004)	11 (±1)	-1.9 (±0.3)
PC7C2	Izhma (59° N)	6	0.19	0.56	0.700 (±0.003)	24 (±1)	1.0 (±0.3)
PC9G23	Izhma (59° N)	5	-0.79	0.52	0.702 (±0.007)	23 (±3)	0.8 (±0.5)
PC9G8	Izhma (59° N)	7	1.16	0.98	0.688 (±0.005)	29 (±2)	2.4 (±0.4)
D2E	Speeton (40° N)	2	-0.46	-0.36	0.690 (±0.007)	28 (±3)	0.9 (±0.5)
D3D	Speeton (40° N)	2	-0.09	-0.21	0.680 (±0.020)	32 (±8)	1.8 (±1.5)
D4A	Speeton (40° N)	6	0.51	0.41	0.683 (±0.004)	31 (±2)	2.2 (±0.3)
SP1181	Speeton (40° N)	5	-0.12	-0.60	0.711 (±0.004)	20 (±2)	-1.0 (±0.3)
SP1297	Speeton (40° N)	4	0.60	-0.89	0.699 (±0.005)	24 (±2)	-0.4 (±0.4)
SP1S22C	Speeton (40° N)	5	0.60	-0.36	0.688 (±0.005)	29 (±2)	1.0 (±0.4)

Table continued on next page…

… table continued from previous page.

59-4.68	DSDP Site 511 (53° S)	5	-0.28	-1.25	0.699 (±0.009)	24 (±3)	-0.7 (±0.7)
60-2.21	DSDP Site 511 (53° S)	4	-0.02	-0.33	0.697 (±0.005)	25 (±2)	0.3 (±0.4)
60-2.93	DSDP Site 511 (53° S)	5	-0.22	-0.89	0.707 (±0.015)	21 (±6)	-0.9 (±1.1)
60-3.28	DSDP Site 511 (53° S)	4	-0.30	-0.39	0.707 (±0.012)	21 (±5)	-0.4 (±0.9)
62-5.82	DSDP Site 511 (53° S)	6	-0.52	-2.17	0.700 (±0.010)	24 (±4)	-1.7 (±0.8)
66-2.10	DSDP Site 511 (53° S)	5	-0.07	-1.65	0.690 (±0.004)	28 (±2)	-0.5 (±0.3)
66-2.53	DSDP Site 511 (53° S)	4	0.30	-1.59	0.691 (±0.007)	28 (±3)	-0.4 (±0.5)
66-4.65	DSDP Site 511 (53° S)	4	0.02	-1.43	0.699 (±0.007)	24 (±3)	-0.9 (±0.5)
66-4.119	DSDP Site 511 (53° S)	4	0.27	-1.22	0.698 (±0.013)	25 (±5)	-0.6 (±1.0)
67-4.LTH	DSDP Site 511 (53° S)	5	-0.90	-0.47	0.696 (±0.011)	25 (±4)	0.3 (±0.9)
70-2.125	DSDP Site 511 (53° S)	4	1.45	-0.89	0.690 (±0.011)	28 (±4)	0.3 (±0.8)

Figure A3.1 | Microphotos of three polished belemnite thick sections from DSDP Site 511.
These rostra are representative of all the samples investigated in this study. Most of the rostra are made of translucent light brown calcite. Calcite adjacent to the apical line is cloudy in appearance. For the clumped isotope analyses, only the translucent parts were sampled.

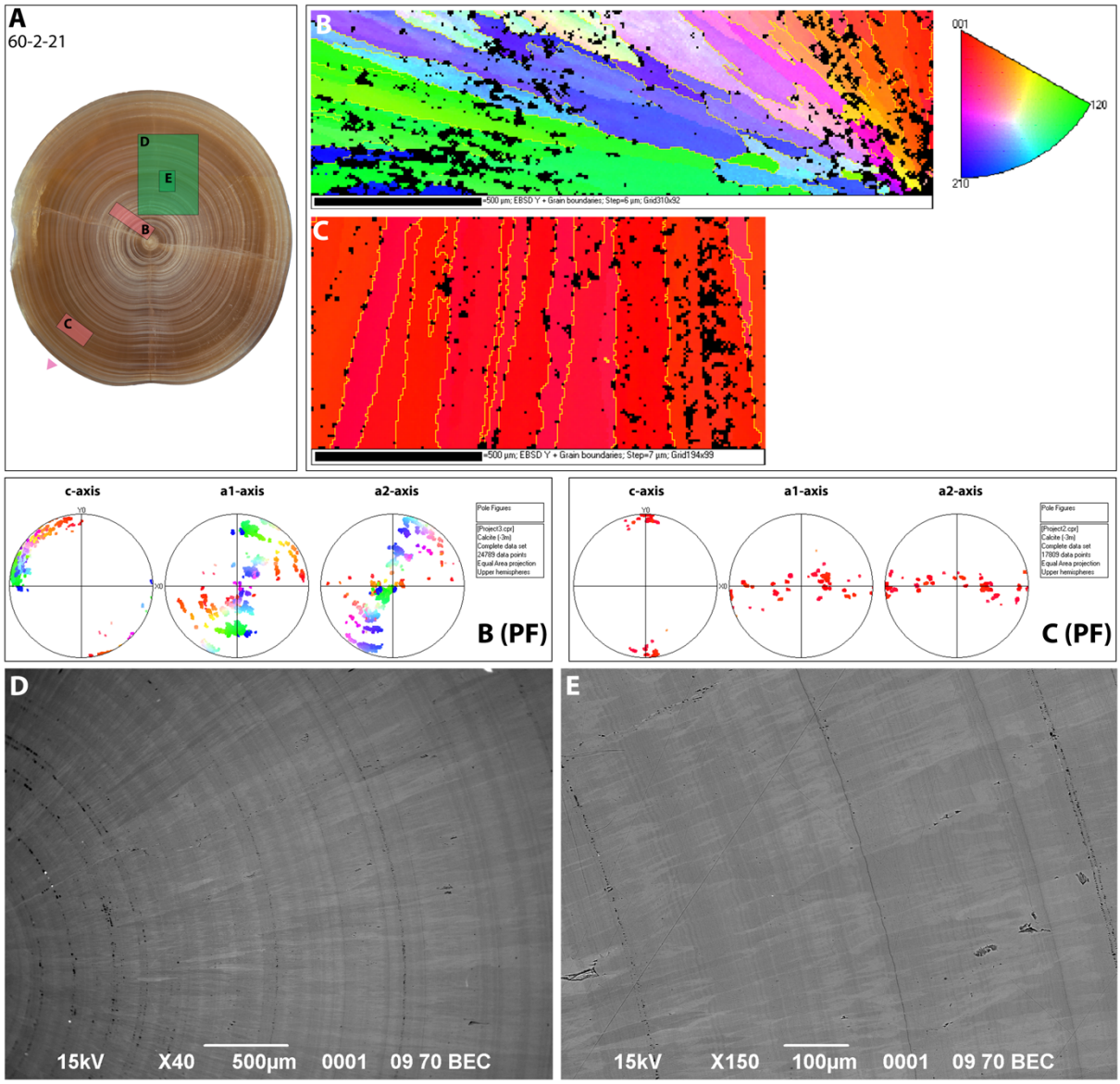

Figure A3.2 | Preservation of sample 60-2-21.
(A) Approximate positions of the SEM images and EBSD maps. The pink arrow marks the orientation of the sample during the EBSD analyses. **(B,C)** EBSD Y maps of the calcite rostra with grain boundaries (yellow lines, misorientation > 10°). Black indicates pixels where the orientation of the crystal could not be determined. On both maps X direction is horizontal, Y direction is vertical. **(B PF, C PF)** Pole figures of calcite c- and a-axes corresponding to the EBSD maps with analogous colouring. **(D,E)** SEM-BSE images of the rostra.

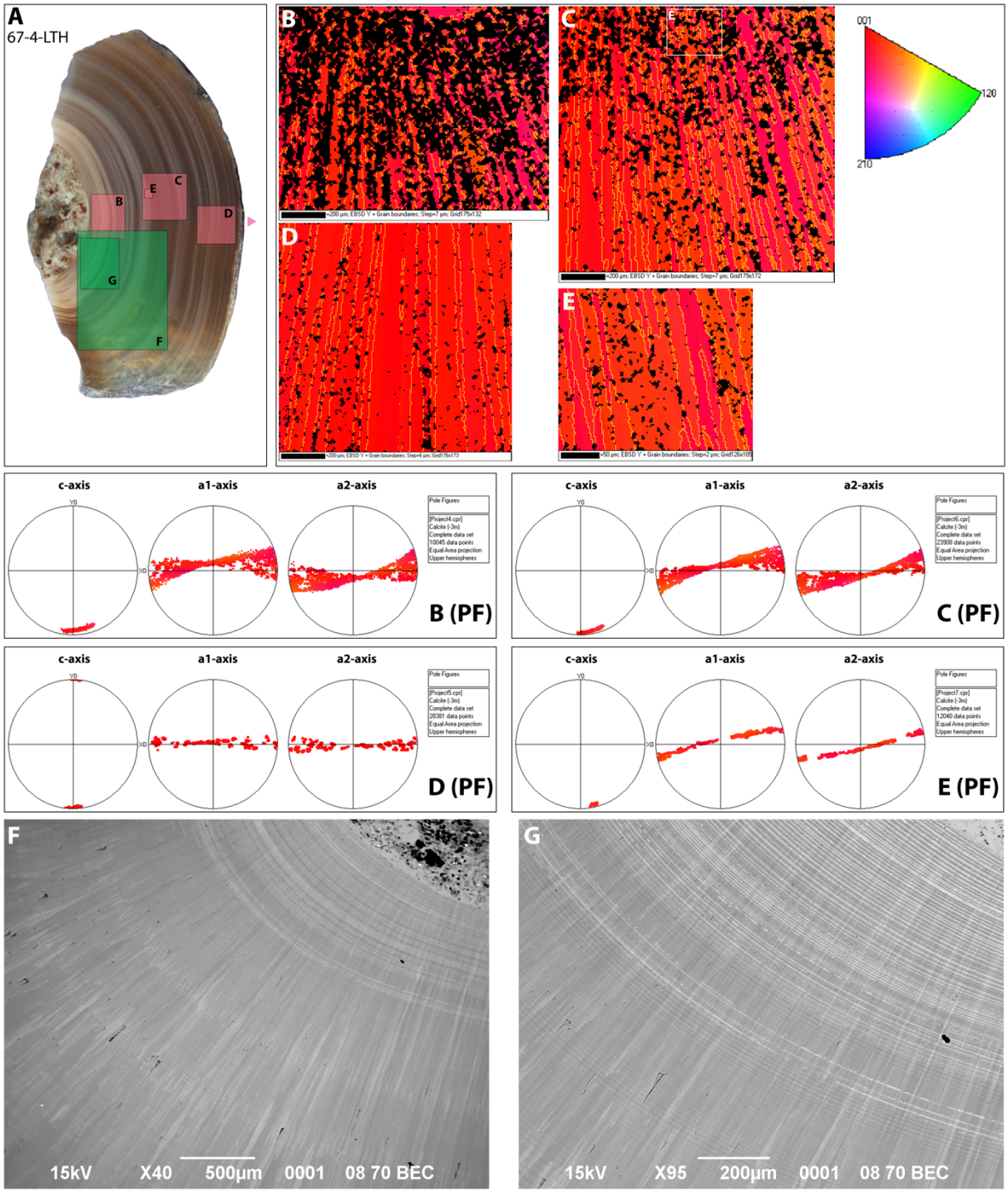

Figure A3.3 | Preservation of sample 67-4-LTH.
(A) Approximate positions of the SEM images and EBSD maps. The pink arrow marks the orientation of the sample during the EBSD analyses. **(B,C)** EBSD Y maps of the calcite rostra with grain boundaries (yellow lines, misorientation > 10°). Black indicates pixels where the orientation of the crystal could not be determined. On both maps X direction is horizontal, Y direction is vertical. **(B PF, C PF)** Pole figures of calcite c- and a-axes corresponding to the EBSD maps with analogous colouring. **(D,E)** SEM-BSE images of the rostra.

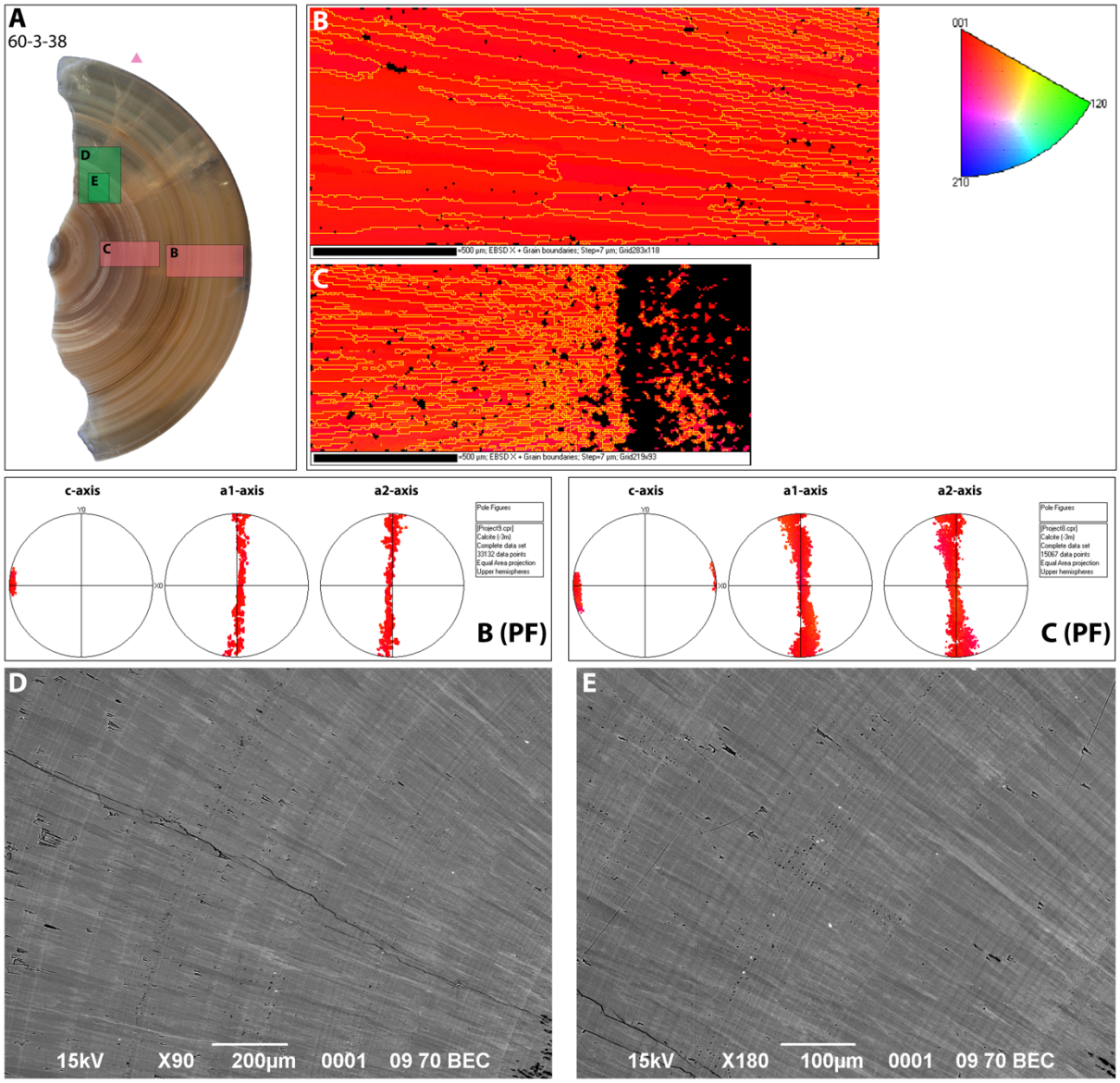

Figure A3.4 | Preservation of sample 60-3-38.
(A) Approximate positions of the SEM images and EBSD maps. The pink arrow marks the orientation of the sample during the EBSD analyses. **(B,C)** EBSD X maps of the calcite rostra with grain boundaries (yellow lines, misorientation > 10°). Black indicates pixels where the orientation of the crystal could not be determined. On both maps X direction is horizontal, Y direction is vertical. **(B PF, C PF)** Pole figures of calcite c- and a-axes corresponding to the EBSD maps with analogous colouring. **(D,E)** SEM-BSE images of the rostra.

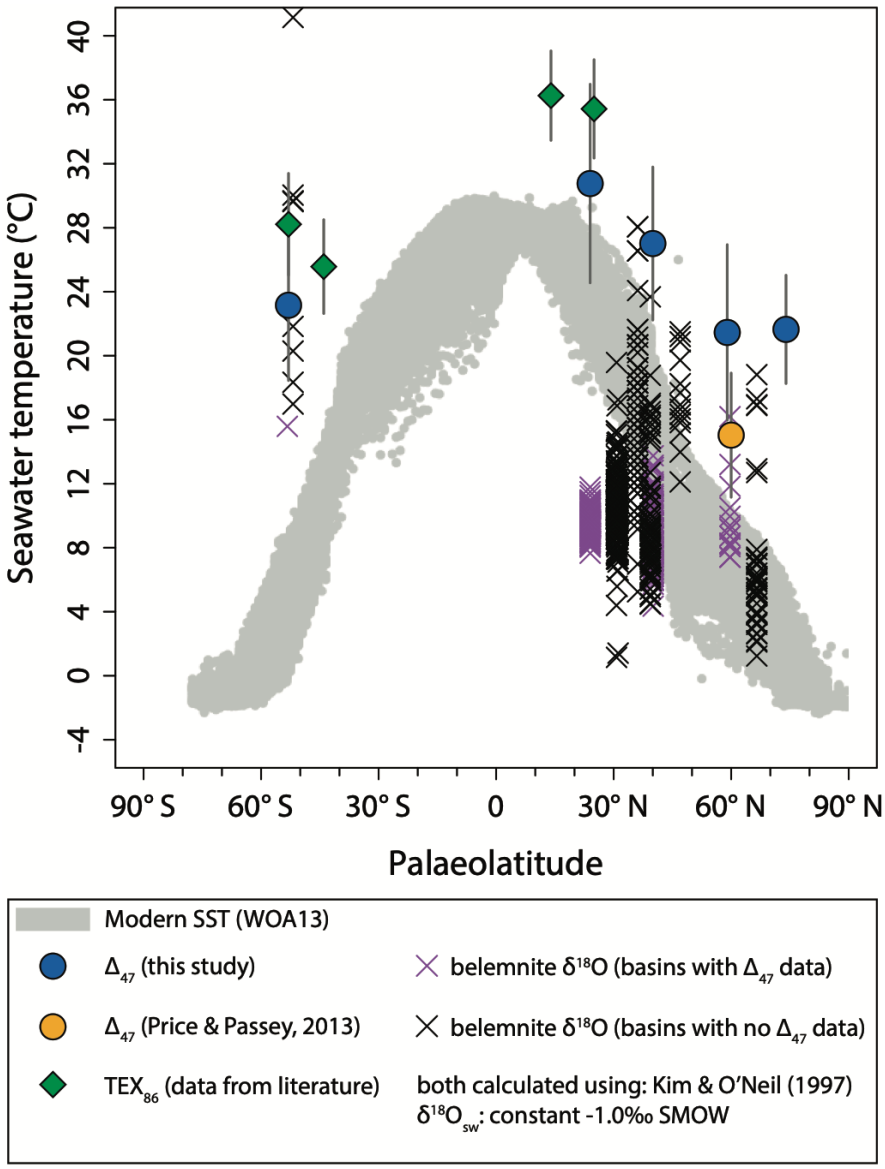

Figure A3.5 | Compilation of Early Cretaceous belemnite $\delta^{18}O$-based seawater temperatures (Kim & O'Neil, 1997).

With an erroneous $\delta^{18}O_{sw}$ estimate belemnite $\delta^{18}O$-based palaeoseawater temperatures could be significantly underestimated, especially around the tropics. For a detailed description of the data on this figure, see Figure 3.4. Plotted belemnites are Berriasian–Valanginian–Hauterivian in age (ca. 131–145 million years ago) and show no stratigraphically significant temporal temperature evolution. Belemnites deriving from basins that have no Δ_{47} data are highlighted. Temperature estimates above 40 °C are discarded because they highly likely represent altered values. Data for this figure can be found in Supplementary Data 3.1, 3.2, and 7.1.

Appendix Chapter 4

Table A4.1 | Bulk and clumped isotope data of the analysed samples from the Russian Platform.
The [*Brand*]/IUPAC Δ_{47} values are reported on the reference frame considering a 25–90 °C acid fractionation factor of 0.088‰ (Petersen *et al.*, in review). Seawater temperatures are calculated using the reprocessed calibration of Wacker *et al.* (2014) (Equation 1.9). Water $\delta^{18}O$ values are calculated using the equation of Coplen (2007). An extended table with all clumped isotope replicate measurements along with the ETFs are presented in Supplementary Data 4.1.

Sample	Taxonomy	N	$\delta^{18}O$ (‰, VPDB)	Δ_{47} (‰, RFAC)	Temp. (°C)	Water $\delta^{18}O$ (‰, SMOW)
R111.1	ammonite	6	0.31	0.719 (±0.007)	17 (±3)	-0.7 (±0.6)
R124	cylindroteuthid	6	1.62	0.714 (±0.007)	19 (±3)	1.0 (±0.6)
R134a	cylindroteuthid	7	1.63	0.707 (±0.008)	21 (±3)	1.6 (±0.7)
R137a	mesohibolithid	6	0.89	0.699 (±0.004)	24 (±2)	1.4 (±0.4)
R150	cylindroteuthid	4	1.97	0.719 (±0.008)	17 (±3)	1.0 (±0.7)
R37	cylindroteuthid	5	1.71	0.708 (±0.006)	21 (±2)	1.6 (±0.5)
R48.1	ammonite	9	1.20	0.718 (±0.006)	17 (±2)	0.3 (±0.5)
R96	mesohibolithid	7	0.96	0.705 (±0.006)	22 (±3)	1.1 (±0.5)
RM1	cylindroteuthid	9	0.24	0.687 (±0.004)	29 (±2)	1.7 (±0.4)
RM100b	cylindroteuthid	8	0.4	0.702 (±0.005)	23 (±2)	0.7 (±0.4)
RM15	cylindroteuthid	8	0.10	0.711 (±0.007)	20 (±3)	-0.3 (±0.5)
RM98a	cylindroteuthid	6	-1.08	0.699 (±0.005)	23 (±2)	-0.6 (±0.4)
RMII103b	ammonite	5	-1.48	0.731 (±0.012)	13 (±5)	-3.3 (±1.0)
RMII42	cylindroteuthid	7	-0.93	0.708 (±0.005)	21 (±2)	-1.0 (±0.4)
RMII43	cylindroteuthid	8	-0.76	0.708 (±0.008)	21 (±3)	-0.9 (±0.6)
RMII50	ammonite	13	-1.78	0.706 (±0.003)	22 (±1)	-1.7 (±0.2)
RMII52a	cylindroteuthid	10	1.66	0.710 (±0.006)	20 (±2)	1.4 (±0.5)
RMII63	cylindroteuthid	7	1.61	0.691 (±0.008)	27 (±3)	2.7 (±0.6)
RMII92	cylindroteuthid	5	1.63	0.721 (±0.004)	16 (±2)	0.5 (±0.3)
RT10	cylindroteuthid	7	-1.33	0.707 (±0.006)	21 (±2)	-1.4 (±0.5)
RT15	cylindroteuthid	7	-1.55	0.718 (±0.007)	17 (±3)	-2.4 (±0.6)
RT16	cylindroteuthid	6	-1.36	0.706 (±0.007)	22 (±3)	-1.3 (±0.6)
RT17	cylindroteuthid	6	-1.30	0.706 (±0.005)	22 (±2)	-1.3 (±0.4)
RT20	cylindroteuthid	7	-1.71	0.715 (±0.004)	18 (±1)	-2.4 (±0.3)

Table A4.2 | Correlation between Submediterranean and (Sub)Boreal ammonite zonal schemes of the uppermost Callovian–lowermost Upper Kimmeridgian.

After Matyja and Wierzbowski (2000); Głowniak *et al.* (2010); Wierzbowski *et al.* (2013); Wierzbowski and Matyja (2014); Scherzinger *et al.* (2016). Position of the base of each stratigraphical division is given in stratigraphical unit scale based on the assumed equal duration of Submediterranean ammonite subchrons.

SUBMEDITERRANEAN PROVINCE				(SUB)BOREAL PROVINCE			
Substage	Zone	Subzone	Position of the base	Position of the base	Subzone	Zone	Substage
Up. Kimmeridgian (pars)	Acanthicum		26.5	27.5	Lallieranum	Mutabilis	Up. Kimmeridgian (pars)
				26.5	Mutabilis		
Lower Kimmeridgian	Divisum	Uhlandi	25.5	24.25	Askepta	Cymodoce	Lower Kimmeridgian
		Tenuicostata	24.5				
	Hypselocyclum	Lothari	23.5	19.77	Cymodoce		
		Hyppolytense	22.5				
	Platynota	Guilherandense	21.5				
		Desmoides	20.5				
		Polygyratus	19.5				
"Former uppermost Oxfordian"	Planula	Galar	18.5	17.24	Normandiana	Baylei	
		Planula	17				
	Bimammatum	Hauffianum	16	15	Densicostata		
		Bimammatum	15				
Upper Oxfordian	Hypselum		14	14		Rosenkrantzi	Upper Oxfordian
	Bifurcatus	Grossouvrei	13	13.1		Regulare	
				12.73	Serratum	Serratum	
		Stenocycloides	12	12.33	Koldeweyense		
		Wartae	11	10.94	Glosense	Glosense	
Middle Oxfordian	Transversarium	Elisabethae	10	10.44	Ilovaiskii		Middle Oxfordian
				9.75	Blakei	Tenuiserratum	
		Buckmani	9	9.5	Tenuiserratum		
	Plicatilis	Arkelli	8	8.5	Maltonense	Densiplicatum	
		Ouatius	7	6	Vertebrale		
		Patturatensis	6				
Lower Oxfordian	Cordatum	Cordatum	5	5	Cordatum	Cordatum	Lower Oxfordian
		Costicardia	4	4	Costicardia		
		Bukowskii	3	3	Bukowskii		
	Mariae	Praecordatum	2	2	Praecordatum	Mariae	
		Scarburgense	1	1	Scarburgense		
Up. Callov. (pars)	Lamberti (pars)	Lamberti	0	0	Lamberti	Lamberti (pars)	Up. Callov. (pars)

Appendix Chapter 5

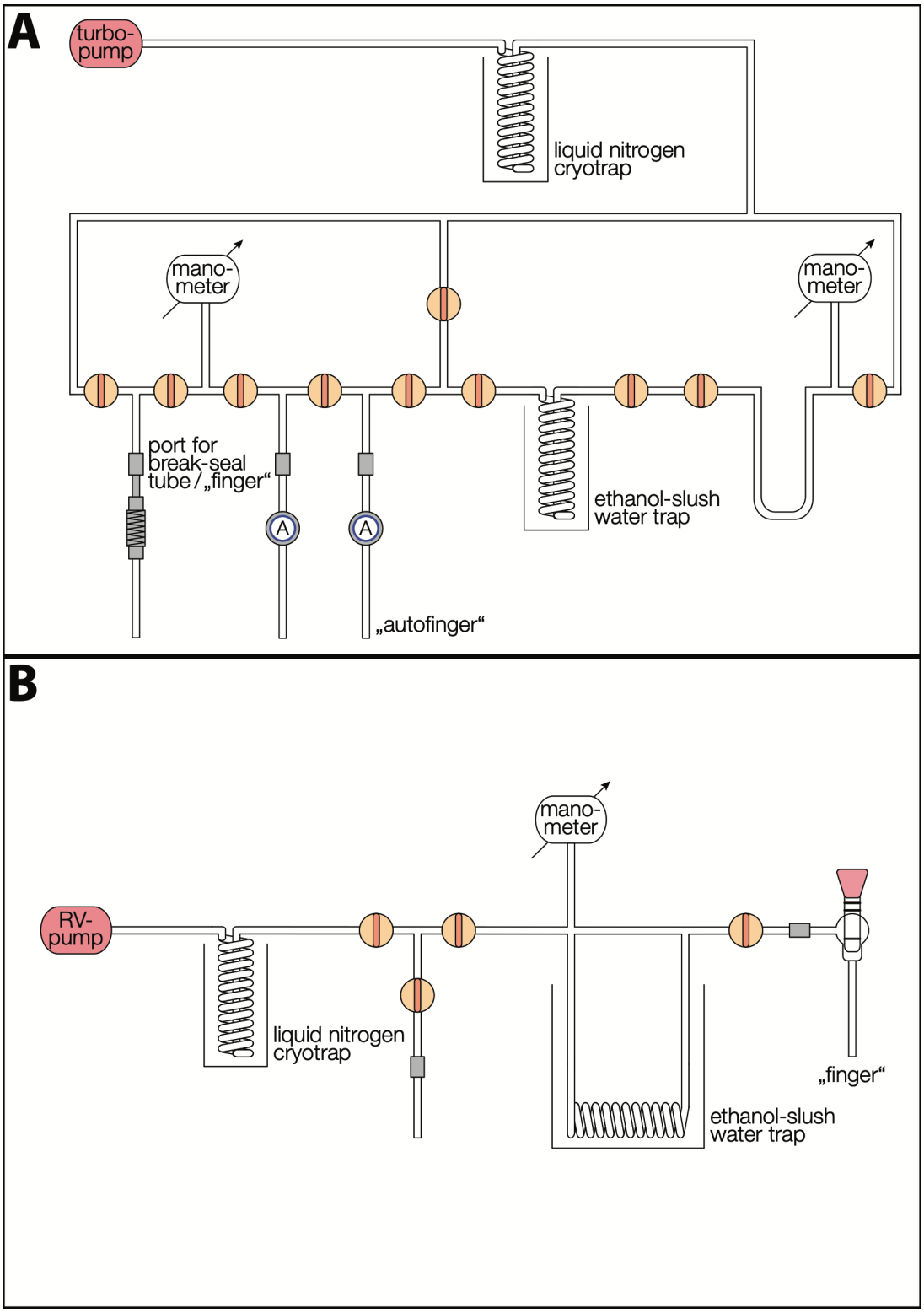

Figure A5.1 | Schematic of the vacuum lines used for the preparation of the equilibrated gases.
(A) High-vacuum line pumped with a turbomolecular pump. The average pressure we commonly achieve while preparing the equilibrated gases is 4.0 x 10^{-7} mBar, measured at the turbopump. **(B)** Vacuum line pumped with a rotary vane pump, on which the 25 °C gases are initially stripped of water.

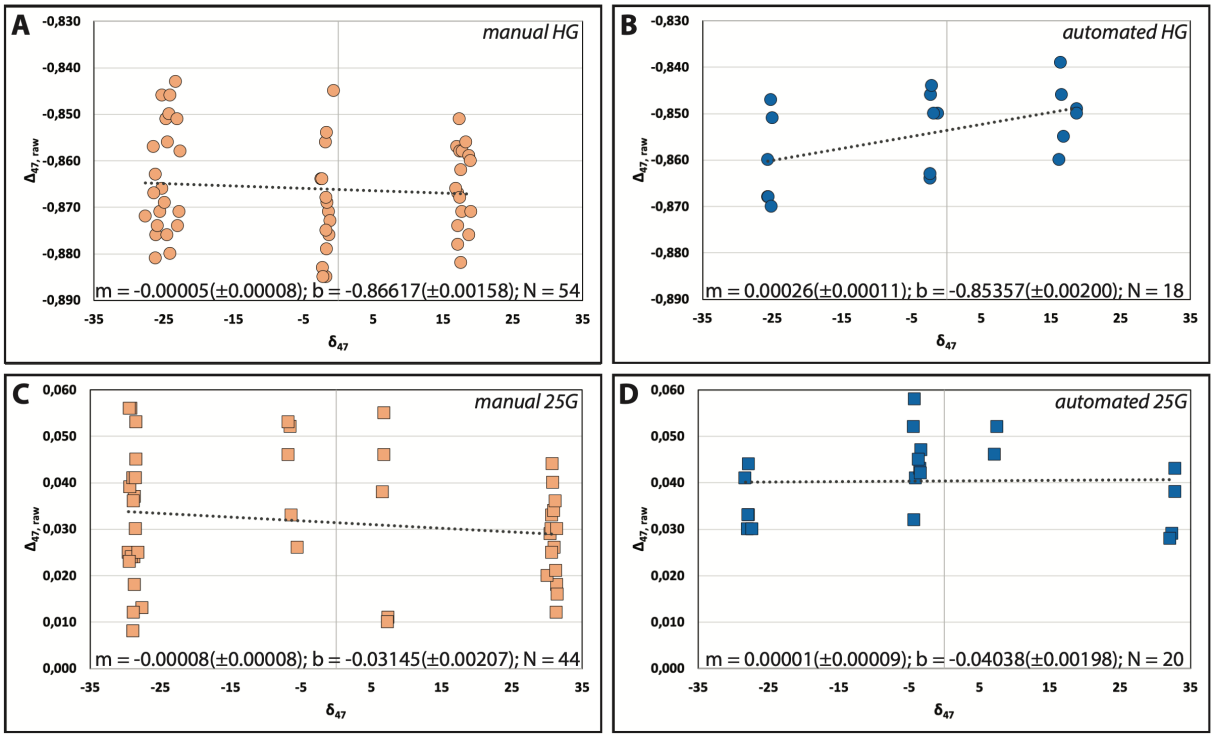

Figure A5.2 | Plots of $\Delta_{47,\,raw}$ *vs.* δ_{47} for the equilibrated gases (1000 °C and 25 °C) prepared using the manual and the automated technique.

(A) $\Delta_{47,\,raw}$ *vs.* δ_{47} of 1000 °C gases prepared using the manual technique. **(B)** $\Delta_{47,\,raw}$ *vs.* δ_{47} of 1000 °C gases prepared using the automated technique. **(C)** $\Delta_{47,\,raw}$ *vs.* δ_{47} of 25 °C gases prepared using the manual technique. **(D)** $\Delta_{47,\,raw}$ *vs.* δ_{47} of 25 °C gases prepared using the automated technique. For all plots: m = slope, b = intercept of a simple linear regression, N = number of replicate analyses.

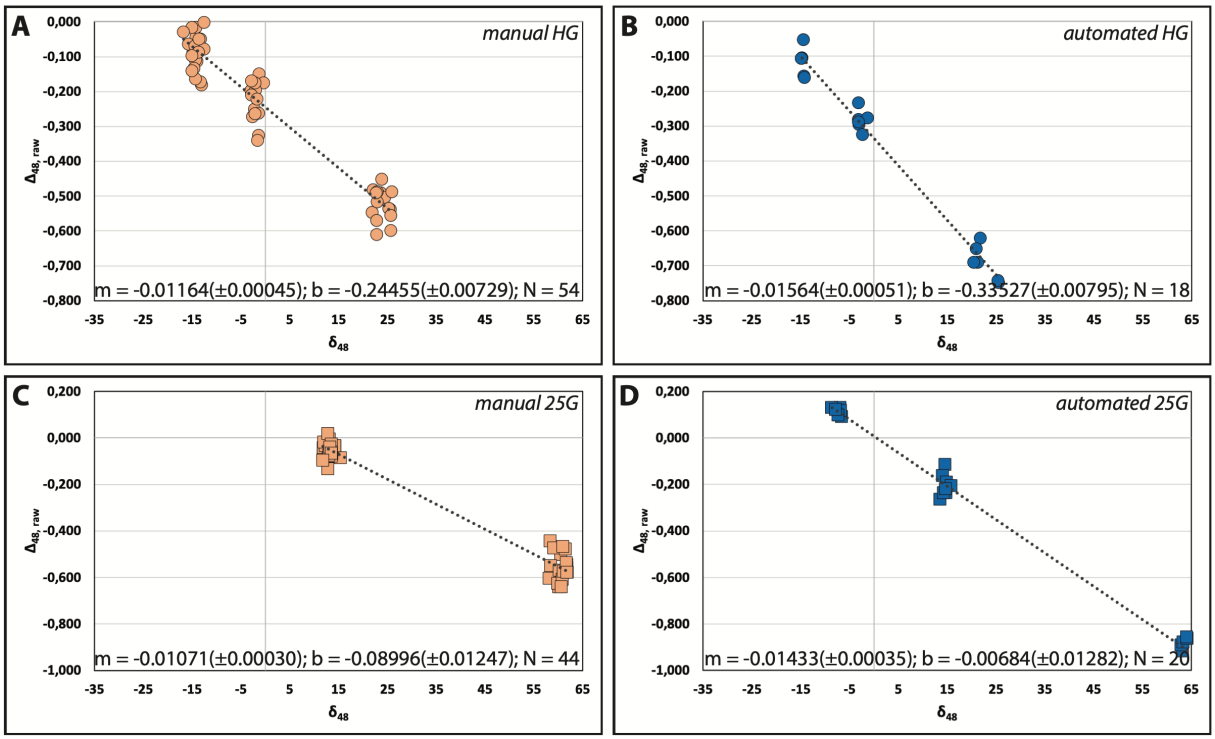

Figure A5.3 | Plots of $\Delta_{48,\,raw}$ *vs.* δ_{48} for the equilibrated gases (1000 °C and 25 °C) prepared using the manual and the automated technique.

(A) $\Delta_{48,\,raw}$ *vs.* δ_{48} of 1000 °C gases prepared using the manual technique. **(B)** $\Delta_{48,\,raw}$ *vs.* δ_{48} of 1000 °C gases prepared using the automated technique. **(C)** $\Delta_{48,\,raw}$ *vs.* δ_{48} of 25 °C gases prepared using the manual technique. **(D)** $\Delta_{48,\,raw}$ *vs.* δ_{48} of 25 °C gases prepared using the automated technique. For all plots: m = slope, b = intercept of a simple linear regression, N = number of replicate analyses.

Zusammenfassung

Die stabile Sauerstoffisotopenzusammensetzung ($\delta^{18}O$) der $CaCO_3$-Skelette von marinen Organismen diente lange Zeit als Proxy zur Rekonstruktion vergangener Ozeantemperaturen. Die Genauigkeit des $\delta^{18}O$-Karbonat-Thermometers wird jedoch durch zwei wesentliche Einschränkungen limitiert: (1) Es muss eine Sauerstoffisotopenzusammensetzung für das Paläo-Meerwasser ($\delta^{18}O_{sw}$) angenommen werden, um Meerwassertemperarekonstruieren zu können. Es ist zur Zeit noch Gegenstand der Forschung, ob sich $\delta^{18}O_{sw}$ über geologische Zeiträume hinweg durch die an den ozeanischen Rückensystemen stattfindenden Wasser-Gesteinswechselwirkungen signifikant verändert haben könnte (> 6‰). Dortige Hochtemperatur (> 350 °C) Gesteins-Wasser-Wechselwirkungen führen zu einer ^{18}O-Anreicherung im Meerwasser, während der Austausch von Sauerstoffisotopen zwischen Silikaten und Wasser unterhalb 350 °C zu einer ^{18}O-Abreicherung führt. Zur Erklärung der unverhältnismäßig warmen paläozoischen, aus $\delta^{18}O$ (Karbonat) Messungen abgeleiteten, Temperaturen wurde postuliert, dass sich das Verhältnis von Hoch- zu Tieftemperaturalteration im Laufe des Paläozoikums geändert haben könnte. Darüber hinaus gibt es selbst in den modernen Ozeanen eine erhebliche Variation (bis zu 4‰) in $\delta^{18}O_{sw}$ entlang der Breitengrade und verschiedener Meeresumgebungen, die hauptsächlich auf eine durch die Verdunstung verursachte ^{18}O-Anreicherung von oberflächennahem Meerwasser und auf einen variablen kontinentalen Süßwasserzufluss zurückzuführen sind. Im Gegensatz zum $\delta^{18}O$-Thermometer ist das Clumped Isotope Thermometer unabhängig von der Sauerstoffisotopenzusammensetzung des Meerwassers (und des Mutterfluids im Allgemeinen), da es auf der Fraktionierung von Isotopen innerhalb einer einzigen Karbonatphase basiert.

(2) Eine zweite Einschränkung des $\delta^{18}O$-Thermometers besteht darin, dass kinetische Effekte (Vitaleffekte) während der Biomineralisation die Isotopenzusammensetzung

der Karbonate beeinflussen können. Wachstumsraten- oder pH-abhängige Vitaleffekte auf $\delta^{18}O$ wurden unter anderem bei Brachiopoden und Korallen erkannt. Jüngste Studien beobachteten kinetische Effekte auf die Clumped Isotope Zusammensetzung (Δ_{47}) von Korallen, bestimmten Foraminiferen und Stachelhäutern. Da Brachiopoden aufgrund ihres häufigen Auftretens in Sedimenten und ihrer allgemein guten Erhaltung das am weitesten verbreitete Archiv für eine Rekonstruktion der Paläoozeanographie sind, ist es unerlässlich, an ihnen Art und Ausmaß der kinetischen Effekte auf Δ_{47} zu untersuchen. In **Kapitel 2** dieser Arbeit untersuchte ich, ob wir systematische Trends in $\delta^{18}O$(Karb) und Δ_{47} von Brachiopodenschalen beobachten können. Hierzu analysierte ich 18 moderne Proben, für welche die Wachstumstemperatur und $\delta^{18}O_{sw}$ unabhängig voneinander bekannt waren. Ich habe festgestellt, dass es eine signifikante negative Korrelation zwischen „offset Δ_{47}“ und „offset $\delta^{18}O$“ gibt, wobei der jeweilige „offset“ die Differenz zum erwarteten Gleichgewicht darstellt (**Abbildung 2.2 auf Seite 23**). Ein solcher Trend deutet auf kinetische Effekte hin, welche entweder durch Knudsen-Diffusion oder unvollständige $CO_{2\,(aq)}$ Hydratations- und Hydroxylierungsreaktionen verursacht werden. Korrelationen zwischen Schalenwachstumsraten und obig erklärten offset-Werten (**Abbildung 2.4 auf Seite 28**) sowie zwischen Schalen-$\delta^{18}O$ und -$\delta^{13}C$ liefern weitere Argumente für das Auftreten solcher kinetischen Effekte.

Bei Brachiopoden hängt das Ausmaß der kinetischen Effekte auf Δ_{47} und $\delta^{18}O$ von der Wachstumsrate der Schale ab. Da es schwierig ist, die Wachstumsraten von ausgestorbenen Brachiopoden zu bestimmen, sind sie vielleicht nicht das zuverlässigste Archiv, um an ihnen Meerestemperaturen in die Tiefe der Zeit zu rekonstruieren. In den **Kapiteln 3 und 4** wende ich mich fossilen Belemniten zu, um an Ihnen über Δ_{47}-Messungen mesozoische Meereswassertemperaturen zu rekonstruieren. Bisherige $\delta^{18}O$-basierte Untersuchungen an zeit- und ortsgleich abgelagerten Belemniten und Brachiopoden ergaben wärmere Meerwassertemperaturen für Brachiopoden. Wie ich jedoch in **Kapitel 2**

dargelegt habe, führt letztlich die in die Mineralisation von Brachiopodenschalen involvierte Kinetik zu diesen wärmeren Temperaturabschätzungen. Im Vergleich zu Brachiopoden scheiden Belemniten ihr Karbonat vermutlich näher am Gleichgewicht ab und ermöglichen somit eine genauere Temperaturrekonstruktion.

Insgesamt habe ich 56 jurassisch–kretazische (vor etwa 160–125 Millionen Jahren) Belemnitenrostren für Δ_{47} untersucht (**Abbildung Z**). Oberjurassiche bis unterkretazische Belemniten aus der DSDP Site 511 liefern milde (25±4 °C) Meerwassertemperaturen in hohen südlichen Breitengraden, die im Bereich der TEX_{86}^{H}-Temperaturen liegen, die am gleichen Standort gemessen wurden (**Abbildung 3.2 auf Seite 42**). Im Vergleich dazu liefert das $\delta^{18}O$-Thermometer für die gleichen Rostra, unter der Annahme eines $\delta^{18}O_{sw}$ von -1‰ SMOW und unter Verwendung der von Kim und O'Neil (1997) bestimmten Temperaturabhängigkeit der Sauerstoffisotopenfraktionierung zwischen Kalzit und Wasser, 10 °C kältere Temperaturen. Mit Δ_{47}-Daten konsistente Temperaturen werden

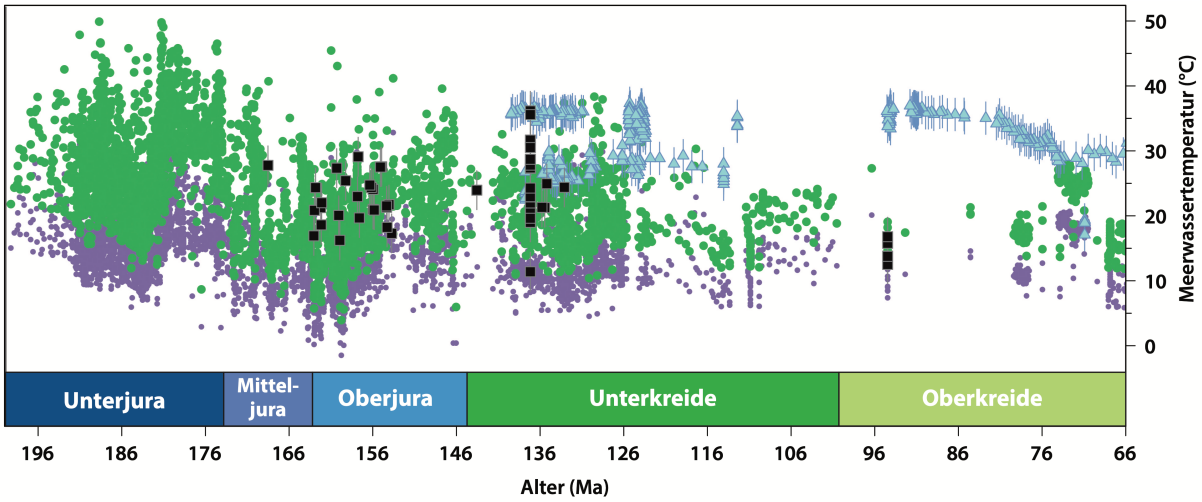

Abbildung Z | Die Temperaturentwicklung der Jura- und Kreidemeere, wie sie aus den $\delta^{18}O$ und Δ_{47} Analysen von Belemniten sowie aus bisherigen TEX_{86} Untersuchungen hervorgeht.
Die 56, auf Belemnit-Δ_{47} basierenden Temperaturabschätzungen aus dieser Studie (schwarze Quadrate), werden zusammen mit bereits publizierten TEX_{86}^{H}-Temperaturen (blaue Dreiecke) und Belemnit-$\delta^{18}O$-Temperaturen dargestellt. Belemnit $\delta^{18}O$-basierte Temperatubestimmungen konvergieren mit aus Δ_{47}- und TEX_{86} abgeleiteten Temperaturen, wenn die Coplen (2007) Formel zur Temperaturabhäbgigkeit der Sauerstoffisotopenfraktionierung zwischen Kalzit und Wasser und ein moderner Wert für $\delta^{18}O_{sw}$ verwendet werden. Die Verwendung der entsprechenden Kim & O'Neil (1997) Formel und eines $\delta^{18}O_{sw}$ von -1‰ SMOW führt hingegen zu einer Unterschätzung der Meerwassertemperaturen. Die Variation der auf $\delta^{18}O$ basierenden Temperaturen hängt vermutlich mit einem inhomogenen $\delta^{18}O_{sw}$ zusammen, welcher womöglich lokal und breitengradabhängig varierte (**Kapitel 3**).

hingegen erzielt, wenn die Temperaturabhängigkeit der Sauerstoffisotopenfraktionierung zwischen Kalzit und Wasser nach Coplen (2007) verwendet wird. Diese unterscheidet sich von der von Kim & O'Neil (1997) dadurch, dass sie näher am Gleichgewicht liegt. Zusätzlich untersuchte ich valanginische (Unterkreide, vor etwa 135 Millionen Jahren) Belemniten aus den mittleren und nördlichen Breiten der nördlichen Hemisphäre, die an vier Standorten in Spanien, Großbritannien und Russland beprobt wurden. Die Δ_{47} Schätzungen der Meeresoberflächentemperatur (21±5 °C bis 31±6 °C) sind konstant wärmer als moderne Äquivalente und deuten auf einen gegenüber heute deutlich verringerten Breitengrad-abhängigen Temperaturgradienten hin (**Abbildung 3.3 auf Seite 45**). Die in **Kapitel 3** vorgestellten milden Temperaturen in nördlichen und südlichen hohen Breitengraden deuten vermutlich auf die Abwesenheit von Polareis hin und liefern ein zusätzliches Argument für die Bedeutung der polaren Amplifikation in einer Welt mit hohem pCO_2. Aus dem Kalzit-$\delta^{18}O$ und den gemessenen Δ_{47}-Temperaturen konnten $\delta^{18}O_{sw}$ Werte berechnet werden, die positiver sind als erwartet (valanginischer Mittelwert: 0,5‰ SMOW) und im Bereich der modernen Werte liegen (**Abbildung 3.4 auf Seite 50**). Das damalige Meerwasser besaß wahrscheinlich eine heterogene Zusammensetzung bezüglich $\delta^{18}O$ über die Ozeanbecken hinweg, und die Verdunstung und der kontinentale Süßwasserzufluss spielten eine wichtige Rolle in der Kontrolle lokaler $\delta^{18}O_{sw}$-Werte. In **Kapitel 4** wende ich mich einer Jura-Lokalität in Russland zu, für welchen mittels des Karbonat-Sauerstoff-Isotopen-Thermometers unter der Annahme eines konstanten $\delta^{18}O_{sw}$ für den beprobten Zeitraum eine Erwärmung von etwa 10 °C postuliert wurde. Im Gegensatz dazu implizieren die Δ_{47}-Messungen an diesen Belemniten konstante Meerwassertemperaturen von etwa 21(±2) °C (**Abbildung 4.2 auf Seite 63**). Eine durch Aussüßung verursachte zeitliche Abnahme von $\delta^{18}O_{sw}$ kann die Diskrepanz zwischen den beiden Datensätzen erklären. Eine für denselben Zeitabschnitt auftretende Verringerung von εNd sowie

Veränderungen der Ammoniten- und Ostrakoden-Biotope stehen im Einklang mit einem erhöhten Süßwassereintrag in das Becken.

Belemniten scheinen ein gutes geochemisches Archiv für die Paläothermometrie darzustellen. Da sie jedoch ausgestorben sind, können wir moderne Proben nicht auf eine mögliche Bedeutung von Vitaleffekten untersuchen. Eine neue Methode ist notwendig, um für biogene Karbonatarchive, die keine modernen Analoga mehr haben, das Ausmaß und die Art der kinetischen Effekte auf Δ_{47} und $\delta^{18}O$ zu erfassen. In den **Kapiteln 5 und 6** zeige ich, dass wir nun an der Goethe-Universität weltweit erstmals hochpräzise Δ_{48}-Messungen neben herkömmlichen Δ_{47} Karbonatanalysen vornehmen können (**Abbildung 6.5 auf Seite 97**). Der Δ_{48}-Wert eines Karbonats ist, wie sein Δ_{47}-Wert, unabhängig von der isotopischen Zusammensetzung des Mutterfluids. In einer Auftragung von Δ_{48} *vs.* Δ_{47} wird die Position eines Karbonats, wenn es im thermodynamischen Gleichgewicht ausgefällt wird, nur durch seine Bildungstemperatur bestimmt. Eine aktuelle Studie hat gezeigt, dass kinetische Effekte zu einer systematischen Ablenkung von der temperaturabhängigen Gleichgewichtslinie führen: So wird in einer Auftragung von Δ_{48} *vs.* Δ_{47} beispielsweise erwartet, dass Brachiopodendaten, abhängig von dem der Fällung zugrunde liegendem geschwindigkeitsbestimmenden Schritt, entweder unterhalb oder oberhalb der Gleichgewichtslinie liegen sollten (**Abbildung 7.2 auf Seite 102**). Ihre wahren Präzipitationstemperaturen könnten aus einer solchen Auftragung rekonstruiert werden, wenn der "kinetische" Punkt mit einer für die jeweilige Kinetik charakteristischen Steigung auf die Gleichgewichtslinie projiziert wird. Belemniten hingegen sollten, falls sie wirklich Ihr Karbonat im thermodynamischen Gleichgewicht präzipitiert hätten, auf der Gleichgewichtslinie plotten. Die kombinierte Analyse von Δ_{48} und Δ_{47} Analyse von Karbonaten ist somit ein vielversprechendes Werkzeug für die Rekonstruktion von vergangenen Erdoberflächentemperaturen und zur Untersuchung und Rekonstruktion der Biomineralisation von (fossilen) Karbonatarchiven.